

# Measurement of the Ratios of Branching Fractions

$$\mathcal{B}(B_s^0 \rightarrow D_s^- \pi^+ \pi^+ \pi^-) / \mathcal{B}(B^0 \rightarrow D^- \pi^+ \pi^+ \pi^-)$$

and

$$\mathcal{B}(B_s^0 \rightarrow D_s^- \pi^+) / \mathcal{B}(B^0 \rightarrow D^- \pi^+)$$

with the CDF Detector

by

Arkadiy Bolshov

Submitted to the Department of Physics  
in partial fulfillment of the requirements for the degree of

Doctor of Philosophy

at the

MASSACHUSETTS INSTITUTE OF TECHNOLOGY

December 2006

[February 2007]

© Arkadiy Bolshov, MMVI. All rights reserved.

The author hereby grants to MIT permission to reproduce and  
distribute publicly paper and electronic copies of this thesis document  
in whole or in part.

Author .....

Department of Physics

December 28, 2006

Certified by .....

Christoph M. E. Paus

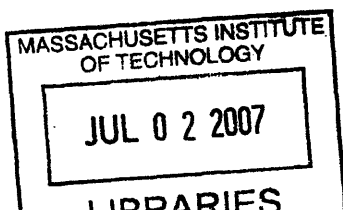
Professor

Thesis Supervisor

Accepted by .....

Thomas J. Greytak

Associate Department Head for Education, Professor



ARCHIVES



# Measurement of the Ratios of Branching Fractions

$$\mathcal{B}(B_s^0 \rightarrow D_s^- \pi^+ \pi^+ \pi^-) / \mathcal{B}(B^0 \rightarrow D^- \pi^+ \pi^+ \pi^-)$$

and

$$\mathcal{B}(B_s^0 \rightarrow D_s^- \pi^+) / \mathcal{B}(B^0 \rightarrow D^- \pi^+)$$

with the CDF Detector

by

Arkadiy Bolshov

Submitted to the Department of Physics  
on December 28, 2006, in partial fulfillment of the  
requirements for the degree of  
Doctor of Philosophy

## Abstract

We present the measurement of the ratios of branching fractions  $\mathcal{B}(B_s^0 \rightarrow D_s^- \pi^+)$  to  $\mathcal{B}(B^0 \rightarrow D^- \pi^+)$ , and  $\mathcal{B}(B_s^0 \rightarrow D_s^- \pi^+ \pi^+ \pi^-)$  to  $\mathcal{B}(B^0 \rightarrow D^- \pi^+ \pi^+ \pi^-)$ . We analyze data taken with the CDF II detector that corresponds to an integrated luminosity of  $355 \text{ pb}^{-1}$  in  $p\bar{p}$  collisions at  $\sqrt{s} = 1.96 \text{ TeV}$  at the Fermilab Tevatron. Using a novel displaced track trigger we reconstruct  $494 \pm 28$   $B_s^0 \rightarrow D_s^- \pi^+$  decays,  $8098 \pm 114$   $B^0 \rightarrow D^- \pi^+$  decays,  $159 \pm 17$   $B_s^0 \rightarrow D_s^- \pi^+ \pi^+ \pi^-$  decays, and  $3288 \pm 76$   $B^0 \rightarrow D^- \pi^+ \pi^+ \pi^-$  decays. Using the world average value of the  $B_s^0$ -to- $B^0$  production ratio  $f_s/f_d = 0.259 \pm 0.038$ , we determine the ratios of branching fractions

$$\frac{\mathcal{B}(B_s^0 \rightarrow D_s^- \pi^+)}{\mathcal{B}(B^0 \rightarrow D^- \pi^+)} = 1.13 \pm 0.08(\text{stat.}) \pm 0.05(\text{syst.}) \pm 0.15(\text{BR}) \pm 0.17(\text{PR}),$$

$$\frac{\mathcal{B}(B_s^0 \rightarrow D_s^- \pi^+ \pi^+ \pi^-)}{\mathcal{B}(B^0 \rightarrow D^- \pi^+ \pi^+ \pi^-)} = 1.01 \pm 0.11(\text{stat.}) \pm 0.06(\text{syst.}) \pm 0.14(\text{BR}) \pm 0.15(\text{PR}),$$

where the uncertainties labeled BR and PR refer to the uncertainty on the  $D$  meson branching fractions and the production ratio  $f_s/f_d$ , respectively.

Thesis Supervisor: Christoph M. E. Paus  
Title: Professor





# Contents

<b>1</b>	<b>Theoretical Overview</b>	<b>9</b>
1.1	The Standard Model . . . . .	10
1.2	Quantum Chromodynamics . . . . .	12
1.3	Heavy Quark Effective Theory . . . . .	15
1.4	Factorization . . . . .	16
1.5	Predictions for our measurements . . . . .	21
1.5.1	Diagrams and input parameters . . . . .	21
1.5.2	Analysis of possible approximations . . . . .	23
1.5.3	Analysis discussion . . . . .	24
1.5.4	Conclusion . . . . .	25
<b>2</b>	<b>Experimental Apparatus</b>	<b>27</b>
2.1	The Tevatron — the source of $p\bar{p}$ collisions . . . . .	28
2.1.1	Interaction point . . . . .	31
2.2	The CDF detector . . . . .	32
2.3	Track parametrization . . . . .	34
2.4	Tracking systems . . . . .	36
2.4.1	Silicon tracking detectors . . . . .	36
2.4.2	Central Outer Tracker . . . . .	39
2.4.3	Pattern recognition algorithms . . . . .	41
2.5	Time of flight . . . . .	42
2.6	Calorimeters . . . . .	44
2.7	Muon systems . . . . .	45

2.7.1	CMU . . . . .	46
2.7.2	CMP . . . . .	46
2.7.3	CMX . . . . .	46
2.8	Trigger . . . . .	47
2.8.1	Fast Track Trigger (XFT) . . . . .	49
2.8.2	Silicon Vertex Trigger (SVT) . . . . .	51
2.8.3	Two-Track Trigger: Level 1 and Level 2 . . . . .	52
2.8.4	Level 3 trigger . . . . .	54
<b>3</b>	<b>Dataset and Candidate Selection</b>	<b>57</b>
3.1	Good runs . . . . .	58
3.2	Trigger paths . . . . .	60
3.2.1	The B-CHARM trigger path . . . . .	60
3.2.2	The B-CHARM-LOWPT trigger path . . . . .	61
3.2.3	Trigger prescales . . . . .	62
3.3	Event selection . . . . .	64
3.3.1	Track preparation . . . . .	65
3.3.2	Trigger confirmation . . . . .	67
3.3.3	Candidate reconstruction . . . . .	68
3.3.4	Combinatorial background . . . . .	69
3.3.5	Selection requirements . . . . .	70
3.3.6	Optimization of selection requirements . . . . .	71
3.3.7	Duplicate candidates . . . . .	80
3.4	Summary . . . . .	81
<b>4</b>	<b>Branching Ratio Measurement</b>	<b>83</b>
4.1	Monte Carlo simulation . . . . .	84
4.1.1	$b$ hadron production and decay . . . . .	84
4.1.2	Detector simulation . . . . .	85
4.2	Validation of Monte Carlo simulation . . . . .	86
4.2.1	Reweighting procedure . . . . .	99

4.3	Background composition studies . . . . .	102
4.3.1	Fit models . . . . .	105
4.4	Normalization of backgrounds under signal . . . . .	119
4.4.1	Cabibbo suppressed backgrounds . . . . .	120
4.4.2	$\Lambda_b$ background . . . . .	122
4.4.3	$B_s^0$ reconstructed as $B^0$ . . . . .	123
4.5	$B$ meson yields . . . . .	124
4.6	Ratio of Monte Carlo efficiencies . . . . .	127
4.7	Ratio of branching fractions . . . . .	130
<b>5</b>	<b>Systematic Uncertainties</b>	<b>131</b>
5.1	Monte Carlo generation . . . . .	131
5.1.1	The $B$ $p_T$ spectrum . . . . .	132
5.1.2	$B$ and $D$ lifetimes . . . . .	133
5.1.3	Resonance structure of the $\pi^+\pi^+\pi^-$ system . . . . .	133
5.2	Detector description . . . . .	136
5.2.1	Run range dependence systematic . . . . .	136
5.2.2	XFT efficiency for kaons relative to pions . . . . .	138
5.3	Analysis . . . . .	140
5.3.1	Cut efficiencies . . . . .	140
5.3.2	The $\phi^0$ mass requirement . . . . .	142
5.3.3	Fitting systematics . . . . .	144
5.4	External inputs . . . . .	158
5.5	Summary of systematic effects . . . . .	159
<b>6</b>	<b>Conclusion</b>	<b>161</b>
	<b>Appendices</b>	<b>164</b>
<b>A</b>	<b>Data fit parameters</b>	<b>165</b>



# Chapter 1

## Theoretical Overview

The bottom quark was discovered at Fermilab in 1977 [1]. Since then our understanding of heavy flavor physics has been vastly improved.  $B$  mesons are produced in large quantities by the currently operating  $B$ -factories at SLAC, KEK, and at the Tevatron. The large samples of  $B^0$  mesons which have been recorded have allowed for the precise measurement of the  $\Delta m_d$  [2] — the mass difference between the heavy and light  $B^0$  mass eigenstates.

$B$  mesons come in four different species: charged  $B^+$  and  $B_c^+$ , made of  $(\bar{b}u)$  and  $(\bar{b}c)$  quarks pairs respectively, and neutral  $B^0$  and  $B_s^0$ , made of  $(\bar{b}d)$  and  $(\bar{b}s)$  pairs. The  $B$ -factories operating at the  $\Upsilon(4S)$  resonance, i.e at a center of mass energy of 10.54 GeV, have a greatly enhanced production cross-section for  $e^+e^- \rightarrow b\bar{b}$ , but only produce  $B^0$  and  $B^+$ . The  $B_s^0$  and  $B_c^+$  mesons are too heavy to be produced at this energy. This is why they remain relatively less well studied and their properties are poorly known. The  $B_s^0$  and  $B_c^+$  mesons are produced at the Fermilab Tevatron. One of the advantages of studying  $B$  physics in a hadronic environment is the very high  $b\bar{b}$  production cross-section, which is three orders of magnitude larger than the corresponding cross section at the  $B$ -factories. The D0 experiment and especially CDF, where fully reconstructed  $B_s^0$  final states are available, are in the unique position to study the  $B_s^0$  decay properties.

This thesis presents a measurement of the branching fractions  $\mathcal{B}(B_s^0 \rightarrow D_s^- \pi^+)$  and  $\mathcal{B}(B_s^0 \rightarrow D_s^- \pi^+ \pi^+ \pi^-)$ , where  $D_s^- \rightarrow \phi^0 \pi^-$  and  $\phi^0 \rightarrow K^+ K^-$ . The reconstructed

sample of  $B_s^0 \rightarrow D_s^- \pi^+$  decays allows for a precise measurement of the branching fraction, while the sample of  $B_s^0 \rightarrow D_s^- \pi^+ \pi^+ \pi^-$  is the first observation of  $B_s^0$  decays in this channel. These two samples of fully reconstructed  $B_s^0$  decays also serve an important role in the search for, and recently the measurement of,  $B_s^0$  oscillations at CDF [3, 4].

The measurement of the ratios of branching fractions  $\mathcal{B}(B_s^0 \rightarrow D_s^- \pi^+ [\pi^+ \pi^-]) / \mathcal{B}(B^0 \rightarrow D^- \pi^+ [\pi^+ \pi^-])$  reveals information about  $B$  decay mechanisms. One can attempt to separate the contributions of tree and sub-leading diagrams in  $B^0 \rightarrow D^- \pi^+$  decay and then predict  $B_s^0 \rightarrow D_s^- \pi^+$  branching fraction using  $SU(3)$  [5], and further estimate flavor  $SU(3)$  symmetry breaking effects [6], which can be sizable and could modify the predictions of naive factorization [7].

## 1.1 The Standard Model

The Standard Model of particle physics is a theory that describes the fundamental strong, weak, and electromagnetic forces between structureless, or fundamental, particles. Historically, the advent of the Standard Model occurred with the development of the electroweak theory in the late 1960's and early 1970's [8, 9, 10]. The term "Standard Model" was coined in the late 1970's and included the theory of quantum chromodynamics (QCD) [11] and electroweak theory. The discovery of the  $W$  [12, 13] and  $Z$  [14, 15] bosons in 1983 by the UA1 and UA2 collaborations at the CERN  $p\bar{p}$  collider provided a direct confirmation of the unification of the weak and electromagnetic interactions.

The Standard Model is a relativistic gauge quantum field theory that is based on the symmetry group  $SU(3) \otimes SU(2) \otimes U(1)$ . The  $SU(3)$  symmetry is related to the color symmetries of the QCD color field. The  $SU(2)$  symmetry describes the weak interaction. Under  $SU(2)$  the left-handed fermion fields transform as doublets, whereas right-handed fields are  $SU(2)$  singlets. The  $U(1)$  symmetry describes the electromagnetic field. Quantum field theory uses a Lagrangian formalism to completely describe a system of particles and their interactions. The fundamental Lagrangian

is constructed from first principles and is based on the theory symmetry group. Local gauge invariance in field theories is a requirement for the renormalizability of the theory, *i.e* the ability to subtract off divergences to obtain finite results.

The Standard Model arranges the fundamental particles, quarks and leptons, in three generations of pairs in order of increasing mass. Quarks and leptons are assigned to be left-handed doublets and right-handed singlets. Quarks participate in both the strong and electroweak interactions while leptons are only sensitive to the electroweak field. The masses of quarks, leptons, and gauge bosons are free parameters of the model.

All the interactions between quarks and leptons are described by Standard Model Lagrangian terms, in which fermionic fields are coupled to the gauge bosons. The formula for the parts of the  $SU(3) \otimes SU(2) \otimes U(1)$  interaction Lagrangian for the first generation of fermions is:

$$\begin{aligned}
\mathcal{L} = & e \sum_{f=\nu,e,u,d} Q_f (\bar{f} \gamma^\mu f) A_\mu \\
& + \frac{g_2}{\cos \theta_w} \sum_{f=\nu,e,u,d} \{ (\bar{f}_L \gamma^\mu f_L) [T_f^3 - Q_f \sin^2 \theta_w] + (\bar{f}_R \gamma^\mu f_R) [-Q_f \sin^2 \theta_w] \} Z_\mu \\
& + \frac{g_2}{\sqrt{2}} [ ((\bar{u}_L \gamma^\mu d'_L) + (\bar{\nu}_L \gamma^\mu e_L)) W_\mu^+ + ((\bar{d}'_L \gamma^\mu u_L) + (\bar{e}_L \gamma^\mu \nu_L)) W_\mu^- ] \\
& + \frac{g_3}{2} \sum_{q=u,d} (\bar{q}_\alpha \gamma^\mu \lambda_{\alpha\beta}^a q_\beta G_\mu^a), \tag{1.1}
\end{aligned}$$

where  $A_\mu$  is the photon field,  $W_\mu^\pm$  and  $Z_\mu$  are the massive charged and neutral weak boson fields,  $G_\mu^a$  is the strong field. The  $f_L, u_L$ , and  $\nu_L$  are quark and lepton spinors. The “L” and “R” subscripts denote the left-handedness and right-handedness, respectively. The  $Q_f$  and  $T$  are the operators of the  $U(1)$  and  $SU(2)$  groups. In Equation 1.1 the first sum represents the electromagnetic interaction, the second and third lines express the weak interaction due to neutral and charged currents respectively, and the last line describes strong interactions. The factors in front of each line are coupling constants, characterizing the strength of each interaction. The relation between  $e$  and  $g_2$  is  $e = g_2 \sin \theta_w$ , where  $\theta_w$  is the weak angle — a parameter, which relates

the strengths of electromagnetic and weak interactions for both charged and neutral currents. By setting  $\hbar = c = 1$  we can express the values of the coupling constants in natural units:

$$\alpha = \frac{e^2}{4\pi} \approx \frac{1}{137}, \quad \alpha_w = \frac{g_2^2}{4\pi} = \frac{\sqrt{2}G_F M_W^2}{\pi} \approx \frac{1}{30}, \quad \alpha_s = \frac{g_3^2}{4\pi} \approx \frac{1}{10}, \quad (1.2)$$

where the charge of electron  $e$ , the Fermi constant  $G_F$ , and the  $W$  boson mass  $M_W$  are additional parameters of the Standard Model. The coupling constants  $\alpha$ ,  $\alpha_w$ , and  $\alpha_s$  are *running* constants, which refers to the fact that they depend on the interaction energy. The constants normally increase with the interaction energy, except for  $\alpha_s$ , which, surprisingly, decreases.

The weak eigenstates of the quark fields are not the mass eigenstates, so that the quark fields  $d'$  which appear in the electroweak Lagrangian are related to the mass eigenstates of the QCD Lagrangian by

$$d'_i = \sum_j V_{ij} d_j, \quad (1.3)$$

where  $V_{ij}$  is the 3-by-3 Cabibbo-Kobayashi-Maskawa (C-K-M) matrix.

In the following sections, we look at the fundamental QCD Lagrangian in detail, and we review the approximation methods used in calculating the dynamics of fully reconstructed hadronic  $B$  decays, and finally, theoretical predictions for the value of the branching fraction  $B_s^0 \rightarrow D_s^- \pi^+$ .

## 1.2 Quantum Chromodynamics

Quantum Chromodynamics (QCD) is the gauge field theory which describes the strong interactions of colored quarks and gluons. It was developed to explain the patterns of flavor  $SU(3)$  symmetry observed in meson and baryon mass spectra measured in the late 1960's [16]. In the quark model the baryons are interpreted as bound states of three quarks, and the measured half-integral spin of baryons necessitates a



1/2 spin for the quarks as well. However, spin 1/2 particles are fermions, and Fermi statistics requires the total wave function of a baryon to be antisymmetric. The observation of a spin 3/2 baryon ( $\Delta^{++}$ ) containing three quarks of the same flavor and having a symmetric total wave function is in contradiction with Fermi statistics. Color is postulated to be an additional quantum number to solve this problem. With the introduction of an additional quantum number the total wave function for the  $\Delta^{++}$  baryon can be antisymmetric.

A quark of specific flavor (such as a charm quark) comes in three colors. Gluons, the mediators of the strong force, come in eight color-anticolor combinations. Hadrons are color-singlet combinations of quarks, anti-quarks, and gluons. A color-singlet configuration is a combination of colored objects with zero total color charge. The Lagrangian describing the interaction of quarks and gluons is (up to the gauge-fixing terms):

$$\mathcal{L} = -\frac{1}{4}G_{\mu\nu}^a G^{a\mu\nu} + i \sum_q \bar{\psi}_q^i \gamma^\mu (D_\mu)_{ij} \psi_q^i - \sum_q m_q \bar{\psi}_q^i \psi_{qi}, \quad (1.4)$$

where the  $G_{\mu\nu}^a$  is the gluon field tensor,  $D_\mu$  is the  $SU(3)$  covariant derivative, and the  $\psi_q^i(x)$  are the 4-component Dirac spinors associated with each quark field for color  $i$  and flavor  $q$ . The gluon field tensor is:

$$G_{\mu\nu}^a = \partial_\mu A_\nu^a - \partial_\nu A_\mu^a - g_s f_{abc} A_\mu^b A_\nu^c, \quad (1.5)$$

where the  $A_\mu^a$  are eight Yang-Mills gluon fields,  $g_s$  is the QCD coupling constant, and the  $f_{abc}$  are the structure constants of the  $SU(3)$  algebra. The  $SU(3)$  covariant derivative  $D_\mu$  is:

$$(D_\mu)_{ij} = \delta_{ij} \partial_\mu + i g_s \sum_a \frac{\lambda_{ij}^a}{2} A_\mu^a, \quad (1.6)$$

where  $\lambda_{ij}^a$  are eight generators of the  $SU(3)$  group. The third term in Equation 1.5 is the non-Abelian term. It is responsible for the self-interactions of gluons, illustrated in Figure 1-1.

In an Abelian group, all of the generators of the group commute. In a non-Abelian group, the generators do not commute, and the commutation relations are dictated

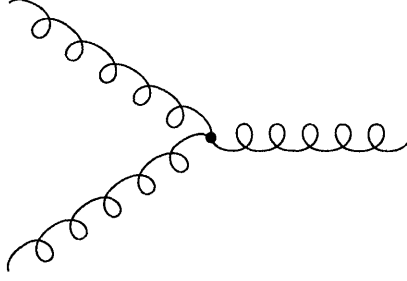


Figure 1-1: Feynman diagram of gluon self-interaction.

by the structure constants of the group algebra. The structure constants  $f_{abc}$  of the  $SU(3)$  group are defined by the commutation relation of the eight generators of the theory:

$$[\lambda_a, \lambda_b] = 2if_{abc}\lambda_c. \quad (1.7)$$

This feature of the  $SU(3)$  group sets quantum chromodynamics apart from quantum electrodynamics, which is based on the Abelian group  $U(1)$ .

After renormalization of the QCD coupling constant  $g_s$ , *i.e.* absorbing infinite higher order corrections into the definition of  $g_s$ , the coupling constant becomes a function of momentum scale  $Q^2$ , where  $Q$  is defined as a momentum transfer in the strong interaction. The difference in QCD compared to Abelian QED arises from the fact that gluons couple to each other. This difference has enormous consequences. It leads to a variation of  $g_s$  with  $Q^2$  which is opposite to that in QED:  $g_s$  *decreases* with  $Q^2$ , a property known as *asymptotic freedom*.

In QCD we do not have equivalent  $Q^2 \rightarrow 0$  definition of the coupling, which is also the consequence of gluon self interaction. Because of this in QCD we have to introduce a mass parameter,  $\Lambda_{QCD}$ , to compensate for this lack of knowledge of the coupling at zero momentum transfer.

QCD becomes strongly coupled (*i.e.*  $g_s$  is no longer much less than unity) at  $\Lambda_{QCD} \approx 200 \text{ MeV}/c^2$ . The perturbation approach works well at short distances or large momentum transfers, *i.e.* where  $g_s \ll 1$ , but breaks down for larger distances. This has a very unfortunate consequence for the theory of  $B$  decays, because it requires an understanding of long distance nonperturbative properties of QCD, in

addition to its short distance behavior.

In the situation where a theory based on fundamental principles leads to very few quantitative predictions, various approximate approaches have been developed. Among these are the Heavy Quark Effective Theory, factorization approximations, and chiral symmetry. Such approaches can be used to a varying degrees of success to calculate quantitative predictions for the branching fractions of hadronic  $B$  meson decays. In the following sections we briefly review the tools used to derive theoretical predictions for  $B$  mixing and decays. We describe various approximations in calculating the hadronic decay amplitudes. In Chapter 6 we make some quantitative statements about their relative merits by comparing their predictions with our measurements.

### 1.3 Heavy Quark Effective Theory

The  $B^0$  meson is made of a heavy  $\bar{b}$  quark and a light  $d$  quark. The binding energy of the quarks, which is of the order  $\Lambda_{QCD}$ , is quite small compared to the mass of the heavy quark  $m_b$ . In the limit  $m_b \gg \Lambda_{QCD}$ , the heavy quark acts approximately as a static color-triplet source. To a large extent, the spin and flavor of the heavy quark do not affect the light degrees of freedom (light quark, virtual quark-antiquarks pairs, and gluons). This property of the  $B^0$  meson, made of a heavy and a light quark, is related by the symmetry called Heavy Quark Symmetry (HQS).

The construction of a heavy quark effective Lagrangian starts by making the dependence of all quantities on  $m_b$  in the QCD Lagrangian explicit, and then doing a perturbative expansion in inverse powers of  $m_b$ . One introduces a field  $h_v(x)$ , which removes the mass dependent piece of the quark field:

$$h_v(x) = e^{im_q v \cdot x} P_+(v) Q(x), \quad (1.8)$$

where  $Q(x)$  is the quark field in full QCD, and  $P_+(v) = \frac{1+\not{v}}{2}$  is a projection operator. Here the interpretation of the projection operator  $P_+$  is that  $h_v$  represents just the

heavy quark (rather than antiquark) component of  $Q$ .

The HQET Lagrangian is then constructed from the field  $h_v$ . We show here only the final result including the leading  $1/m_q$  terms:

$$\mathcal{L} = \bar{h}_v i v \cdot D h_v + \frac{1}{2m_q} [O_{kin} + C_{mag}(\mu) O_{mag}(\mu)] + O(1/m_q^2), \quad (1.9)$$

where  $D^\mu$  is the color  $SU(3)$  covariant derivative. The leading term in Equation 1.9 respects both the spin and flavor symmetries. The symmetry breaking operators are:

$$O_{kin} = \bar{h}_v (iD)^2 h_v, \quad O_{mag} = \frac{g_s}{2} \bar{h}_v \sigma_{\mu\nu} G^{\mu\nu} h_v. \quad (1.10)$$

Here  $G^{\mu\nu}$  is the gluon field tensor, and  $\sigma_{\mu\nu}$  are the Pauli matrices. In the rest frame of the hadron  $O_{kin}$  describes the kinetic energy of the heavy quark, and  $O_{mag}$  corresponds to the chromomagnetic coupling of the heavy quark spin to the gluon field. While  $O_{kin}$  violates only the heavy quark symmetry,  $O_{mag}$  violates the spin symmetry as well.

Heavy quark effective theory is helpful for understanding many aspects of the spectroscopy and decays of heavy hadrons from first principles. For example, the mass difference between various  $b$ -flavored hadrons can be related to those for charmed hadrons [17].

## 1.4 Factorization

The hypothesis of *factorization* [18] is the most popular approach to calculating the dynamics of hadronic  $B$  decays. This approach applies to certain types of nonleptonic decays. A favorite example is  $B^0 \rightarrow D^- \pi^+$  decay, which involves tree-level diagrams where the  $\bar{b} \rightarrow \bar{c}$  transition leads to a charmed meson and a virtual  $W$  boson that emerges as a charged pion. The pair of  $u$  and  $\bar{d}$  quarks, produced in the decay of a virtual  $W$  boson, has a large momentum, and finds itself in the middle of a medium of gluons and light quark-antiquark pairs, with which the pair interacts strongly. Since, in addition, they have opposite color charge, then they interact with the medium not

individually but as a single color dipole. The distance between the  $u$  and the  $\bar{d}$  grows much slower than the distance which the pair with high momentum as a whole travels through the colored environment. It is possible that the pair will have left the colored environment completely before its dipole moment is large enough for its interactions to be significant. In this case, the pair hadronizes as a single charged pion. This phenomenon is also known as “color transparency” [19].

If, on the other hand, the pair of the  $u\bar{d}$  pair has a small momentum, then the quarks interact strongly with the medium. In this case, it is unlikely that the quarks will regroup into a single  $\pi$ . We hypothesize that the decay  $B^0 \rightarrow D^-\pi^+$  is dominated by the former scenario. Under this approximation the matrix element factorizes:

$$\langle D\pi | \bar{c}\gamma^\mu(1-\gamma^5)b\bar{d}\gamma_\mu(1-\gamma^5)u | B \rangle = \langle D | \bar{c}\gamma^\mu(1-\gamma^5)b | B \rangle \langle \pi | \bar{d}\gamma_\mu(1-\gamma^5)u | 0 \rangle. \quad (1.11)$$

The two terms in the formula are:  $\langle \pi | \bar{d}\gamma_\mu(1-\gamma^5)u | 0 \rangle$  and  $\langle D | \bar{c}\gamma^\mu(1-\gamma^5)b | B \rangle$ . The first one is related to  $f_\pi$  — the pion decay constant, and the second one may be extracted from semileptonic  $B$  decays. In this scheme, it is possible to obtain relations among various two body decays which can then be tested experimentally.

We can now apply the factorization hypothesis to  $B_s^0 \rightarrow D_s^-\pi^+$  and  $B^0 \rightarrow D^-\pi^+$  decays. Figure 1-2 shows a tree-level Feynman diagram of the  $B \rightarrow D\pi^+$  decay. Diagrams of this kind are called spectator diagrams because the dominant dynamics of the decay comes from the  $b \rightarrow cW$  transition and the  $s$  quark is a “spectator” in the process.

There is a distinction which is often made in literature discussing nonleptonic  $B$  decays, between the decays which are said to be *color-allowed* and those which are *color-suppressed*. Figures 1-2 and 1-3 show the tree-level color-allowed and color-suppressed Feynman diagrams of the  $B \rightarrow D\pi$  and  $B^+ \rightarrow \bar{D}^0\pi^+$  decays, respectively. Also note that the second of these diagrams is not possible for the decays of  $B_s^0$  and  $B^0$  mesons. We will use this distinction later to predict the branching fractions of the  $B_s^0 \rightarrow D_s^-\pi^+$  decay.

To explain what the distinction between color-allowed and color-suppressed dia-

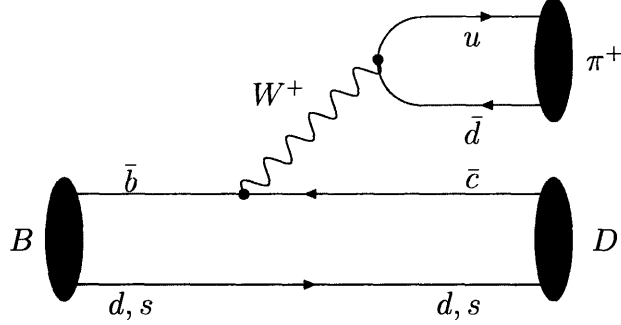


Figure 1-2: The tree-level Feynman diagram describing color-allowed  $B \rightarrow D\pi^+$  decays.

grams is, we start from the effective Hamiltonian obtained by an operator product expansion (OPE) [20], written as a sum of products of quark fields. For example, if one were interested in the semi-inclusive process  $B \rightarrow X_s\psi$ , the Hamiltonian takes the form:

$$C_1 \bar{s}_i \gamma^\mu (1 - \gamma^5) c^j \bar{c}_j \gamma^\mu (1 - \gamma^5) b^i + C_2 \bar{s}_i \gamma^\mu (1 - \gamma^5) c^i \bar{c}_j \gamma_\mu (1 - \gamma^5) b^j, \quad (1.12)$$

where  $i$  and  $j$  are color indices, and  $C_1$  and  $C_2$  are Wilson coefficients, which absorb the short scale dynamics in OPE. Using Fiertz identities [21] we rewrite the Hamiltonian as:

$$(C_1 + \frac{1}{3}C_2) \bar{c} \gamma^\mu (1 - \gamma^5) c \bar{s} \gamma_\mu (1 - \gamma^5) b + 2C_2 \bar{c} T^a \gamma^\mu (1 - \gamma^5) c \bar{s} T^a \gamma_\mu (1 - \gamma^5) b. \quad (1.13)$$

Then the first term can be factorized as in Equation 1.11, while the second which contains the color matrix  $T^a$ , cannot. If the coefficient  $C_1 + \frac{1}{3}C_2$  of the factorizable term is large, that is, if  $C_1 + \frac{1}{3}C_2 \gg 2C_2$ , then the amplitude is said to be color-allowed. If the reverse is true it is said to be color-suppressed.

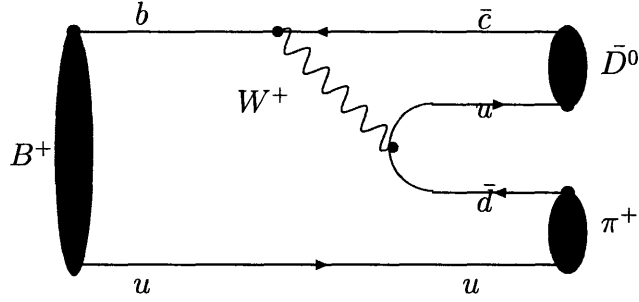


Figure 1-3: The tree-level Feynman diagram describing color-suppressed  $B^+ \rightarrow \bar{D}^0 \pi^+$  decays.

The diagrams in Figures 1-2 and 1-3 are called spectator diagrams. There is an approximation called the “spectator approximation” based on the fact that the dominant dynamics of the decay  $B_s^0 \rightarrow D_s^- \pi^+$  comes from the  $b \rightarrow cW$  transition, and the  $s$  quark is a spectator in this process. In the spectator approximation, we expect the ratio of branching fractions of  $B_s^0 \rightarrow D_s^- \pi^+$  to  $B^0 \rightarrow D^- \pi^+$  to be roughly unity since the only difference between these decays is swapping of  $s$  and  $d$  spectators. However, there are two considerations that slightly change this prediction. First, the lifetimes of the  $B^0$  and  $B_s^0$  mesons are not the same. The current world average for the lifetime of the  $B^0$  meson is  $c\tau(B^0) = c/\Gamma = 460.8 \pm 4.2 \mu\text{m}$ , and for the  $B_s^0$  meson  $c\tau(B_s^0) = 438.3 \pm 17.1 \mu\text{m}$  [2]. The branching fraction of a decay is expressed as  $\Gamma_i/\Gamma$  (where  $\Gamma$  and  $\Gamma_i$  are the full and partial decay widths) and this is, thus, related to the lifetime. Therefore, the different lifetimes of  $B_s^0$  and  $B^0$  lead to a shift in the ratio of branching fractions.

Another effect comes from the diagram in Figure 1-4. This diagram is called “ $W$ -exchange” diagram. Color-allowed and color-suppressed diagrams are zeroth order diagrams in  $\alpha_{QCD}$  but the  $W$ -exchange diagram is a first order in  $\alpha_{QCD}$  diagram and is, therefore, suppressed, and its relative contribution is not known *a priori*. Its amplitude adds to the color-allowed amplitude from the diagram shown in Figure 1-2.

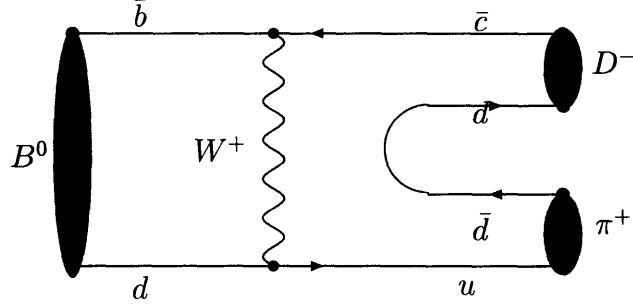


Figure 1-4: The first order Feynman diagram describing  $B^0 \rightarrow D^- \pi^+$  decay that proceeds through  $W$ -exchange.

Also note, that this type of diagram is not possible for  $B_s^0 \rightarrow D_s^- \pi^+$  decay.

There is also an additional complication related to the  $B_s^0 \rightarrow D_s^- \pi^+ \pi^+ \pi^-$  and  $B^0 \rightarrow D^- \pi^+ \pi^+ \pi^-$  decays. The three pions in these decays may arise from resonances such as  $a_1$ ,  $\rho\pi$ , or decays proceed through the  $D\pi^+ \pi^+ \pi^-$  non-resonant channel. The direct application of factorization here is more problematic, since multiple pion production is governed over most of the phase space not by low-energy theorems but by the nonperturbative dynamics of QCD fragmentation.

All of these effects can result in a prediction for the ratios of branching fractions  $B_s^0 \rightarrow D_s^- \pi^+$  to  $B^0 \rightarrow D^- \pi^+$  and  $B_s^0 \rightarrow D_s^- \pi^+ \pi^+ \pi^-$  to  $B^0 \rightarrow D^- \pi^+ \pi^+ \pi^-$ , which differ from spectator approximation prediction. The absolute branching fraction  $B^0 \rightarrow D^- a_1$  decay is calculated in Reference [5]. This is a quasi-two-body decay because the three pions come from the intermediate resonance. The leading diagram in this case is shown in Figure 1-5. However, the situation is more complex for  $B^0 \rightarrow D^- \pi^+ \pi^+ \pi^-$  decay where three pions are non-resonant. Since the weak interaction generates only three quarks, at least one of the quark pairs in a multi-body decay has to be pair produced via gluons as shown in Figure 1-5. Thus, unless the final state is carefully chosen, the utility of factorization is limited. Only if there are no gluons exchanged and the produced pair “stays within” the color singlet flow is factorization



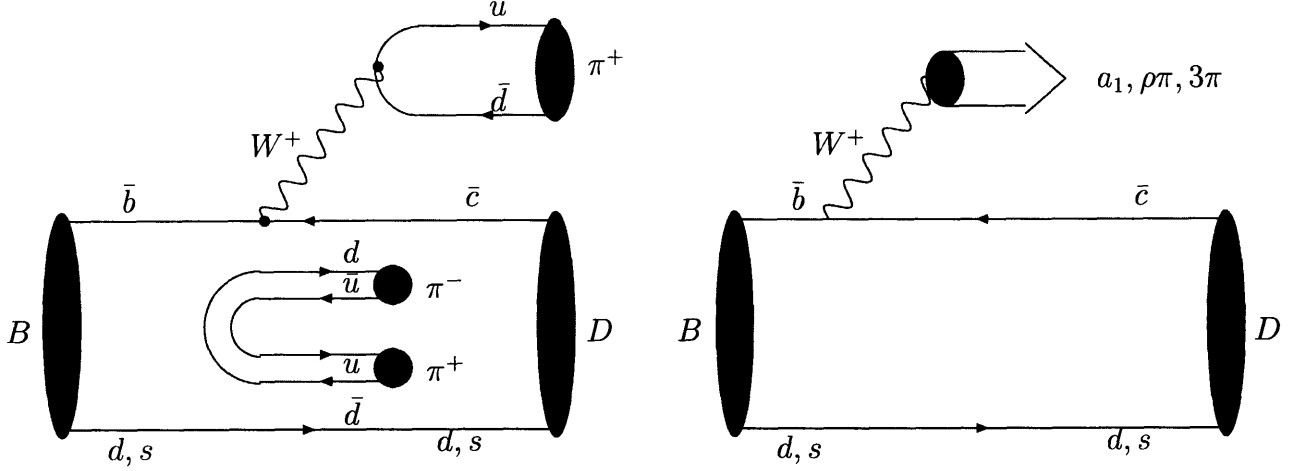


Figure 1-5: The tree-level Feynman diagrams describing  $B^0 \rightarrow D^- \pi^+ \pi^+ \pi^-$  decays.

applicable. This implies in general that there are only limited kinematic regions of validity for a factorization approximation, for instance, where there are intermediate resonances, such that the decay is a quasi-two-body decay. Predictions for neither  $\mathcal{B}(B^0 \rightarrow D^- \rho^0 \pi^+)$  nor  $\mathcal{B}(B^0 \rightarrow D^- \pi^+ \pi^+ \pi^-)$  non-resonant decay are available in the literature.

## 1.5 Predictions for our measurements

In the previous sections we introduced factorization, color-allowed and  $W$ -exchange diagrams, and Heavy Quark Effective Theory. In this section we use these ideas and flavor  $SU(3)$  symmetry to calculate the ratio of branching fractions  $\mathcal{B}(B_s^0 \rightarrow D_s^- \pi^+)/\mathcal{B}(B^0 \rightarrow D^- \pi^+)$ . The discussion here follows for the most part Reference [6].

### 1.5.1 Diagrams and input parameters

The mode  $B_s^0 \rightarrow D_s^- \pi^+$  has only one color-allowed diagram, as shown in Figure 1-6. In contrast, there are two diagrams relevant to the mode  $B^0 \rightarrow D^- \pi^+$ : color-allowed tree and  $W$ -exchange diagrams as shown in Figure 1-7.

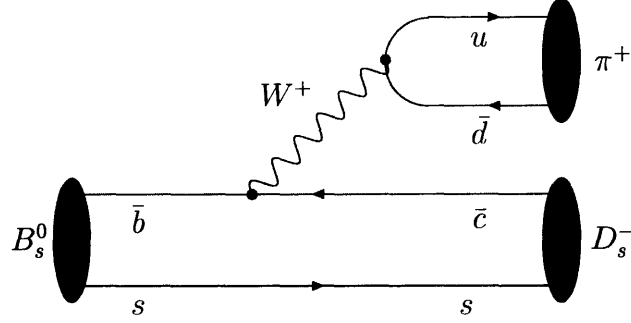


Figure 1-6: The tree-level Feynman diagram describing the color-allowed  $B_s^0 \rightarrow D_s^- \pi^+$  decay.

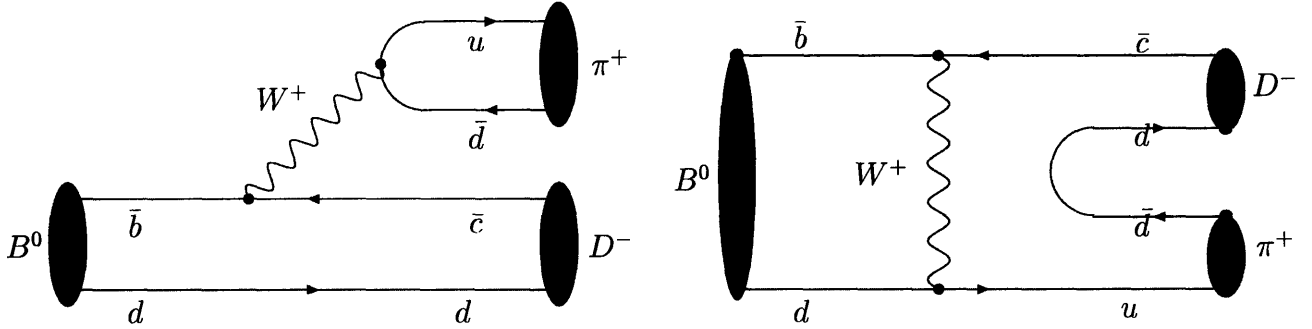


Figure 1-7: The Feynman diagrams contributing to  $B^0 \rightarrow D^- \pi^+$  decay: color-allowed (left) and W-exchange (right).

Theoretically [5], the ratio of branching fractions is:

$$\frac{\mathcal{B}(B_s^0 \rightarrow D_s^- \pi^+)}{\mathcal{B}(B^0 \rightarrow D^- \pi^+)} = \frac{|T_{B_s^0}^{D\pi}|^2}{|T_{B^0}^{D\pi} + E_{B^0}^{D\pi}|^2} \frac{\Pi_{B_s^0} \tau_{B_s^0}}{\Pi_{B^0} \tau_{B^0}}, \quad (1.14)$$

where  $T_{B_s^0}^{D\pi}$  and  $E_{B^0}^{D\pi}$  are the color-allowed tree and  $W$ -exchange amplitudes, respectively.  $\Pi_{B_s^0(B^0)}$  and  $\tau_{B_s^0(B^0)}$  denote the phase space factor and lifetime for the  $B_s^0(B^0)$  meson. Necessary parameters for the calculation of the phase space factors are [2]:

$$M_{B_s^0} = 5.3696 \pm 0.0024 \text{ GeV}/c^2, \quad \tau_{B_s^0} = 1.461 \pm 0.057 \times 10^{-12} \text{ s} \quad (1.15)$$

$$M_{B^0} = 5.2793 \pm 0.0007 \text{ GeV}/c^2, \tau_{B^0} = 1.536 \pm 0.014 \times 10^{-12} \text{ s} \quad (1.16)$$

$$M_{D_s^-} = 1.9690 \pm 0.0014 \text{ GeV}/c^2, M_{D^-} = 1.8694 \pm 0.0005 \text{ GeV}/c^2. \quad (1.17)$$

We can safely approximate the ratio of phase space factors  $\Pi_{B_s^0}/\Pi_{B^0} \approx M_{B^0}/M_{B_s^0} = 0.98$  and the ratio of lifetimes  $\tau_{B_s^0}/\tau_{B^0} = 0.95$ .

### 1.5.2 Analysis of possible approximations

*Case 1* ( $SU(3)$  without  $W$ -exchange): Can the  $W$ -exchange contribution be ignored, as it is ignored in the naive factorization scheme? In this case, does flavor  $SU(3)$  symmetry work well? When the  $W$ -exchange diagram is ignored, Equation 1.14 is reduced to

$$\frac{\mathcal{B}(B_s^0 \rightarrow D_s^- \pi^+)}{\mathcal{B}(B^0 \rightarrow D^- \pi^+)} \approx 0.93 \times \frac{|T_{B_s^0}^{D\pi}|^2}{|T_{B^0}^{D\pi}|^2}. \quad (1.18)$$

If the flavor  $SU(3)$  symmetry is good, it becomes

$$\frac{\mathcal{B}(B_s^0 \rightarrow D_s^- \pi^+)}{\mathcal{B}(B^0 \rightarrow D^- \pi^+)} \approx 0.93. \quad (1.19)$$

*Case 2* ( $SU(3)$  plus  $W$ -exchange): The current theoretical viewpoint is that the  $W$ -exchange contribution cannot be ignored and may be sizable, especially as stressed in the PQCD scheme [22]. In this case, in order to estimate the  $W$ -exchange contribution, we may invoke flavor  $SU(3)$  symmetry between the modes  $B^0 \rightarrow D_s^- \pi^+$  and  $B^0 \rightarrow D_s^- K^+$ , and obtain from the known  $\mathcal{B}(B^0 \rightarrow D_s^- K^+) |E_{B^0}^{D\pi}| = 0.71 \times 10^{-7}$  [6]. The relevant diagram is shown in Figure 1-8.

To proceed further, we follow the approach used in Reference [23] to obtain  $\delta_{ET}$  — the strong phase of the “exchange” amplitude relative to the “tree” amplitude, and use flavor  $SU(3)$  symmetry:

$$|T_{B_s^0}^{D\pi}| = |T_{B^0}^{D\pi}| = |T_{B^0}^{DK}| \left( \frac{V_{ud}}{V_{us}} \frac{f_\pi}{f_K} \right) = 1.6 \times 10^{-7} \times \frac{0.97}{0.22} \times \frac{0.130}{0.160} = 5.7 \times 10^{-7}, \quad (1.20)$$

$$\delta_{ET} = 1.22. \quad (1.21)$$

Then, we obtain

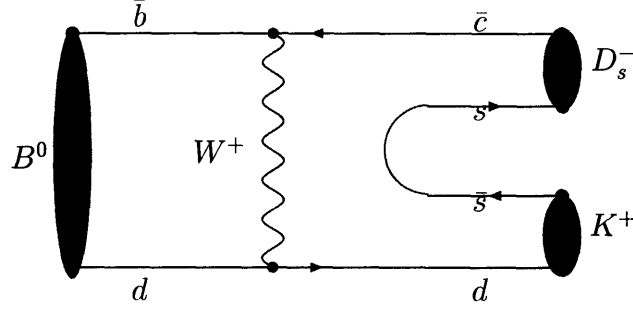


Figure 1-8: The first order Feynman diagram describing  $B^0 \rightarrow D_s^- K^+$  decay that proceeds through “W-exchange”.

$$\frac{\mathcal{B}(B_s^0 \rightarrow D_s^- \pi^+)}{B^0 \rightarrow D^- \pi^+} \approx 0.93 \times \frac{|T_{B_s^0}|^2}{|T_{B^0} + E_{B^0}|^2} = 0.93 \times 0.91 = 0.85. \quad (1.22)$$

### 1.5.3 Analysis discussion

An interesting question is whether the approximation that we made in Equation 1.19 is valid. Does flavor  $SU(3)$  symmetry work well, *i.e* should  $|T_{B_s^0}^{D\pi}|$  be equal to  $|T_{B^0}^{D\pi}|$ ? Theoretically, the color-allowed decay amplitudes for both  $B_s^0 \rightarrow D_s^- \pi^+$  and  $B^0 \rightarrow D^- \pi^+$  modes have the same quark configuration except for the spectator quark. So, the  $B_{(s)} \rightarrow D_{(s)}$  form factor can be the only  $SU(3)$  breaking source at the amplitude level. Within the bounds of heavy quark symmetry, the transition amplitudes can be expressed as

$$\langle D(v') | V_\mu | B(v) \rangle = \sqrt{m_B m_D} [\xi_+(y)(v + v')_\mu + \xi_-(y)(v - v')_\mu], \quad (1.23)$$

where  $y = vv'$  ( $v$  and  $v'$  are the 4-momenta of  $B$  and  $D$  meson respectively),  $V_\mu = \bar{c}\gamma_\mu b$ , and the form factors  $\xi_i$  ( $i = +, -$ ) are written in terms of the universal Isgur-Wise function  $\xi(y)$  as:

$$\xi_i(y) = [\alpha_i + \beta_i(y) + \gamma_i(y)]\xi(y), \quad (1.24)$$

with  $\alpha_+ = 1$ ,  $\alpha_- = 0$ . The functions  $\beta_i(y)$  and  $\gamma_i(y)$  arise from perturbative QCD and  $1/m$  corrections to the heavy symmetry, respectively.

In the heavy quark limit, the  $SU(3)$  breaking for the  $B \rightarrow D$  and  $B_s^0 \rightarrow D_s^-$  transition form factors is of the order  $O(\frac{m_{B_s^0} - m_B}{m_B}) \approx 2\%$ . Therefore, we may ignore the  $SU(3)$  breaking effect for the transition form factors, which leads to  $|T_{B_s^0}| \approx |T_{B^0}|$ .

### 1.5.4 Conclusion

There are two conclusions that can be made from the above arguments.

- The flavor  $SU(3)$  symmetry prediction (see Equation 1.19) compares well with the spectator approximation for the ratio of  $\mathcal{B}(B_s^0 \rightarrow D_s^- \pi^+)/\mathcal{B}(B^0 \rightarrow D^- \pi^+)$  within the naive factorization scheme (or when the  $W$ -exchange contribution is neglected).
- When we include the  $W$ -exchange diagram, a bigger deviation (as in Equation 1.22) from unity in the ratio of branching fractions is possible.

In Chapter 6 we test the suitability of the  $SU(3)$  approximation by comparing its predictions for  $\mathcal{B}(B_s^0 \rightarrow D_s^- \pi)/\mathcal{B}(B^0 \rightarrow D^- \pi)$  with measurements.

Additionally,  $B_s^0 \rightarrow D_s^- \pi^+$  and  $B^0 \rightarrow D^- \pi^+$  decays are similar to the semileptonic decays  $B_s^0 \rightarrow D_s^- l \nu$  and  $B^0 \rightarrow D^- l \nu$ , respectively, except for the sub-leading effects from  $W$ -exchange and hard spectator interactions. If the measurements for both semileptonic decays are available, one can estimate the  $SU(3)$  breaking effect at the leading order from the ratio  $\mathcal{B}(B^0 \rightarrow D^- l \nu)/\mathcal{B}(B_s^0 \rightarrow D_s^- l \nu)$ . The branching ratio of the  $B^0 \rightarrow D^- l \nu$  decay is currently available in literature, but that of  $B_s^0 \rightarrow D_s^- l \nu$  is not measured yet. From the PDG [2] we have:  $\mathcal{B}(B^0 \rightarrow D^- l \nu) = 0.0214 \pm 0.0020$ , but only  $\mathcal{B}(B_s^0 \rightarrow D_s^- l \nu X) = 0.079 \pm 0.024$ . After the branching fraction of  $B_s^0 \rightarrow D_s^- l \nu$  is measured, one can also estimate the effect of sub-leading terms, by comparing the ratio  $\mathcal{B}(B^0 \rightarrow D^- l \nu)/\mathcal{B}(B_s^0 \rightarrow D_s^- l \nu)$  with the measurement of  $\mathcal{B}(B_s^0 \rightarrow D_s^- \pi^+)/\mathcal{B}(B^0 \rightarrow D^- \pi^+)$ .



## Chapter 2

# Experimental Apparatus

Fermilab's Tevatron is currently the highest energy accelerator in the world. It is a source of  $p\bar{p}$  collisions with the center of mass energy of 1.96 TeV. The circumference of the main Tevatron ring is about four miles. The collisions occur at two points of the underground ring called B0 and D0. There are two detectors built at the collision points: the Collider Detector at Fermilab (CDF) and D0, which is named after the point where its collisions occur. This analysis uses data recorded by the CDF experiment.

Since Run I (which ended in 1996), the accelerator complex has undergone major upgrades mostly aimed at increasing the luminosity of the collider. Previously the Tevatron operated with six bunches each of protons and antiprotons, whereas now it collides  $36 \times 36$  bunches. This means that the average time between bunch crossings has decreased from  $3.5 \mu\text{s}$  to 396 ns for the current collider. Both detectors have also been extensively upgraded between 1997 and 2001. The trigger and data acquisition systems have been completely replaced to achieve a maximum response time close to the time between bunch crossings. In particular, the Silicon Vertex Trigger was built, which allows triggering on displaced tracks at a rate of over 25 kHz, a feature never attempted before in a hadronic collider environment. Up to now (October 2006), the Tevatron has delivered about  $2 \text{ fb}^{-1}$  of data making possible various exciting measurements at the energy frontier. In the following pages, we describe how proton and antiproton beams are produced, accelerated to their final center of mass energy

of 1.96 TeV, and collided. We then describe the components of the detector used to identify and measure properties of the particles produced in the collision.

## 2.1 The Tevatron — the source of $p\bar{p}$ collisions

The Tevatron is a proton-antiproton collider located near Batavia, Illinois, at Fermi National Accelerator Laboratory (Fermilab). The Fermilab complex comprises several smaller accelerators and storage rings, which serve two main purposes. The accelerators supply particle beams to fixed target experiments, and they supply protons and anti-protons to the Tevatron colliding ring (see Figure 2-1). Negatively charged hydrogen ions are produced in the magnetron, located inside the Cockroft-Walton pre-accelerator. Those ions are accelerated to a kinetic energy of approximately 750 KeV before being sent into a linear accelerator [24]. The linear accelerator receives the hydrogen ions, accelerates them and injects them into the Booster. The first half-length of the Linac is the Drift Tube Linac, which accelerates the ions to 116 MeV. The second half of the (old-fashioned) Drift Tube Linac has been replaced, allowing ions to achieve an ultimate energy of 400 MeV. Before the beam is injected into the Booster Ring, the ions pass through a carbon foil. The carbon foil strips off the electrons attached to the protons and permits ions to pass on. In the Booster Ring the protons are accelerated until they reach peak kinetic energy of 8 GeV. The Main Injector accepts these protons and continues the acceleration process, increasing their energy to 150 GeV. The 150 GeV protons from the Main Injector are delivered to the Tevatron ring. The Tevatron is a superconducting synchrotron located in a circular tunnel four miles in circumference, around which the protons and antiprotons travel. Various magnets placed around the ring bend and focus the beams of particles. It is here that the particles are accelerated to their final energies of approximately 1 TeV each, supplying collisions with center of mass energies ( $\sqrt{s}$ ) of 1.96 TeV. Thirty-six bunches of protons, and the same for antiprotons, are distributed around the circumference of the Tevatron. For this reason the collisions are referred to as “ $36 \times 36$ ”, *i.e.* 36 bunches of protons collide with 36 bunches of antiprotons. One bunch of protons



## FERMILAB'S ACCELERATOR CHAIN

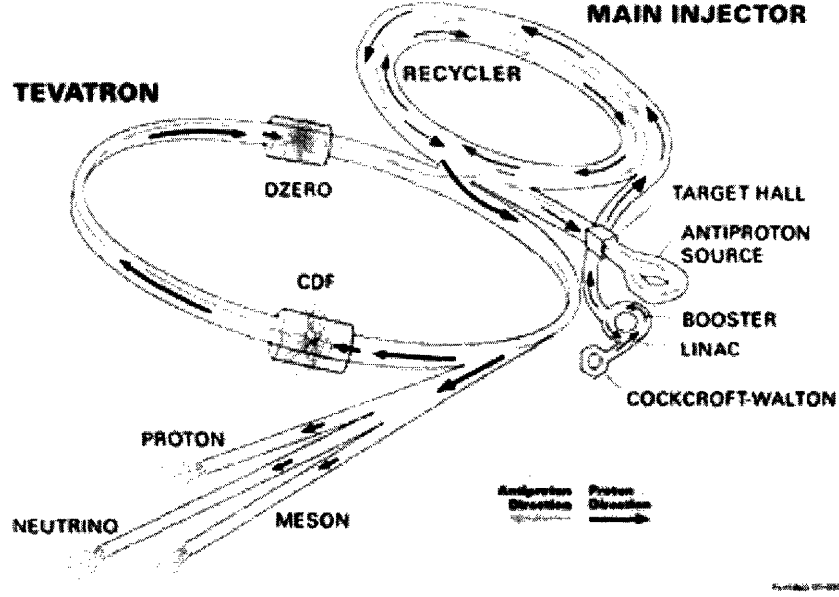


Figure 2-1: Layout of the Fermilab accelerator complex.

collides with one bunch of antiprotons every 396 nanoseconds at the two collision points, B0 and D0.

Protons, earmarked for use in antiproton production, are sent from the Main Injector to the antiproton source where they collide with a nickel target. The secondary particles produced in these collisions are, in part, antiprotons. The collisions of the protons with the target cause the resulting antiprotons to have a large momentum spread. The momentum spread leads to a large emittance of the antiproton beam. The emittance is related to the luminosity  $\mathcal{L}$  of the collisions. In fact, increased emittance leads to a smaller luminosity of the collisions. Luminosity is a critical performance characteristic of a collider. It is defined as:

$$\mathcal{L} = \frac{f N_B N_p N_{\bar{p}}}{2\pi(\epsilon_p \times \epsilon_{\bar{p}})}, \quad (2.1)$$

where  $f$  is the bunch revolution frequency,  $N_B$  is the number of bunches,  $\epsilon_p$  ( $\epsilon_{\bar{p}}$ ) is the emittance of the proton (antiproton) beam,  $N_p$  and  $N_{\bar{p}}$  are the number of protons and antiprotons. Instantaneous luminosity quantifies the rate of collisions received at

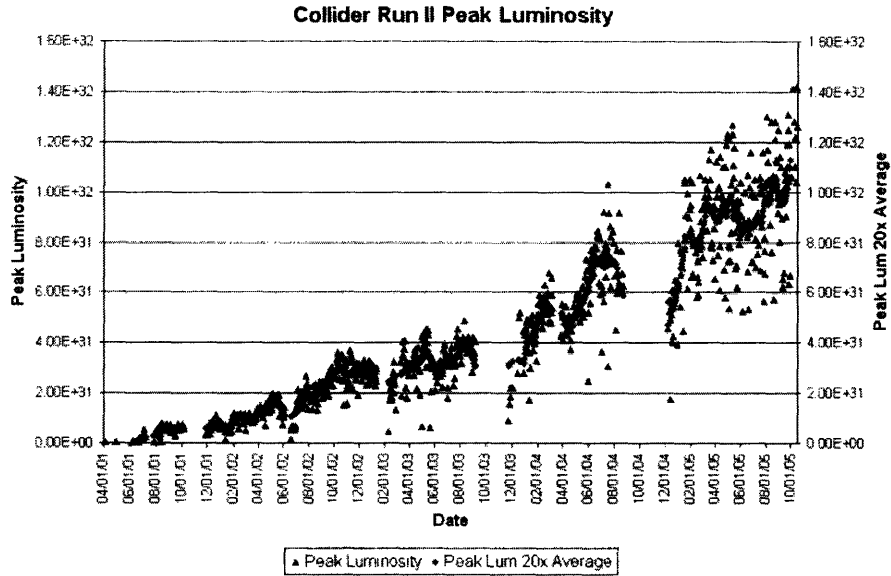


Figure 2-2: Peak luminosities for stores collided between April 2001 and September 2005. Blue dots indicate luminosities of the individual stored. The trend is shown in red.

the detector and, thus used in an analysis.

After the creation and capture of the antiprotons, they are stored in the Accumulator ring (labeled as “antiproton source” in Figure 2-1). The process of *stochastic cooling* is introduced to reduce both the longitudinal and transverse momentum spread of the antiproton beam [25]. In the process of stochastic cooling particles orbit the storage ring and go past pairs of electrodes placed around the beam. A differential pickup signal is applied to these pairs. A differential signal is a signal proportional to particle’s deviation from the nominal orbit. This signal effectively damps the amplitude of oscillations around the nominal orbit. When the intensity and emittance of the antiprotons are satisfactory for collisions, they are sent back into the Main Injector to be accelerated and injected into the Tevatron.

There are two general purpose detectors at the Tevatron: the Collider Detector at Fermilab (CDF) and D0. Quadrupole magnets at B0 and D0 focus the proton and antiproton beams, increasing the rate of the collisions in the center of these detectors. The data used for this thesis have been recorded using the CDF detector [26].

Figure 2-2 shows peak luminosities for stores collided between April 2001 and

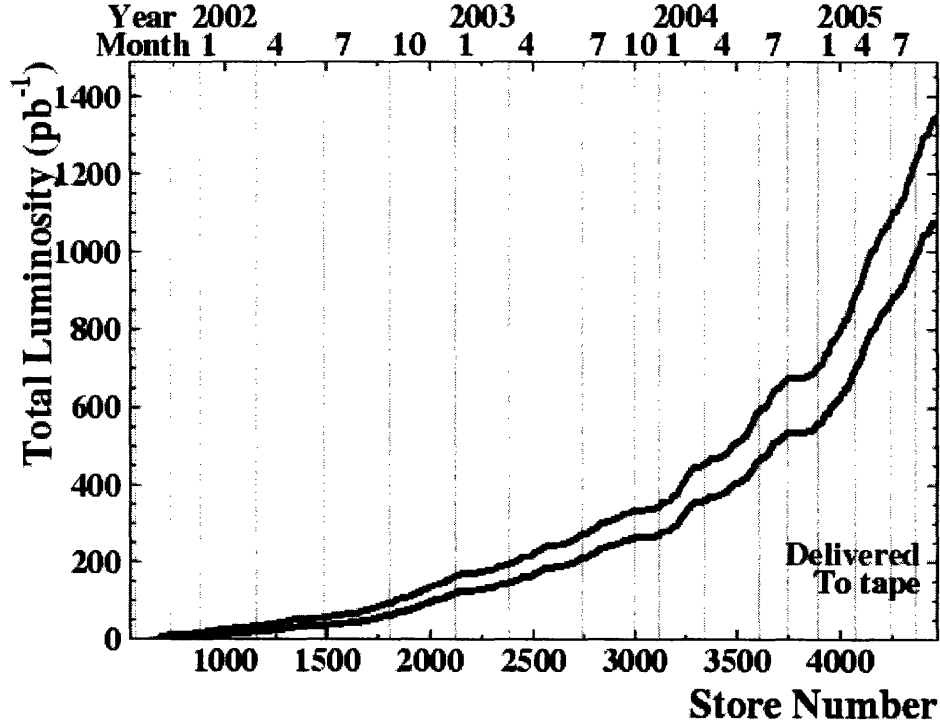


Figure 2-3: The higher curve shows the luminosity delivered to CDF by the Tevatron between April 2002 and July 2005. The lower curve shows how much data has actually been written to tape.

September 2005. The average instantaneous luminosity of data runs used in the analysis is  $5.0 \times 10^{31} \text{ cm}^{-2}\text{s}^{-1}$ . At the time of this writing the record instantaneous luminosity seen at CDF is  $1.4 \times 10^{32} \text{ cm}^{-2}\text{s}^{-1}$ . Since the start of physics-quality data taking at CDF in April 2002, the Tevatron has delivered a total of about  $1.4 \text{ fb}^{-1}$  to CDF, of which  $355 \text{ pb}^{-1}$  is used for this analysis. Figure 2-3 shows the luminosity accumulated by the CDF detector between April 2002 and July 2005. The higher curve shows the luminosity delivered to CDF by the Tevatron. The lower curve shows how much data has actually been written to tape.

### 2.1.1 Interaction point

The  $p$  and  $\bar{p}$  beams circulating in the Tevatron are unpolarized, and bunches exhibit a longitudinal density profile such that the resulting distribution of collisions along the beam axis is approximately Gaussian, with an r.m.s of about 30 cm. Daughter particles from a  $p\bar{p}$  collision are produced not at rest but have a significant momentum.

The total energy of  $p\bar{p}$  collisions is not utilized for the creation of new particles. The colliding partons carry only a fraction of the total proton energy. As a result, the center-of-mass system of colliding partons is boosted in the longitudinal direction by an unknown amount. On the other hand, the quantities defined in the transverse plane do not have this ambiguity. For example, the sum of all transverse momenta of particles in the collisions is zero ( $\sum \vec{p}_T = 0$ ). This is the reason why CDF physics analyses often choose to work with quantities like  $p_T$  — the transverse momentum and  $E_T$  — the transverse energy, rather than use full momentum and full energy.

## 2.2 The CDF detector

The Collider Detector at Fermilab (CDF) is a multi-purpose detector designed to study the physics of high-energy  $p\bar{p}$  collisions [26]. CDF provides charged particle tracking in a solenoidal magnetic field, time-of-flight measurements, electromagnetic and hadronic calorimetry, and muon detection. A cut-away diagram of the detector is shown in Figure 2-4.

The overall geometry of the detector is cylindrical, with the Tevatron beamline running through the center, along the axis of symmetry. CDF employs a right-handed global coordinate system, with the origin at the interaction point in the very center of the detector. The sets of coordinates used  $(r, \phi, z, x, y, \theta, \eta)$  are defined in Figure 2-5. Note that the detector is azimuthally symmetric about the  $z$  axis, and mirror symmetric about the plane transverse to the beamline, centered at  $z = 0$ .

It is useful to define two variables: rapidity and pseudo-rapidity.

- rapidity,  $y$ , is defined as

$$y = \frac{1}{2} \ln\left(\frac{E + p_z}{E - p_z}\right), \quad (2.2)$$

where  $E$  is the energy of a particle, and  $p_z$  is the component of its momentum along the  $z$  axis. Rapidity is additive under Lorentz boosts in the  $z$  direction, and, thus, rapidity differences are invariant under such boosts. Particle production is empirically observed to be flat only within  $|y| < 1.0$ , but at large

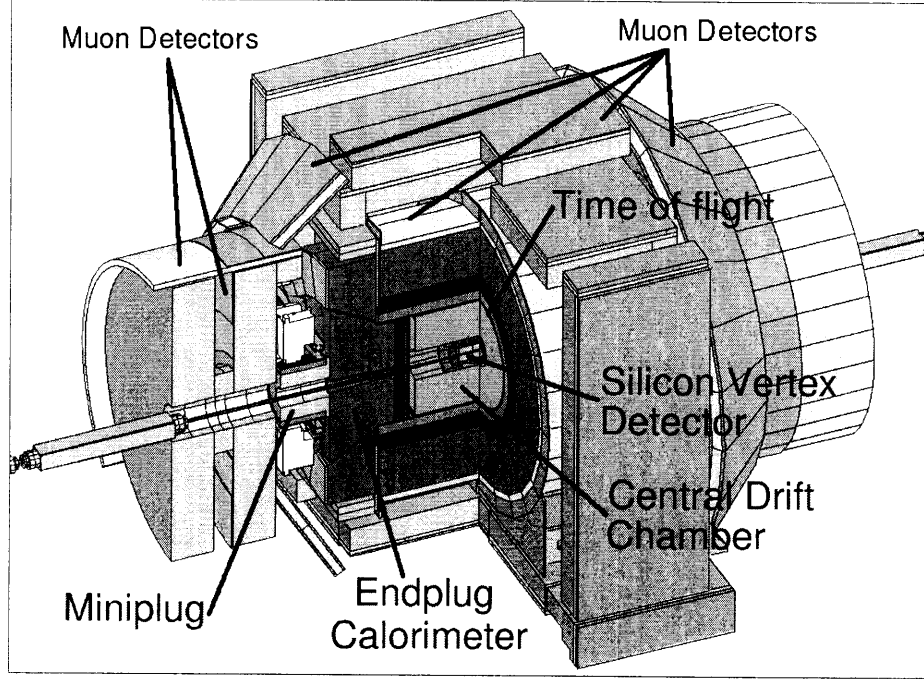


Figure 2-4: The CDF detector with a quadrant cut away to expose the different sub-detectors.

rapidities there is a kinematic cutoff that turns off production. The kinematic cutoff is actually mass dependent. So, for example, top quark production is flat within  $|y| < 1.0$ , whereas for bottom quarks flat rapidity range is longer.

- pseudo-rapidity,  $\eta$ , is defined as

$$\eta \equiv -\ln \tan(\theta/2), \quad (2.3)$$

where  $\theta$  is the polar angle measured from  $z$  axis as shown in Figure 2-5. Pseudo-rapidity is equivalent to rapidity for massless particles, and is approximately equivalent for particles with momentum much greater than their rest mass. Pseudo-rapidity is experimentally more convenient as a coordinate because it does not require knowledge of the particle mass for its calculation.

Similar to the Fermilab accelerator complex, CDF is a complex entity which is comprised of many subsystems. Those, most important to this analysis are described in the following sections, beginning nearest the interaction point and moving radially

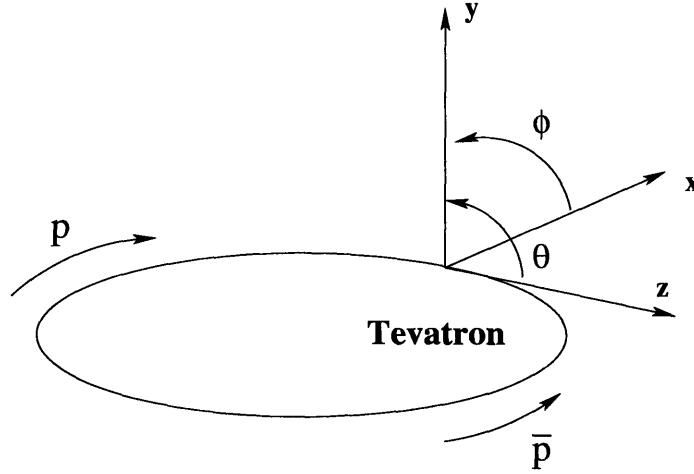


Figure 2-5: Definition of coordinates used with the CDF Run II detector.

out-wards.

## 2.3 Track parametrization

In the previous section we described the CDF coordinate system. In this section we concentrate on explaining what a “track” is and how it is defined for CDF. Particles moving through a uniform magnetic field follow helical trajectories. The trajectories of the particles are reconstructed from hits left in the tracking system and are referred to as “tracks”.

To uniquely parametrize a helix in three dimensions, five parameters are needed. The CDF coordinate system chooses three of these parameters to describe a position, and two more to describe the momentum vector at that position. The three parameters which describe a position describe the point of closest approach of the helix to the beam line. These parameters are  $d_0$ ,  $\phi_0$ , and  $z_0$ , which are the  $\rho$ ,  $\phi$  and  $z$  cylindrical coordinates of the point of closest approach of the helix to the beam (see Figure 2-6). The momentum vector is described by the track curvature ( $C$ ) and the angle of the momentum in the  $r - z$  plane ( $\cot \theta$ ). From the track curvature we can calculate the transverse momentum. The plane perpendicular to the beam is called the “transverse plane”, and the transverse momentum of the track is called  $p_T$ . The curvature is signed, so that the charge of the particle matches the sign of

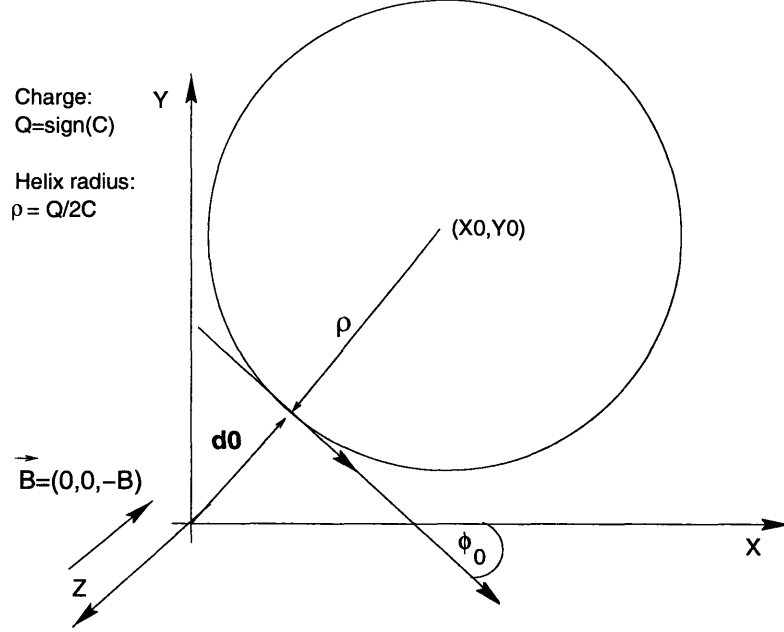


Figure 2-6: Illustration of transverse plane tracking parameters

the curvature. From  $\cot \theta$  we can calculate  $p_z$ . At any given point of the helix, the track momentum is a tangent to the helix. This basically means that the angle  $\phi_0$  implicitly defines the direction of the transverse momentum vector at the point of closest approach. The following relations summarize the correspondence between the measured parameters  $C$ ,  $\theta$ , and  $\phi_0$  and components of the momentum vector:

$$\begin{aligned}
 p_T &= \frac{c \cdot B}{2|C|}, \\
 p_x &= p_T \cdot \cos \phi_0, \\
 p_y &= p_T \cdot \sin \phi_0, \\
 p_z &= p_T \cdot \cot \theta.
 \end{aligned} \tag{2.4}$$

For decaying particles, we often define the  $L_{xy}$ :

$$L_{xy} = \vec{d} \cdot \frac{\vec{p}_T}{|p_T|}, \tag{2.5}$$

where  $\vec{d}$  is the displacement of the decay vertex in the transverse plane, and  $\frac{\vec{p}_T}{|\vec{p}_T|}$  is the unit vector in the direction of  $\vec{p}_T$ . The  $L_{xy}$  significance is defined as the ratio of  $L_{xy}$  and the  $L_{xy}$  uncertainty.

## 2.4 Tracking systems

The tracking system is used to distinguish charged particles from neutral particles and to measure the position and momenta of charged particles in the detector. Figure 2-7 shows a longitudinal view of the tracking detectors. The innermost tracking detector is the Silicon Vertex Detector. It consists of Layer 00 (an innermost layer of silicon installed directly onto the beam pipe), the SVX II detector with five layers of silicon, and the ISL (the layer of silicon surrounding SVX II). The Silicon Vertex Detector provides tracking information out to  $|\eta| < 2$  thanks to the geometry of the ISL which extends in the  $z$  direction such that it still produces hits for tracks almost parallel to the beam direction (see Figure 2-7). Surrounding the silicon tracking system is the central outer tracker (COT), a drift chamber, which provides tracking coverage for  $|\eta| < 1$ . Finally, the entire tracking system is surrounded by a 1.4 T solenoidal magnet.

### 2.4.1 Silicon tracking detectors

Silicon tracking detectors are used to obtain precise position measurements of the paths of charged particles. A silicon tracking detector functions as a series of reverse-biased p-n junction transistors. When a charged particle passes through the detector material it produces ionization. In case of a semi-conductor material, this means that  $e^-$ -hole pairs are produced. Electrons drift toward the anode, and holes drift toward the cathode, where the charge is gathered. The amount of charge is, to first order, proportional to the path length traversed in the detector material by the charged particle.

By segmenting the p or n side of the junction into “strips” and reading out the charge deposition separately on every strip, one can obtain sensitivity to the position



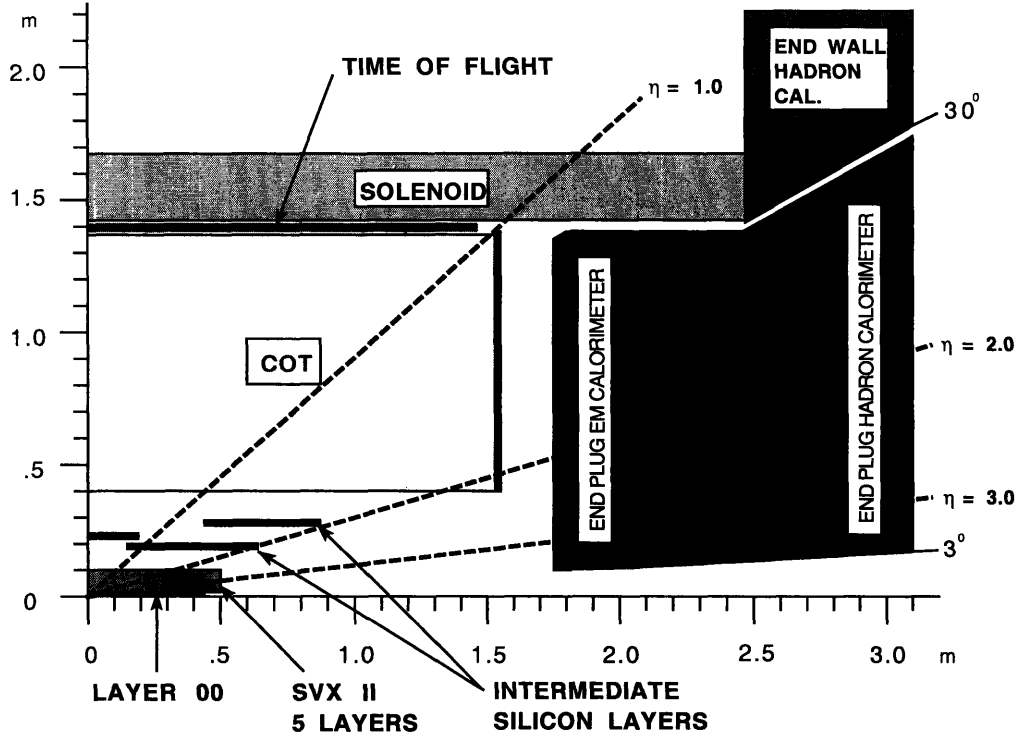


Figure 2-7: Longitudinal view of one quadrant of the CDF detector.

of the charged particle. All the CDF silicon tracking detectors are implemented as micro-strip detectors. The typical distance between two strips is about  $60 \mu\text{m}$ . Charge deposition from a single particle passing through the silicon sensor may span several strips, and therefore charge deposition is read out on one or more strips. The collection of hits associated with this charge deposition is called a “cluster”. There are two types of microstrip detectors used by CDF: single and double-sided. In single-sided detectors, only one (p) side of the junction is segmented into strips. Double-sided detectors have both sides of the junction segmented into strips. The benefit of double-sided detectors is that while one (p) side has strips parallel to the  $z$  direction, providing  $r - \phi$  position measurements, the other (n) side can have strips at an angle (stereo angle) with respect to the  $z$  direction, which give  $z$  position information.

There are three subsystems in the silicon tracking system. The innermost detector, located immediately outside the beampipe is Layer 00 [27]. Its sensors are mounted

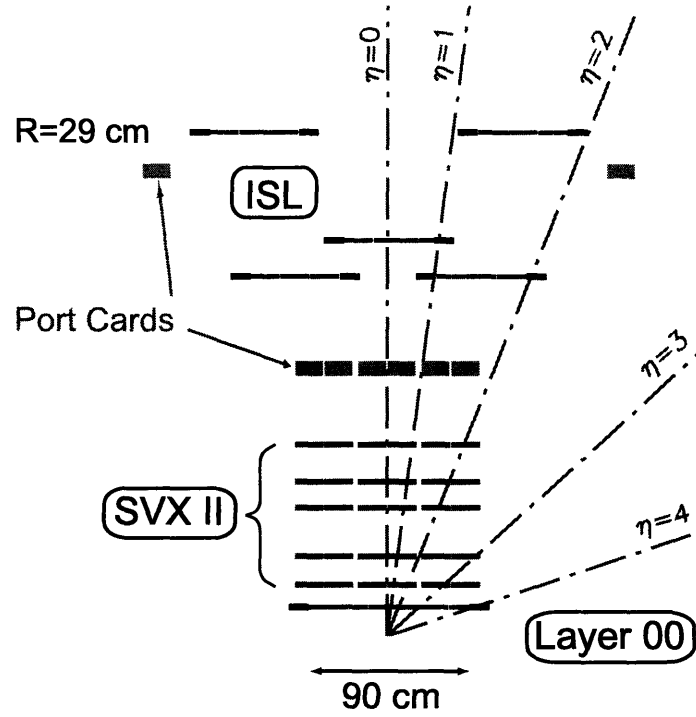


Figure 2-8: Coverage of the different silicon sub-detector systems projected into the  $r - z$  plane. The  $r$  and  $z$  axes have different scales.

on a carbon-fiber support structure which also provides cooling. The sensors are made of light-weight radiation-hard silicon (different from that of the SVX) and are single-sided with a  $25 \mu\text{m}$  readout pitch. Layer 00 provides  $r - \phi$  measurements only.

The SVX is located outside Layer 00 with inner radius 2.44 cm and outer radius 10.6 cm [28]. It consists of 3 barrels placed end to end. Each barrel is 29 cm in length for a total combined length of 87 cm. Each barrel consists of 5 layers of double sided silicon and is segmented into 12 wedges in  $\phi$ . This design is shown in Figure 2-8. The double-sided silicon sensors of SVX-II have different stereo angles. Two layers have a small ( $1.2^\circ$ ) stereo angle and three have a  $90^\circ$  stereo angle. While the SVX provides good impact parameter resolution for secondary vertex reconstruction, further information is necessary to improve the matching of the silicon tracks to tracks in the central outer tracker, whose inner radius is located at 43.4 cm. The intermediate silicon layer (ISL) serve this purpose in the central region (see Figure 2-8) by supplying a layer of silicon at a radius of 22 cm with  $|\eta| < 1$  coverage [29]. Additionally, in the plug region, specifically  $1 < |\eta| < 2$ , the ISL consists of two more

silicon layers at radii 20 cm and 28 cm. These layers extend to  $|z| < 65$  cm and  $|z| < 87.5$  cm, respectively, and provide additional coverage, where tracks do not pass through all COT super-layers. The ISL detector provides small-angle ( $1.2^\circ$ ) stereo information. Further information on the SVX and ISL can be found in the CDF II Technical Design Report [30].

## 2.4.2 Central Outer Tracker

The Central Outer Tracker (COT) is a 96-layer open-cell drift chamber used for charged particle tracking in the  $|\eta| < 1.1$  region [31]. The COT surrounds the silicon detector with its inner radius located at 43.4 cm and outer radius at 132 cm. The mechanical structure of the COT is defined by the two 1.4 m radius aluminum end-plates separated by 310 cm in  $z$ . The inner and outer walls of the COT cylinder are made of 0.25 inch aluminum sheets with the inner radius at 0.4 m.

The sense wires are divided into 8 super layers (SL), 4 axial layers (for  $r - \phi$  measurement), and 4 stereo layers (for  $z$  measurement) with the structure shown in Figure 2-9. Each super layer is then subdivided into cells by Mylar field sheets strung between the end plates. A cell contains  $25\ \mu\text{m}$  diameter gold-plated copper-beryllium wires that alternate between potential and sense wires as shown in Figure 2-10. The wire spacing is about 7.5 mm in all super layers. Each wire is strung between the two end-plates with a tension of 1.3 N, giving a total load on the end-plates of 40 tons from all the wires. At the longitudinal center of the COT, a mylar wire support is epoxied to all of the sense and potential wires to provide additional electrostatic stability. The spacing between wires and the field sheets is just under 1 cm and varies slightly between super layers. The design of three cells from super layer 2 can be seen in Figure 2-10.

Argon-Ethane gas (60:40 mixture) fills the active chamber volume and both provides a source of ionized electrons and defines the drift velocity of the gas. From the drift velocity and maximal path length (defined by the cell size), the maximum drift time is calculated. For the COT, the maximum drift time is about 100 ns, which is less than the minimum bunch spacing of 132 ns proposed for the high luminosity



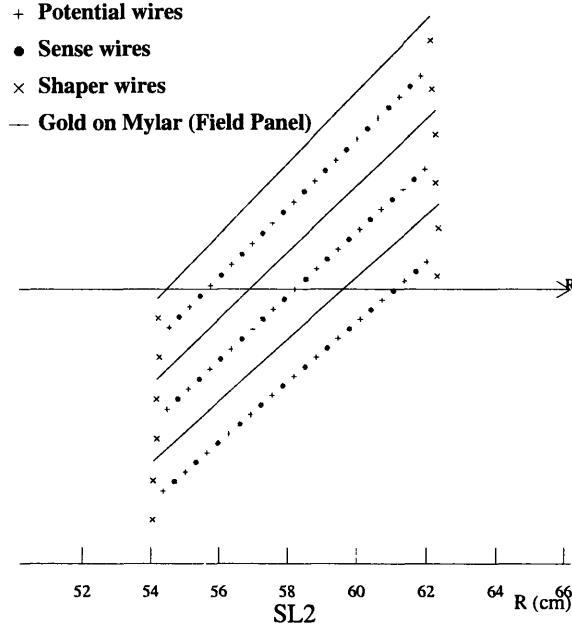


Figure 2-10: Layout of wires in a COT supercell.

combined with the large lever arm, gives the COT a transverse momentum resolution of

$$\frac{\sigma_{p_T}}{p_T^2} = 0.15\%, \quad (2.6)$$

where the transverse momentum is in units of GeV/c [31]. The large geometric coverage of the COT along with its excellent momentum resolution make the COT the primary tracker for event reconstruction.

### 2.4.3 Pattern recognition algorithms

The hits collected in the COT and SVX need to be grouped together to make the tracks. The track reconstruction begins using only the COT information. The first step is to look for a circular path in the axial super-layers of the COT. The algorithm looks for four or more hits in each axial super-layer to form a straight line, or “segment”. The hits in the segment are reconstructed using the time difference between the time when ionization occurs,  $t_0$ , *i.e.* the collision time plus the time of flight of the charged particle, and the time when the signal is picked up by the wire (the leading edge time of the digital pulse from the TDC). The global time offset, readout time

of the wires and cables, electronic channel pedestals, charge-based time slewing and non-uniform drift velocities are corrected before using the time difference (or “drift time”) in the tracking. Once segments are found, there are two approaches to track reconstruction. One of them is to link together the super-layer segments which are consistent with being tangent to the same circle. The other approach is to constrain the track circle fit to pass through the beamline, and then add hits which are consistent with the path. Once the circular path is found in the  $r - \phi$  plane, segments and hits in the stereo super-layers are added depending on their proximity to the circular fit, resulting in a three-dimensional track fit. The two algorithms are designed to be complimentary and optimize the track reconstruction efficiency.

Once a track is reconstructed in the COT, it is extrapolated into the SVX-II. A three-dimensional “road” is formed around the extrapolated track, based on the estimated uncertainties on the track parameters. Starting from the outermost Si layer, and working inward, silicon clusters found inside the road are added to the track. As a cluster is added, a new track fit is performed, which modifies the error matrix for the track parameters and produces a narrower road. In the first pass of the algorithm,  $r - \phi$  clusters are added. In the second pass, stereo clusters are added to the track. If there is more than one track candidate with different combinations of SVX hits associated with the same COT parent, the track with maximum number of SVX hits is chosen. The track reconstruction efficiency in the COT is  $\approx 95\%$  for tracks which pass through all 8 super-layers ( $p_T > 400$  MeV/c) and  $98\%$  for tracks with  $p_T > 10$  GeV/c. The SVX track reconstruction efficiency for tracks that have a COT parent is about  $93\%$  for the tracks with at least 3 SVX  $r - \phi$  hits.

## 2.5 Time of flight

The CDF Time-of-Flight (TOF) system is located just outside the COT, and inside the superconducting magnetic coil, as shown in Figure 2-7. The TOF system is designed to distinguish low-momentum pions, kaons, and protons by measuring the time it takes these particles to reach the TOF system from the interaction vertex.

The particle momentum is known from the tracking system, and therefore the time-of-flight measurement provides an indirect determination of the mass [32].

The TOF system is composed of 216 bars of Saint-Gobain (formerly Bicron) BC-408 blue-emitting plastic scintillator, forming an annulus 300 cm long with a radius of 144 cm. The bars have a slightly trapezoidal shape to accommodate the annulus shape, with an approximate width and height of 4 cm for each.

When fast moving charged particles pass through the scintillator bars, they excite the atoms in the plastic through ionization energy-loss. The excited atoms lose part of this energy by emitting photons of light. Good scintillator materials are characterized by short relaxation times and low attenuation of the generated light.

The scintillator light is converted to a signal voltage by Hamamatsu R5946mod 19-stage fine-mesh photo-multiplier tubes (PMTs) installed on both ends of the scintillator bars. The 19-stage high-gain design is needed to ensure adequate gain inside the 1.4 T magnetic field. The photo-multiplier tubes are followed by dual-range pre-amplifiers before transmission to the readout electronics over shielded twisted pair cables. The dual range increases the dynamic range of the TOF electronics for a magnetic monopole search [33] without adversely affecting the performance for ordinary particles. An initial high-gain region for ordinary tracks is followed by a second low-gain region for larger pulses, as would arise for monopoles.

The digitization of the pre-amplified PMT pulses is performed by TOF Transition (TOMAIN) and ADC/Memory (ADMEM) [34] boards. The TOMAIN boards begin ramping an output voltage as soon as the incoming pulse exceeds a threshold, and stops ramping on command from a common stop signal. The ramping voltage is proportional to a time measurement. The output voltage is digitized by the ADMEMs. Because a large pulse goes above threshold faster than a small pulse, an integrated charge measurement is needed to correct this time-walk effect, so both charge and time measurement are actually done. The TOMAIN boards integrate the charge for a fixed time interval, then converts the integrated charge to an output voltage, which is digitized by the ADMEM. The timing resolution of the TOF system is about 110 ps for particles crossing the bar exactly in front of one of the photomultiplier tubes. Be-

cause light is attenuated in the bar, the timing resolution is worse for tracks crossing far from a PMT.

## 2.6 Calorimeters

Outside the solenoid are the electromagnetic calorimeters [35] followed by the hadronic calorimeters [36]. The calorimeter systems are not used in this analysis and, thus, only briefly summarized.

Comparison of the energy depositions in electromagnetic and hadronic calorimeters provides separation between electrons and photons (which deposit most of their energy in the electromagnetic calorimeter ) from hadrons (which deposit most of the energy in the hadronic calorimeter). Both electromagnetic and hadronic calorimeters are segmented in  $\phi$  and  $\eta$  towers so that each tower points to the interaction region. This arrangement is called a projective tower geometry. The calorimeters are divided into central and forward subsystems corresponding to  $|\eta| < 1$  and  $1.1 < |\eta| < 3.6$  respectively.

Each calorimeter tower is  $15^\circ$  in azimuth and 0.11 in pseudo-rapidity. The electromagnetic towers consist of alternating layers of lead and scintillator and have a depth of  $\sim 18$  radiation lengths of material. The hadronic towers are composed of alternating layers of iron and scintillator and correspond to  $\sim 4.7$  interaction lengths of material. The wall hadronic calorimeter is situated between the central and the forward calorimeters as seen in Figure 2-7, and it has a similar design as the central hadronic calorimeter. The plug calorimeter covers the region  $1.1 < |\eta| < 3.6$  and is segmented in  $7.5^\circ$  in azimuth and 0.11 in pseudo-rapidity towers for the  $\eta < 2.1$  region, and  $15^\circ$  in azimuth and 0.11 in pseudo-rapidity towers for the  $\eta > 2.1$  region. The plug electromagnetic calorimeter corresponds to  $\sim 23$  radiation lengths while the plug hadronic calorimeter has a depth of  $\sim 7$  interaction lengths. For each calorimeter subsystem, the scintillation light is directed to photomultiplier tubes that measure the energy depositions.

The central pre-radiator detector (CPR) [37] is located between the solenoid coil



and the central electromagnetic calorimeter at a radius of  $\sim 168$  cm. It is a series of single plane multi-wire proportional chambers with 32 sense wires per wedge along the  $z$ -direction. The chambers are  $\sim 116$  cm long. They sample the electromagnetic showers that begin in the material of the solenoidal magnet in front of them. The shapes of electromagnetic showers are different for electrons, photons and minimum ionizing particle like muons and hadrons, so CPR provides greatly enhanced photon and soft electron identification.

The shower maximum detector (CES) [38] is a multi-wire proportional chamber located inside the central electromagnetic calorimeter. CES uses strip readout along the beamline and wire readout in the  $\phi$  direction. The position resolution in both directions is about 2 mm. CES is used for identification of electrons, which produce tracks in the COT, by matching the position of electromagnetic showers with incident tracks. The transverse shower profile is used to separate photons from neutral pions, and the pulse height helps to identify electromagnetic showers.

## 2.7 Muon systems

There are four muon systems in CDF: the Central Muon Detector (CMU), Central Muon Upgrade Detector (CMP), Central Muon Extension Detector (CMX), and Intermediate Muon Detector (IMU). All muon systems are located behind both the electromagnetic and hadronic calorimeters, which function as absorbers for particles other than muons. Electrons are absorbed in the electromagnetic calorimeter, where their energy loss is dominated by bremsstrahlung. Like electrons, muons also do not interact hadronically. Furthermore, since the rate of electromagnetic energy loss is proportional to  $1/m^2$ , muons, being 200 times heavier than electrons, undergo 40000 times less bremsstrahlung radiation, and pass through. Pions and kaons are absorbed in the hadronic calorimeter where they interact strongly. A small portion of pions and kaons which survive passage through the calorimeter is a source of non-muon background, and is referred to as “punch-through”.

### 2.7.1 CMU

The CMU is the oldest muon detector in CDF, and is fully documented in Reference [39]. It covers  $|\eta| < 0.6$ , and is mounted on the outside of the cylindrically symmetric central calorimeter, at a radius of 347 cm. The CMU chambers are segmented in  $\phi$  into  $12.6^\circ$  wedges. The wedges are divided further in  $\phi$  into three modules. Each of these modules contains 4 layers of 4 rectangular drift cells, with dimensions 63.5 mm (in  $x$ )  $\times$  26.8 mm (in  $y$ )  $\times$  2262 mm (in  $z$ ). Each has a  $50\ \mu\text{m}$  sense wire, which runs parallel to the  $z$ -axis, located at the center of the cell. Adjacent layers in CMX, CMP, and CMU are offset by one half cell in order to reduce ambiguities for tracking algorithms.

### 2.7.2 CMP

The CMP is a second set of muon chambers, again with coverage up to  $|\eta| < 0.6$  [40]. It covers 53% of the azimuth, and forms a box around the central detector. As in the CMU, the drift cells are rectangular, but with cross-sectional dimensions of 2.5 cm  $\times$  15 cm. Approximately 0.5% of charged pions are sources of punch through in the CMU [39]. To reduce this background, the CMP is situated behind an additional 60 cm of steel. Because of the rectangular shape CMP coverage varies as a function of  $\phi$ . The important thing though is that the CMU  $\phi$  gaps are covered, and a large fraction of CMU muons with  $p_T$  above 2.2 GeV/c get “CMP confirmation”, which allows for extremely clean muon selection. Muons with  $p_T$  lower than 2.2 GeV/c are absorbed in the material of the CDF detector before they reach CMP.

### 2.7.3 CMX

The CMX covers  $0.6 < |\eta| < 1.0$ . It consists of a conical arrangement of drift chambers and scintillation counters, where the latter are used to reject background based on timing information [41]. The CMX covers  $240^\circ$  in  $\phi$ . In Run I there was a  $30^\circ$  gap at the top and there was a  $90^\circ$  gap at the bottom, due to interference with the floor of the collision hall. For Run II these gaps are instrumented by the key

stone (top) and the mini skirt (bottom) additions.

The drift chambers differ from those of the CMP only in length. They are arranged in azimuthal sections, as is the case in the central detector: in each of the 24  $\phi$  sectors, there are 4 layers of 12 drift cells.

## 2.8 Trigger

Modern hadron colliders are unique in the sense of how much data they produce. The average size of an event at CDF is about 250 KBytes. The bunch crossing time in Fermilab's Tevatron is 132 ns with collisions happening at a rate of 2.5 MHz. This produces an incredible potential data flow for CDF alone of about 625 Gbyte per second. It is physically very difficult to simply read out this amount of information, let alone storing and analyzing the volume of data accumulated over several years of running the Tevatron. Therefore, it is necessary to use an online filtering system which reduces the data flow to manageable levels. This is the purpose of the CDF triggering system.

The CDF triggering system is designed to distinguish events which are potentially interesting from the physics point of view from the vast majority of background events. There are several requirements that a good trigger system has to satisfy. The first requirement is that it has to be extremely fast. In the case of CDF this means that it should be able to perform the trigger decision in a time interval close to 132 ns, the designed time between collisions imposed by the Tevatron upgrade for Run II. Second, it should have zero dead time. In other words, it is preferable to make a trigger decision based on physics quantities as opposed to randomly throwing events away which overfill the trigger system. Another requirement is imposed by the CDF data logging system which is designed to write to tape at a maximum of 20 MBytes per second. This number is limited by the costs of data storage and computational power needed to do the analysis on the data. All of these requirements are achieved by staging the trigger in three layers, called Level 1, Level 2, and Level 3, as shown in Figure 2-11.

The Level 1 trigger is extremely limited in the time allocated for making the trigger decision. Level 1 has memory buffers which can record up to 42 events. The product of 132 ns time between bunch crossings and 42 available event buffers in the Level 1 storage pipeline gives about  $5\mu\text{s}$  for the time available to make a trigger decision. Level 1 is equipped with custom electronics designed to perform very rough and quick pattern recognition for filtering events. The rejection factor after Level 1 is about 150. So, the Level 1 accept rate is below 50 kHz. The Level 2 trigger buffer can hold and analyze simultaneously up to 4 events, giving it  $20\mu\text{s}$  for the average trigger decision. This time is sufficient to perform more complicated selection algorithms. The Level 2 trigger includes unique custom electronics designed for triggering on displaced tracks (see SVT Section 2.8.2), a feature never attempted before in a hadronic collider environment. This ability is crucial for this analysis. The Level 2 reject rate is also about 150, giving Level 2 an accept rate of about 300 Hz. The Level 3 trigger is implemented with 300 PC's in a farm allowing about 2 seconds per event to make a trigger decision. The nodes of the Level 3 farm run the physics selection based on the offline code. The events that are accepted by Level 3 are then written to tape.

The CDF detector is a multi-purpose detector. It is designed to collect data interesting for a large number of very different physics measurements. For this reason the CDF trigger decision is fragmented in over 100 trigger paths. A trigger path is a set of requirements that an event has to satisfy at Level 1, Level 2 and Level 3. The trigger system performs simultaneous selection with all trigger paths. It is designed to eliminate volunteer events. A volunteer event is an event that passed a higher level trigger requirements (Level 2 or Level 3) but did not pass the corresponding (for this particular path) lower level trigger requirements (Level 1 or Level 2). In the end, an event is accepted only if it satisfies the complete set of requirements of some particular trigger path. If the volunteer events were present, it would make the determination of the  $B$  meson reconstruction efficiency difficult because these events are not described by the Monte Carlo simulation. The set of trigger paths used in this analysis is called the Two-Track Trigger. The flow of the trigger data for the Two-Track Trigger is shown in Figure 2-12.

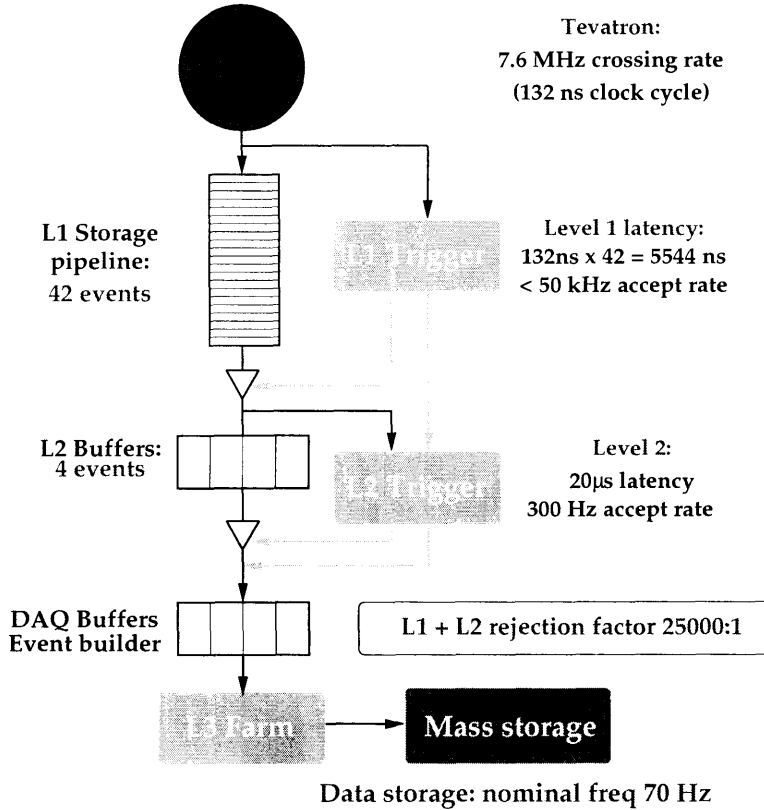


Figure 2-11: Diagram of the CDF trigger system.

The Two-Track Trigger is designed for finding charm and bottom mesons that decay in hadronic final states. It is a new trigger created for Run II with the measurement of CP-violation in  $B \rightarrow \pi\pi$  decay in mind. The Two-Track Trigger was later adopted for the  $B_s^0$  mixing analysis in fully reconstructed hadronic modes.

As shown in Figure 2-12 the pieces of the trigger system participating in the Two-Track-Trigger decision are XFT and XTRP at Level 1 and SVT at Level 2. We therefore describe these systems in detail in the next sections followed by the description of the Two-Track Trigger requirements at Level 1 and Level 2.

### 2.8.1 Fast Track Trigger (XFT)

The eXtremely Fast Tracker [42] is a synchronous, parallel, pipelined track processor. It identifies high-transverse-momentum tracks in the COT quickly enough for the results to be used in the CDF Level 1 trigger. tracks from XFT are also known as

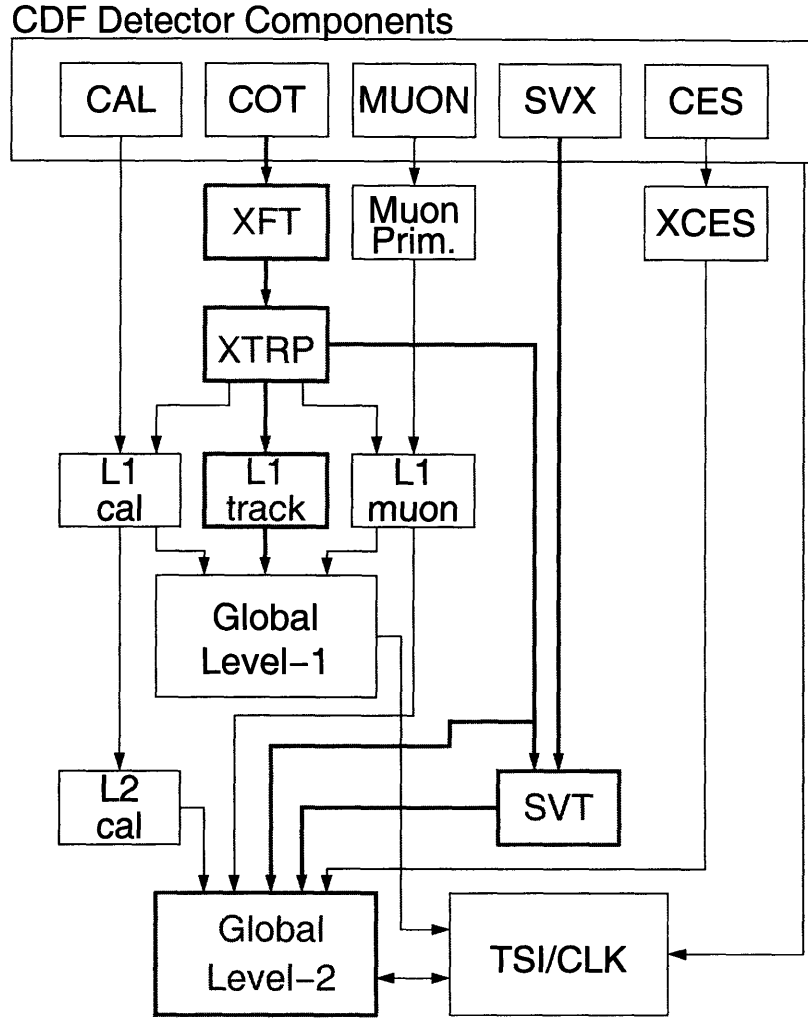


Figure 2-12: Diagram of the trigger decisions at Level 1 and 2. The Two-Track Trigger data (shown in red) flows through XFT, XTRP, L1 track at Level 1 and SVX and SVT at Level 2.

trigger primitives because they are elementary objects upon which the trigger decision logic is based.

The XFT examines the hit information of the COT. Based on pre-loaded patterns of COT hits, it is capable of recognizing track segments for tracks with  $p_T > 1.5$  GeV/c in  $15^\circ$  wedges in  $\phi$ . It reports the measurement of the track  $p_T$  and  $\phi_6$ , the angle of the transverse momentum at the sixth super-layer of the COT, which is located 106 cm radially from the beamline. A maximum of two tracks are reported from a given  $15^\circ$  wedge, i.e the two tracks which are closest to the left and right boundary of the wedge.

The performance characteristics for XFT are the following:

- track finding efficiency exceeding 96% for tracks above 1.5 GeV/c,
- low fake rate,
- momentum resolution  $\Delta p_T/p_T^2 < 2\%/GeV/c$ ,
- $\phi_0$  resolution better than 8  $\mu rad$ .

An extrapolator module (XTRP) (see Figure 2-12) is a part of Level 1 trigger. It is used to propagate the tracks found by XFT into the other parts of the CDF detector such as the calorimeters and the muon chambers. Matching XFT tracks with EM calorimeter towers or muon stubs (muon chambers) creates more complex primitives (electrons and muons). A trigger decision based on electrons and muons provides an additional rejection at Level 1. Finally, XFT tracks are used to “seed” the Level 2 silicon trigger (SVT), which is described in Section 2.8.2.

The actual Level 1 decision is done by the Global Level 1 processor (see Figure 2-12). By design, the Level 1 trigger should be able to very quickly make a trigger decision, i.e. within the nominal 5  $\mu s$  available before the Level 1 buffers fill up. The events accepted by the Level 1 are then passed to the Level 2 trigger.

## 2.8.2 Silicon Vertex Trigger (SVT)

Triggering on displaced tracks at high rates is essential to the study of fully reconstructed hadronic  $B$  decays in a hadron collider. Some interesting channels, such as  $B^0 \rightarrow \pi^+\pi^-$ , can only be extracted from the background by requiring the presence of displaced tracks at an early trigger level. Without such a trigger it would be impossible to collect sufficient statistics at a realistic event recording rate.

The Silicon Vertex Trigger [43], or SVT, is a track processor designed to identify secondary vertices at the second level of the CDF trigger. The input to the SVT is the list of axial COT tracks found by XFT, and the data from four axial silicon layers. It filters XFT tracks, discarding those with  $p_T$  below 2 GeV/c. It then associates a set of silicon hits to each high- $p_T$  XFT track, and fits the results to a circle in the

transverse plane. The fit result determines the impact parameter ( $d_0$ ) — the distance of closest approach of the track helix to the beam, and improved measurements of  $p_T$  and  $\phi_0$ . The Level 2 trigger primitive or SVT track is created. The time allotted to the Level 2 trigger is of the order of 20  $\mu$ s. The SVT performs its task spending about 10  $\mu$ s on the average event.

Figure 2-13 shows the principle of SVT operation. As mentioned in Section 2.4.1, the SVX-II is segmented into 12 wedges in  $\phi$  and three mechanical barrels in  $z$ . The SVT makes use of this symmetry and does tracking separately for each wedge and barrel. Tracks which cross wedge and barrel boundaries are only reconstructed under certain circumstances. An SVT track starts with a two dimensional XFT “seed.” The XFT track is extrapolated into the SVX-II, forming a “road” in  $r - \phi$ . Silicon clusters on the inner four  $r - \phi$  layers of the given wedge have to be found inside this road. The silicon cluster information and the XFT segment information are fed into a linearized fitter which returns measurements of  $p_t$ ,  $\phi_0$ , and  $d_0$  for the track.

Another function of the SVT is determining the beamlines on a run-by-run basis. They are defined in terms of  $(x, y)$  coordinates at  $z = 0$ , and slopes with respect to the  $x$  and  $y$  axes. The beamline is typically shifted by  $\approx 50\mu$ m in both  $x$  and  $y$  direction, while the slopes are very small, on the order of 0.1  $\mu$ rad. The SVT beamlines are further processed offline and improved beamlines are stored in the CDF database and used by the offline analysis to determine the position of the primary interaction point.

### 2.8.3 Two-Track Trigger: Level 1 and Level 2

An event is accepted at by the Two-Track-Trigger at Level 1 if two XFT tracks are found in the event such that they have opposite charge, both tracks have  $p_T > 2$  GeV/c, the scalar sum of transverse momenta  $p_{T1} + p_{T2} > 5.5$  GeV/c and the  $\phi$  separation between the tracks at super-layer 6 is  $|\Delta\phi_6| < 135^\circ$ .

At Level 2, the rough tracking information from the XFT is combined with SVX-II cluster information by the Silicon Vertex Trigger (SVT) [43]. The goal of the second level of the trigger is to obtain a precise measurement of the track  $d_0$  — the distance of the closest approach of the track helix to the beam, and improved measurements



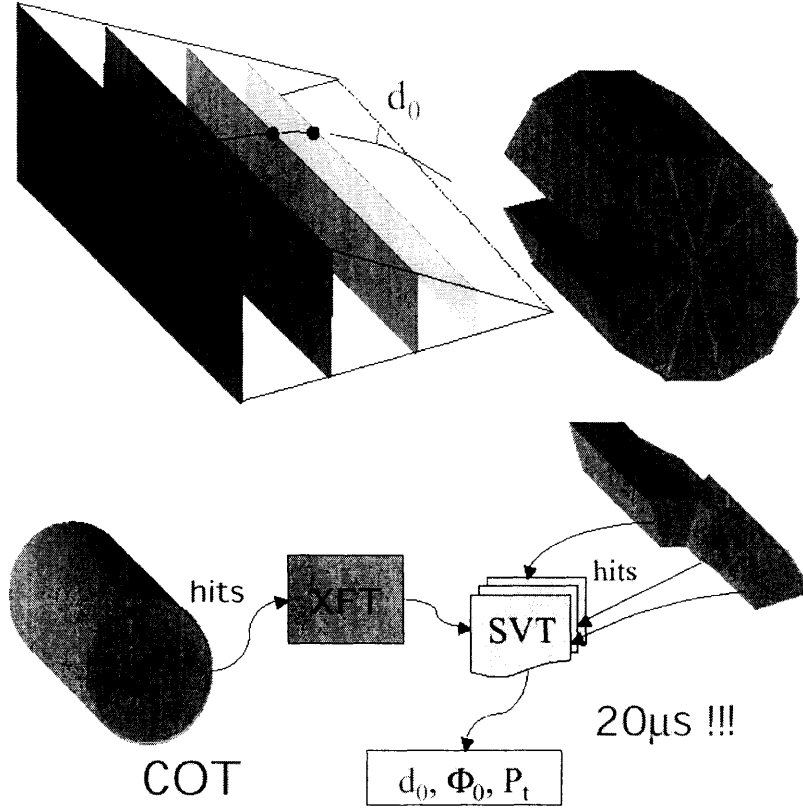


Figure 2-13: SVT principle of operation. The XFT examines the hit information of the COT. The SVT fits XFT tracks in association with silicon hits and determines the  $d_0$ ,  $p_T$ , and  $\phi_0$ . The cylinder in blue depicts 12 wedges of the SVX-II. Each wedge consists of 5 layers of double sided silicon. The Level 2 performs its task spending less than  $20 \mu s$  per event.

of  $p_T$  and  $\phi_0$ . The Level 1 trigger conditions must be confirmed with the improved measurements of  $p_T$  and  $\phi_0$ . An event passes the Level 2 selection if there are a pair of tracks reconstructed in the SVT such that the tracks have opposite charge, each track has  $p_T > 2.0 \text{ GeV}/c$  and  $120 \mu m < |d_0| < 1 \text{ mm}$ . The vertex of the track pair has to have  $L_{xy} > 200 \mu m$  with respect to the beamline.

The width of the Gaussian fit for the distribution of track impact parameters in Figure 2-14 is  $47 \mu m$ . This width is a combination of the intrinsic impact parameter resolution of the SVT measurement, and the transverse intensity profile of the interaction region. The region profile is roughly circular in the transverse plane and can be approximated by a Gaussian distribution. The intrinsic SVT resolution is obtained by subtracting the beamline width from the width of the  $d_0$  distribution in

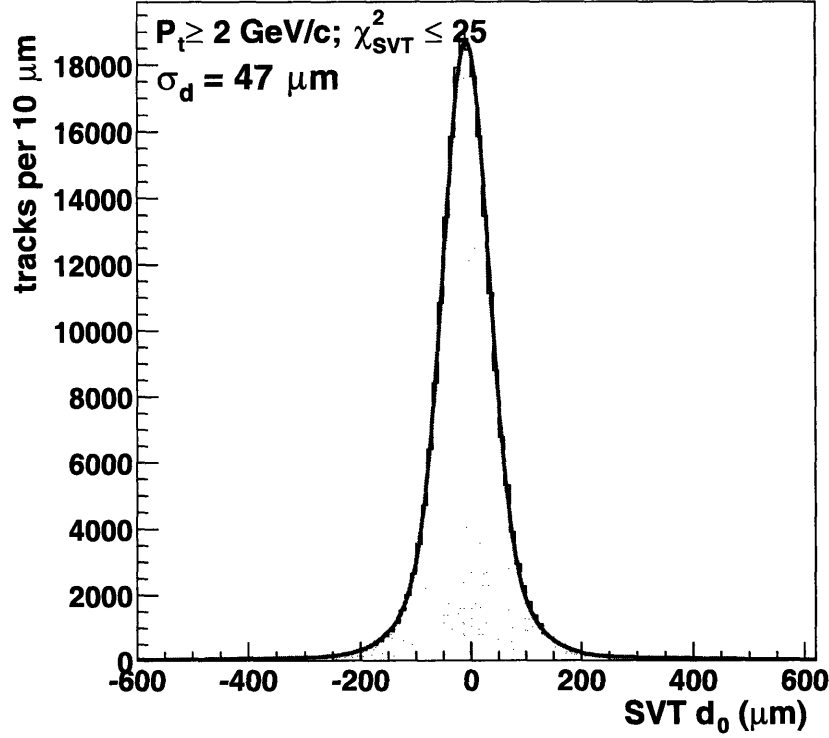


Figure 2-14: SVT impact parameter resolution.

quadrature. The SVT track impact parameter resolution is about  $35 \mu\text{m}$  for tracks with  $p_T > 2 \text{ GeV}/c$ .

#### 2.8.4 Level 3 trigger

The third level of the trigger system is implemented as a PC farm consisting of dual CPU machines. Every CPU in the farm provides a processing slot for one event. With roughly 300 CPU's, and a input rate of roughly 300 Hz, this allocates approximately 1 second to do event reconstruction and reach a trigger decision.

Figure 2-15 shows the implementation of the Level 3 farm. The detector readout from the Level 2 buffers is received via an Asynchronous Transfer Mode (ATM) switch and distributed to 16 “converter” node PC's, indicated in Figure 2-15 as “CV”. The main task of these nodes is to assemble all the pieces of the same event as they are delivered from different sub-detector systems through the ATM switch. The event is then passed via an Ethernet connection to a “processor” node, of which there are about 150 in the farm and are shown in Figure 2-15 as “PR”. Each processor node

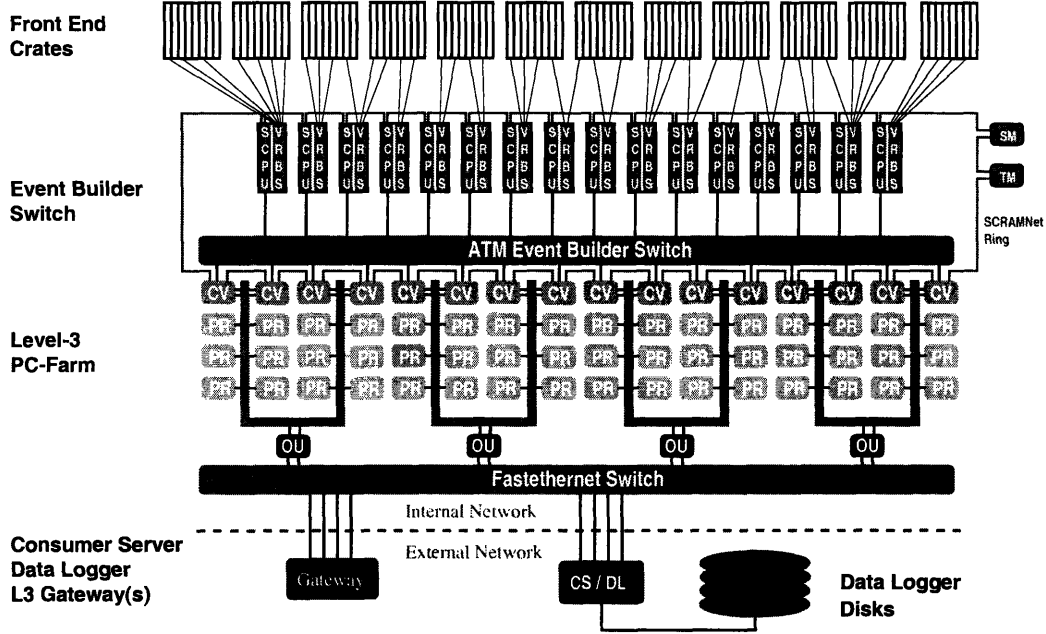


Figure 2-15: Structure and operating principles of the Event Builder and Level 3: data from the front end crates is prepared by Scanner CPU's (SCPU) and fed into ATM switch. The output of the switch is fed to converter nodes ("CV") where data fragments are assembled into complete events and then passed onto the processor nodes ("PR"). Events accepted by filter algorithms running in these nodes are passed to output nodes ("OU"), which then pass them to the Consumer Server and data logging systems.

is a separate dual-processor PC. Each of the two CPU's on the node process a single event at a time. The Level 3 decision is based on "near-final" quality reconstruction performed by a "filter" executable. The quality is "near-final" since filter executable is limited in using online calibrations. If the executable decides to accept an event, it is then passed to the "output" nodes of the farm, which are shown in Figure 2-15 as "OU". These nodes send the event onward to the Consumer- Server/Data-Logger (CSL) system for storage first on disk, and later on tape. The Level 3 farm sends data to CSL at maximum of 20 MB per second, where the limiting factor is the CSL processing rate.

For most of the data used for this analysis, full COT tracking is used to reconstruct tracks at Level 3. The measurements of  $p_T$ ,  $z_0$ ,  $\phi_0$  and  $\cot \theta$  from the COT are combined with the  $d_0$  measurement from the SVT to create a further improved track.



# Chapter 3

## Dataset and Candidate Selection

The analysis described in this thesis is performed on a data set collected with the CDF detector between February 2002 and August 2004 corresponding to an integrated luminosity of  $355 \text{ pb}^{-1}$  of  $p\bar{p}$  collisions at  $\sqrt{s} = 1.96 \text{ TeV}$ . The sample we use is based on a new displaced track trigger that is designed for CDF in Run II. This trigger has the largest requirement in terms of needed trigger bandwidth of all the triggers used at CDF. The design of the displaced track trigger is based on minimum-bias data and Monte Carlo simulation of the  $B \rightarrow \pi^+\pi^-$  and  $B \rightarrow D\pi^+$  signals [44, 45]. It predicts the needed bandwidth for the trigger and the purity of the sample. To efficiently utilize the bandwidth of the CDF trigger system three scenarios were proposed that differ in the value of the minimum  $p_T$  requirements applied to trigger tracks, and the charges and the angles between the trigger tracks. The name of the first scenario is B\_CHARM\_LOWPT. It has the loosest requirements and is intended to be used during low luminosity running conditions. The trigger path closest to the originally proposed multi-body hadronic trigger is called B\_CHARM. The third scenario is called B\_CHARM\_HIGHPT, which has tight requirements and is optimized for the reconstruction of multi-hadronic fully reconstructed  $B$  decays at high luminosities.

We start this chapter by describing the trigger paths that are simulated for our dataset (B\_CHARM and B\_CHARM\_LOWPT). We then follow with the procedures applied to the data in order to obtain a sample in which the relative rate of  $B_s^0$  and  $B^0$  meson production is understood and reproduced with detailed simulation. In the next step

we describe finding a set of selection requirements that maximizes the statistical significance of the signal. We want to reduce the background while at the same time keeping the number of signal  $B$  candidates high. We keep the reconstruction requirements for  $B_s^0$  and  $B^0$  as similar as possible to minimize potential systematic biases.

We also describe the quality requirements which the data used in this analysis must satisfy. Our goal is measuring the rates of decays of  $B_s^0$  mesons with respect to  $B^0$  mesons. Our measurement should be independent of the running conditions of the detector. We apply quality requirements to the data to make sure that Monte Carlo simulation is able to describe data.

### 3.1 Good runs

The CDF detector does not take data continuously. The data accumulation period when the Tevatron provides collisions and the subsystems of the CDF detector are on constitutes a *run*. From the technical point of view data accumulated within this period are numbered with six digit number and stored in a file containing this run number in its name. When talking about the data in this file, it is common to refer to it as simply a *run*.

The data that passed the Level 3 trigger selection is written to tape and then goes for the next round of processing by the production farm. The production farm further improves the quality of tracks by refitting tracks using calibration information which cannot be made available online. The data processed by the production farm is then written to tape and made available through the CDF Data Handling System for the offline analysis. When we talk about the offline or production quality quantities, we mean the quantities from the events that were processed by the production farm.

In order for a particular run on tape to be potentially useful for an offline  $B$  physics analysis it has to satisfy some basic data quality requirements. The information about data quality is stored in the run database for each subsystem of the detector for each run [46]. In addition, a run may be declared bad by the shift crew responsible for

data taking, and by data taking control programs. The following boolean conditions have to be true for the run to be included in the good run list.

- `RUNCONTROL_STATUS` is set automatically to true if there are 10000 Level 1 accepts, 1000 Level 2 accepts and at least  $1 \text{ nb}^{-1}$  of integrated luminosity in the run. Runs shorter than this are most likely stopped due to technical problems with the detector setup.
- `SHIFTCREW_STATUS` bit is manually set by the data acquisition shifter who confirms a valid run setup and the correct trigger table is in use.
- `OFFLINE_STATUS` bit is set by the offline production farm if the production executable successfully processed all events in the run.
- `CLC_STATUS` bit is set if the Čerenkov Luminosity Counters are able to provide a good luminosity measurement.
- `L1T_STATUS` and `L2T_STATUS` bits are set by the shift crew monitoring expert if the Level 1 and Level 2 monitoring plots are reasonable, indicating that Level 1 and Level 2 are functioning properly.
- `L3T_STATUS` bit is set if the rate of data corruption detected by the Level 3 reformatter is below 1% and the run number for the run is set.
- `SVX_STATUS` bit is set on if the SVX high voltage is on.
- `COT_OFFLINE` bit to be set if the integrated luminosity of the run has to be larger than  $10 \text{ nb}^{-1}$  and the number of bad COT channels has to be less than 1%. The first requirement is a slightly tighter requirement on the run length, and the second guarantees good COT performance for tracking.

The set of these requirements is essential to guarantee that the data from various pieces of the detector are present, passed the minimum quality check, and actually can be used for the *B*-physics analysis.

## 3.2 Trigger paths

There are three scenarios for the CDF displaced track trigger: `B_CHARM`, `B_CHARM_LOWPT`, and `B_CHARM_HIGHPT`. A set of physics requirements is applied to each of these scenarios at Level 1, Level 2, and Level 3. These requirements were not fixed at the beginning of Run II, but evolved over time, especially during the period between 2001 and 2002. By the end of 2003 the set of selection requirements stabilized. To keep track of the versions of various triggers, CDF has implemented a naming scheme for the trigger paths. The name of the trigger starts from its name at Level 1 followed by the version. The name of the trigger at Level 2 and Level 3 are pre-pended to Level 1 name. We do not get into details of the naming conventions of triggers, that can be found in Reference [45].

### 3.2.1 The `B_CHARM` trigger path

The `B_CHARM` trigger path is the closest to the original “multi-body hadronic trigger path” [44] proposed for gathering hadronic multi-body decays of  $B$  mesons. The Silicon Vertex Trigger at Level 2 allows for the selection of long-lived heavy flavor particles by cutting on the track impact parameter with a precision similar to that achieved by the full offline reconstruction. At Level 3 the requirements of Level 2 are reproduced using Level 3 quality tracks, and some additional requirements are also applied. The quality of tracks at Level 3 is higher because Level 3 tracks use the full COT hit information to reconstruct 3-dimensional tracks, and have been already matched to SVT tracks. The same is also true for Level 1 and Level 2 quantities. Level 1 selection quantities are reconstructed by the XFT with very little time to create good tracks resulting in large track parameter uncertainties. At Level 2 there is more time available per event, and the uncertainties of the SVT tracks are much smaller. The selection requirements as of August 2004 at each level of the trigger are listed below:

1. Level 1



- two XFT tracks with opposite charge
- each track has hits on at least 4 XFT layers
- each track has  $p_T^{\text{XFT}} > 2.0 \text{ GeV/c}$
- $\sum p_T^{\text{XFT}} > 5.5 \text{ GeV/c}$
- the angle between trigger tracks  $0^\circ < \Delta\phi_6 < 135^\circ$

## 2. Level 2

- each SVT track must be matched to an XFT track
- each track has  $100 \mu\text{m} \leq |d_0^{\text{SVT}}| \leq 1 \text{ mm}$
- each track has a  $p_T^{\text{SVT}} > 2.0 \text{ GeV/c}$
- $\sum p_T^{\text{SVT}} > 5.5 \text{ GeV/c}$
- $2^\circ < \Delta\phi < 90^\circ$
- two track vertex  $L_{xy} > 200 \mu\text{m}$
- SVT vertex fit  $\chi^2 < 25$

## 3. Level 3

- repeat Level 2 requirements
- $|\Delta z| < 5 \text{ cm},$

where  $p_T^{\text{XFT}}$  is the transverse momentum as measured in the XFT,  $\Delta\phi_6$  is the opening angle in super-layer 6 of the COT,  $d_0^{\text{SVT}}$  is the impact parameter as measured in the SVT,  $\Delta z$  is the distance between the two tracks in  $z$  measured at the distance of closest approach to the beamline in the transverse plane, and  $L_{xy}$  is the distance in the transverse plane of the two-track vertex with respect to the primary vertex.

### 3.2.2 The B\_CHARM\_LOWPPT trigger path

The B\_CHARM\_LOWPPT trigger path is designed with looser trigger requirements in order to fully exploit the trigger bandwidth in the low luminosity running conditions for

obtaining a sample rich in heavy flavor decays. This trigger is prescaled most of the time (prescales are discussed in Section 3.2.3), and the effective size in terms of number of events of collected data is comparable with the size of B\_CHARM data. The selection is looser in two ways: the opposite charge requirement for the trigger tracks and the requirement on the scalar sum of the track  $p_T$ 's are not applied. The full set of the requirements at each level of the trigger are:

1. Level 1

- two XFT tracks
- each track has hits on at least 4 XFT layers
- each track has  $p_T^{\text{XFT}} > 2.0 \text{ GeV}/c$
- $\Delta\phi_6 < 90^\circ$

2. Level 2

- each track must be matched by the SVT to an XFT track
- each track has  $100 \mu\text{m} \leq |d_0^{\text{SVT}}| \leq 1 \text{ mm}$
- each track has a  $p_T^{\text{SVT}} > 2.0 \text{ GeV}/c$
- $\Delta\phi < 90^\circ$
- two track vertex  $L_{xy} > 200 \mu\text{m}$
- two track vertex  $\chi^2 < 25$

3. Level 3

- repeat Level 2 requirements
- $|\Delta z| < 5 \text{ cm}$ .

### 3.2.3 Trigger prescales

In addition to various physics requirements, the CDF trigger system has an ability to randomly discard events at Level 1. This feature of the trigger is called prescaling.

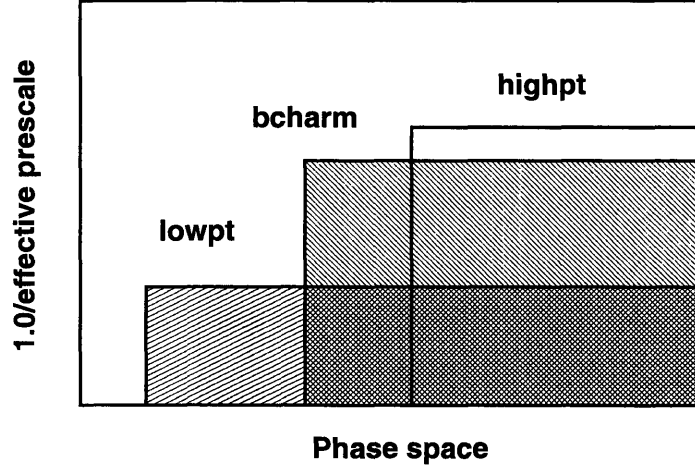


Figure 3-1: A plot schematically representing the set of selection requirements of the triggers (phase space) versus the effective trigger prescale.

The basic idea is that events are randomly discarded at high luminosity in order to control high accept rates. For example, a trigger prescaled with a factor  $N$  only passes every  $N$ th event which satisfies that physics trigger's requirements. Originally, a “dynamic” prescale system was used which modified the prescale value depending on the current luminosity. The “dynamic” prescale system was replaced with a “floating” prescale system, where the value  $N$  is taken out of every 256 events that would pass the appropriate trigger. Currently CDF uses a sophisticated “Über” prescale scheme which allows one to fully populate the trigger bandwidth at any given time. It sends an event passed Level 1 whenever empty Level 2 buffers are available (there is four Level 2 buffers total). Only a “dynamic” and “floating” prescale schemes apply to the dataset used in this analysis.

Figure 3-1 shows a sketch of the triggers inverse effective prescale versus the set of selection requirements of the two track trigger (phase space). The trigger which is most strongly prescaled is the trigger with the loose selection requirements (B\_CHARM\_LOWPT). The other feature to note is that the regions of the trigger parameter space overlap.

We perform this analysis on the combined B\_CHARM and B\_CHARM\_LOWPT samples. Duplicate events that passed both triggers are, of course, present in these two samples

because their effective phase spaces overlap. In our combined sample selection we check for duplicate events and drop extra events. The part of `B_CHARM_LOWPT` sample that is not a part of the `B_CHARM` sample constitutes about 30% of the total dataset. The part of the phase space of `B_CHARM_HIGHPT` trigger which is not a part of the `B_CHARM` trigger is not used in this analysis. The number of events in that part is negligible because for the `B_CHARM_HIGHPT` trigger the selection requirements are tighter than for `B_CHARM`. Thus, for the event to end up in the part of the sample with no shading (see Figure 3-1) the corresponding `B_CHARM` event has to be prescaled, otherwise the event is a part of `B_CHARM` sample.

### 3.3 Event selection

As we have already mentioned before, the `B_CHARM` triggers are the highest rate triggers at CDF. This fact makes the analysis of the data collected with this trigger technically challenging. The size of the dataset collected with this trigger and put to tape is roughly 13 TByte which consists of approximately 270 million events. One needs enormous computing power to be able to analyze this amount of data in a reasonable time.

The offline reconstruction is done with the 5.3.4 release of CDF software.  $B$  candidate reconstruction starts with a collection of tracks which are combined together by the reconstruction executable to form  $B$  meson candidates. We are interested in reconstruction of four hadronic  $B$  decays:  $B^0 \rightarrow D^-\pi$ ,  $B^0 \rightarrow D^-\pi^+\pi^+\pi^-$ ,  $B_s^0 \rightarrow D_s^-\pi^+$ , and  $B_s^0 \rightarrow D_s^-\pi^+\pi^+\pi^-$ , where  $D^- \rightarrow K^+\pi^-\pi^-$ , and  $D_s^- \rightarrow \phi^0\pi$ , respectively. These are fully reconstructed hadronic decays, and in this analysis we only use track objects recorded with COT and SVX. This feature sets this analysis apart from majority of other analyses at CDF which extensively rely on muon and electron objects, and, as in the case of top physics, on jets.

Candidates for each particle decay tree are reconstructed from the bottom up. This means that, for example, in the case of a  $B_s^0 \rightarrow D_s^-\pi^+$  decay, we start from  $\phi^0 \rightarrow K^+K^-$  decay which is then combined with another track to make a  $D_s^-$  candidate.

The  $D_s^-$  candidate is combined with yet another track to create a  $B_s^0$  candidate. In all cases, daughter tracks are fitted together to create secondary vertices, and selection requirements on the fit probability of the vertex fit and the mass of  $D_s^-$  and  $\phi^0$  mesons are applied.

The reconstructed candidates are stored in the data structure called an Stntuple provided by the BStntuple package [47], which is a  $B$  physics extension to the Stntuple framework [48]. Before we start the offline analysis, we skim the Stntuple two times, reducing the size of the offline dataset to  $\approx 1$  GB. The skimming is done based on the physics selection requirements which are much looser than the requirements applied in the offline analysis.

In the following sections we describe how the tracks for the reconstructions are prepared. We discuss the necessary procedures for the branching ratio analysis, including track matching to SVT information and trigger confirmation. We cover candidate reconstruction in detail, and describe how the optimization of selection requirements is performed. In the last section we talk about duplicate candidates and the combinatorial background.

### 3.3.1 Track preparation

Tracks are the building blocks that make  $B$  meson candidates, and therefore a detailed understanding and treatment of tracks is essential for this analysis. For example, the impact parameter resolution shows a strong dependence on the number of hits the track is made of. Also, tracks that have few hits are likely to be fake. Tracks having low transverse momentum produce a highly curved helix in the COT, which degrades tracking efficiency and the uncertainty on the measurement of the transverse momentum.

We select tracks which have at least three SVX  $r$ - $\phi$  hits and have a COT parent. We also require the track to have a physical covariance matrix. Those requirements remove very few tracks, but they are the ones which tend to cause the software to fail. To prepare the track for further analysis the following procedure is applied:

- the covariance matrix of the COT track is rescaled using the recipe and values in Reference [49]. The purpose of the rescaling is to correct for the residual effects of the multiple Coulomb scattering inside the COT volume, making a better starting point for the silicon track re-fitter.
- the refit of the tracks starts from the offline track parameters. It uses the rescaled covariance matrix and takes into account energy loss corrections for kaon or pion hypothesis according to the mass hypothesis of interest. The model for the material description is based on the GEANT package [50].
- the refit starts with the silicon hits which have been originally assigned to the track.
- silicon hits from the intermediate silicon layer, the ISL, and from Layer 00 are kept.

The primary interaction vertex is the point of  $p\bar{p}$  collisions. For the primary interaction vertex we use the beamline coordinate at the  $z$  position of each candidate vertex. As we describe in Section 2.8.2, the beamlines are determined by the SVT on run by run basis, and then recalculated offline in a preproduction step. There is a small uncertainty in determination of the primary vertex from the beamline information. The alternative is to reconstruct the primary vertex on event-by-event basis by doing vertex fit for the collection of tracks in every event. For the purposes of this analysis this uncertainty is very small and can be safely neglected.

The calibration and alignment information is stored in the CDF database. The calibration information includes pedestals in various detectors, and the alignment contains geometrical positions of parts of the detector with respect to the CDF reference frame. This information evolved over time especially at the beginning of Run II as better calibrations were produced by the tracking group. The end users are supposed to pick the alignment table they wish to use in their reconstruction executable. By the time this analysis started the alignment information stabilized. For track refitting we use alignment table specified by the so called “pass 17” in the CDF database, which is approved by the tracking group for physics analyses.

### 3.3.2 Trigger confirmation

The confirmation of the trigger is a crucial aspect for this analysis because it is required for understanding of relative rates of  $B$  mesons. There are two types of trigger confirmations we perform: at the *event level* and at the *candidate level*.

The first type is the confirmation of the trigger at the *event level*. This type of confirmation is essential because in our Monte Carlo simulation we simulate only one trigger at a time, so we need to check that the data we use comes from exactly the trigger we simulate, otherwise our simulation does not describe our data. The confirmation of the trigger in data is performed by checking the Level 3 trigger bit, while the confirmation of the trigger in Monte Carlo simulation is done by checking the Level 2 trigger bit because the Level 3 trigger is not simulated by the CDF Monte Carlo package. This means that confirmation of the trigger in data is done on higher quality quantities, and this is the reason we introduce the second type of trigger confirmation: on the *candidate level*.

This confirmation is done by requiring that each candidate that passes selection also contains a corresponding trigger pair (B\_CHARM or B\_CHARM\_LOWPT). The *candidate level* trigger confirmation is important because in this way we reject candidates that are produced by several background scenarios. One possible scenario could be that only one track of the  $B$  passes the trigger criteria while the second one is provided by a fake XFT track which got several accidental hits assigned and has thus a high probability to have a large impact parameter. Another example is an additional track from the opposite side  $B$ . All of these cases are sources of background.

In the Monte Carlo simulation we only generate the decay products of exactly one  $b$  hadron per event, and the underlying event is not considered. This is one of the reasons we do not want to inflate our signals by the signal events which were not properly triggered because these events are not reproduced by the Monte Carlo simulation and, thus, the efficiencies extracted from our Monte Carlo simulation would not describe our signal samples.

In Section 2.8.1 and 2.8.2 we describe Level 1 and Level 2 trigger primitives (XFT

and SVT tracks). In the offline reconstruction the tracks are refitted, so there is no direct correspondence between the offline quantities and the quantities on which the trigger decision is made. We need to take additional steps to implement the correct trigger confirmation.

We introduce a procedure of matching offline tracks to SVT tracks to correct for this problem. The SVT matching algorithm is based on the SVTSIM [51] package. It allows one to calculate the distance between the two tracks in the matching space, and tracks are declared matched if this distance is below some predefined value. Tracks are further rejected if the SVT  $\chi^2$  — the  $\chi^2$  of the two dimensional SVT vertex fit — is more than 25, the default value.

To classify a track to be an *online trigger track* (when we refer to the online trigger track we implicitly mean a track that has been reconstructed by SVT) we require the  $p_T$  and  $d_0$  as determined by Level 2 to comply with:  $p_T > 2.0$  GeV/c and  $0.0120 \text{ mm} < |d_0| < 1.0 \text{ mm}$ . Such online trigger tracks are used to make various trigger decisions based on *trigger pairs*. The following quantities are available in trigger pairs to cut on: track charges, the linear SVT  $p_T$  sum, the  $\Delta\phi$  angle between the SVT tracks and the  $L_{xy}$  as calculated from the SVT quantities  $p_T$ ,  $d_0$  and  $\phi_0$ . All these quantities are available during the analysis based on the full reconstruction, and the trigger decision is repeated with these refined inputs. Confirmation of the trigger on an event and candidate level removes  $\approx 10\%$  of the events in the dataset. For the specific requirements refer to Sections 3.2.1 and 3.2.2.

### 3.3.3 Candidate reconstruction

The offline reconstruction starts with a collection of tracks produced in the tracking system by charged particles. We do not use particle identification in this analysis and tracks are assumed to be either a pion or a kaon to match the reconstruction hypothesis. The track combinations making the  $\phi^0$ ,  $D^-$ ,  $D_s^-$ ,  $B^0$ , and  $B_s^0$  candidates are required to form three dimensional vertices, and combinations that fall outside a wide window around the mass of the respective meson are rejected. In each step the candidates are subjected to a set of cuts which are optimized to quickly reject



background candidates and keep the number of combinatorial combinations under control. The typical sequence is

- cut on charge correlations, where applicable.
- trigger confirmation: for the  $D$  no online trigger tracks are required, for the full  $B$  decays two online trigger tracks are required.
- accept candidates in a broad window of the raw candidate mass, which is calculated from the track momenta with the correct mass hypothesis for each track (otherwise, the candidate mass is obtained from the candidate vertex fit)
- a vertex fit is performed and the resulting fit  $\chi^2$  is used to reject candidates.

For the vertex fit a CTVMFT [52] fit is applied. CTVMFT is a package for vertex fitting widely used in CDF. It fits tracks to a variety of possible constraints on primary and secondary vertices. The quantity that is minimized in the fit is called  $\chi^2$  and is defined as:

$$\chi^2 = \sum_i (\vec{\xi}(\vec{x}, \vec{\alpha}_i) - \vec{\xi}_i^0)^T G_i^{-1} (\vec{\xi}(\vec{x}, \vec{\alpha}_i) - \vec{\xi}_i^0), \quad (3.1)$$

where  $\vec{\xi}_i^0$  and  $\vec{\xi}_i$  are the five-dimensional vectors of track parameters before and after the vertex fit, respectively.  $G_i$  are the  $5 \times 5$  track covariance matrices as determined by the previous track fitting. If we assume that all tracks originate from the same vertex we can express the  $\vec{\xi}_i$  as a function of only three of the track parameters  $\vec{\alpha} = (p_T, \phi_0, \cot(\theta))$ , and of the three coordinates of the common vertex  $\vec{x} = (x, y, z)$ . The vertex coordinates are then obtained by minimizing  $\chi^2$ .

For the  $B$  meson candidate fits, the mass of the  $D$  meson is constrained to its PDG value [2]. We store the fit results for each candidate in order to apply selection requirements at the analysis stage.

### 3.3.4 Combinatorial background

As we describe in Section 3.3.3, we reconstruct  $B$  mesons by considering all possible track combinations making the  $\phi^0$ ,  $D^-$ ,  $D_s^-$ ,  $B^0$ , and  $B_s^0$  candidates. We require

these track combinations to form three dimensional vertices, and combinations that fall outside a wide window around the mass of the respective meson are rejected. Since the average number of tracks per event is  $\approx 50$ , the number of combinations, especially for  $B \rightarrow D\pi^+\pi^+\pi^-$  decays with six tracks in the final state, is huge. These combinations are often referred to as simply *combinatorial background*.

Simulation of combinatorial background in a hadronic collider environment is a challenging task, since it requires a detailed understanding of the underlying event and interactions of the charged particles with the material of the detector. The commonly used approach to this problem is not to try to simulate combinatorics but rather choose an empirical parametrization of the combinatorial background which is compatible with the data. The shapes used to fit the combinatorial background for the  $B$  meson mass spectra for this analysis are described in Section 4.2.

### 3.3.5 Selection requirements

The data sample obtained from offline reconstruction is dominated by the combinatorial background. This is especially true for the  $B^0 \rightarrow D^-\pi^+\pi^+\pi^-$  decay where there are six tracks in the final state. In order to suppress the combinatorial background, we use a set of selection requirements which are optimized to keep the number of signal events high while reducing the background as much as possible. The exact procedure of how we achieve this is described in Section 3.3.6.

The choice of a set of selection requirements is motivated by the topology of the decays and their kinematic properties. Figure 3-2 depicts the decay topology for  $B \rightarrow D\pi^+$  and  $B \rightarrow D\pi^+\pi^+\pi^-$  decays. A  $B$  hadron at CDF is produced with a momentum of a few GeV/c. After being produced, it typically flies about 1.0 mm before its weak decay, so the decay vertex is noticeably displaced from the primary vertex. In addition, the  $D$  meson also decays weakly and its decay vertex is displaced from the  $B$  decay vertex. The resulting topology has three independent vertices. In the case of a  $B \rightarrow D\pi^+$  decay there is a bachelor track originating from the  $B$  vertex. Three pions from  $B \rightarrow D\pi^+\pi^+\pi^-$  decays may arise from a resonance, but the resonance decays strongly and the resulting  $\pi^+\pi^+\pi^-$  vertex coincides with the  $B$

vertex. We use several quantities to separate signal from background. These include:

- $\chi^2_{r-\phi}$  is a  $\chi^2$ -like goodness-of-fit quantity for the fits of  $B$  and  $D$  vertices using only the track parameters in the transverse plane.
- $p_T(B)$  — the transverse momentum of  $B$  meson.
- $L_{xy}/\sigma$  -the significance of the measurement of  $L_{xy}$  for both  $B$  and  $D$  vertices with respect to the primary vertex.
- the transverse momentum  $p_T$  of the bachelor pion.
- $B$  meson impact parameter  $d_0$  with respect to the primary vertex.

### 3.3.6 Optimization of selection requirements

We start the optimization by choosing a set of cuts we want to optimize. The choice of the cuts is motivated by the kinematics of the decays and decays topology as we describe in Section 3.3.5. Ultimately in our analysis, we want to extract the numbers of reconstructed  $B$  mesons with the smallest relative statistical uncertainty. In order to achieve this goal, we implement a procedure which optimizes the statistical significance of the signal, defined as:

$$\mathcal{S} = \frac{N_S}{\sqrt{N_S + N_B}} \quad (3.2)$$

where  $N_S$  is the number of signal events, and  $N_B$  is the number of background events.

In this procedure, the number of signal events is extracted from Monte Carlo simulation and the number of background of events is estimated from the data sample called the “sideband” which should be made of background but at the same time be kinematically similar to signal.

The optimization procedure should also be unbiased in the sense that it should not prefer selection cuts that artificially increase or decrease signal yields. In particular, the mass spectrum of  $B$  decays has large reflection peaks just below the  $B$  mass peaks, so sampling events from the immediate low-mass sideband cannot be done easily.

Our solution to the problem is to do the mass fit away from the signal and the main reflections by not extending the fit to the low mass range and blinding the fit directly under the mass peak. The background is fitted to a simplified model consisting of a sum of exponential and linear distributions. The integral of such a background function under the signal is used to determine the number of background events. The number of signal events is always determined from Monte Carlo simulation to make sure that cuts are unbiased. The scaling factor between Monte Carlo simulation and data is the ratio of signal events obtained from Monte Carlo and data fits for a given set of cuts. It is determined each time the optimization is done for a given cut.

The plot in Figure 3-3 depicts the fit used to determine the number of background events under the peak. A templated background fit is used and it is limited to the range away from the signal and reflections. A templated fit is a fit where a fitting function that consists of several pieces corresponding to various backgrounds, is “templated”, *i.e* the values of the parameters of the functions corresponding to these backgrounds are obtained from the Monte Carlo and the majority of them are fixed in the overall fit. The background fit is extrapolated into the signal region to determine how many background events are in the  $\pm 3\sigma$  range under the signal Gaussian. The number of signal events is determined from signal Monte Carlo simulation which is rescaled to the number of events seen in the mass peak in the data before the cut in optimization is applied.

Figures 3-4 to 3-11 show the quantitative cut scans in the last iteration of the optimization procedure. The iteration process needs to start with a set of some selection requirements. We chose to start from the cut values that have a high  $\sim 90\%$  efficiency. Before we start the iteration procedure, we exploit the narrow  $\phi^0 \rightarrow K^+ K^-$  resonance to suppress background by requiring that the mass of the two kaon system from  $\phi^0$  decay be between 1010 and 1029 MeV/c<sup>2</sup>. The two variables that are monitored while optimizing cuts are the signal significance ( $\sigma = S/\sqrt{S+B}$ ) and the analysis efficiency. When given a set of points with similar significance, the point with the highest cut efficiency is chosen. While varying one cut, the values of all the other cuts are kept fixed. The optimization process is iterative, and the selection

requirements are changed to new values at the beginning of every iteration.

The optimization procedure defined in this way optimizes the selection requirements with respect to combinatorial background found in the high mass sideband. So, it may not find the absolute optimal point because it neglects the structure of the low mass background, but it simplifies the problem and allows one to ignore the issues related to the dependence of the background shape on the values of the selection cuts. The final selection requirements are shown in Table 3.3.6.

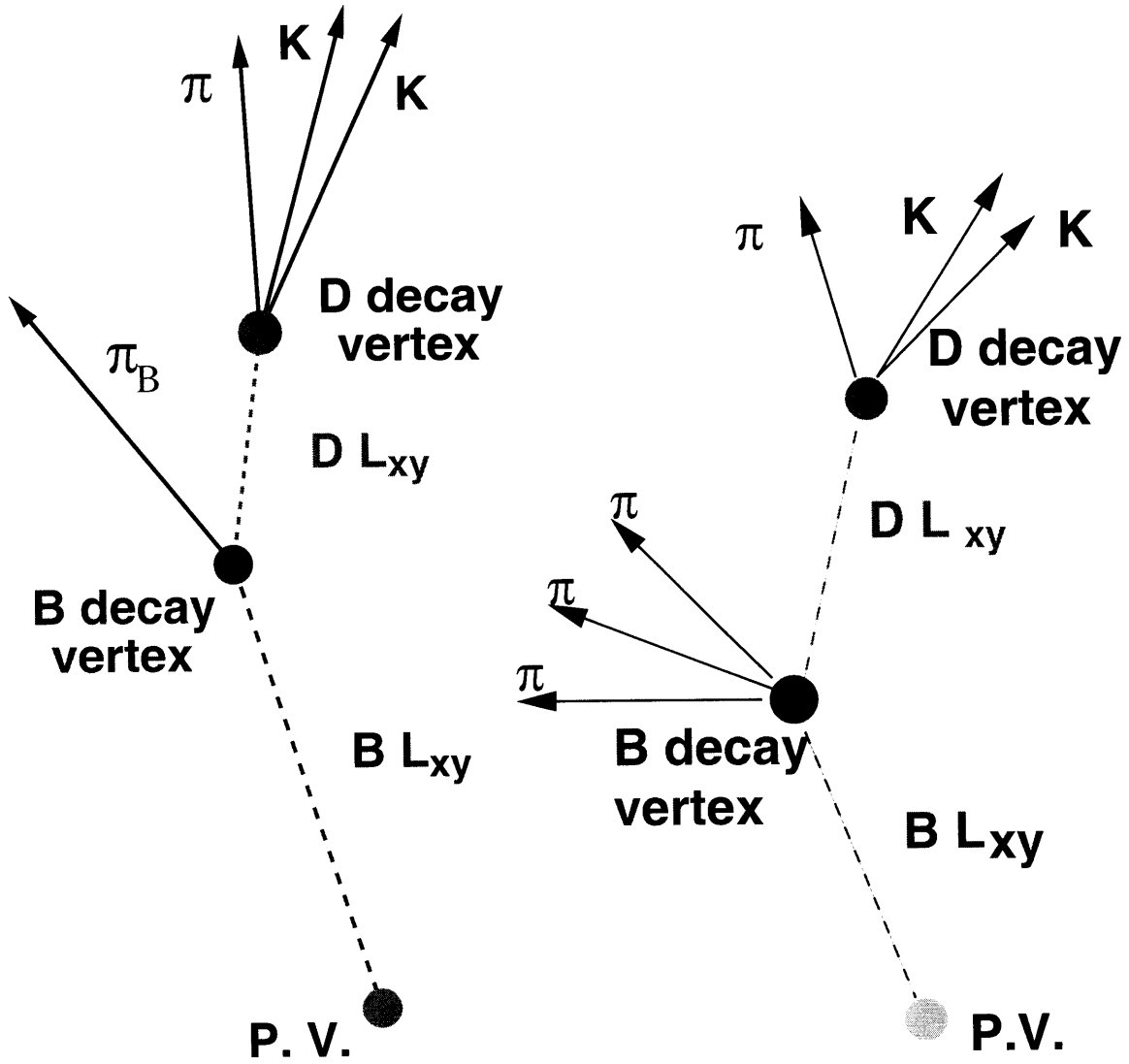


Figure 3-2: Typical topology of a  $B \rightarrow D\pi$  and  $B \rightarrow D\pi^+\pi^+\pi^-$  decays.  $\pi_B$  corresponds to a bachelor pion from  $B \rightarrow D\pi^+$  decay.

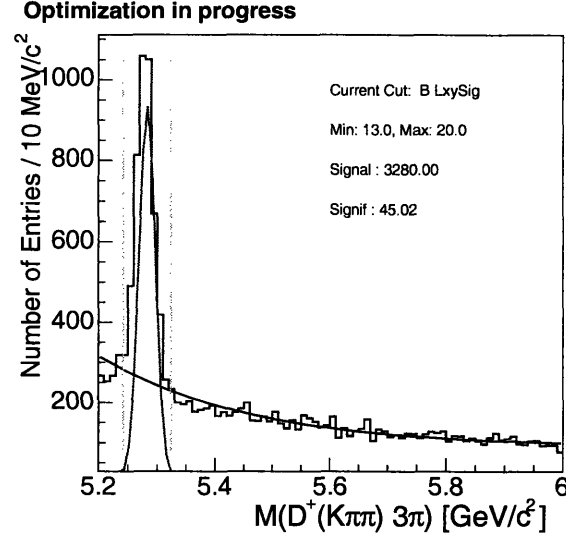


Figure 3-3: The plot depicts the fit used to determine the number of background events under the peak. The fit is limited to the signal and high mass range. The background template fit is extrapolated into the signal region to determine how many background events are in a  $\pm 3\sigma$  range of the signal Gaussian. The vertical bars on the figure indicate the  $\pm 3\sigma$  signal region.

Cut	$B^0 \rightarrow D^- \pi$	$B_s^0 \rightarrow D_s^- \pi$	$B^0 \rightarrow D^- 3\pi$	$B_s^0 \rightarrow D_s^- 3\pi$
$d0(B)[\mu\text{m}]$	$< 70$	$< 75$	$< 65$	$< 60$
$\chi^2_{r-\phi}(B)$	$< 15$	$< 15$	$< 14$	$< 10$
$L_{xy}/\sigma(B)$	$> 7$	$> 8$	$> 16$	$> 15$
$L_{xy}/\sigma(D)$	n/a	n/a	$> 15$	$> 10$
$p_T(\pi_B)[\text{GeV}/c]$	$> 1$	$> 1$	n/a	n/a
$L_{xy}^B(D)[\mu\text{m}]$	$> -200$	$> -200$	$> 150$	$> -50$
Min $p_T[\text{GeV}/c]$	$> 0.35$	$> 0.35$	$> 0.35$	$> 0.35$

Table 3.1: Final selection requirements for reconstructed hadronic  $B$  decays.

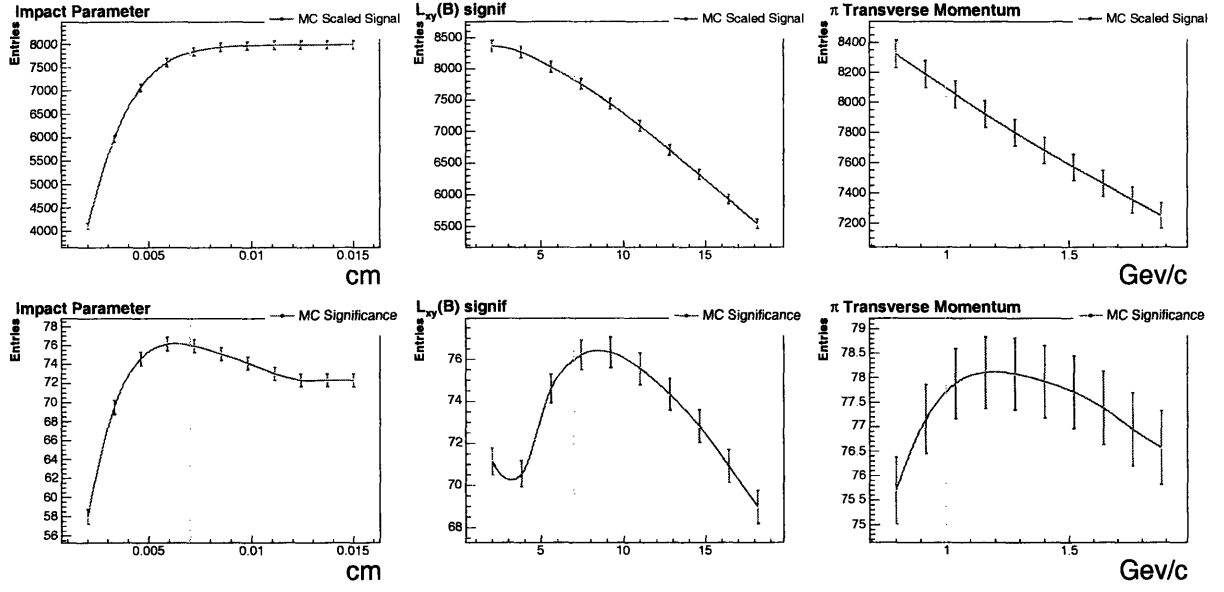


Figure 3-4:  $B^0 \rightarrow D^- \pi^+$  optimization for  $d_0(B^0)$  (left),  $L_{xy}(B^0)/\sigma$  (center), and  $p_T(\pi_{B^0})$  (right). Top plots show the cut efficiency as a function of the cut value, and the bottom plots show significance of the signal.

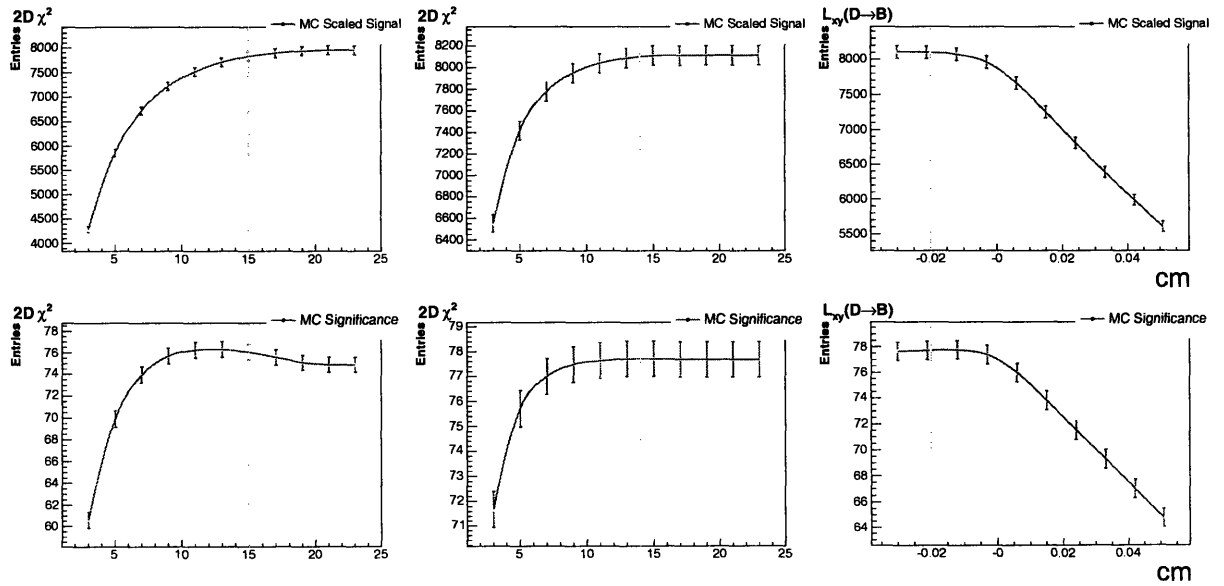


Figure 3-5:  $B^0 \rightarrow D^- \pi^+$  optimization for  $\chi^2_{r-\phi}(B^0)$  (left),  $\chi^2_{r-\phi}(D)$  (center), and  $L_{xy}(D \rightarrow B)$  (right). Top plots show the cut efficiency as a function of the cut value, and the bottom plots show significance of the signal.



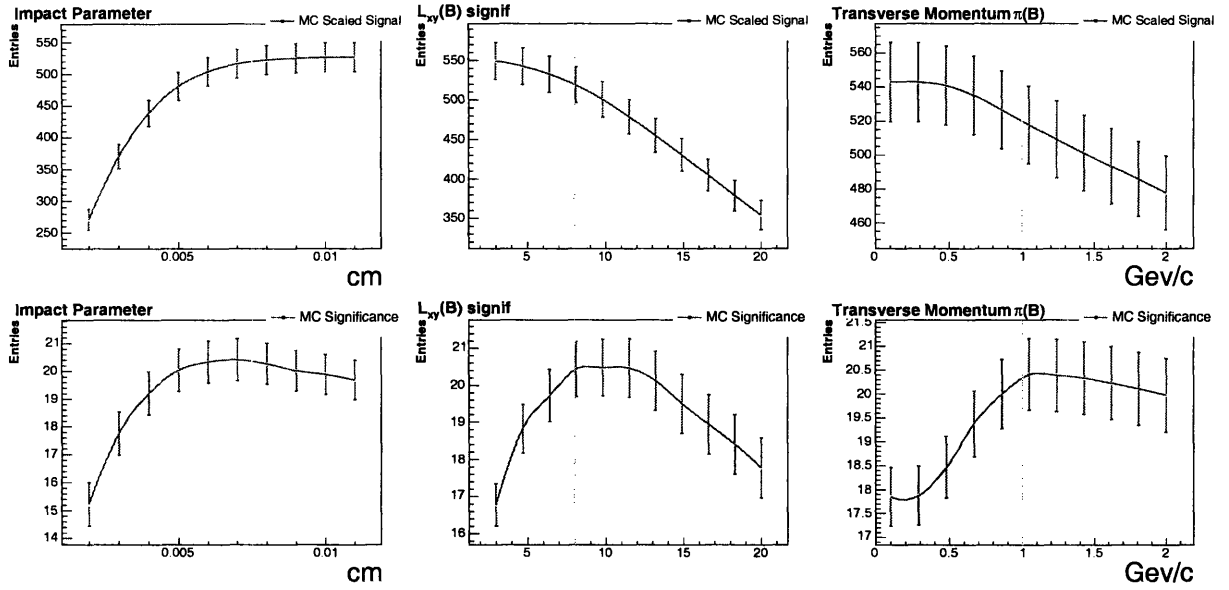


Figure 3-6:  $B_s^0 \rightarrow D_s^- \pi^+$  optimization for  $d_0(B_s^0)$  (left),  $L_{xy}(B_s^0)/\sigma$  (center), and  $p_T(\pi_{B^0})$  (right). Top plots show the cut efficiency as a function of the cut value, and the bottom plots show significance of the signal.

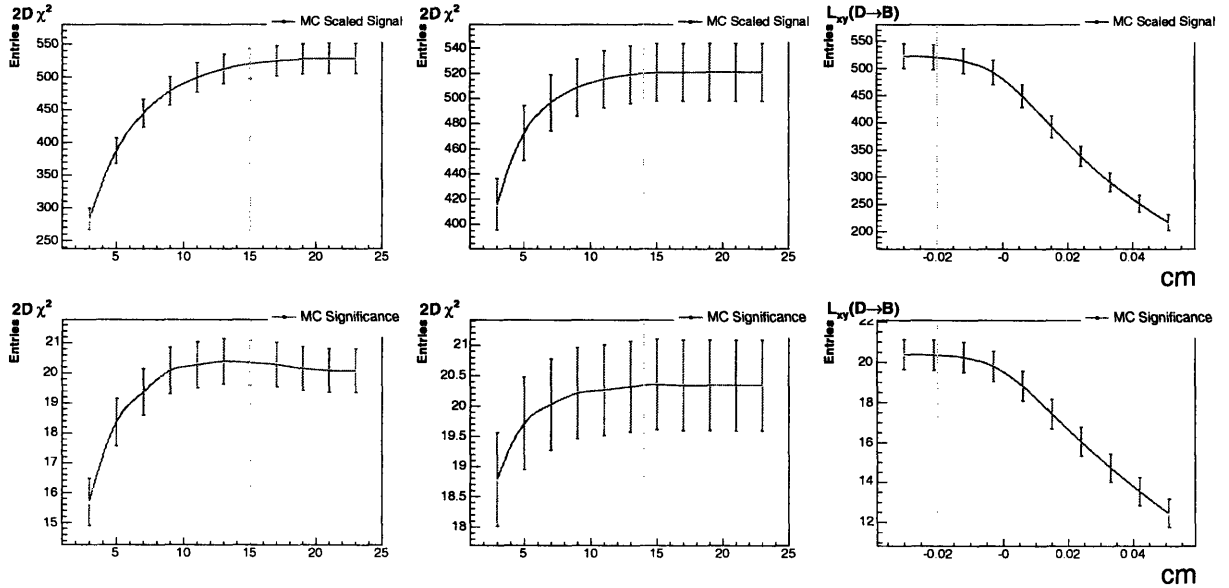


Figure 3-7:  $B_s^0 \rightarrow D_s^- \pi^+$  optimization for  $\chi^2_{r-\phi}(B_s^0)$  (left),  $\chi^2_{r-\phi}(D)$  (center), and  $L_{xy}(D \rightarrow B)$  (right). Top plots show the cut efficiency as a function of the cut value, and the bottom plots show significance of the signal.

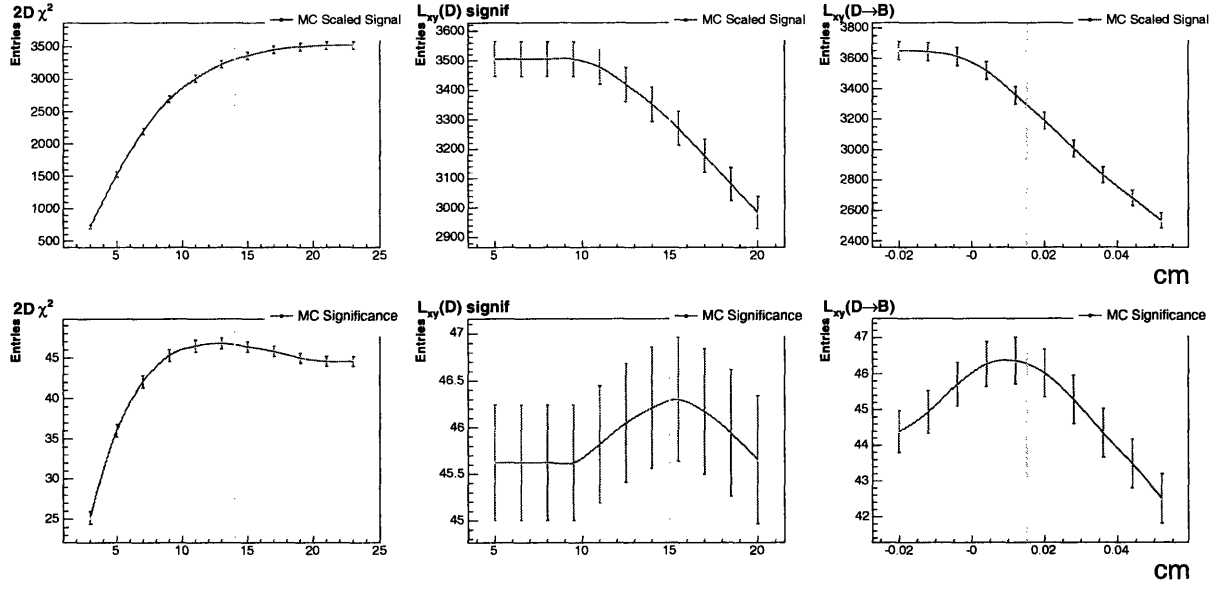


Figure 3-8:  $B^0 \rightarrow D^- \pi^+ \pi^+ \pi^-$  optimization for  $\chi^2_{r-\phi}(B^0)$  (left),  $L_{xy}(D^+)/\sigma$  (center), and  $L_{xy}(D \rightarrow B)$  (right). Top plots show the cut efficiency as a function of the cut value, and the bottom plots show significance of the signal.

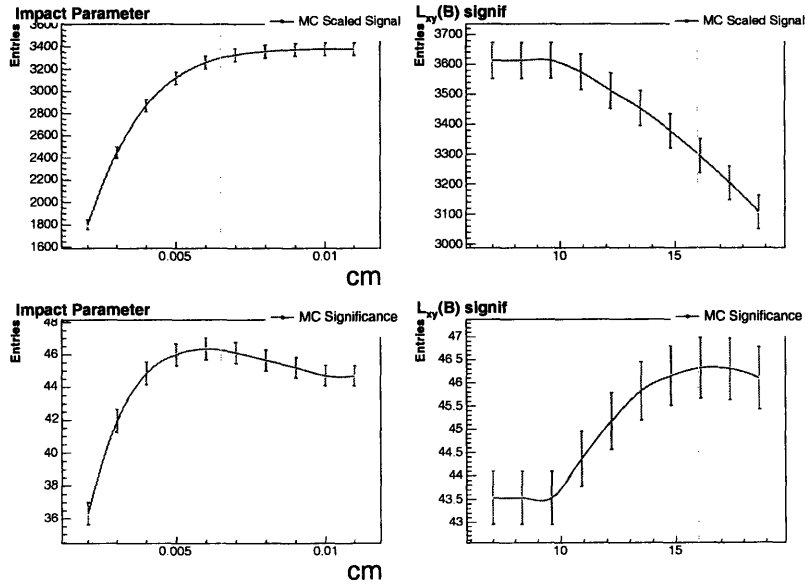


Figure 3-9:  $B^0 \rightarrow D^- \pi^+ \pi^+ \pi^-$  optimization for  $d_0(B^0)$  (left) and  $L_{xy}(B^0)/\sigma$  (right). Top plots show the cut efficiency as a function of the cut value, and the bottom plots show significance of the signal.

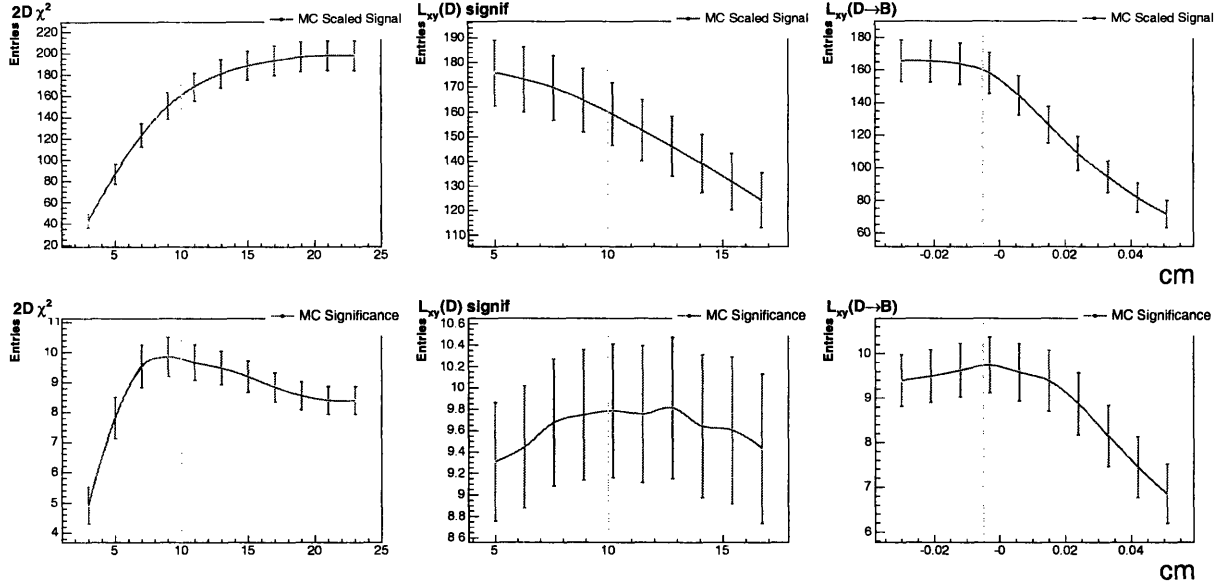


Figure 3-10:  $B_s^0 \rightarrow D_s^- \pi^+ \pi^+ \pi^-$  optimization for  $\chi_{r-\phi}^2(B_s^0)$  (left),  $L_{xy}(D_s)/\sigma$  (center) and  $L_{xy}(D \rightarrow B)$  (right). Top plots show the cut efficiency as a function of the cut value, and the bottom plots show significance of the signal.

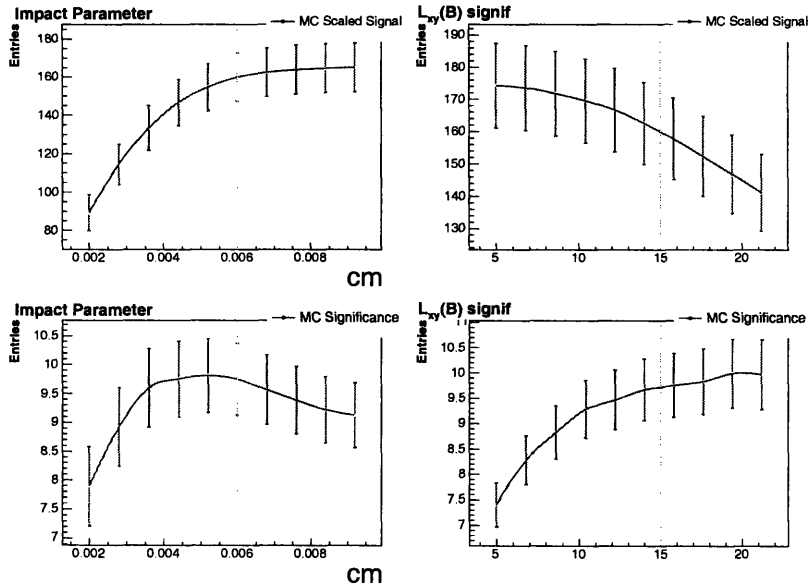


Figure 3-11:  $B_s^0 \rightarrow D_s^- \pi^+ \pi^+ \pi^-$  optimization for  $d_0(B_s^0)$  (left) and  $L_{xy}(B_s^0)/\sigma$  (right). Top plots show the cut efficiency as a function of the cut value, and the bottom plots show significance of the signal.

### 3.3.7 Duplicate candidates

The term “duplicate candidate” refers to the problem of having more than one signal candidate in an event after reconstruction and selection requirements are applied. From the physics point of view duplicates are a source of background because usually the cross section of an interesting physics process is so small, that having more than one true signal candidate in one event is very unlikely.

The problem of duplicate candidates is especially important for decays with many tracks in the final state, since for a decay the number of combinations found by the reconstruction executable grows exponentially with the number of tracks in the final state.

In the case of  $B \rightarrow D\pi^+$  and  $B \rightarrow D\pi^+\pi^+\pi^-$  decays it is essential to be able to suppress the duplicates because they are a source of the background, and also because if they have some structure in the mass distribution of  $B$  meson candidates this structure would be very difficult to simulate.

We distinguish three potential sources of duplicate candidates. The first source of duplicates is due to candidate track content. For example, when we reconstruct  $D^- \rightarrow K^+\pi^-\pi^-$  decay we take all possible combinations of one positively charged track and two negatively charged tracks and fit them in a decay vertex. One could think of the situation where we pick one positively charged track and two identical negatively charged tracks. If we then swap the two negatively charged tracks, we create two candidates, when both of these candidates pass the selection. This source of duplicates is trivial and easy to suppress by requiring a unique track content in each of the  $D$  and  $B$  candidates we reconstruct.

The second source of duplicates is easy to illustrate on  $B^0 \rightarrow D^-\pi^+\pi^+\pi^-$  decay. If we take a pion that originates from the  $B$  candidate vertex and swap it with the pion of the same charge in a  $D$  candidate, we create two  $B$  decay candidates. These duplicate candidates are often called *self-reflections*. Self-reflection candidates have kinematic characteristics very similar to the kinematics of true signal. If self-reflections survive reconstruction and analysis selection requirements, they effectively

amplify the signal. We implement a procedure to remove this source of duplicates. We identify tracks in  $B$  candidates by their transverse momentum, and if an event has two  $B$  candidates with similar track content (two tracks with very close momenta), we remove the candidate that has a lower momentum track.

The third source of duplicates is due to configuration having a real  $D$  plus random track. In this case we can think of two  $B$  decay candidates. The first one is true  $B$  signal. The second one is made of true  $D$  candidate, two pion tracks coming from the decay of true  $B$  signal and a random track, which turned out to be compatible with  $B$  decay topology. This type of duplicate events contribute to the combinatorial background that we discuss in Section 3.3.4.

The mass spectra after applying optimized selection requirements and after removing duplicates are shown in Figures 3-12 and 3-13. We observe a good signal to background ratio. We also notice some structure in the backgrounds in the low mass region in all four plots. The general origin of the physics backgrounds, and this low mass structure in particular, are covered in Chapter 4.

## 3.4 Summary

In this chapter we have reviewed the data sets used in this analysis. We described B\_CHARM and B\_CHARM\_LOWPT trigger paths, good runs and data quality conditions. We use Monte Carlo simulation and data to optimize selection requirements without biasing the yields. We observe mass spectra of  $B^0$  and  $B_s^0$  mesons with a good signal-to-background ratio as shown in Figures 3-12 and 3-13. In the next chapter we describe how we extract the yields from the mass spectra we observe in the data.

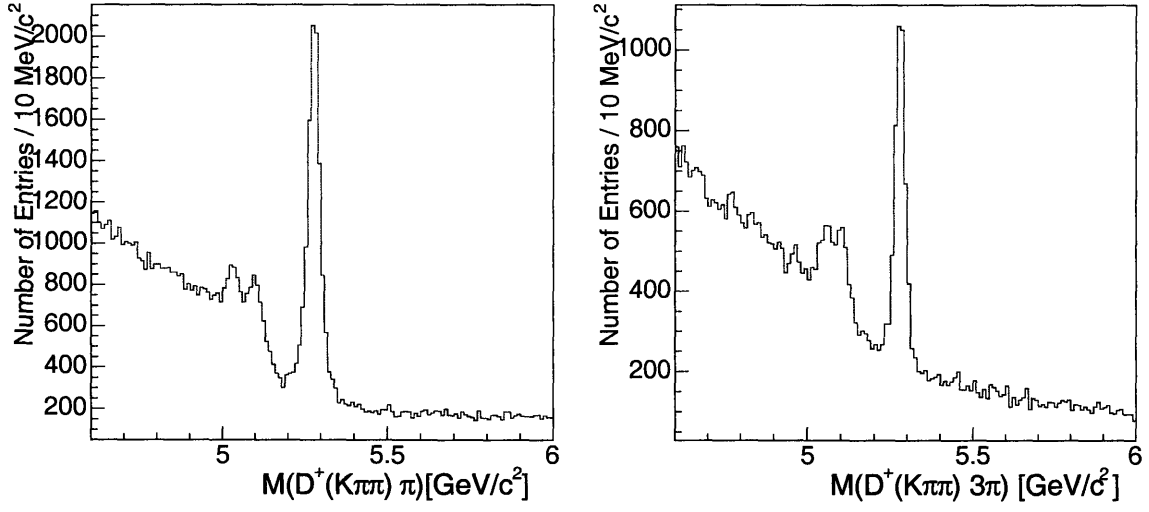


Figure 3-12: The data mass spectrum for  $B^0 \rightarrow D^- \pi^+$  (left) and  $B^0 \rightarrow D^- \pi^+ \pi^+ \pi^-$  (right) decays with optimized selection requirements.

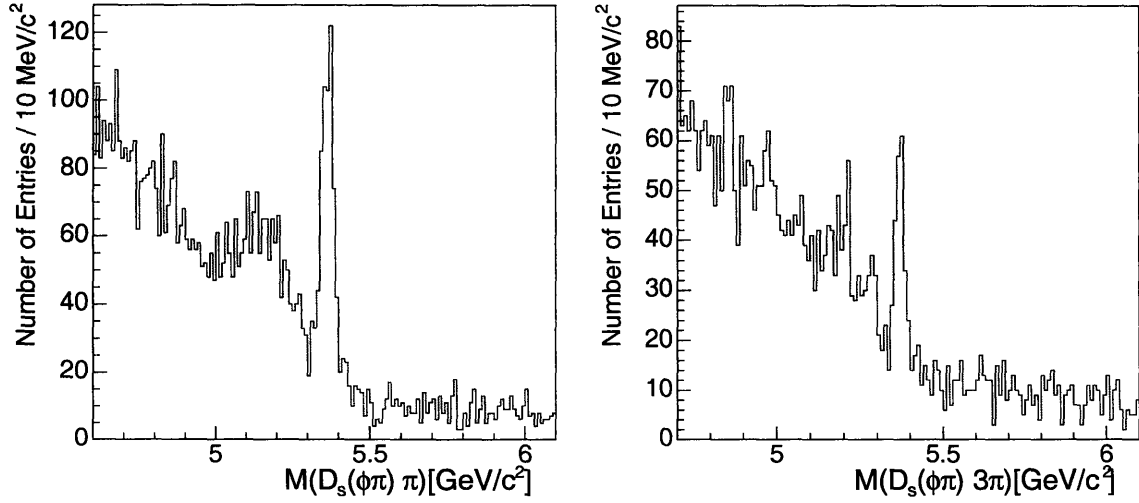


Figure 3-13: The data mass spectrum for  $B_s^0 \rightarrow D_s^- \pi^+$  (left) and  $B_s^0 \rightarrow D_s^- \pi^+ \pi^+ \pi^-$  (right) decays with optimized selection requirements.

# Chapter 4

## Branching Ratio Measurement

In order to perform the measurement of the relative branching fractions  $\mathcal{B}(B_s^0 \rightarrow D_s^- \pi^+)/\mathcal{B}(B^0 \rightarrow D^- \pi^+)$  and  $\mathcal{B}(B_s^0 \rightarrow D_s^- \pi^+ \pi^+ \pi^-)/\mathcal{B}(B^0 \rightarrow D^- \pi^+ \pi^+ \pi^-)$  we need to extract the numbers of signal events from the data and the ratio of efficiencies from Monte Carlo simulation. This chapter deals with both of these issues. The reconstructed mass spectra shown in the previous chapter show some distinctive shapes coming from various physics backgrounds. We study these backgrounds using simulation and develop a fitting framework to extract the signal yields. The ratio of efficiencies is also obtained from Monte Carlo simulation. In order to validate the simulation we perform a detailed comparison of various physics distributions as found in data and Monte Carlo simulation to make sure that simulation reproduces data well. Finally, we extract the ratio of branching fractions by using the inputs from data, Monte Carlo simulation, and world average values for the branching fractions of the  $D$  mesons. We choose kinematically similar modes with large statistics as our normalization, *i.e.*  $B^0 \rightarrow D^- \pi^+ \pi^+ \pi^-$  and  $B^0 \rightarrow D^- \pi^+$ . It should also be pointed out that we do not directly depend on the absolute efficiencies since to first order the differences in the reconstruction of  $B_s^0$  and  $B^0$  mesons cancel in the ratio of branching ratios. We discuss the differences in Chapter 5 dealing with systematic uncertainties.

## 4.1 Monte Carlo simulation

Monte Carlo simulation has for a long time been used to study the behavior of physics events in detectors. It becomes particularly useful when physics events are studied which have, for some reason, not been registered by the detector. In some cases the sheer complexity of physics phenomena makes analytical description not feasible, so numerical approaches are used instead. We use Monte Carlo simulation in particular for the following two purposes. The first application is the determination of trigger and reconstruction efficiencies of the signal events. The second application is to model the fitting shapes of the backgrounds as it is crucial to understand the exact composition of the candidates we reconstruct.

Before going into detail on those two topics, it is crucial to understand what the Monte Carlo simulation is based on. Only if we understand each issue can we evaluate how accurate our simulation is. There are several components in the simulation:

- quark production mechanism
- parton fragmentation
- $B$  meson decay kinematics
- decay branching fractions
- simulation of the trigger
- simulation of the reconstructed quantities.

The first three issues are related to theory while the last two are related to the simulation of the detector. The decay branching fractions are driven by recent measurements and theory predictions.

### 4.1.1 $b$ hadron production and decay

In an exclusive reconstruction analysis we can confine ourselves to simulating only the  $B$  meson which makes our candidate. Sideband subtraction techniques allows one to



study any of the quantities of a particular  $B$  meson decay and compare them to the Monte Carlo simulation. Additionally, the production mechanism and fragmentation process can be ignored as long as the correct transverse momentum spectrum and angular distribution are produced. The remaining decay characteristics are in general well reproduced by the commonly used decay programs. We use BGenerator [53] as the Monte Carlo program to create  $B$  mesons. It is based on NLO calculations [54] and the fragmentation is implemented using the Peterson fragmentation function [55]. Although recently more up-to-date fragmentation models have become available [56], it is not critical to this analysis since we modify the  $p_T$  and  $\eta$  dependencies in our systematics studies to correct for imperfect description of the underlying processes. BGenerator only produces  $b$  hadrons, no fragmentation products or proton remnants are present.

We use the BGenerator spectrum for single  $b$  quarks, and set the minimum  $b$  quark  $p_T$  to 0 GeV/c, and the pseudo-rapidity of the  $b$  quark spans the range  $|\eta| < 6$ . For the  $b$  hadron decays we use the EvtGen program [57]. This program has been extensively tuned by the experiments at the  $\Upsilon(4S)$  resonance [58, 59]. The  $B^+$  and  $B^0$  components are thus very well understood. Much less so the  $B_s^0$  and the  $b$  baryon decays. The missing knowledge about  $B_s^0$  decay properties is filled by  $SU(3)_f$  extrapolations from  $B^0$  to  $B_s^0$  (with  $SU(3)_f$  breaking corrections made if relevant).

### 4.1.2 Detector simulation

The detector simulation, which is subdivided into simulation of the trigger and detector, is more complicated. The detector geometry and the behavior of detector active components are simulated using the GEANT [60] framework. It allows one to model the detector response at the hit level, and the standard data reconstruction program is applied to the simulation outputs.

In its simplest form, the simulation models the detector functions under ideal operating conditions, which means that all components have the proper high voltage and the electronics react to traversing particles as designed. This is not the case in real life. In particular, fractions of the silicon detector have been off temporarily or

even for good. The parameters of the trigger subsystems have also evolved over time. The positioning of the beams with respect to the detector and the positioning of the silicon is only known to a certain precision and has to be taken into account when performing simulations.

To account for these imperfections, we have implemented the simulation in a more sophisticated fashion whereby the simulation tracks these operational imperfections. The simulation divides the data taking period in sub-periods where the detector performance is constant. This includes the parameters of the triggers at Level 1 and Level 2, the position of the beamline, the silicon detector conditions and the alignment. The central outer tracker, COT, is assumed to have constant behavior.

The output of the `BGenerator` program is run through four executables: the first one being responsible for the `GEANT` simulation of the detector response, the second one performs the trigger simulation, the third one processes the Monte Carlo output in a way identical to production farm processing, which we explain in Chapter 3, and the last one is the same reconstruction executable that is used for running on data.

## 4.2 Validation of Monte Carlo simulation

One of the biggest challenges in this analysis is doing a proper sideband subtraction in the data samples to allow a proper comparison to the Monte Carlo simulation. The problem comes from the fact that at masses just below the signal peak, which is where one would usually sample the low-mass sideband, there are large reflection structures. We need to use the knowledge of background shapes, which are discussed in Section 4.3 to solve this problem.

Our solution to the problem is based on the study of the background in Section 4.3. We find that the background under the signal peak (after we correct for the pollution from the backgrounds leaking under the signal) is completely “combinatorial”, which is to say that it is equivalent to the background we find in the high-mass sideband. The low-mass sideband has an additional component which comes from  $B \rightarrow DX$ -type decays which are not present under the signal peak, and should therefore not be

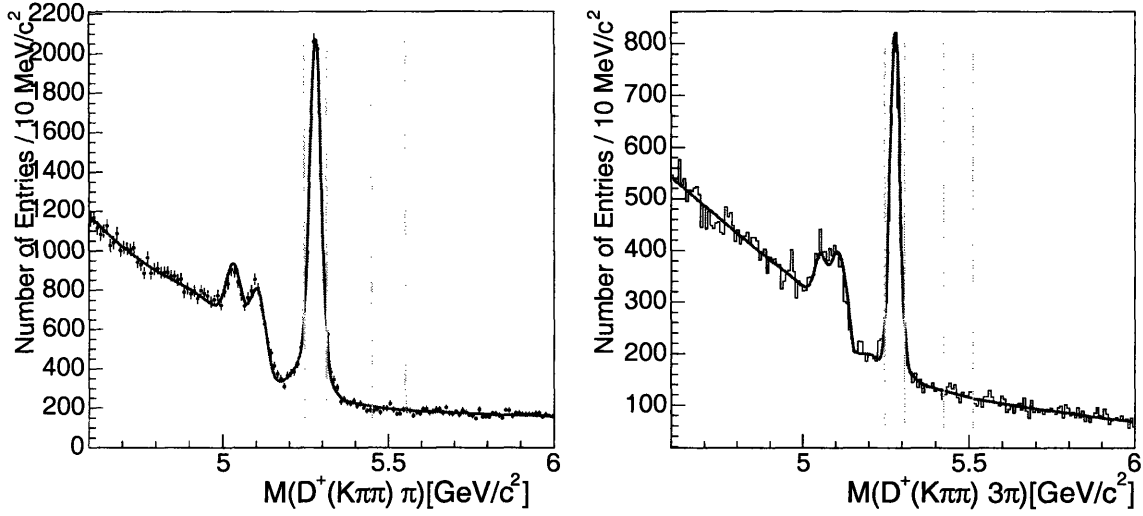


Figure 4-1: Signal and high-mass sideband region definitions for sideband subtraction. The left plot shows the mass spectrum for the  $B^0 \rightarrow D^- \pi^+$  decays, and the right plot shows the same distribution for the  $B^0 \rightarrow D^- \pi^+ \pi^+ \pi^-$  decays. The gray lines indicate signal and background region for sideband subtraction. The fitting curves are explained in Section 4.3.1.

directly subtracted from the signal distributions without somehow taking into account the distributions of  $B \rightarrow DX$ -type backgrounds.

Furthermore, the shape of the background distribution under the signal peak and to the right of signal are described by an exponential function plus a constant. In doing sideband subtraction we need to take into account that the background level in the high-mass sideband range chosen for sideband subtraction and signal regions are not the same. Fitting the mass spectrum at masses higher than the signal peak with an exponential function plus constant provides us with a weighting factor that accounts for this effect.

Figure 4-1 shows the definitions of the signal and sideband regions for our comparisons. The signal region is defined to be within  $2\sigma$  of the mass peak. The sideband is defined to be the interval  $m(B) \in [m(B) + 10\sigma(B); m(B) + 16\sigma(B)]$ . The fit results for the number of events in signal mass range in Monte Carlo and in both signal and sideband range in data are used to obtain weighting scale factors for the sideband subtraction procedure.

In Figures 4-2 through 4-19, the comparison between data and Monte Carlo simulation is summarized. We compare the shapes of various distributions between signal and sideband subtracted data and calculate probability of their matching. The final  $B$  meson selection requirements (Table 3.3.6) are applied to both data and Monte Carlo samples. If the quantity being compared is one of the  $B$  selection requirements, than that requirement is released to be able to compare the distributions in data and Monte Carlo samples in a wider range. Good agreement is observed in most distributions. The largest discrepancy are present in the  $M(\pi^+\pi^+\pi^-)$  distribution in Figure 4-22, and this is due to the discrepancy in the low mass range of the  $\pi^+\pi^+\pi^-$  mass spectrum. We address this issue in Section 4.2.1. There is also a small discrepancy in the  $p_T(B)$  distribution in Figure 4-2. It is discussed in Section 5.1.1.

Figures 4-2 through 4-19 also show the comparison of the distributions of quantities from the Monte Carlo signal sample and data sideband. The data sideband essentially represents a sample of combinatorial background events. For a quantity to be a good cut, it is desirable to observe a separation between the Monte Carlo signal sample and the background sample. Most of the quantities shown in Figures 4-2 through 4-19 are also used as a selection requirements. The rest are shown for validation purposes only.

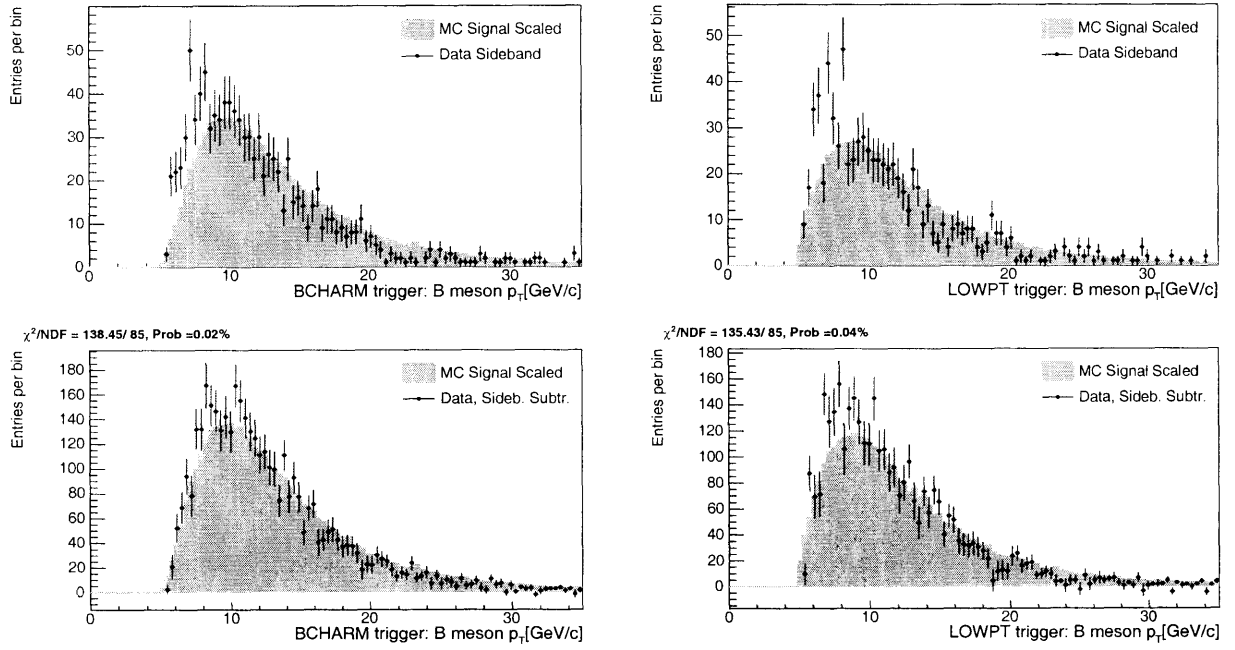


Figure 4-2: Comparison of data and Monte Carlo distributions of the  $p_T(B)$  for  $B^0 \rightarrow D^- \pi^+$  decays for B\_CHARM (left) and B\_CHARM\_LOWPT (right) triggers.

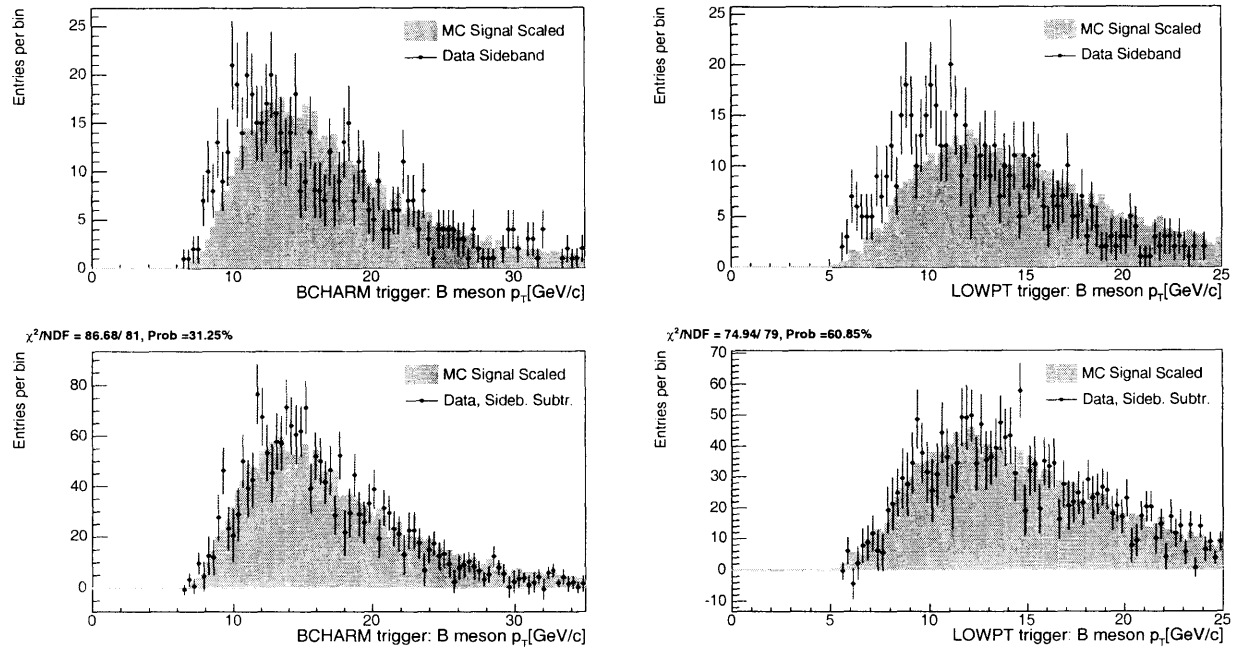


Figure 4-3: Comparison of data and Monte Carlo distributions of the  $p_T(B)$  for  $B^0 \rightarrow D^- \pi^+ \pi^+ \pi^-$  decays for B\_CHARM (left) and B\_CHARM\_LOWPT (right) triggers.

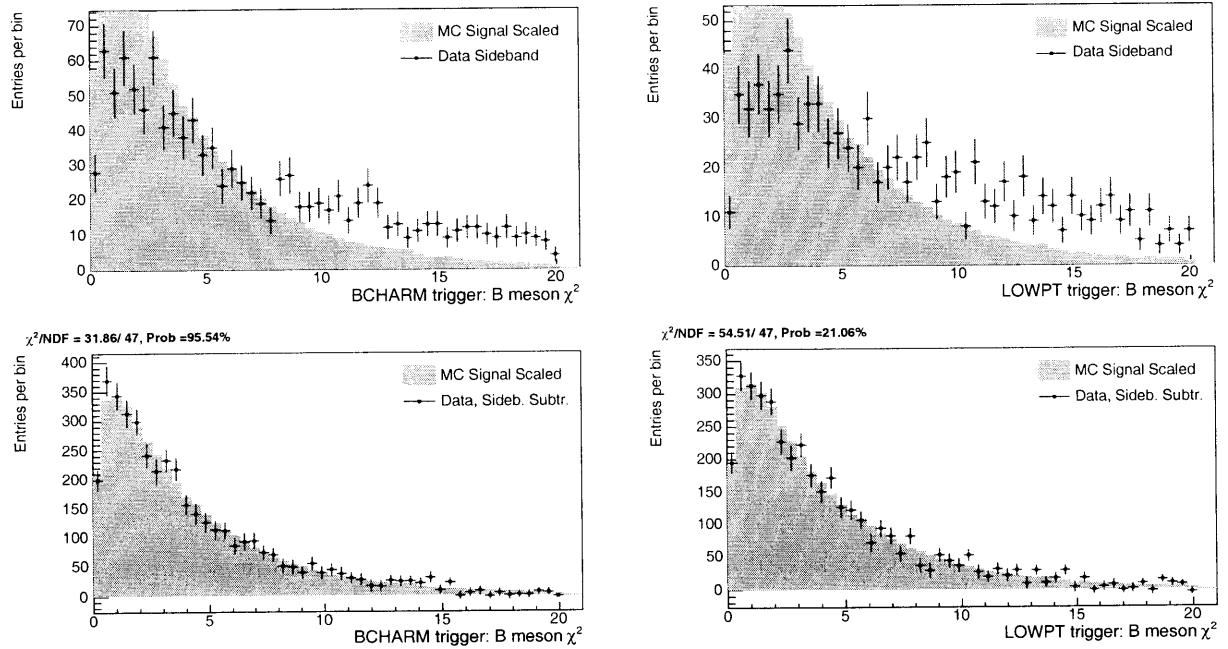


Figure 4-4: Comparison of data and Monte Carlo distributions of the  $\chi^2(B)$  for  $B^0 \rightarrow D^-\pi^+$  decays for B\_CHARM (left) and B\_CHARM\_LOWPT (right) triggers.

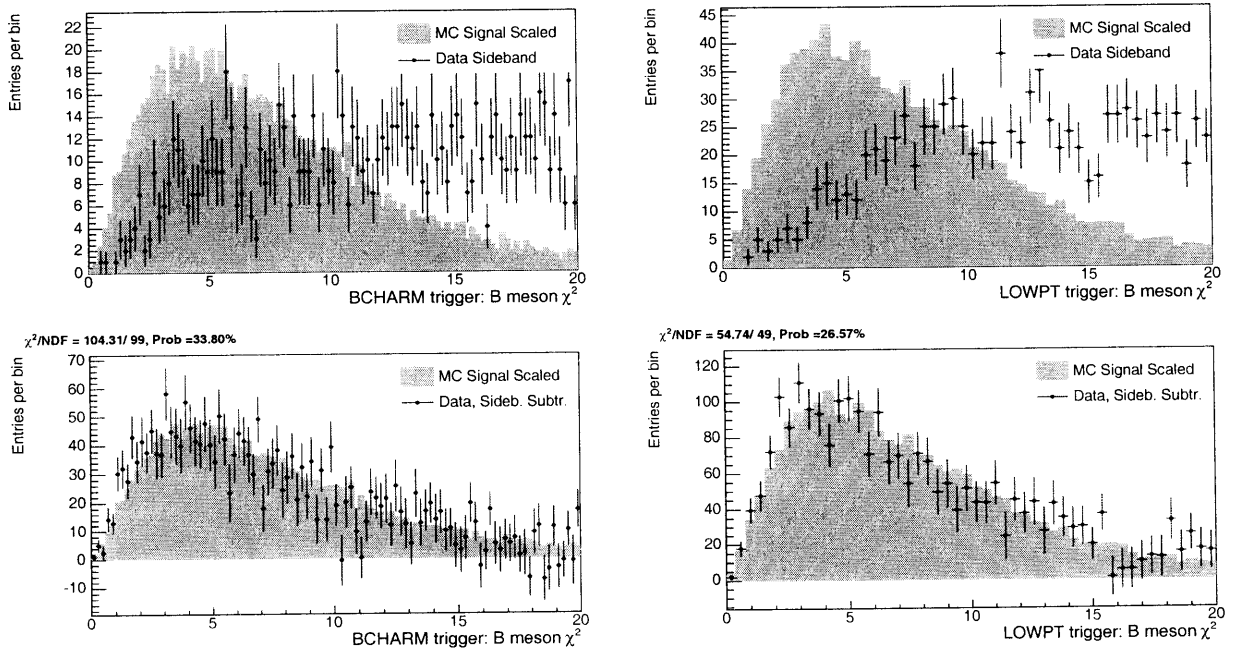


Figure 4-5: Comparison of data and Monte Carlo distributions of the  $\chi^2(B)$  for  $B^0 \rightarrow D^-\pi^+\pi^+\pi^-$  decays for B\_CHARM (left) and B\_CHARM\_LOWPT (right) triggers.

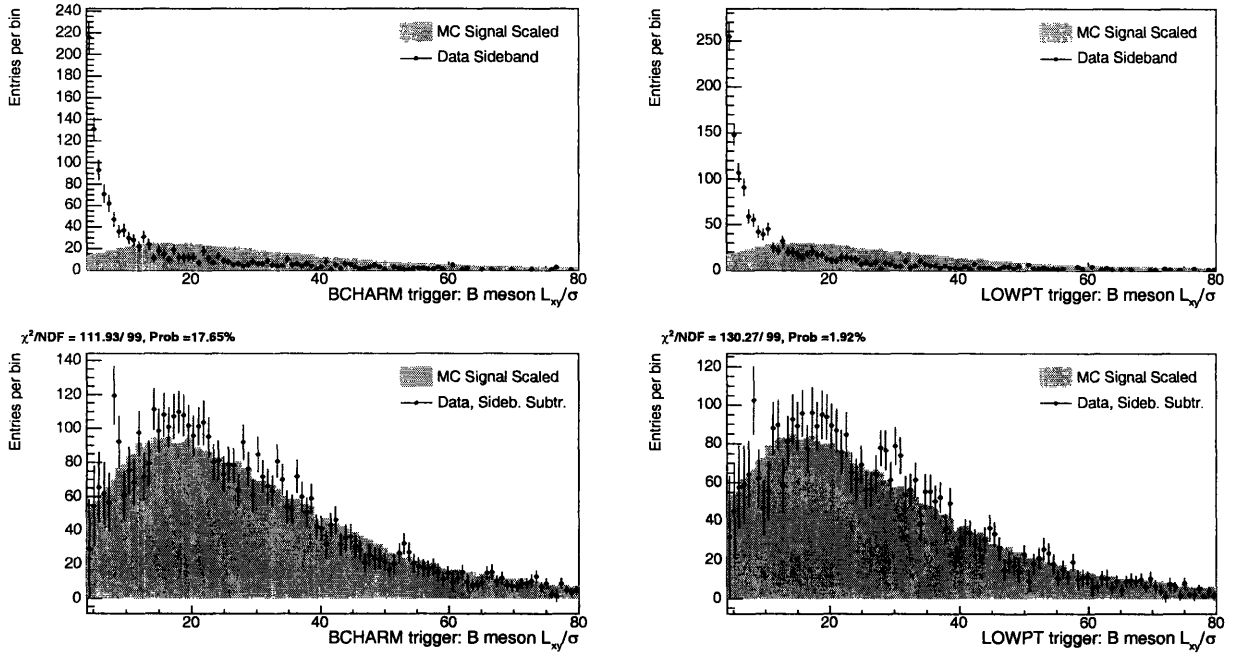


Figure 4-6: Comparison of data and Monte Carlo distributions of the  $L_{xy}/\sigma(B)$  for  $B^0 \rightarrow D^-\pi^+$  decays for B\_CHARM (left) and B\_CHARM\_LOWPT (right) triggers.

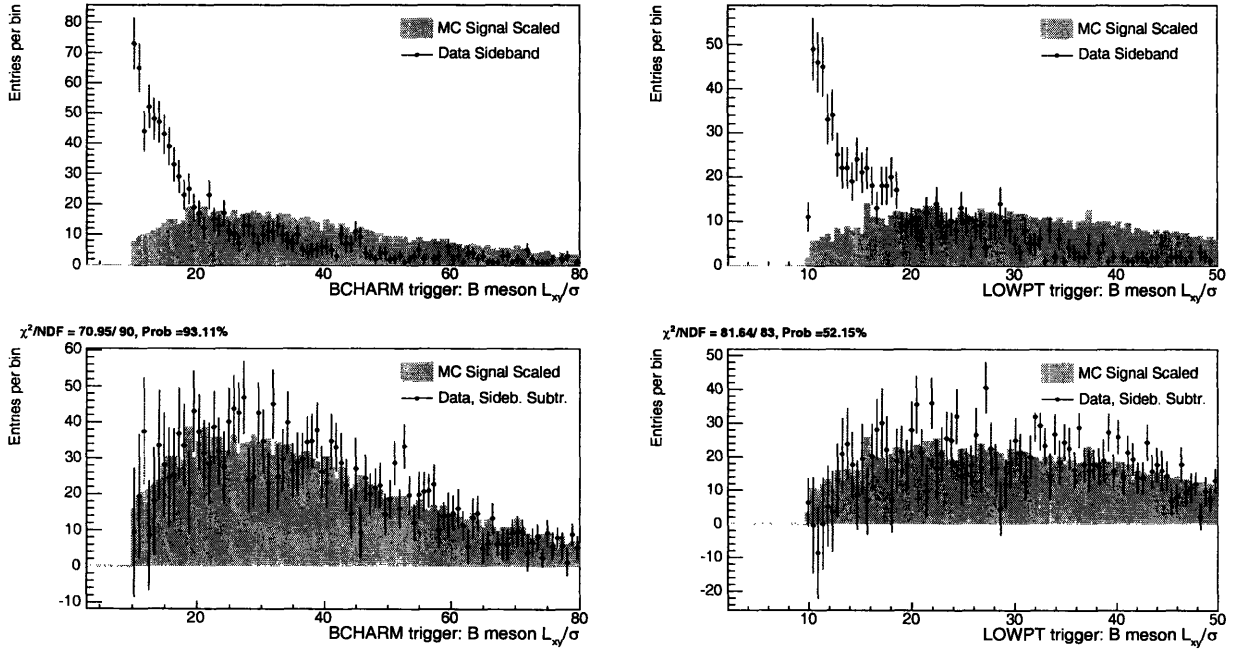


Figure 4-7: Comparison of data and Monte Carlo distributions of the  $L_{xy}/\sigma(B)$  for  $B^0 \rightarrow D^-\pi^+\pi^+\pi^-$  decays for B\_CHARM (left) and B\_CHARM\_LOWPT (right) triggers.

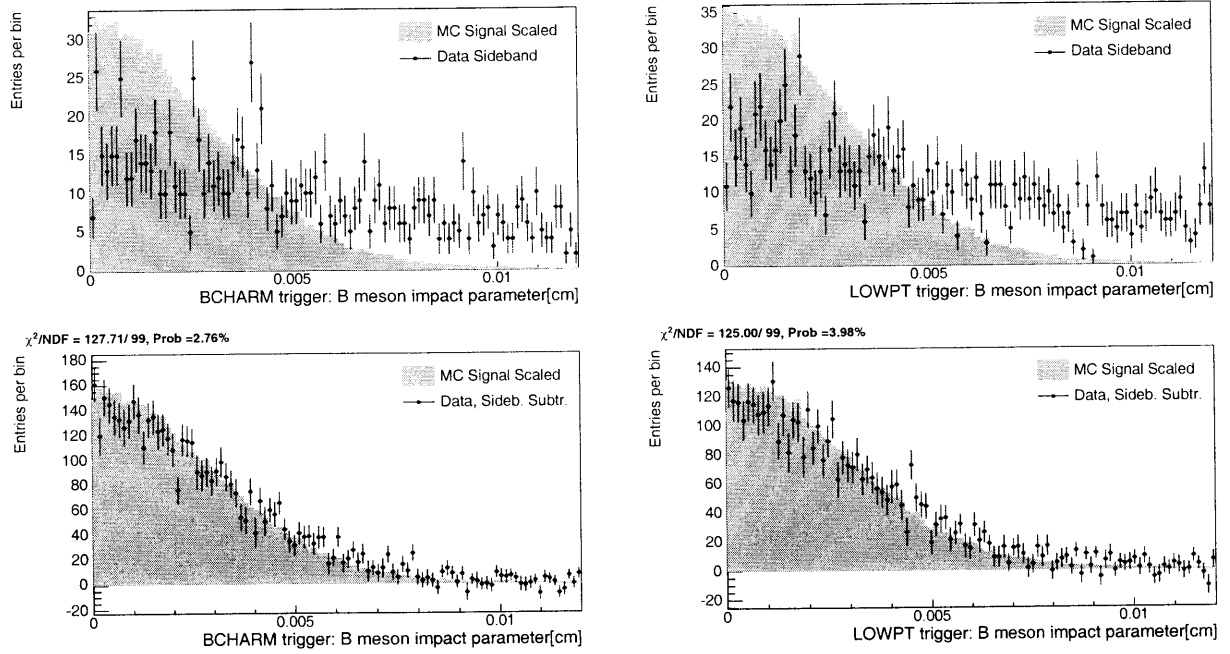


Figure 4-8: Comparison of data and Monte Carlo distributions of the  $d_0(B)$  for  $B^0 \rightarrow D^-\pi^+$  decays for B\_CHARM (left) and B\_CHARM.LOWPT (right) triggers.

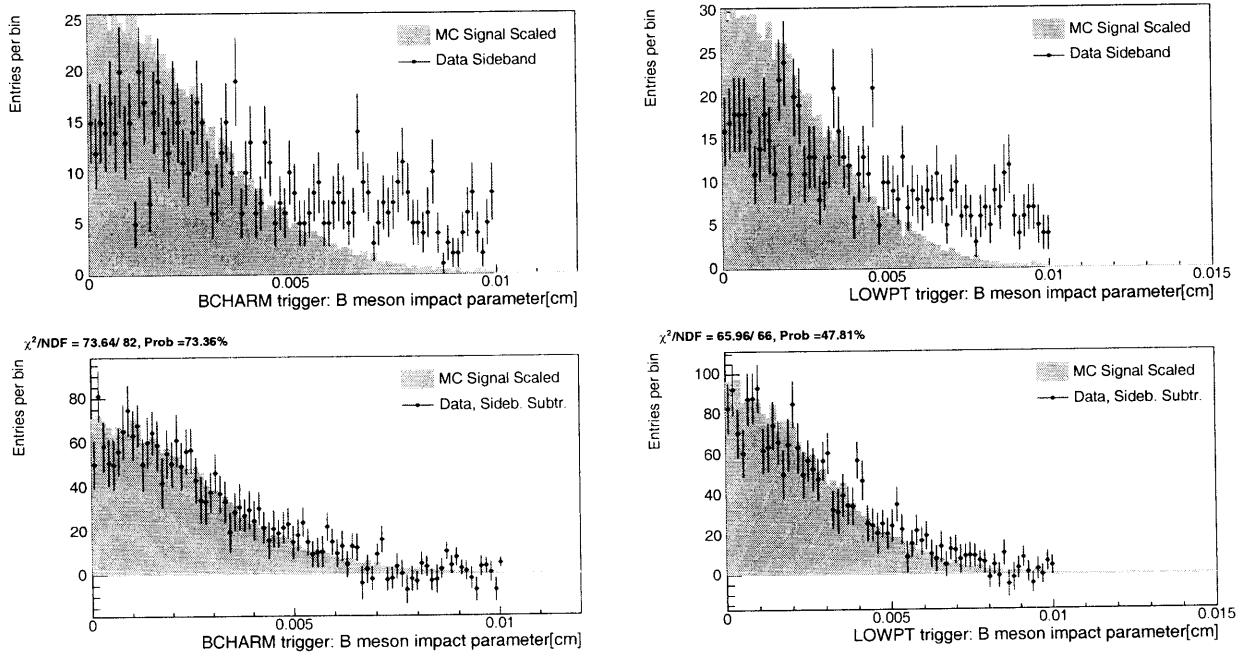


Figure 4-9: Comparison of data and Monte Carlo distributions of the  $d_0(B)$  for  $B^0 \rightarrow D^-\pi^+\pi^+\pi^-$  decays for B\_CHARM (left) and B\_CHARM.LOWPT (right) triggers.



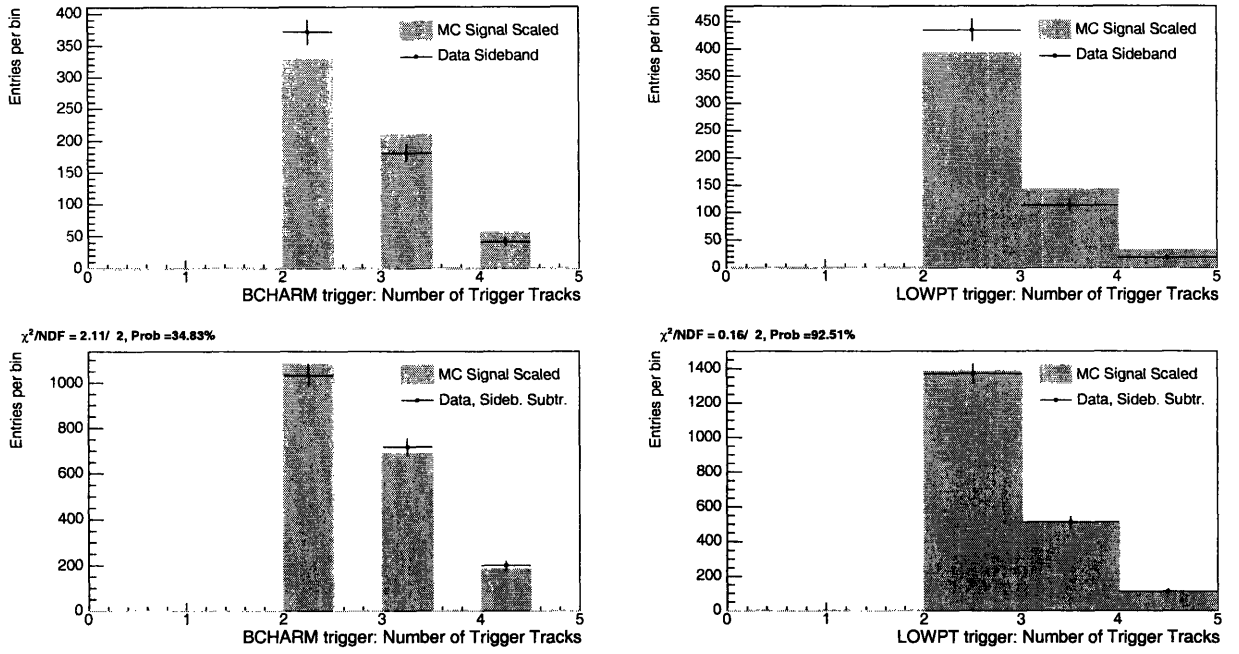


Figure 4-10: Comparison of data and Monte Carlo distributions of the number of trigger tracks for  $B^0 \rightarrow D^- \pi^+ \pi^+ \pi^-$  decays for B\_CHARM and B\_CHARM.LOWPT triggers.

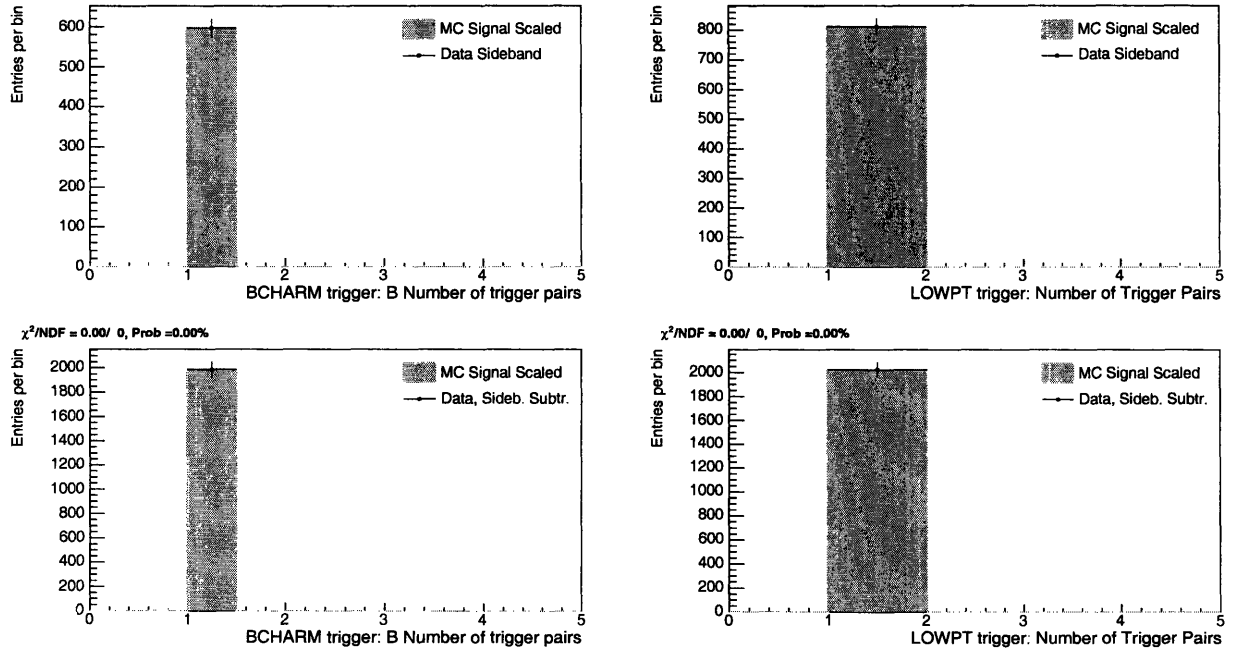


Figure 4-11: Comparison of data and Monte Carlo distributions of the number of trigger pairs for  $B^0 \rightarrow D^- \pi^+ \pi^+ \pi^-$  decays for B\_CHARM and B\_CHARM.LOWPT triggers.

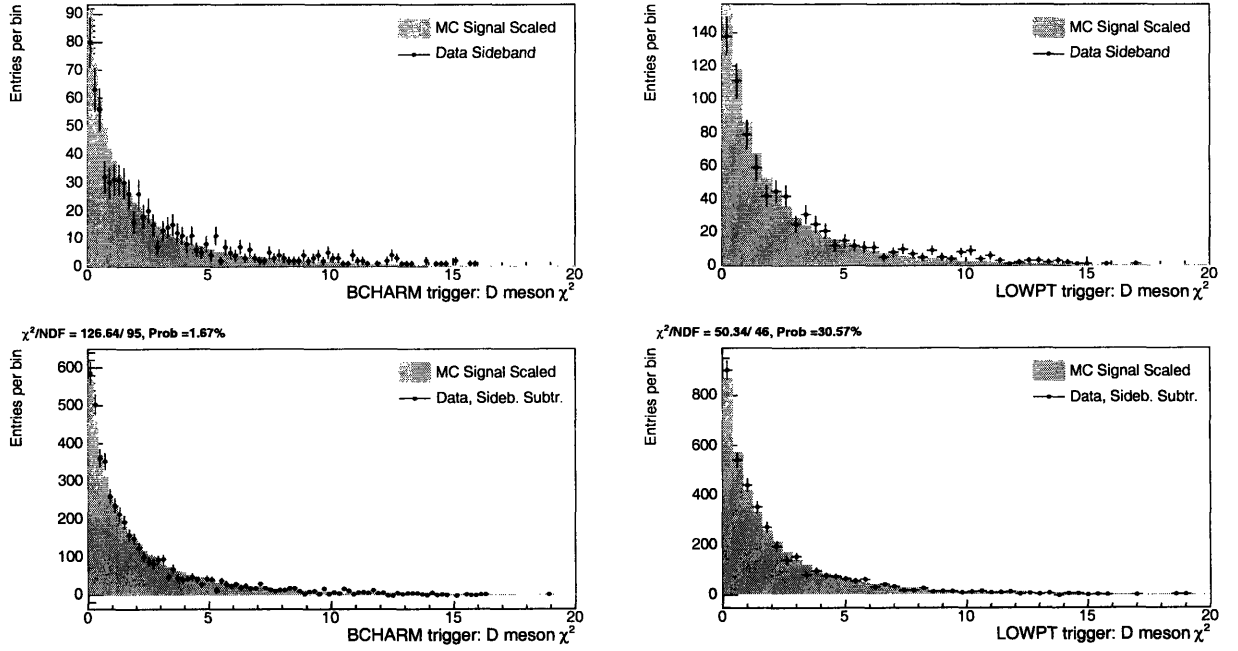


Figure 4-12: Comparison of data and Monte Carlo distributions of the  $\chi^2(D)$  for  $B^0 \rightarrow D^-\pi^+$  decays for B\_CHARM (left) and B\_CHARM\_LOWPT (right) triggers.

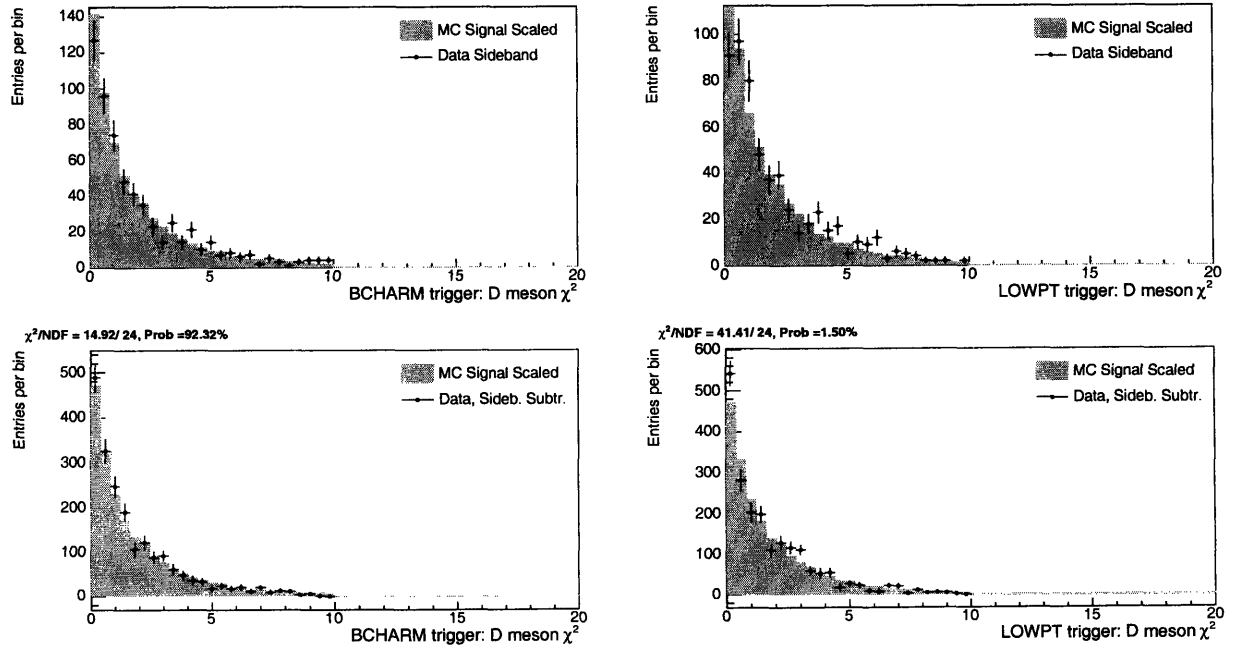


Figure 4-13: Comparison of data and Monte Carlo distributions of the  $\chi^2(D)$  for  $B^0 \rightarrow D^-\pi^+\pi^+\pi^-$  decays for B\_CHARM (left) and B\_CHARM\_LOWPT (right) triggers.

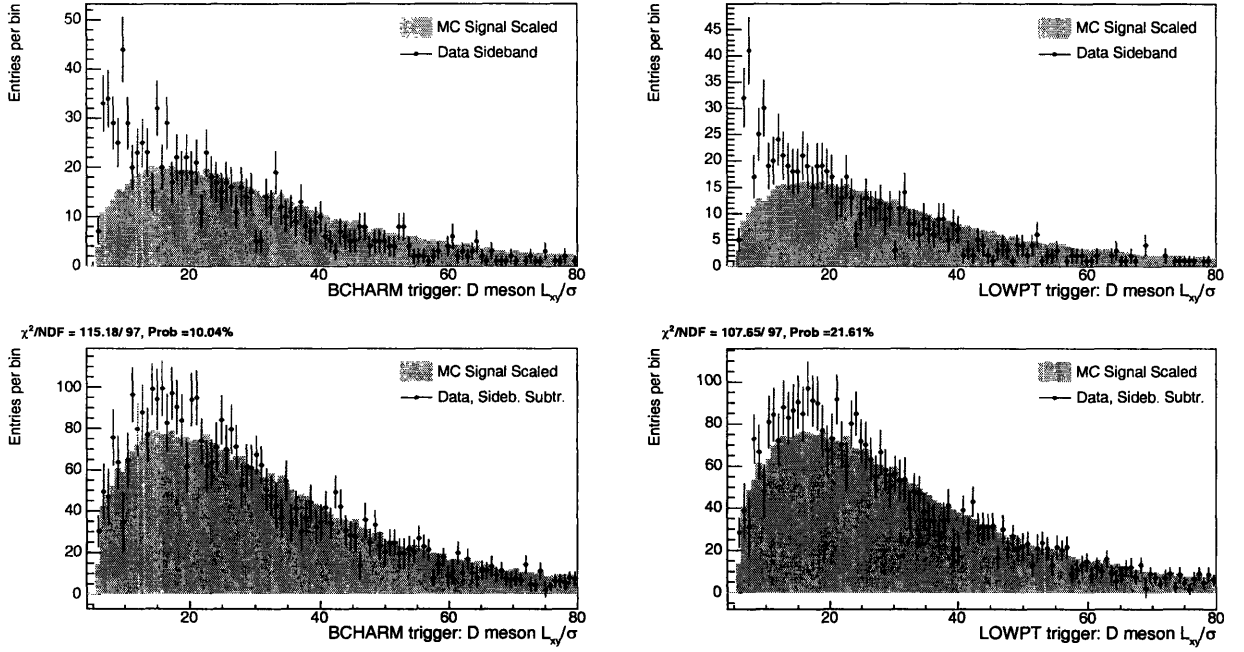


Figure 4-14: Comparison of data and Monte Carlo distributions of the  $L_{xy}/\sigma(D)$  for  $B^0 \rightarrow D^-\pi^+$  decays for B\_CHARM (left) and B\_CHARM\_LOWPT (right) triggers.

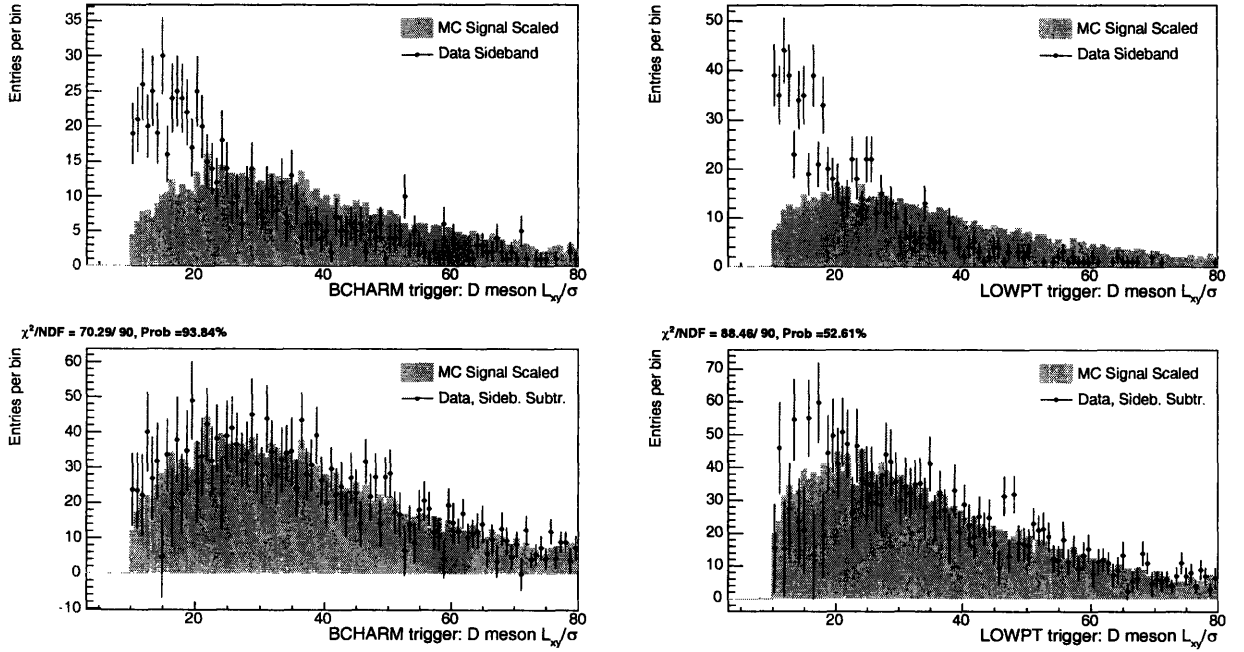


Figure 4-15: Comparison of data and Monte Carlo distributions of the  $L_{xy}/\sigma(D)$  for  $B^0 \rightarrow D^-\pi^+\pi^+\pi^-$  decays for B\_CHARM (left) and B\_CHARM\_LOWPT (right) triggers.

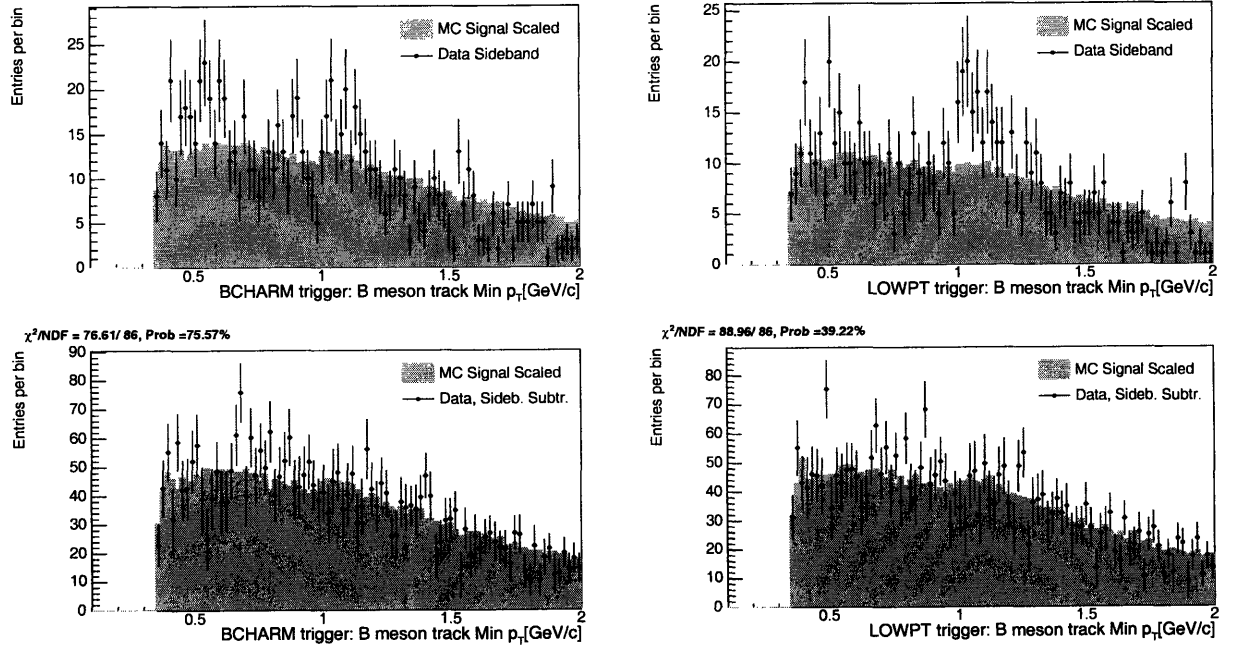


Figure 4-16: Comparison of data and Monte Carlo distributions of the  $\text{Min } p_T(B)$  for  $B^0 \rightarrow D^- \pi^+$  decays for B\_CHARM (left) and B\_CHARM\_LOWPT (right) triggers.

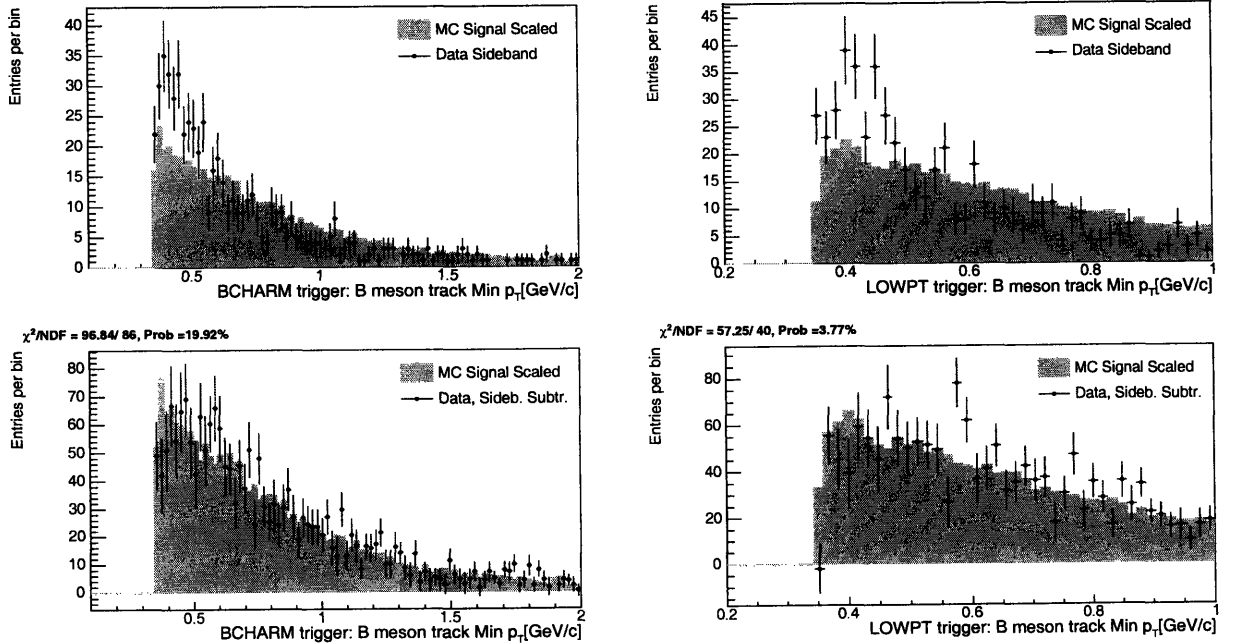


Figure 4-17: Comparison of data and Monte Carlo distributions of the  $\text{Min } p_T(B)$  for  $B^0 \rightarrow D^- \pi^+ \pi^+ \pi^-$  decays for B\_CHARM (left) and B\_CHARM\_LOWPT (right) triggers.

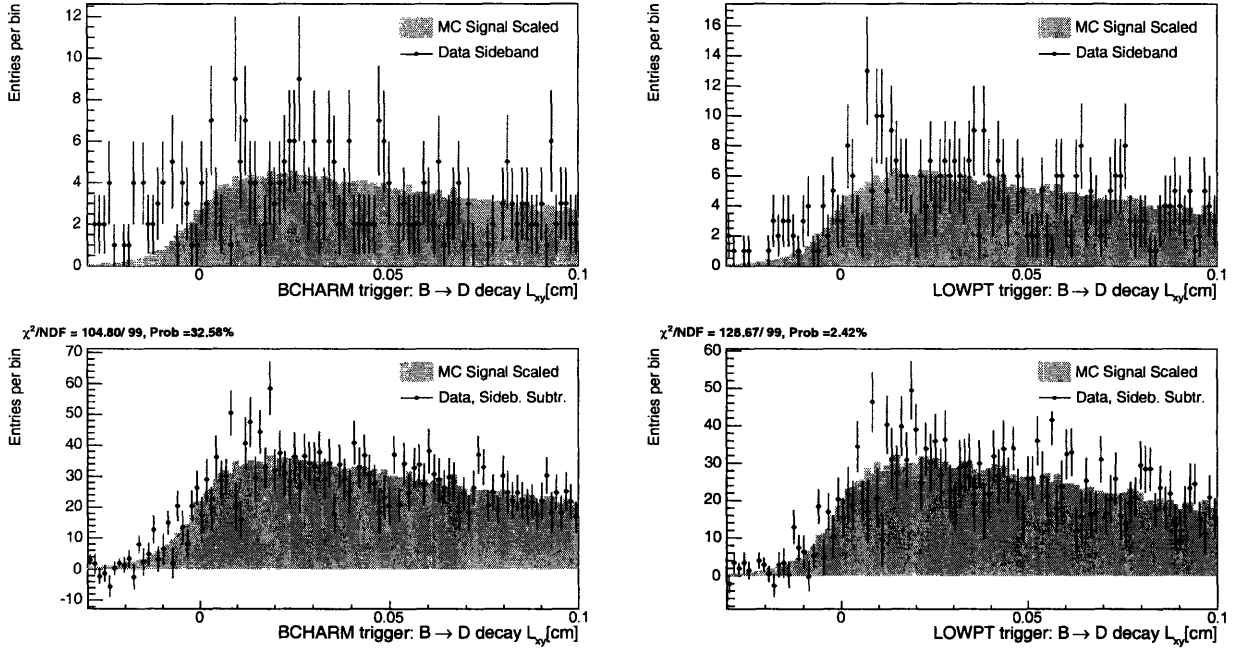


Figure 4-18: Comparison of data and Monte Carlo distributions of the  $L_{xy}(D)$  for  $B^0 \rightarrow D^- \pi^+$  decays for B\_CHARM (left) and B\_CHARM\_LOWPT (right) triggers.

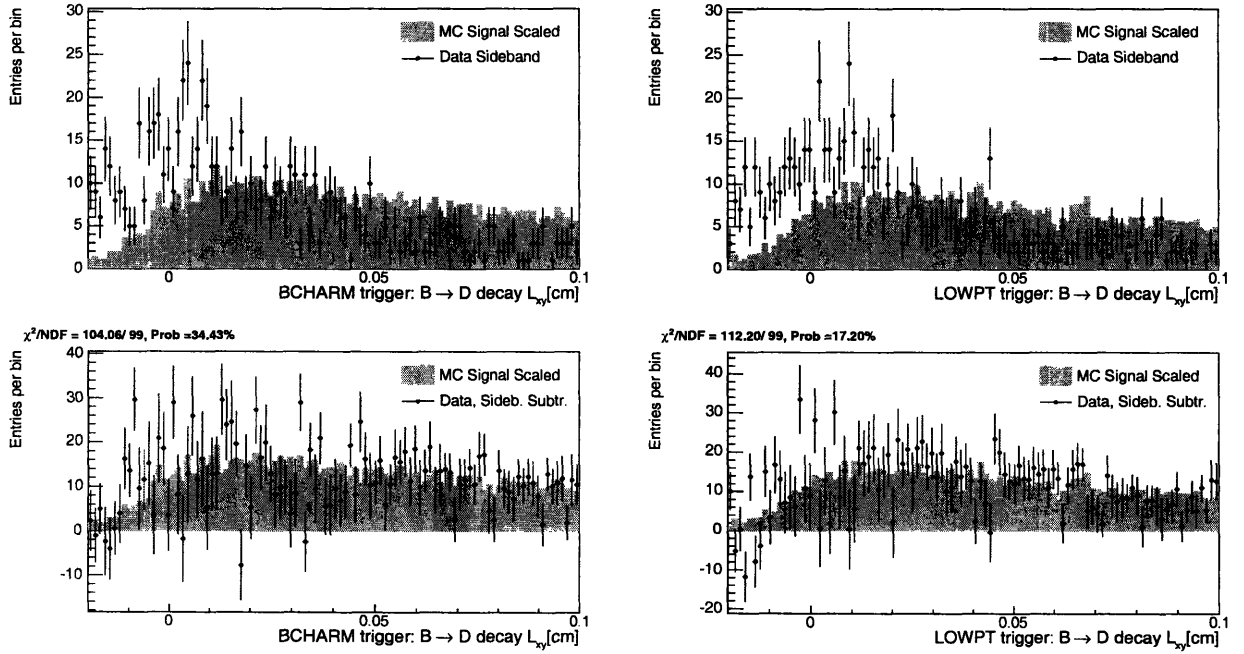


Figure 4-19: Comparison of data and Monte Carlo distributions of the  $L_{xy}(D)$  for  $B^0 \rightarrow D^- \pi^+ \pi^+ \pi^-$  decays for B\_CHARM (left) and B\_CHARM\_LOWPT (right) triggers.

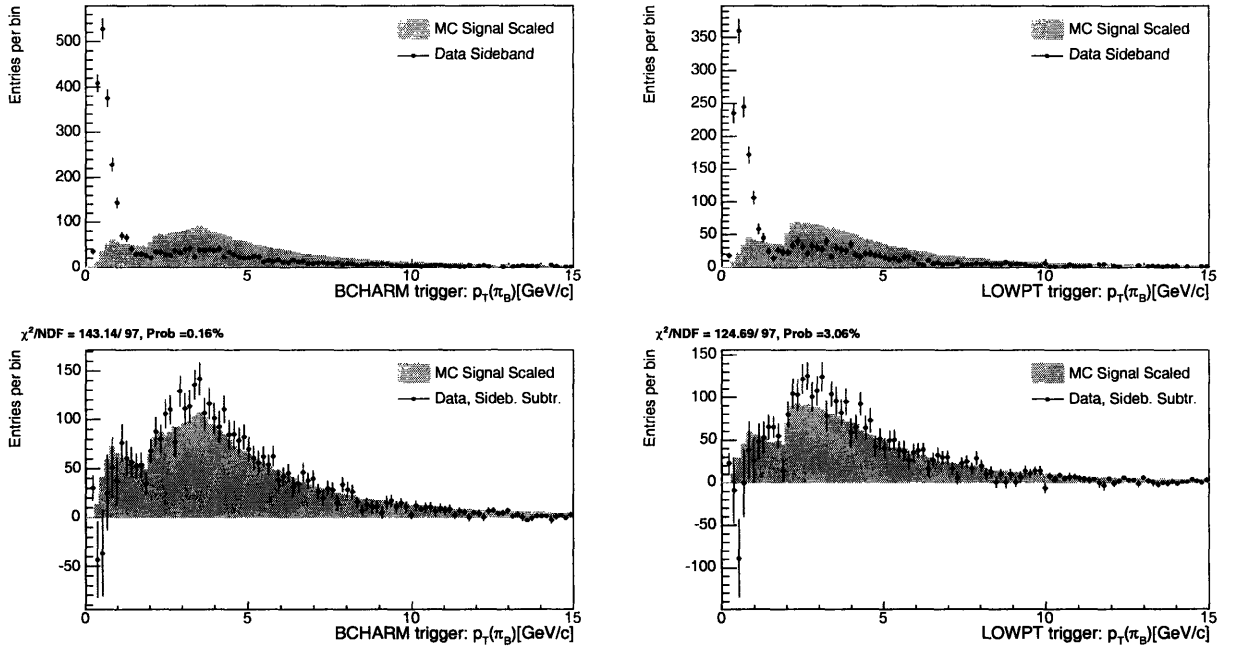


Figure 4-20: Comparison of data and Monte Carlo distributions of the  $p_T(\pi_B)$  for  $B^0 \rightarrow D^- \pi^+$  decays for B\_CHARM (left) and B\_CHARM\_LOWPT (right) triggers.

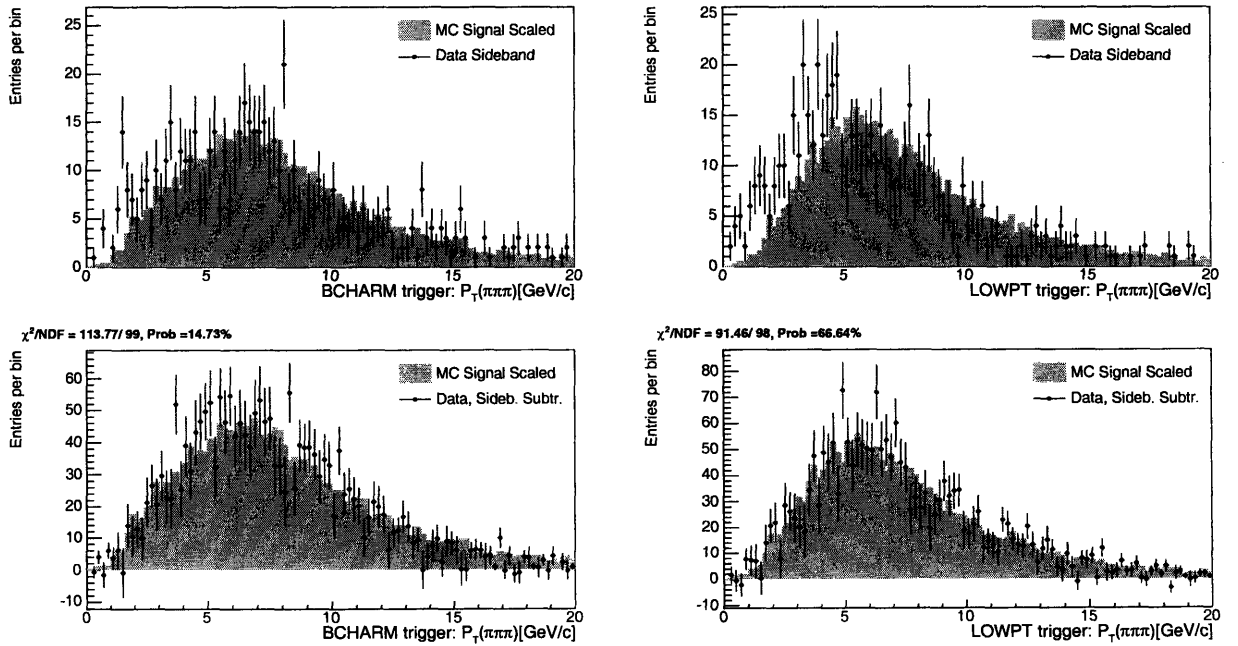


Figure 4-21: Comparison of data and Monte Carlo distributions of the  $p_T(\pi^+ \pi^+ \pi^-)$  for  $B^0 \rightarrow D^- \pi^+ \pi^+ \pi^-$  decays for B\_CHARM (left) and B\_CHARM\_LOWPT (right) triggers.

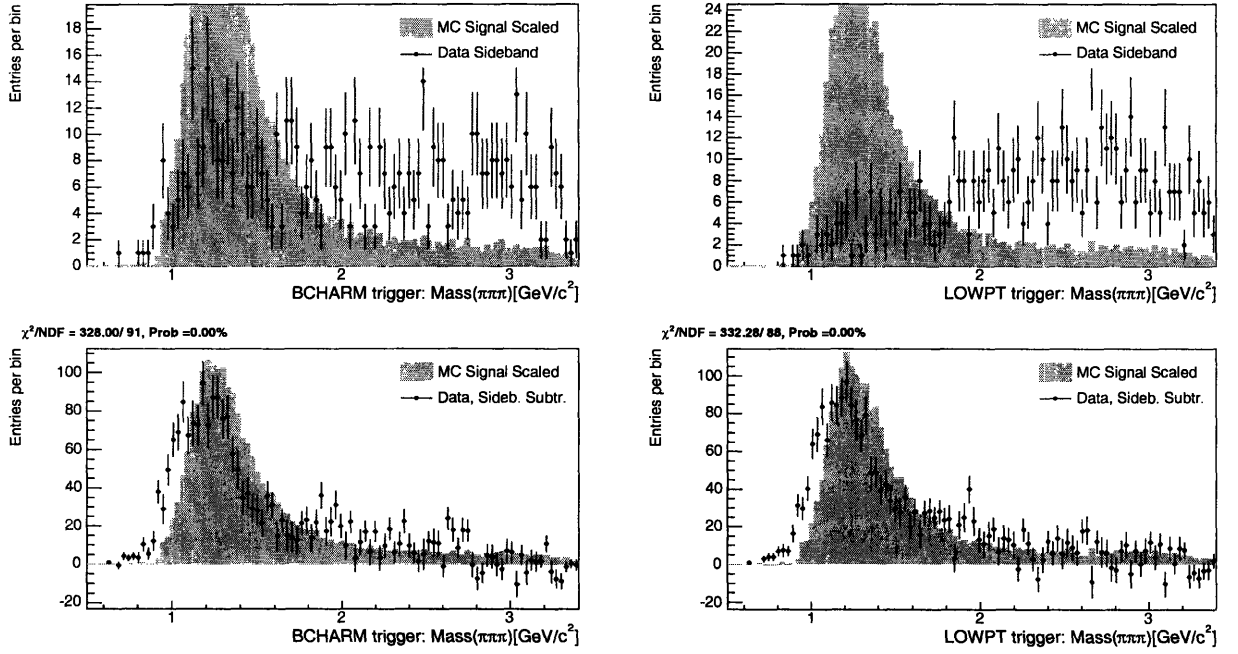


Figure 4-22: Comparison of data and Monte Carlo distributions of the  $M(\pi\pi\pi)$  for  $B^0 \rightarrow D^-\pi^+\pi^+\pi^-$  decays for B\_CHARM (left) and B\_CHARM\_LOWPT (right) triggers.

#### 4.2.1 Reweighting procedure

We noticed a discrepancy in the spectrum of  $\pi^+\pi^+\pi^-$  system originating from  $B^0 \rightarrow D^-\pi^+\pi^+\pi^-$  decay (see Figure 4-22) in the default Monte Carlo simulation and the distribution seen in data. The shape of this distribution is defined by the resonant structure of  $\pi^+\pi^+\pi^-$  coming from  $B^0 \rightarrow D^-\pi^+\pi^+\pi^-$  meson decay.

There are four major contributions to the inclusive  $B^0 \rightarrow D^-\pi^+\pi^+\pi^-$  sample. The first and biggest contribution is the  $B^0 \rightarrow D^-a_1$  decay, where the  $a_1(1260)$  decays into three pions. The second contribution is the  $B^0 \rightarrow D^-\rho^0\pi^+$  decay with  $\rho^0(770)$  meson decaying to two pions of opposite charge. The third contribution is the  $B^0 \rightarrow D^-\pi^+\pi^+\pi^-$  non-resonant decay and the last contribution we consider is  $B^0 \rightarrow D_s^-\pi^+\pi^+\pi^-$ , ( $D_s^- \rightarrow \pi^-\pi^+\pi^-$ ) decay. Those four contributions are expected to have characteristic shapes clearly distinguishable from each other.

The default Monte Carlo simulation shows a discrepancy in the  $\pi^+\pi^+\pi^-$  mass spectrum because the branching fractions of different resonant contributions are

Decay	Old BR's [ $\times 10^{-3}$ ]	New BR's [ $\times 10^{-3}$ ]
$B^0 \rightarrow D^- a_1$	$3.0 \pm 3.3$	9.0
$B^0 \rightarrow D^- \rho^0 \pi^+$	$1.1 \pm 1.0$	0.5
$B^0 \rightarrow D^- \pi^+ \pi^+ \pi^-$	$2.2 \pm 1.9$	0.5

Table 4.1: Branching fractions from the default CDF decay file and updated branching fractions in agreement with the most recent BaBar measurement [61]. The values and uncertainties in the second column are taken from PDG [2].

poorly measured. We therefore adjust those fractions by tuning our Monte Carlo simulation to represent the data well.

Figure 4-23 shows the shapes of the  $B^0 \rightarrow D^- \pi^+ \pi^+ \pi^-$ ,  $B^0 \rightarrow D^- \rho^0 \pi^+$ , and  $B^0 \rightarrow D^- a_1$  distributions. Table 4.1 shows the branching fractions in the decay file before and after tuning. The resulting composition of the signal is shown on the bottom right plot of Figure 4-23.

Figure 4-22 shows the agreement between data and Monte Carlo simulation for the  $\pi^+ \pi^+ \pi^-$  mass spectrum after tuning is done. The left over discrepancy observed on the low mass range can be removed if we shift the Monte Carlo simulation mass of  $a_1$  resonance by  $\approx 100 \text{ MeV}/c^2$ . According to PDG the mass of  $a_1$  is  $1230 \pm 40 \text{ MeV}/c^2$ . We do not understand the origin of this discrepancy in our data. The issue of this remaining discrepancy in the  $\pi^+ \pi^+ \pi^-$  mass spectrum and how it affects our measurement is discussed further in Chapter 5.



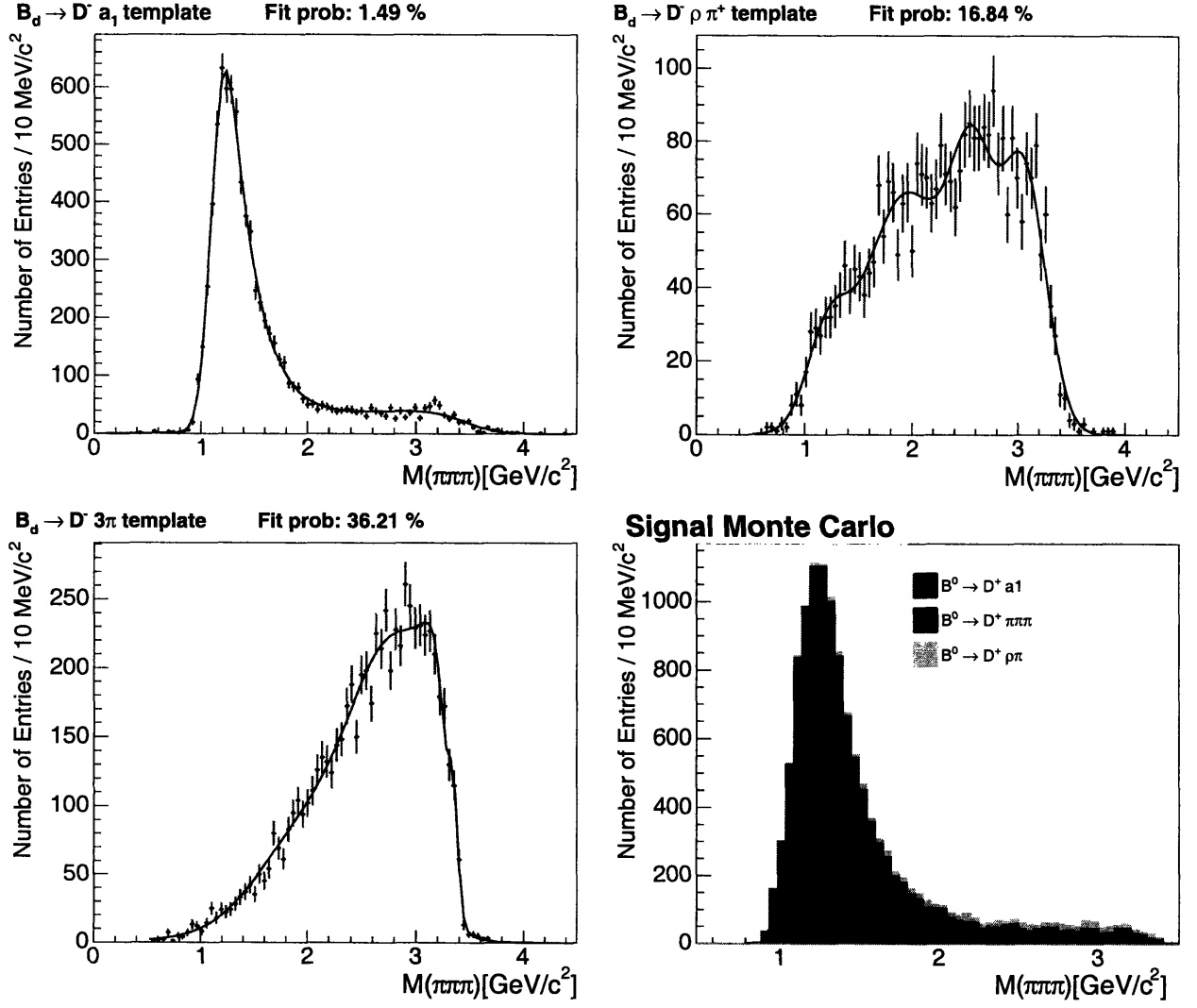


Figure 4-23: Top left:  $B^0 \rightarrow D^- a_1$  distribution is shown. Top right:  $B^0 \rightarrow D^- \rho^0 \pi^+$ . Bottom left:  $B^0 \rightarrow D^- \pi^+ \pi^+ \pi^-$ . Bottom right: composition of resonant contributions in  $B^0 \rightarrow D^- \pi^+ \pi^+ \pi^-$  signal Monte Carlo.

### 4.3 Background composition studies

The mass spectra for all four  $B$  meson decays have interesting features which are already visible when looking at the mass spectra with unoptimized cuts. Figures 3-12 and 3-13 show at least one peak below the main, signal peak for each flavor of the  $B$  meson investigated. When the optimized cuts are applied, the structures get even more pronounced. We attempt to understand these structures using specific Monte Carlo samples.

We generate single  $b$  hadrons using **BGenerator** and decay them using **EvtGen**. We generate two inclusive Monte Carlo samples: inclusive  $b \rightarrow D_s^- X$ , where the  $D_s^-$  decay is forced to decay as  $D_s^- \rightarrow \phi^0 \pi^-$  ( $\phi^0 \rightarrow K^+ K^-$ ), and inclusive  $b \rightarrow D^- X$ , where the  $D^-$  decay is forced to decay as  $D^- \rightarrow K^+ \pi^- \pi^-$ . By “inclusive samples” we mean that a mixture of  $B^+$ ,  $B^0$ ,  $B_s^0$  and  $b$  baryons are generated based on the measured probabilities  $f_d$ ,  $f_u$ ,  $f_s$ , and  $f_\Lambda$  for a  $b$  quark to fragment into these various species.

Inclusive samples are used to study the structure of the continuum background in the low mass range of the  $B$  mass spectrum distribution. When we want to study the structure of the continuum background for  $B_s^0 \rightarrow D_s^- \pi^+$  decay, we use inclusive  $D_s^- \rightarrow \phi^0 \pi$  sample only, and not  $D^- \rightarrow K^+ \pi^- \pi^-$  sample. This is justified by the fact that most candidates in the  $B_s^0 \rightarrow D_s^- \pi^+$  mass distribution are due to “real  $D_s^-$  plus anything” scenario.

We make a detailed study of partially reconstructed decays by generating samples of  $B_s^0 \rightarrow D_s^{*-} \pi^+ \pi^+ \pi^-$  with  $D_s^{*-}$  decaying to  $D_s^- \gamma$  or  $D_s^{*-}$  decaying to  $D_s^- \pi^0$ , and  $B^0 \rightarrow D^{*-} \pi^+ \pi^+ \pi^-$  with  $D^{*-}$  decaying to  $D^- \pi^0$ . These samples are used to understand the structure of the background below the main signal peaks.

We generate four signal Monte Carlo samples:  $B^0 \rightarrow D^- \pi^+$ ,  $B^0 \rightarrow D^- \pi^+ \pi^+ \pi^-$ ,  $B_s^0 \rightarrow D_s^- \pi^+$ , and  $B_s^0 \rightarrow D_s^- \pi^+ \pi^+ \pi^-$  with  $D^- \rightarrow K^+ \pi^- \pi^-$  and  $D_s^- \rightarrow \phi^0 \pi^-$ . For signal Monte Carlo samples we typically generate 60 million events, of which about 100000 events pass the trigger and simulation requirements for  $B \rightarrow D \pi^+$  decay. In  $B \rightarrow D \pi^+ \pi^+ \pi^-$  signal the number of selected events is about six to seven times

smaller. This is due to the fact that detector, trigger, and selection efficiency is generally lower for decays with more tracks in the final state.

For the inclusive  $b \rightarrow D_s^- X$  and  $b \rightarrow D^- X$  samples, we generate 600 million to 1 billion events. The selection efficiency for these samples is much lower than for the signal samples. This is a very natural consequence of the fact that the selection requirements are optimized for the signal. Generating 1 billion events is very computationally intensive task, but it is required since we need an order of magnitude more events in the Monte Carlo samples than in our data for a detailed understanding of the backgrounds.

We also generate several Monte Carlo simulations to study the Cabibbo suppressed contributions to the background. For  $B^0 \rightarrow D^- \pi^+ \pi^+ \pi^-$  decay we generate  $B^0 \rightarrow D^- \pi^+ \pi^- K^+$ , for  $B^0 \rightarrow D^- \rho^0 \pi^+$  we generate  $B^0 \rightarrow D^- \rho^0 K^+$  and for  $B^0 \rightarrow D^- a_1$  we generate  $B^0 \rightarrow D^- K_1$ . For  $B^0 \rightarrow D^- \pi^+$  decay we generate  $B^0 \rightarrow D^- K^+$  and for  $B_s^0 \rightarrow D_s^- \pi^+$  we generate  $B_s^0 \rightarrow D_s^- K^+$  and  $B^0 \rightarrow D_s^- \pi^+$ . And lastly, we generate  $\Lambda_b \rightarrow \Lambda_c^+ \pi^-$  and  $\Lambda_b \rightarrow \Lambda_c^+ \pi^+ \pi^+ \pi^-$ , with  $\Lambda_c^+ \rightarrow p^+ K^- \pi^+$ .

The events for all of the above mentioned samples are reconstructed and filtered using the simulation framework, and analyzed with the same reconstruction software and selection requirements that are used to reconstruct the different  $B$  mesons in data.

The resulting mass spectra are then decomposed, based on which decay mode was actually being simulated, to separate the contributions from different decay modes. The spectra with their various contributions are shown in Figures 4-24 and 4-25. The relative normalizations of the individual modes and the assumptions about their branching fractions are discussed in Section 4.4.

If we now come back to the plots, shown in Figures 3-12 and 3-13 and using input from the plots in Figures 4-24 and 4-25, we draw several conclusions. All the  $B$  backgrounds have common features: in the high mass region the background is smooth and can be described by an exponential plus a constant. In the low mass region there is a pronounced structure associated with  $B \rightarrow D^*$  decays. Additionally, there is a rich variety of continuum backgrounds which still do not pollute the signal region. In

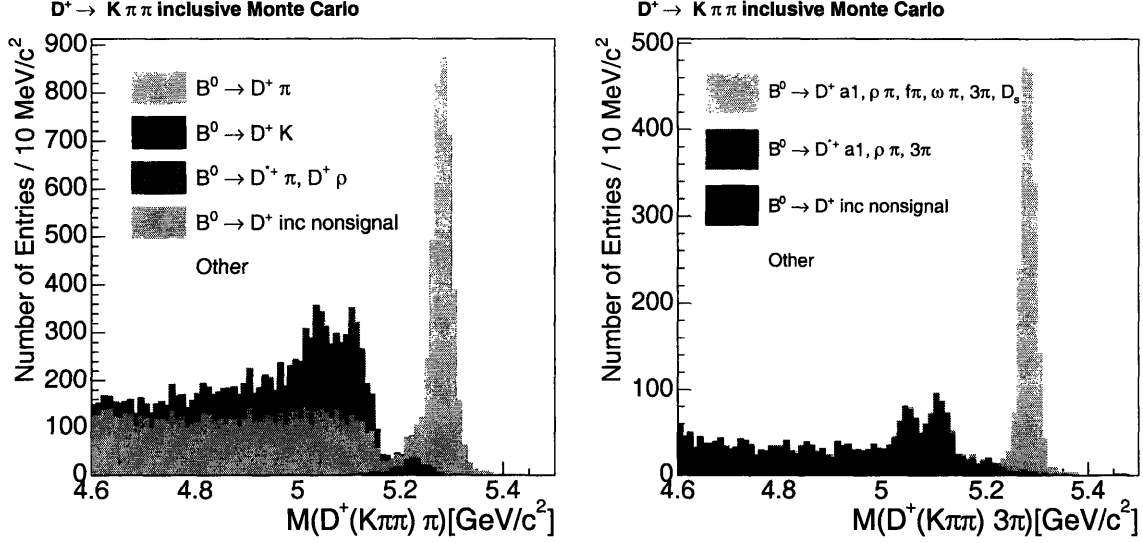


Figure 4-24: Decomposition of the inclusive background for  $B^0 \rightarrow D^-\pi^+$  (left plot) and  $B^0 \rightarrow D^-\pi^+\pi^+\pi^-$  (right plot) decays.

the case of the  $B^0$  mesons in Figure 4-24, the structure below the main  $B$  peak has two pronounced spikes. The mechanism that produces this structure is the result of a  $B \rightarrow D^{*-}\pi^+\pi^+\pi^-$  or  $B \rightarrow D^{*-}\pi^+$  decay followed by a  $D^{*-} \rightarrow D^-\pi^0$  decay. The  $D^{*-}$  is partially polarized in this decay. As a result, the angle  $\theta$  between the momenta of the soft pions in the  $D^{*-}$  decay and the  $D^{*-}$  flight direction follows a  $\cos^2(\theta)$  distribution in the  $D^{*-}$  rest frame. Most of the time, the pions are emitted either in the same direction as the  $D^{*-}$  momentum, or in the opposite direction. Consequently, the  $D$  momentum follows the same direction as the  $D^{*-}$  did. Depending whether the pion is released parallel or anti-parallel to the  $D^{*-}$  flight direction, either most of the free energy of the decay is carried away by the soft pion or very little. These two scenarios are responsible for the two separate spikes in the mass distribution.

In addition to the spikes that are visible in the mass distributions, we expect some physics backgrounds to contribute under the main signal mass peaks. In particular, since this analysis is not using particle ID information, we expect a contribution from Cabibbo suppressed  $B \rightarrow DK^+$  and  $B \rightarrow D2\pi K^+$  decays. For these decays a kaon is reconstructed as a pion, and the events end up on the left of the main signal peak. We also expect a contribution from  $B_s^0$  decays directly under the  $B^0$  mass peak, again

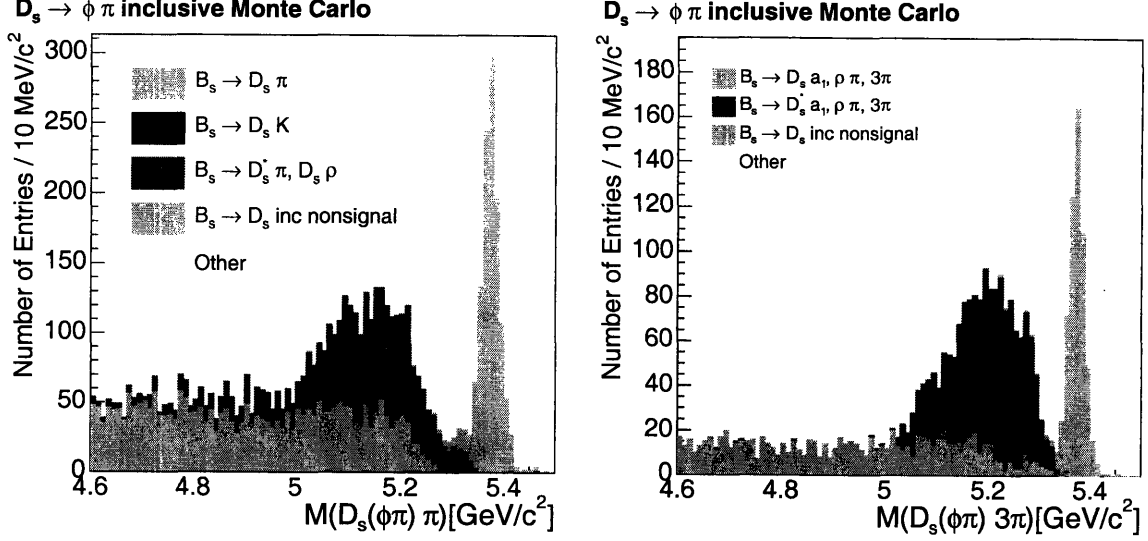


Figure 4-25: Decomposition of the inclusive background for  $B_s^0 \rightarrow D_s^- \pi^+$  (left plot) and  $B_s^0 \rightarrow D_s^- \pi^+ \pi^+ \pi^-$  (right plot) decays.

due to the mis-assignment of a kaon as a pion. There is a small contribution on the right of the signal mass peak due to the mis-reconstructed decays of  $\Lambda_b$ .

For all of the backgrounds under the mass peaks, it is essential to properly normalize their contributions. The procedure to do that is described in Section 4.4. The following sections give a complete, detailed description of the fits and motivate various components.

### 4.3.1 Fit models

When we talk about modeling of the background using Monte Carlo simulation, we mean that we look at the mass distribution of the background of interest and choose a function that describes the observed shape. The function is parametrized in terms of coefficients which are determined from a fit of the function to the Monte Carlo distribution. The choice of the function is often trivial. For example, in the case of the distribution for  $B$  signal we know that the natural width of the weak decay is negligible compared to the detector resolution. The resolution, since it is affected by a very large number of pseudo-random factors should be very well approximated by a normal distribution. But most of the time the choice of the fitting function is

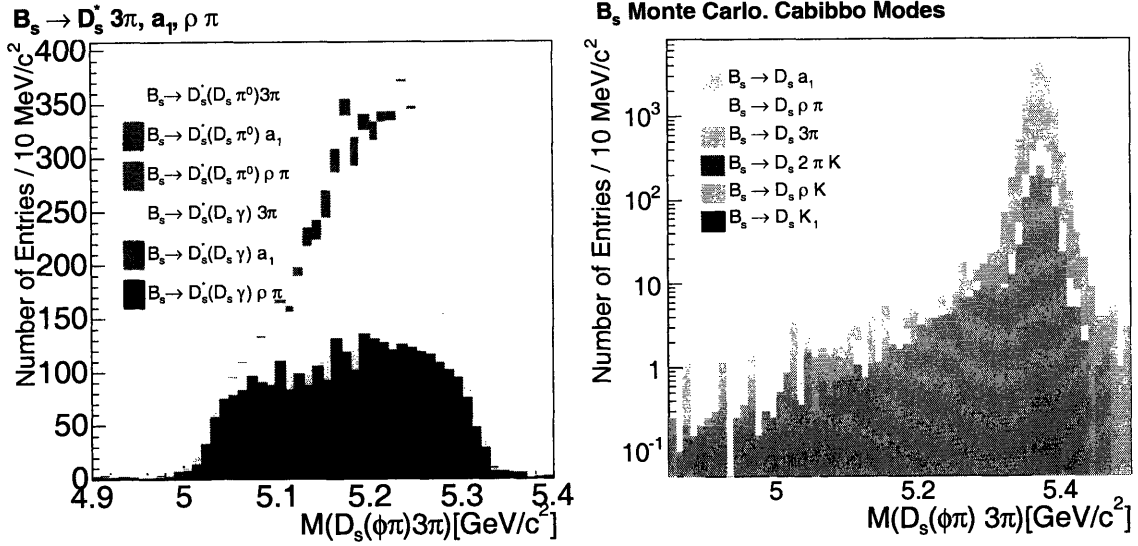


Figure 4-26: Left plot shows the structure of reflections below the mass peak for  $B_s^0 \rightarrow D_s^- \pi^+ \pi^+ \pi^-$  decay. Right plot shows the relative size of the signal and Cabibbo suppressed modes in the log scale.

up to the modeler. In this case, the fitting function, or “theory”, is only partially driven by physics arguments, but also partially by choosing a function that describes the observed shape best using the minimum number of parameters. In this case it is important to have some figure of merit, *i.e* the quantity that tells a “good fitting function” from a “bad fitting function”.

We use a binned  $\chi^2$  fit for creating templates. The fit is named after  $\chi^2$  which is a quantity that is being minimized. The  $\chi^2$  is defined as:

$$\chi^2 = \sum_i \left( \frac{y_i - f(x_i)}{\sigma_i} \right)^2, \quad (4.1)$$

where the sum is over bins in the histogram,  $y_i$  is the value of data,  $f(x_i)$  is the value of fitting function, and  $\sigma_i$  is the statistical uncertainty in bin  $i$ . In the case of the binned  $\chi^2$  fit, the choice of figure of merit of the fit is trivial. This quantity is the probability of the fit as determined from the fit  $\chi^2$  and its number of degrees of freedom.

From statistical theory we know that when we do a binned  $\chi^2$  fit, the resulting

$\chi^2$  is distributed according to a well known  $\chi^2$  distribution for the known number of degrees of freedom. The number of degrees of freedom is the number of bins in the fitted histogram minus the number of floating parameters in the fit. Once we know the  $\chi^2$  distribution, we calculate the fit probability by integrating the  $\chi^2$  distribution between  $-\infty$  and the observed value of  $\chi^2$ . The fit probability tells us how good our “theory” is, *i.e* how well the fitting function describes the observed shape.

For all main backgrounds it is important to be able to produce good fit probabilities, because ultimately large backgrounds affect the measured yields. For smaller backgrounds, like, for example,  $\Lambda_b$  background, good fit probability is not so critical as we know that our measured yields will not be affected by imprecise modeling of a small contribution. In the following paragraphs we describe the functions and their parameterizations, used to model signal and various backgrounds.

### **Fit model: $B$ Signal**

Our approach to modeling the signal is the same in all cases, so we deal with the general features of its implementation first. The signal is composed of two Gaussians with the same mean value. We use two Gaussians because we observe two contributions in the signal with different resolutions. The narrow Gaussian is used to describe the bulk of the events in the signal peak, and the wide Gaussian is used to describe “fat tails”. The signal fit function is:

$$F_S(m) = N_S \cdot [(1 - f)\mathcal{G}(m|\mu, \sigma) + f\mathcal{G}(m|\mu, k \cdot \sigma)], \quad (4.2)$$

where  $N_S$  is the overall normalization,  $(1 - f)$  is the fraction of the first Gaussian,  $\mu$  and  $\sigma$  are mean and width of the first Gaussian and  $k$  is a scale factor for the second Gaussian. While the parameters  $N_S$ ,  $\mu$  and  $\sigma$  are allowed to float, the parameters  $f$  and  $k$  are fixed from the Monte Carlo simulation. The values of these parameters are fixed to different values for each of the two  $B$  mesons modeled.

The fits are shown in Figures 4-27 through 4-30 (top left). Some of them show low resulting fit probability which is due to the presence of non-gaussian tails starting

from  $\approx 5 \sigma$  away from the mean of the distribution.

The signal yields in this analysis are extracted from the fits to the data distribution. Normally, if one uses single Gaussian to model signal in data, the number of signal events is calculated by integrating the Gaussian in  $\pm 2\sigma$  window which corresponds to approximately 95.45% of the integral between  $-\infty$  and  $+\infty$ . In our case, we use double Gaussian, and, in addition, there are non-gaussian tails in the signal Monte Carlo mass distributions.

To correct for the problem of non-gaussian tails in the signal Monte Carlo templates we implement a procedure of calculating yield in the adjustable mass window. The idea of the method is to choose the mass window such that the resulting integral within the chosen mass window is exactly 95.45% of the total. This method removes the systematics associated with non-gaussian tails because the mass window where the yield is calculated is adjusted in the presence of tails.

### Fit model: $B_s^0 \rightarrow D_s^- \pi^+$ background

For  $B_s^0$  decays, we do not expect to see a “dual spiked” satellite structure as we do for the  $B^0$  meson. The reason for this is the fact that the main contribution to such a structure would be coming from the  $B_s^0 \rightarrow D_s^{*-} \pi^+$  decays, but in this case the  $D_s^{*-}$  decays to  $D_s^- \gamma$  94% of the time. This produces a single, relatively broad structure as seen in our data.

The two decay modes that contribute to the peak below the  $B_s^0$  mass are the  $B_s^0 \rightarrow D_s^{*-} \pi^+$  and the  $B_s^0 \rightarrow D_s^- \rho^+$  decays. We create one template to model these two contributions, and another to model the contribution of all other  $B \rightarrow D_s^- X$  backgrounds.

We model the combined distribution for  $D_s^{*-} \pi^+$  and  $D_s^- \rho^+$  decays with an exponential convoluted with a Gaussian distribution and a Gaussian:

$$F_R(m) = N_R \cdot [(1 - f_r) \cdot \exp(m|\lambda_r) \otimes \mathcal{G}(m|\mu, \sigma_r) + f_r \cdot \mathcal{G}(m|\mu_r, \sigma_r)], \quad (4.3)$$

where  $N_R$  is the normalization,  $f_r$  is the fraction of the events in the Gaussian peak,



$\sigma_r$  is the width of the Gaussian and at the same time the width of the gaussian convolution exponent, and  $\lambda_r$  is the “lifetime” of the low-mass tail. In the fit to the data, all parameters are fixed to Monte Carlo values except for the normalization,  $N_R$ . The fit is shown in Figure 4-27 (top right).

We model the inclusive background from all other  $D_s^- X$  decays with a simple linear function:

$$F_C(m) = N_C \cdot \frac{2}{(\chi_c - L_c)^2} \cdot (\chi_c - m), \quad (4.4)$$

where  $N_C$  is the normalization,  $\chi_c$  is the cutoff point at which the linear function hits zero, and  $L_c$  is the lower boundary of the fitting region. There is an additional radiative tail which is modeled with an exponential function. The fit is shown in Figure 4-27 (second row left).

For the Cabibbo suppressed  $B_s^0 \rightarrow D_s^- K^+$  decays just below the mass peak we use a simple Gaussian function with all the parameters fixed from Monte Carlo simulation. The fit is shown in Figure 4-27 (second row right).

For the mis-reconstructed  $\Lambda_b$  background to the right of the main peak we find the following template:

$$F_\Lambda(m) = \frac{N_\Lambda}{(m - m_{0\Lambda})^2 + \frac{\gamma_\Lambda^2}{4}}, \quad (4.5)$$

where  $N_\Lambda$  is the norm,  $m_{0\Lambda}$  and  $\gamma_\Lambda$  are the mean and the width.

In the fit to the data, all parameters are fixed to Monte Carlo values including the normalization,  $N_\Lambda$  (fixing normalization is discussed in Section 4.4). The fit is shown in Figure 4-27 (bottom left). The plot shown has small statistics, but it is not critical for our measurement since the contribution of  $\Lambda_b$  background is small

The  $B^0 \rightarrow D\pi^+$  reflection under the  $B_s^0$  signal peak is fitted using a simple Gaussian function with all the parameters fixed from Monte Carlo simulation. The fit is shown in Figure 4-27 (bottom right).

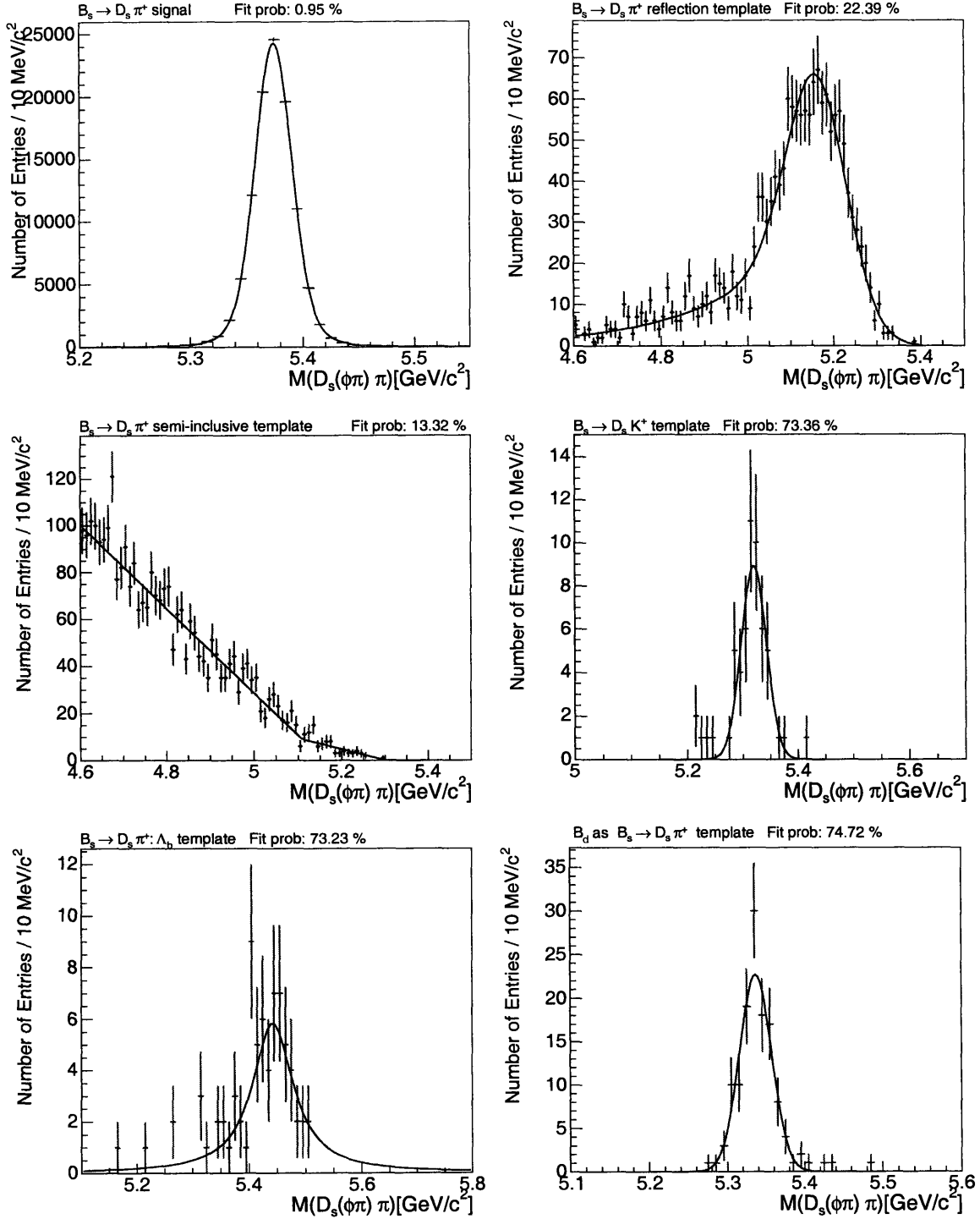


Figure 4-27: Templates used for fitting the  $B_s^0 \rightarrow D_s^- \pi^+$  mass distribution. Top left, double Gaussian is used to fit the signal. Top right, the structure due to  $D_s^{*-} \pi^+$  and  $D_s^- \rho$  decays. Second row left plot shows the distribution from other  $D_s^- X$  decays. Second row right plot shows the distribution for the Cabibbo suppressed  $D_s^- K^+$  decays. Bottom left plot shows  $\Lambda_b$  mis-reconstructed decays. Bottom right plot shows the distribution from the  $B^0$  meson reflection as  $D_s^- \pi^+$ .

### Fit model: $B_s^0 \rightarrow D_s^- \pi^+ \pi^+ \pi^-$ background

In the case of  $B_s^0 \rightarrow D_s^- \pi^+ \pi^+ \pi^-$  decay, as in  $B_s^0 \rightarrow D_s^- \pi^+$ , we do not expect to see a spiky satellite structure. The three decay modes that contribute to the peak below the  $B_s^0$  mass are the  $B_s^0 \rightarrow D_s^{*-} a_1$ ,  $B_s^0 \rightarrow D_s^{*-} \rho^0 \pi^+$  and  $B_s^0 \rightarrow D_s^{*-} \pi^+ \pi^+ \pi^-$  decays. We create one template to model this contribution, and another to model the contribution of all other  $B \rightarrow D_s^- X$  backgrounds.

We model the combined distribution for  $D_s^{*-} a_1$ ,  $D_s^{*-} \rho^0 \pi^+$  and  $D_s^{*-} \pi^+ \pi^+ \pi^-$  decays with an exponential convoluted with Gaussian distribution and a sum of three Gaussians:

$$f_R(m) = N_R \cdot [(1 - f_1 - f_2 - f_3) \cdot \exp(m|\lambda_r) \otimes \mathcal{G}(m|\mu_r, \sigma_r) + f_1 \cdot \mathcal{G}(m|\mu_1, \sigma_1) + f_2 \cdot \mathcal{G}(m|\mu_2, \sigma_2) + f_3 \cdot \mathcal{G}(m|\mu_3, \sigma_3)], \quad (4.6)$$

where  $N_R$  is the normalization,  $f_1, f_2$ , and  $f_3$  are the fractions of the events in the three Gaussians,  $\sigma_1, \sigma_2$ , and  $\sigma_3$  are the widths of the Gaussians,  $\sigma_r$  is the resolution of the “lifetime” distribution,  $\mu_1, \mu_2$ , and  $\mu_3$  are the means of the Gaussians, and  $\lambda_r$  is the “lifetime” of the low-mass tail. In the fit to the data, all parameters are fixed to Monte Carlo values except for the normalization,  $N_R$ . The resulting template is shown in Figure 4-28 (top right).

We model the continuum background from all other  $D_s^- X$  decays with a sum of two reversed exponentials with turnoffs and a linear function

$$F_C(m) = N_C \cdot [f_1 \cdot \mathcal{RE}(m|k_1, \mu_1, \tau_1) + f_2 \cdot \mathcal{RE}(m|k_2, \mu_2, \tau_2) + \frac{2.0}{(k_c - L_c)^2} \cdot (k_c - m)], \quad (4.7)$$

where  $N_C$  is an overall normalization. For the reversed exponential we use

$$\mathcal{RE}(m|k, \mu, \tau) = (1 - (m - 5.1) \cdot k) \cdot (1 - \exp((m - \mu)\tau)). \quad (4.8)$$

This is the definition of a reversed exponent with slope  $k$ , turnoff point at  $\mu$  and  $\tau$  is the parameter of the exponential decay. In the linear function  $k$  is a cutoff, and  $L$  is

the lower boundary of the fitting region. In the fit to the data, all the parameters of continuum background except overall normalization are fixed. The value of 5.1 enters the definition of the function as a “midpoint” of the fitting range [4.6;5.6] in Figure 4-28 (second row right).

For the Cabibbo suppressed  $B_s^0 \rightarrow D_s^- \pi^+ \pi^- K^+$  decays just below the mass peak we find the following template:

$$F_{\text{Cab}}(m) = N_{\text{Cab}} \cdot \exp(m|\lambda) \otimes \mathcal{G}(m|\mu, \sigma) \cdot \left( a + b \cdot m + \frac{1}{2} \cdot (\text{Erf}(m|\mu_1, \sigma_1) + \text{Erf}(-m|\mu_2, \sigma_2)) \right), \quad (4.9)$$

where  $N_{\text{Cab}}$  is the overall normalization,  $\lambda$  is the “lifetime” of the smeared exponential,  $\mu, \sigma$  are the mean and resolution of the smeared exponential,  $\mu_1, \sigma_1, \mu_2$ , and  $\sigma_2$  are the means and resolutions of the Error functions. The sum of the two Error functions with the opposite signs of their arguments creates the plateau shape where the function is constant within some range and does not modify the function it multiplies. Beyond this range the plateau function falls off to zero killing the long tails for the smeared exponential. In the fit to the data, all the parameters of the Cabibbo template are fixed including the overall normalization. The template is shown in Figure 4-28 (second row left).

For the  $\Lambda_b$  background to the right of the main peak we find the following template:

$$F_{\Lambda}(m) = \frac{N_{\Lambda}}{(m - m_{0\Lambda})^2 + \frac{\gamma_{\Lambda}^2}{4}}, \quad (4.10)$$

where  $N_{\Lambda}$  is the overall normalization,  $m_{0\Lambda}$  is the mean and  $\gamma_{\Lambda}$  is the width of Breit-Wigner function. All of the parameters of the template including the normalization are fixed from Monte Carlo simulation. The resulting template is shown in Figure 4-28 (bottom).

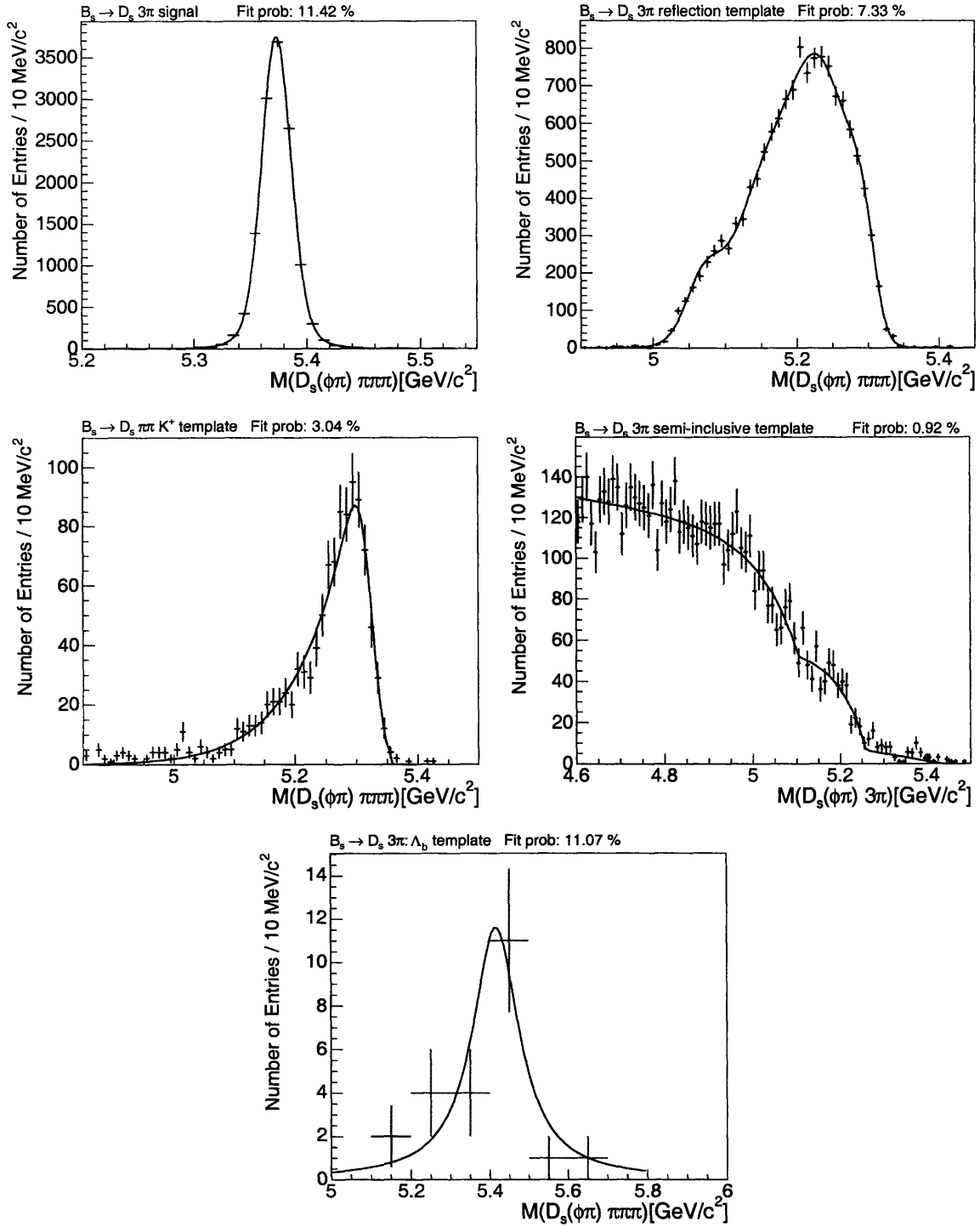


Figure 4-28: Templates used for fitting the  $B_s^0 \rightarrow D_s^- \pi^+ \pi^+ \pi^-$  mass distribution. Top left, double Gaussian is used to fit the signal. Top right, the structure due to  $D_s^{*-} \pi^+ \pi^+ \pi^-$ ,  $D_s^{*-} a_1$  and  $D_s^{*-} \rho^0 \pi^+$  decays. Second row left plot shows the distribution for the Cabibbo suppressed  $D_s^- 2\pi K$  decays. Second row right plot shows the distribution from other  $D_s^- X$  decays. Bottom plot shows the distribution from the mis-reconstructed  $\Lambda_b$  decays.

### Fit model: $B^0 \rightarrow D^- \pi^+$ background

The mass distribution for  $B^0$  decay candidates has a pronounced structure with two spikes, which we will also refer to as horns. The “spiky” structure here mostly originates from the  $B^0 \rightarrow D^{*-} \pi^+$  and the  $B^0 \rightarrow D^- \rho^+$  decays.

To make up the “spiky” template  $B^0 \rightarrow D^{*-} \pi^+$  and  $B^0 \rightarrow D^- \rho^+$  are combined. In this case we use the same function as for the  $B_s^0$  decays and add two Gaussians to generate the two spikes:

$$f_R = N_R \cdot [(1 - f_G - f_H) \cdot \exp(m|\lambda) \otimes \mathcal{G}(m|\mu, \sigma_R) + f_G \cdot \mathcal{G}(m|\mu - \nu, \sigma_R) + f_H \cdot (0.5 \cdot \mathcal{G}(m|\mu - \nu - \delta, \sigma_H) + 0.5 \cdot \mathcal{G}(m|\mu - \nu + \delta, \sigma_H))], \quad (4.11)$$

where  $N_R$  is the signal normalization,  $f_G$  and  $f_H$  are the fractions in the main Gaussian and the horns, respectively,  $\mu$  is the mean of the “lifetime distribution”,  $\nu$  is the offset of the mean of the main Gaussian, and  $\delta$  is the half-distance between the horns. The relevant widths are  $\sigma_R$  for the main Gaussian and the resolution of the “lifetime” convolution and  $\sigma_H$  for the spikes. All the above parameters are fixed from the Monte Carlo simulation, except for the normalization constant  $N_R$ . The template is shown in Figure 4-29 (top right).

We model the continuum background from all other  $D^- X$  decays with a sum of a reversed exponential with turnoff and a linear function

$$F_C(m) = N_C \cdot [f_1 \cdot \mathcal{RE}(m|k, \mu, \tau) + \frac{2.0}{(k_c - L_c)^2} \cdot (k_c - m)], \quad (4.12)$$

where  $N_C$  is an overall normalization,  $k$  is a reversed exponent slope,  $\mu$  and  $\tau$  are the parameters of exponential decay. In the linear function,  $k_c$  is a cutoff, and  $L_c$  is the lower boundary of the fitting region. The template is shown in Figure 4-29 (second row right).

For the Cabibbo suppressed  $B^0 \rightarrow D^- K^+$  decays just below the mass peak we

find the following template:

$$f_C(m) = N_{\text{Cab}} \cdot [(1 - f_1) \cdot \exp(m|\tau) \otimes \mathcal{G}(m|\mu, \sigma) + f_1 \cdot (a + b \cdot m + \frac{1}{2} \cdot (\text{Erf}(m|\mu_1, \sigma_1) + \text{Erf}(-m|\mu_2, \sigma_2))], \quad (4.13)$$

where  $N_{\text{Cab}}$  is the overall normalization,  $f_1$  is the fraction of smeared exponential,  $\tau$  is the “lifetime” of the smeared exponential,  $\mu$  and  $\sigma$  are the mean and resolution of the smeared exponential,  $\mu_1$ ,  $\sigma_1$ ,  $\mu_2$ , and  $\sigma_2$  are the means and resolutions of the Error functions. The sum of two Error functions with the opposite signs of the arguments creates a plateau shape where the function is constant within some range and falls off to zero beyond it. The parameters  $a$  and  $b$  are the parameters of the linear function. In the fit to the data, all parameters of the Cabibbo template are fixed including the overall normalization. The fit is shown in Figure 4-29 (second row left).

The template for the  $\Lambda_b$  background for the  $B^0$  decay is modeled with a sum of three Gaussians:

$$F_{\Lambda_b}(m) = N_{\Lambda_b} \cdot [(1 - f_1 - f_2) \cdot \mathcal{G}(m|\mu_1, \sigma_1) + f_1 \cdot \mathcal{G}(m|\mu_2, \sigma_2) + f_2 \cdot \mathcal{G}(m|\mu_3, \sigma_3)], \quad (4.14)$$

where  $N_{\Lambda_b}$  is the overall normalization,  $f_1$  and  $f_2$  are the fractions of Gaussians,  $\mu_1$ ,  $\mu_2$ , and  $\mu_3$  are the means, and  $\sigma_1$ ,  $\sigma_2$ , and  $\sigma_3$  are the widths of the Gaussians. The template is shown in Figure 4-29 (bottom left).

There is one additional background for the  $B^0$  decay not present in the  $B_s^0$  decays. This is the reflection of the  $B_s^0$  under the  $B^0$  peak due to the misidentification of a kaon as a pion. There is no inverse reflection of the  $B^0$  under the  $B_s^0$  because of the narrow mass window for the  $\phi^0$  resonance. We model this background with the same function used to model the  $\Lambda_b$  background (see Equation 4.14). In the fit to the data, all parameters are fixed to Monte Carlo simulation values including the overall normalization,  $N$ . The template is shown in Figure 4-29 (bottom right).

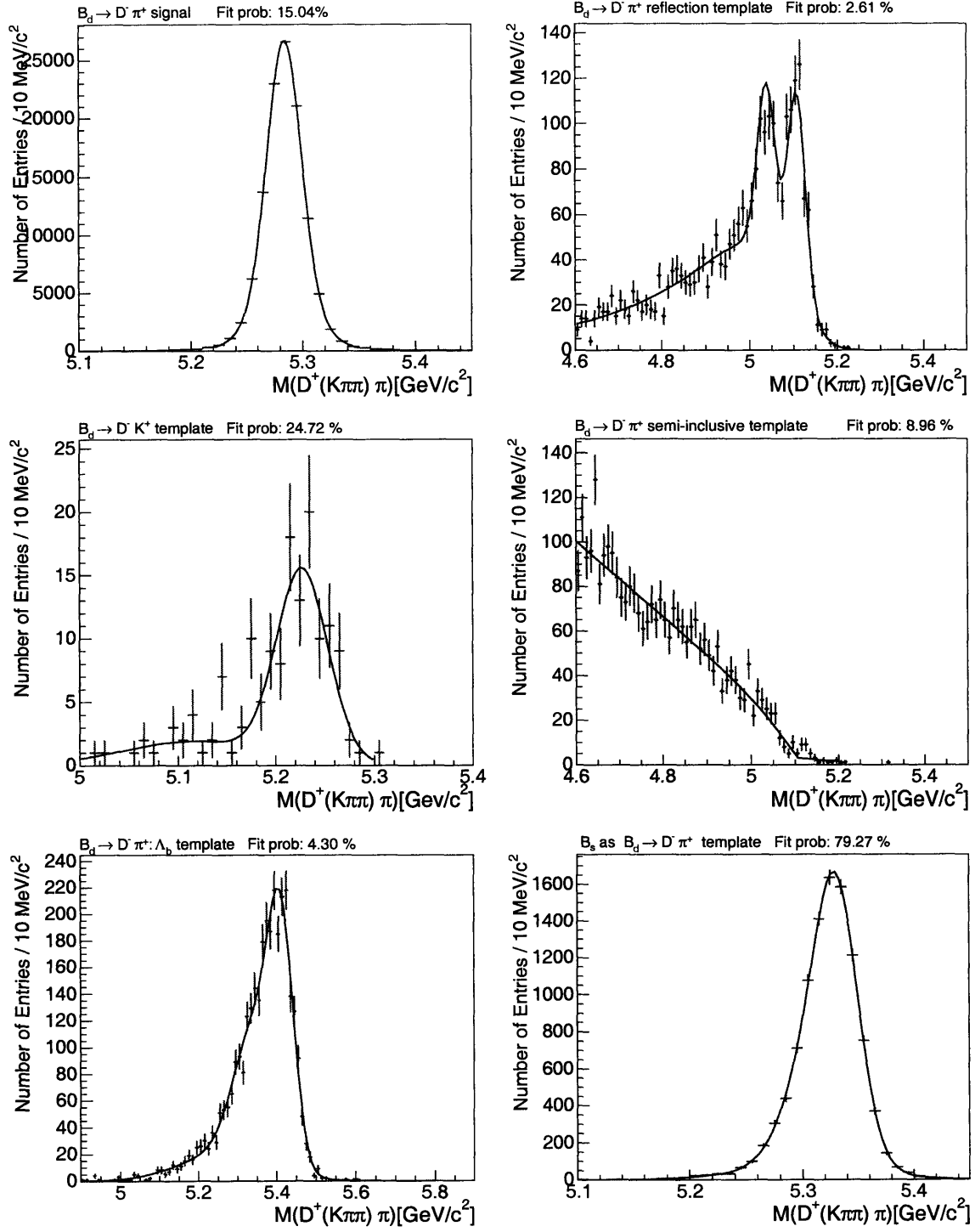


Figure 4-29: Templates used for fitting  $B^0 \rightarrow D^- \pi^+$  mass distribution. Top left, double Gaussian is used to fit the signal. Top right, structure due to  $D^{*-} \pi^+$  and  $D^{*-} \rho$  decays. Second row left plot shows the distribution from Cabibbo suppressed  $D^- K$  decays. Second row right plot shows the template from other  $D^+ X$  decays. Bottom left plot shows the distribution from the mis-reconstructed  $\Lambda_b$  decays. Bottom right plots shows the reflection from  $B_s^0 \rightarrow D_s^- \pi^+$  decay.



### Fit model: $B^0 \rightarrow D^- \pi^+ \pi^+ \pi^-$ background

The mass distribution for  $B^0 \rightarrow D^- \pi^+ \pi^+ \pi^-$  decay also has a pronounced reflection structure. The spiky structure comes from the  $B^0 \rightarrow D^{*-} \pi^+ \pi^+ \pi^-$ ,  $B^0 \rightarrow D^{*-} \rho^0 \pi^+$  and  $B^0 \rightarrow D^{*-} a_1$  decays. To make up the spiky template these three modes are combined. In this case we use a function made of three Gaussians:

$$F_R(m) = N_R \cdot [(1 - f_1 - f_2) \cdot \mathcal{G}(m|\mu, \sigma) + f_1 \cdot \mathcal{G}(m|\mu - \delta_1, \sigma_1) + f_2 \cdot \mathcal{G}(m|\mu - \delta_2, \sigma_2)], \quad (4.15)$$

where  $N_R$  is the overall normalization,  $f_1$  and  $f_2$  are the fractions of second and third Gaussians,  $\mu$  is the mean of the base Gaussian,  $\delta_1$  and  $\delta_2$  are the offsets of the horn Gaussians, and  $\sigma$ ,  $\sigma_1$ , and  $\sigma_2$  are the widths of the three Gaussians. All the above parameters are fixed from the Monte Carlo simulation, except the normalization constant,  $N_R$ . The template is shown in Figure 4-30 (top right).

We model the continuum background for  $B^0$  decay with the same parametrization of two reversed exponentials with similar cutoff distributions as used for the  $B_s^0$  as shown in Equation 4.8, but the values of the parameters are different. In the fit to the data, all the parameters of the continuum background except for the normalization are fixed. The template is shown in Figure 4-30 (second row right). The templates for the Cabibbo suppressed background for the  $B^0$  decay uses the same parametrization as used for  $B_s^0$ , but the values of the parameters are different. The template for this background is shown in Figure 4-30 (second row left).

There is a reflection of the  $B_s^0 \rightarrow D_s^- \pi^+ \pi^+ \pi^-$  under the  $B^0 \rightarrow D^- \pi^+ \pi^+ \pi^-$  peak due to the misidentification of a kaon as a pion. The background from  $B^0$  is not present under  $B_s^0$  because of the very narrow  $\phi^0$  mass width which effectively kills the reflection. We model this background with the sum of three Gaussians:

$$F_{B_s^0}(m) = N_{B_s^0} \cdot [(1 - f_1 - f_2) \cdot \mathcal{G}(m|\mu_1, \sigma_1) + f_1 \cdot \mathcal{G}(m|\mu_2, \sigma_2) + f_2 \cdot \mathcal{G}(m|\mu_3, \sigma_3)], \quad (4.16)$$

where  $N_{B_s^0}$  is the normalization,  $f_1$  and  $f_2$  are the fractions of the events,  $\sigma_1$ ,  $\sigma_2$ , and  $\sigma_3$  are the widths and  $\mu_1$ ,  $\mu_2$ , and  $\mu_3$  are the means of the Gaussians.

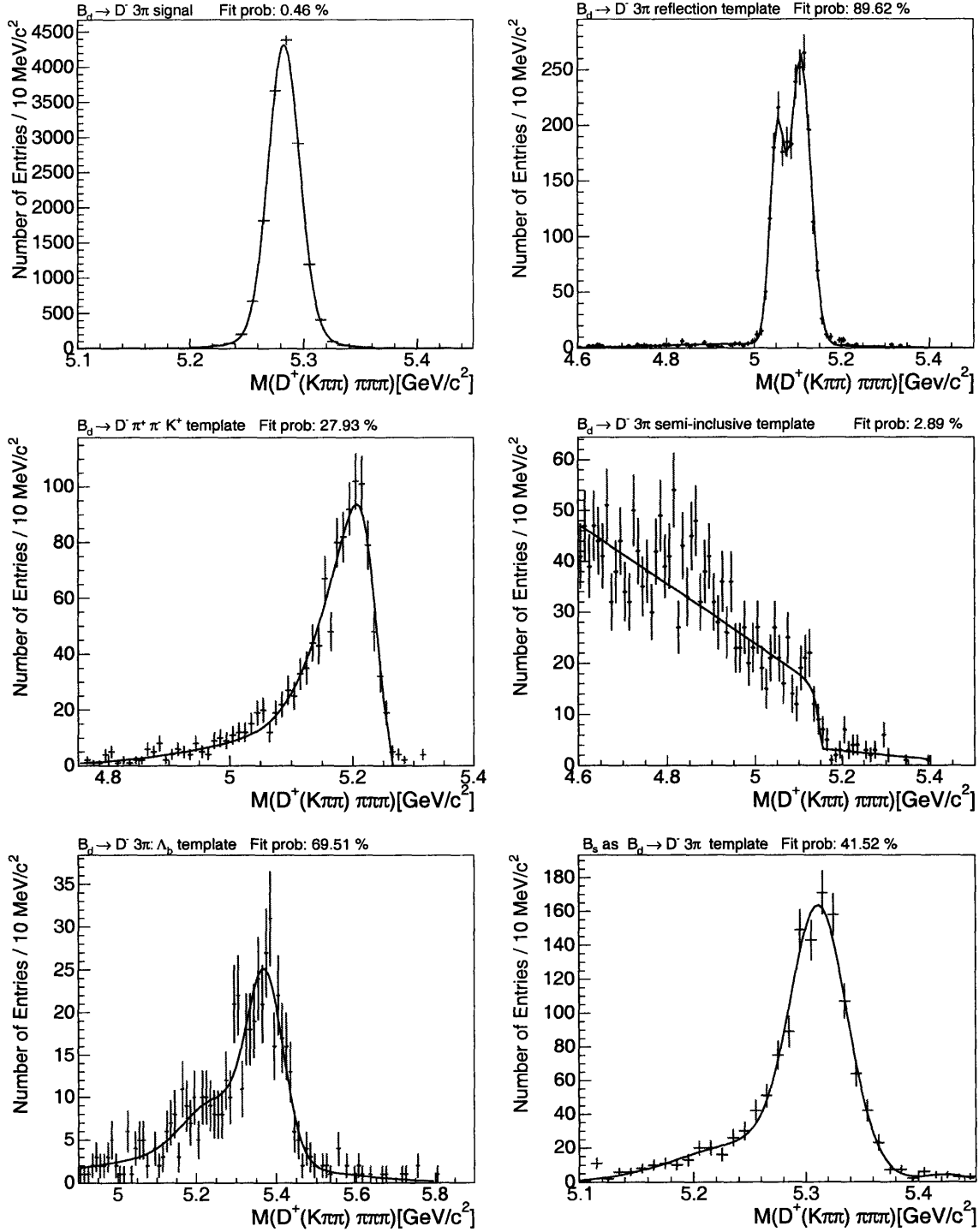


Figure 4-30: Templates used for fitting  $B^0 \rightarrow D^+ \pi^+ \pi^+ \pi^-$  mass distribution. Top left: double Gaussian is used to fit the signal. Top right: structure due to  $D^{*-} \pi^+ \pi^+ \pi^-$ ,  $D^{*-} a_1$  and  $D^{*-} \rho^0 \pi^+$  decays. Second row left plot shows the distribution from Cabibbo suppressed  $D^+ 2\pi K$  decays. Second row right plot shows the template from other  $D^+ X$  decays. Bottom left plot shows the template from mis-reconstructed  $\Lambda_b$  decays. Bottom right plot show the template from the  $B_s^0$  reflection.

In the fit to the data, all parameters are fixed to Monte Carlo simulation values including the overall normalization,  $N$ . The template is shown in Figure 4-30 (bottom right).

In conclusion, we have described the procedure of modeling signal and background for this analysis. In the following sections we cover the procedure of normalization of backgrounds contributing under signal peaks and describe data fitting results.

## 4.4 Normalization of backgrounds under signal

For all of the backgrounds that contribute under the signal mass peaks, it is important to properly normalize their contributions, since in the overall fits of the mass distributions, the fractions of these background are fixed. This section deals with the procedures, used to estimate the fractions of the backgrounds under the signal peaks. The input branching fractions that went into the calculation of the relative fractions of these background are listed in Table 4.2.

When we talk about fractions of normalizations of the backgrounds throughout this section, we actually mean the ratio. The nominator is the integral of the fitting function describing this background computed in the range of the  $B$  mass fit ( $[4.6;6.0]$  GeV/c<sup>2</sup>). The denominator is the fitted number of the signal events.

The backgrounds contributing under the main signal mass peaks are briefly described in Section 4.3. There is a contribution due to the Cabibbo suppressed  $B \rightarrow DK^+$  and  $B \rightarrow D\pi^+\pi^-K^+$  decays to the left of the signal peaks. For these decays a kaon is reconstructed as a pion, producing a bump in the mass distribution of the  $B \rightarrow D\pi^+$  and  $B \rightarrow D\pi^+\pi^+\pi^-$ , respectively. There is a contribution from  $B_s^0$  decays directly under the  $B^0$  mass peak. This is due to the kaon from the  $D_s^- \rightarrow \phi^0(K^+K^-)\pi^+$  decay being reconstructed as a pion. The inverse situation, where a pion from  $D^- \rightarrow K^+\pi^-\pi^-$  decay is reconstructed as a kaon is also possible, but in this case the size of this reflection is highly suppressed due to the very tight cut on the mass of the  $\phi^0$  resonance. However, since there is more  $B^0$  mesons produced than  $B_s^0$  mesons, this contribution has also to be taken into account. There

Branching Ratio	Value
$\mathcal{B}(\Lambda_c^+ \rightarrow p K^- \pi^+)$	$(5.0 \pm 1.3)\%$
$\mathcal{B}(D_s^- \rightarrow \phi^0 \pi^-)$	$(2.16 \pm 0.28)\%$
$\mathcal{B}(D^- \rightarrow K^+ \pi^- \pi^-)$	$(9.51 \pm 0.34)\%$
$\mathcal{B}(B^0 \rightarrow D_s^- \pi^+)$	$(2.2 \pm 0.7) \times 10^{-5}$
$\frac{\mathcal{B}(\Lambda_b \rightarrow \Lambda_c^+ \pi^+)}{\mathcal{B}(B^0 \rightarrow D^- \pi^+)}$	$0.82 \pm 0.25$
$\left[ \frac{\mathcal{B}(\Lambda_b \rightarrow \Lambda_c^+ \pi^+ \pi^+ \pi^-)}{\mathcal{B}(B^0 \rightarrow D^- \pi^+ \pi^+ \pi^-)} \right]^*$	$0.82 \pm 0.25$
$\frac{\mathcal{B}(B^0 \rightarrow D^- K^+)}{\mathcal{B}(B^0 \rightarrow D^- \pi^+)}$	$0.071 \pm 0.021$
$\left[ \frac{\mathcal{B}(B^0 \rightarrow D^- \pi^+ \pi^- K^+)}{\mathcal{B}(B^0 \rightarrow D^- \pi^+ \pi^+ \pi^-)} \right]^*$	$0.05 \pm 0.05$
$\left[ \frac{\mathcal{B}(B_s^0 \rightarrow D_s^- K^+)}{\mathcal{B}(B_s^0 \rightarrow D_s^- \pi^+)} \right]^*$	$0.071 \pm 0.021$
$\left[ \frac{\mathcal{B}(B_s^0 \rightarrow D_s^- \pi^+ \pi^- K^+)}{\mathcal{B}(B_s^0 \rightarrow D_s^- \pi^+ \pi^+ \pi^-)} \right]^*$	$0.05 \pm 0.05$

Table 4.2: Summary of measurements (assumptions) of branching fractions used for calculation of the fractions of background under  $B$  mass peaks. Items denoted by "\*" are the assumptions rather than measurements.

is a contribution from mis-reconstructed  $\Lambda_b \rightarrow \Lambda_c^+ \pi^-$  and  $\Lambda_b \rightarrow \Lambda_c^+ \pi^- \pi^- \pi^+$  decays. Proton from  $\Lambda_c^+ \rightarrow p^+ K^- \pi^+$  is reconstructed as a pion, and mis-reconstructed events contribute to the right of the signal peak.

#### 4.4.1 Cabibbo suppressed backgrounds

In the overall fit it is necessary to fix the normalization of the Cabibbo background together with the shape parameters. The reason being that if we let the normalization float then it is strongly correlated with the normalization of the main signal, normalizations of the continuum background, and the main reflection. For the case of  $B^0 \rightarrow D^- \pi^+$  decay, there is a measurement of ratio of  $\mathcal{B}(B^0 \rightarrow D^- K^+) / \mathcal{B}(B^0 \rightarrow D^- \pi^+)$  (see Table 4.2). Corrected for the relative reconstruction efficiency in these two modes, we calculate 5.8% for the fraction of  $B^0 \rightarrow D^- K^+$  background. The value of 5.8% means that the Cabibbo template shape integrated over the mass interval [4.6-6.0] GeV/c<sup>2</sup> should result in 5.8% of the fitted yield in the signal mass peak.

The  $B^0 \rightarrow D^- K^+$  decay is dominated by the tree-level "color-allowed" diagram, and there are neither "color-suppressed" nor "W-exchange" diagram present. For the

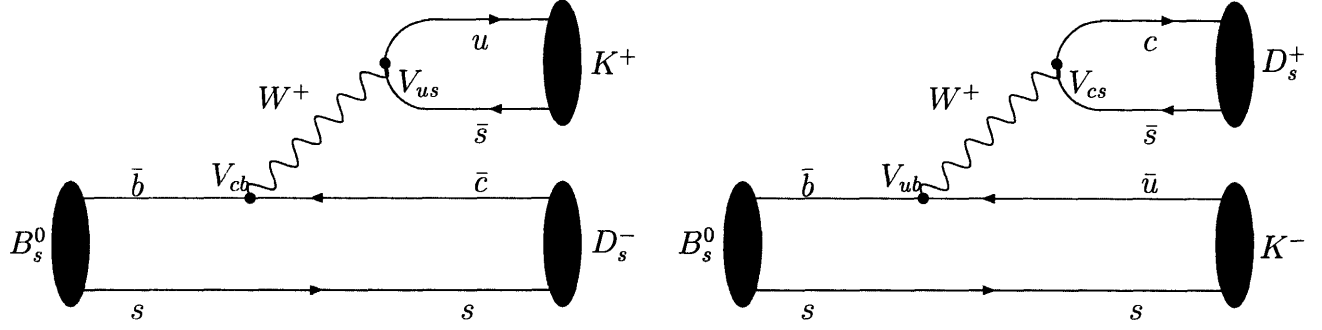


Figure 4-31: The tree-level Feynman diagrams describing  $B_s^0 \rightarrow D_s^- K^+$  decay.

$B_s^0 \rightarrow D_s^- K^+$  decay there is also no “color-suppressed” and “W-exchange” diagrams. However, there are two “color-allowed” diagrams which are the same order of magnitude in  $\lambda$  — the CKM parameter in Wolfenstein parametrization. The diagrams are shown in Figure 4-31. These two diagrams should be added together in the amplitude, and their phase difference is not known *a priori*. So the resulting branching fraction can be between 0 and 10%. We fix the normalization of the Cabibbo suppressed background  $B_s^0 \rightarrow D_s^- K^+$  under  $B_s^0 \rightarrow D_s^- \pi^+$  mass peak to the same 5.8% value for the fraction of Cabibbo suppressed background as for  $B^0$  decay. The issue of the uncertainty of this estimate is discussed in detail in Chapter 5.

There is an additional Cabibbo-like background under the  $B_s^0 \rightarrow D_s^- \pi^+$  mass peak due to  $B^0 \rightarrow D_s^- \pi^+$  decay. The motivation to add this background is due to the fact that Cabibbo suppressed decay of  $B^0 \rightarrow D_s^- \pi^+$  has a sizable branching fraction and could contribute under the mass peak since there are many more  $B^0$  mesons produced than  $B_s^0$  ( $f_d/f_s \gg 1$ ).

To estimate the fraction of  $B^0 \rightarrow D_s^- \pi^+$  background we use the following formula:

$$\frac{N(B^0 \text{ as } B_s^0 \rightarrow D_s^- \pi^+)}{N(B_s^0 \rightarrow D_s^- \pi^+)} = \frac{f_d}{f_s} \cdot \frac{1}{R(\pi)} \cdot \frac{\mathcal{B}(B^0 \rightarrow D_s^- \pi^+)}{\mathcal{B}(B^0 \rightarrow D^- \pi^+)} \cdot \frac{\epsilon(B^0 \rightarrow D_s^- \pi^+ \text{ as } B_s^0 \rightarrow D_s^- \pi^+)}{\epsilon(B_s^0 \rightarrow D_s^- \pi^+)}, \quad (4.17)$$

where  $R(D\pi)$  is the measurement of  $\mathcal{B}(B_s^0 \rightarrow D_s^- \pi^+)/\mathcal{B}(B^0 \rightarrow D^- \pi^+)$  with the fraction of this background fixed to zero, the ratio of branching fractions is known from PDG [2], and the ratio of efficiencies is obtained from the Monte Carlo simulation. In the end the fraction of this background is estimated to be 2.4%. This fraction is

added to the 5.8% fraction for the  $B_s^0 \rightarrow D_s^- K^+$  decay.

For the  $B \rightarrow D\pi^+\pi^+\pi^-$  decays there are no available measurements of the branching fractions of Cabibbo suppressed modes. Cabibbo suppressed modes in these case are:  $B \rightarrow D\pi^+\pi^-K^+$ ,  $B \rightarrow D\rho K^+$ , and  $B \rightarrow DK_1$ . Naively, we expect that the branching fractions of these decays should be scaled by the Cabibbo factor  $\frac{|V_{us}|^2}{|V_{ud}|^2} \approx 0.05$  with respect to corresponding signal decays. Neglecting a small difference in reconstruction efficiencies of the Cabibbo suppressed modes with respect to the main signal, we fix the normalization of Cabibbo background to be 5% of the main signal for both  $B_s^0 \rightarrow D_s^- \pi^+ \pi^+ \pi^-$  and  $B^0 \rightarrow D^- \pi^+ \pi^+ \pi^-$  fits. We discuss the issue of the uncertainty of this estimate in Chapter 5.

#### 4.4.2 $\Lambda_b$ background

There are also background contributions from mis-reconstructed  $\Lambda_b \rightarrow \Lambda_c^+ \pi^-$  and  $\Lambda_b \rightarrow \Lambda_c^+ \pi^- \pi^- \pi^+$  decays in the high mass range to the right of the main signal peak. It is possible to estimate the fraction of  $\Lambda_b$  background under the signal mass peak using inputs from Monte Carlo simulation and recent measurements. Therefore we generate  $\Lambda_b \rightarrow \Lambda_c^+ \pi^-$  and  $\Lambda_b \rightarrow \Lambda_c^+ \pi^- \pi^- \pi^+$  modes with  $\Lambda_c^+ \rightarrow p^+ K^- \pi^+$  and apply the following formulae for the fraction of  $\Lambda_b$  under  $B_s^0$ :

$$\frac{N(\Lambda_b \rightarrow \Lambda_c^+ \pi^-)}{N(B_s^0 \rightarrow D_s^- \pi^+)} = \frac{R(\Lambda_b \rightarrow \Lambda_c^+ \pi^-)}{R(\pi)} \cdot \frac{\mathcal{B}(\Lambda_c^+ \rightarrow p^+ K^- \pi^+)}{\mathcal{B}(D_s^- \rightarrow \phi^0 \pi^-)} \cdot \frac{\epsilon(\Lambda_b \text{ as } B_s^0 \rightarrow D_s^- \pi^+)}{\epsilon(B_s^0 \rightarrow D_s^- \pi^+)}, \quad (4.18)$$

$$\frac{N(\Lambda_b \rightarrow \Lambda_c^+ 3\pi)}{N(B_s^0 \rightarrow D_s^- 3\pi)} = \frac{R(\Lambda_b \rightarrow \Lambda_c^+ 3\pi)}{R(D3\pi)} \cdot \frac{\mathcal{B}(\Lambda_c^+ \rightarrow p^+ K^- \pi^+)}{\mathcal{B}(D_s^- \rightarrow \phi^0 \pi^-)} \cdot \frac{\epsilon(\Lambda_b \text{ as } B_s^0 \rightarrow D_s^- 3\pi)}{\epsilon(B_s^0 \rightarrow D_s^- 3\pi)}, \quad (4.19)$$

where  $R(\Lambda_b \rightarrow \Lambda_c^+ \pi^-)$  is  $\frac{f_\Lambda}{f_d} \cdot \frac{\mathcal{B}(\Lambda_b \rightarrow \Lambda_c^+ \pi^-)}{\mathcal{B}(B^0 \rightarrow D^- \pi^+)}$ ,  $R(\pi)$  is  $\frac{f_s}{f_d} \cdot \frac{\mathcal{B}(B_s^0 \rightarrow D_s^- \pi^+)}{\mathcal{B}(B^0 \rightarrow D^- \pi^+)}$ , and the  $\epsilon$ 's are the Monte Carlo simulation efficiencies to reconstruct the  $B$  meson, and the efficiency to mis-reconstruct  $\Lambda$  as  $B$  meson.

The first ratio of branching fractions  $R(\Lambda_b \rightarrow \Lambda_c^+ \pi^-)$  was measured at CDF [62]. For the ratio  $R(\Lambda_b \rightarrow \Lambda_c^+ \pi^- \pi^- \pi^+)$  we hypothesize that is equal to  $R(\Lambda_b \rightarrow \Lambda_c^+ \pi^-)$ . The ratios  $R(D\pi) = \mathcal{B}(B_s^0 \rightarrow D_s^- \pi^+)/\mathcal{B}(B^0 \rightarrow D^- \pi^+)$  and  $R(D3\pi) = \mathcal{B}(B_s^0 \rightarrow D_s^- \pi^+ \pi^+ \pi^-)/\mathcal{B}(B^0 \rightarrow D^- \pi^+ \pi^+ \pi^-)$  are our measurement results if we fix the fraction

of  $\Lambda_b$  background to zero. We need to set the fractions of the  $\Lambda_b$  background to zero for the original values of  $R(D\pi)$  and  $R(D3\pi)$ . After that we obtain the fraction of  $\Lambda_b$  background and reevaluate  $R(D\pi)$  and  $R(D3\pi)$ . This is very similar to perturbation approach in quantum mechanics. The whole approach is only valid if the size of the perturbation is small compared to the main effect. In practice we do the iteration only once, because the size of the  $\Lambda_b$  background is very small compared to the signal. In the end, the fractions of  $\Lambda_b$  backgrounds were calculated to be 2.2% under  $B^0 \rightarrow D^-\pi^+$  mass peak and 2.0% under  $B^0 \rightarrow D^-\pi^+\pi^+\pi^-$  mass peak.

The formulae to estimate the fraction of  $\Lambda_b$  background under  $B^0$  peak take the following form :

$$\frac{N(\Lambda_b \rightarrow \Lambda_c^+ \pi^-)}{N(B^0 \rightarrow D^-\pi^+)} = R(\Lambda_b \rightarrow \Lambda_c^+ \pi^-) \cdot \frac{\mathcal{B}(\Lambda_c^+ \rightarrow p^+ K^- \pi^+)}{\mathcal{B}(D^- \rightarrow K^+ \pi^- \pi^-)} \cdot \frac{\epsilon(\Lambda_b \text{ as } B^0 \rightarrow D^-\pi^+)}{\epsilon(B^0 \rightarrow D^-\pi^+)} \quad (4.20)$$

$$\frac{N(\Lambda_b \rightarrow \Lambda_c^+ 3\pi)}{N(B^0 \rightarrow D^- 3\pi)} = R(\Lambda_b \rightarrow \Lambda_c^+ 3\pi) \cdot \frac{\mathcal{B}(\Lambda_c^+ \rightarrow p^+ K^- \pi^+)}{\mathcal{B}(D^- \rightarrow K^+ \pi^- \pi^-)} \cdot \frac{\epsilon(\Lambda_b \text{ as } B^0 \rightarrow D^- 3\pi)}{\epsilon(B^0 \rightarrow D^- 3\pi)} \quad (4.21)$$

The fraction of  $\Lambda_b$  was calculated to be 0.5% under  $B_s^0 \rightarrow D_s^- \pi^+$  mass peak and 0.4% under  $B_s^0 \rightarrow D_s^- \pi^+ \pi^+ \pi^-$  mass peak.

#### 4.4.3 $B_s^0$ reconstructed as $B^0$

To estimate the fraction of  $B_s^0$  background under  $B^0$  mass peak we use the following formulae:

$$\frac{N(B_s^0 \text{ as } B^0 \rightarrow D^-\pi^+)}{N(B^0 \rightarrow D^-\pi^+)} = R(D\pi) \cdot \frac{\mathcal{B}(D_s^- \rightarrow \phi^0 \pi^-, K^* K^-)}{\mathcal{B}(D^- \rightarrow K^+ \pi^- \pi^-)} \cdot \frac{\epsilon(B_s^0 \text{ as } B^0 \rightarrow D^-\pi^+)}{\epsilon(B^0 \rightarrow D^-\pi^+)} \quad (4.22)$$

$$\frac{N(B_s^0 \text{ as } B^0 \rightarrow D^- 3\pi)}{N(B^0 \rightarrow D^- 3\pi)} = R(D3\pi) \cdot \frac{\mathcal{B}(D_s^- \rightarrow \phi^0 \pi^-, K^* K^-)}{\mathcal{B}(D^- \rightarrow K^+ \pi^- \pi^-)} \cdot \frac{\epsilon(B_s^0 \text{ as } B^0 \rightarrow D^- 3\pi)}{\epsilon(B^0 \rightarrow D^- 3\pi)}, \quad (4.23)$$

Decay	$B^0 \rightarrow D^- \pi$	$B^0 \rightarrow D^- 3\pi$	$B_s^0 \rightarrow D_s^- \pi$	$B_s^0 \rightarrow D_s^- 3\pi$
Events	$8098 \pm 114$	$3288 \pm 76$	$494 \pm 28$	$159 \pm 17$

Table 4.3: Fit results for the number of signal events. Only statistical uncertainties are quoted.

where  $R(D\pi)$  and  $R(D3\pi)$  are our measurements with fraction of  $B_s^0$  background fixed to zero (again using perturbation approach as in the previous section), the ratio of branching fractions is known and the ratio of efficiencies is extracted from Monte Carlo simulation. In the end we estimate the fraction of  $B_s^0$  background under  $B^0 \rightarrow D^- \pi^+$  to be 1.5% and under  $B^0 \rightarrow D^- \pi^+ \pi^+ \pi^-$  mass peak 2.0%, respectively.

## 4.5 $B$ meson yields

We reconstruct  $B$  mesons using optimized selection requirements described in Section 3.3.6 and apply fits using the analytical templates described in Section 4.3.1 to the spectra. The resulting fits are shown in Figures 4-32 and 4-33, and the corresponding fit template parameters are shown in Tables A.1 through A.27 of the Appendix A. The number of candidates extracted from the fits are listed in Table 4.3. The uncertainties quoted in the tables are statistical only. To determine the systematic uncertainty on the number of candidates, an independent study is performed.

We observe many more  $B^0$  candidates than  $B_s^0$  candidates due to high  $f_d/f_s$  — ratio of production fractions of  $B^0$  and  $B_s^0$  mesons, but  $B_s^0$  yields are generally cleaner. This is due to requiring that the reconstructed mass of the  $\phi^0 \rightarrow K^+ K^-$  be within a tight window around the world average value. The  $B^0$  decay does not have an equivalent requirement. It is also interesting to note that we observe more  $B \rightarrow D\pi^+$  candidates than  $B \rightarrow D\pi^+ \pi^+ \pi^-$  candidates. Although their branching ratios are comparable, the trigger and reconstruction efficiency of the six track candidates is much lower than that of their four track counterparts.



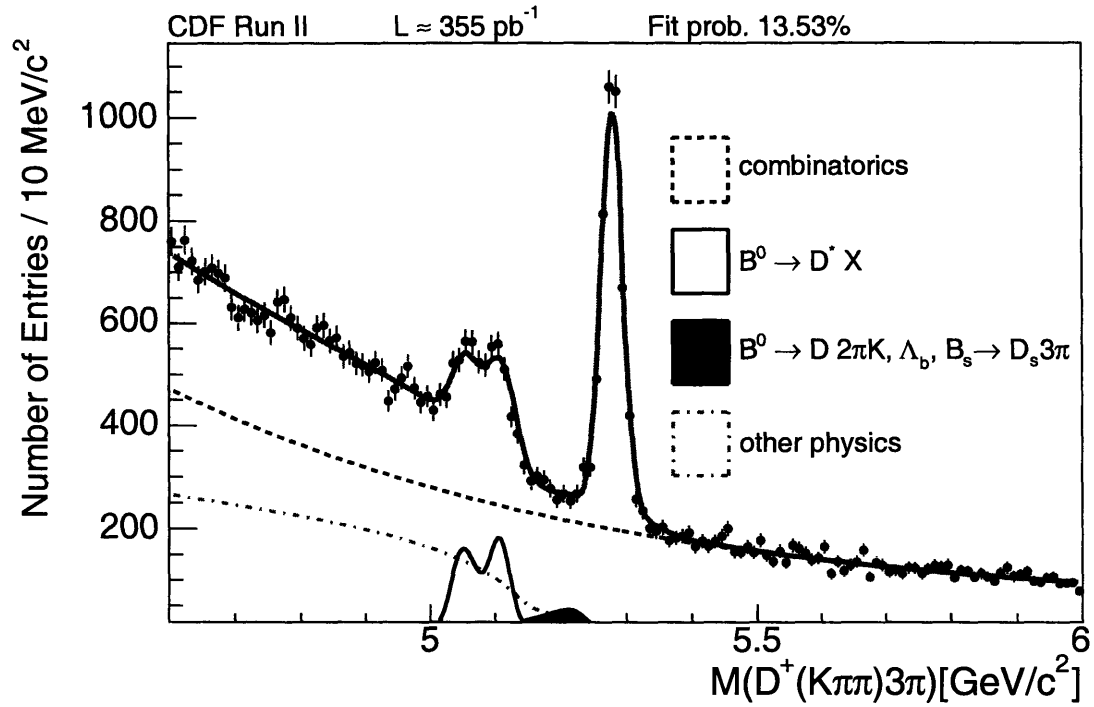
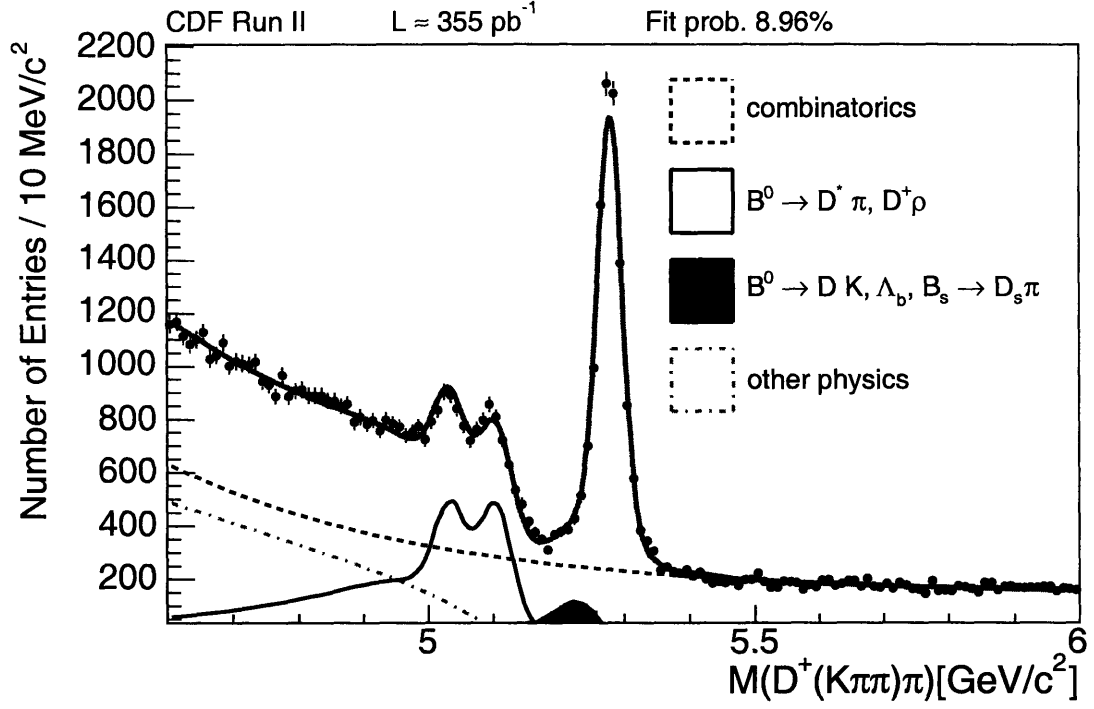


Figure 4-32: The fit result yields  $8098 \pm 114$  for the decay  $B^0 \rightarrow D^- \pi^+$  and  $3288 \pm 76$  for the decay  $B^0 \rightarrow D^- \pi^+ \pi^+ \pi^-$ .

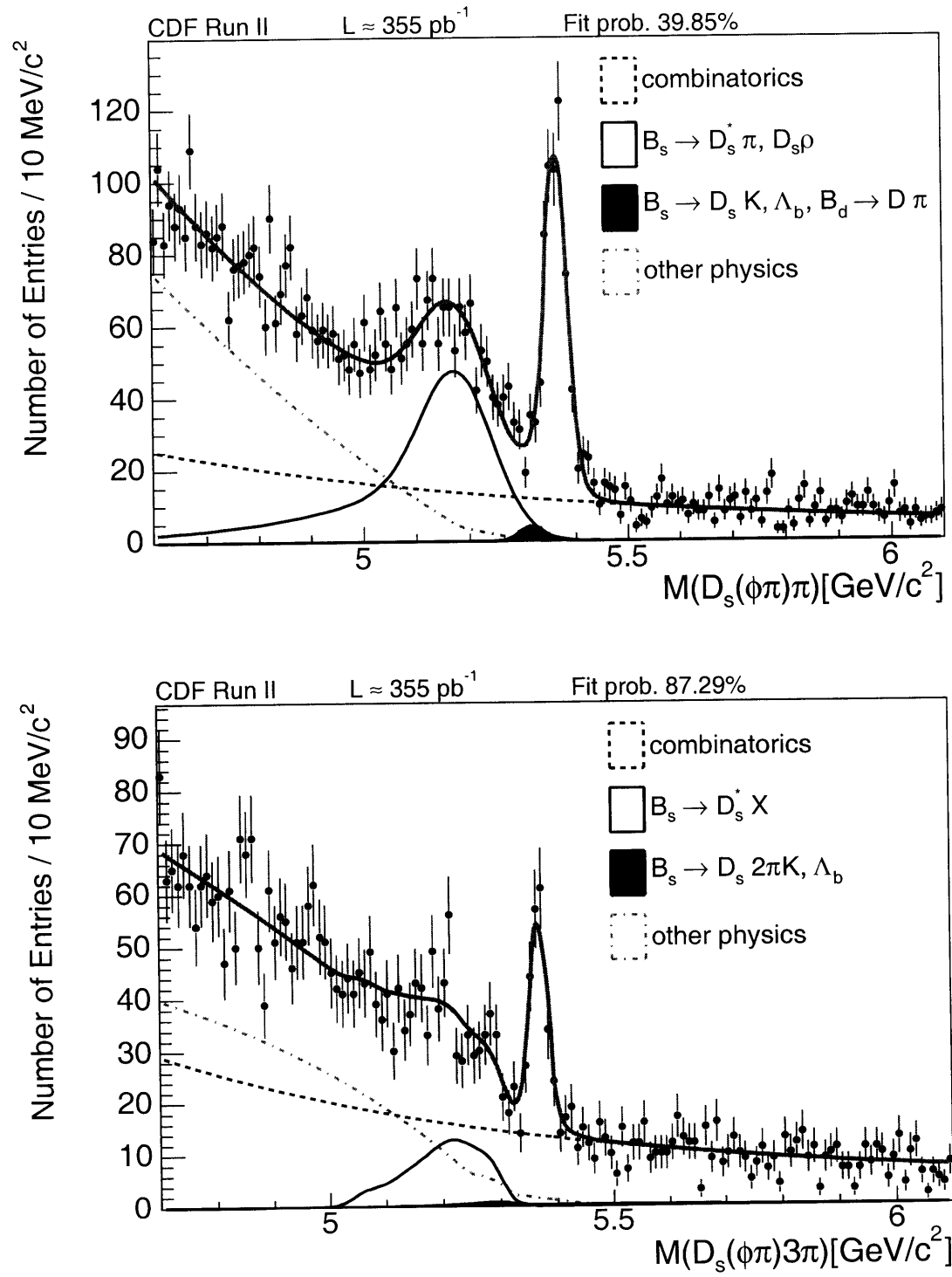


Figure 4-33: The fit result yields  $494 \pm 28$  for the decay  $B_s^0 \rightarrow D_s^- \pi^+$  and  $159 \pm 17$  for the decay  $B_s^0 \rightarrow D_s^- \pi^+ \pi^+ \pi^-$ .

## 4.6 Ratio of Monte Carlo efficiencies

In Section 4.1 we studied the success of reproducing different quantities in the Monte Carlo simulation. In this section, we focus on the various efficiencies that we extract from the simulation.

The detector and analysis efficiencies for finding different  $B$  mesons are not the same. We are interested in understanding the difference in efficiency for detecting  $B_s^0$  decays with respect to  $B^0$  decays and then use the obtained numbers to correct our raw numbers of detected  $B_s^0$  and  $B^0$  decays to give us ratios of branching fractions. The total efficiency is:

$$\epsilon_{\text{tot}} = \frac{N_{\text{analysis}}}{N_{\text{generated}}} = \epsilon_{\text{trig}} \cdot \epsilon_{\text{reco}}. \quad (4.24)$$

The total efficiency takes into account all of the trigger effects, effects of the reconstruction and effects of the analysis cuts applied. For our measurement it is essential to check that the ratio of efficiencies does not change much with trigger conditions. If this ratio is stable, the analysis is essentially robust against any potentially poorly simulated trigger or detector effects, and we expect to have small systematic uncertainties from the Monte Carlo simulation. The study of the ratios of efficiencies as a function of a run number is described in detail in Chapter 5.

As a practical matter, the data set is a collection of files corresponding to certain run numbers and the luminosities they represent. In order to reproduce this aspect of real data, the number of events we generate for each run in our Monte Carlo simulation is proportional to their corresponding luminosity, that is, the  $\overline{\epsilon_{\text{tot}}}$  — the luminosity weighted efficiency is defined as

$$\overline{\epsilon_{\text{tot}}} = \frac{\sum_i \mathcal{L}^i \epsilon_{\text{tot}}^i}{\sum_i \mathcal{L}^i}, \quad (4.25)$$

where  $\mathcal{L}^i$  is the luminosity, and  $\epsilon_{\text{tot}}^i$  is the efficiency of the run  $i$ .

There is a problem with efficiency defined in Equation 4.25 because it does not take into account prescaling of the data, that is, the fact that effective luminosity of

—	$B^0 \rightarrow D^- \pi^+$	$B_s^0 \rightarrow D_s^- \pi^+$	$B^0 \rightarrow D^- 3\pi$	$B_s^0 \rightarrow D_s^- 3\pi$
Generated	59999335	59999335	59999335	59999335
Passed	111470	101611	14819	12062
$\epsilon^{tot}$ (%)	$0.1858 \pm 0.0006$	$0.1694 \pm 0.0005$	$0.0247 \pm 0.0002$	$0.0201 \pm 0.0002$

Table 4.4: The Luminosity averaged and prescaled efficiencies for the combined B\_CHARM and B\_CHARM.LOWPT triggers. Only statistical uncertainties are quoted.

the run might be smaller than the total luminosity  $\mathcal{L}^i$ . To obtain the correct number for the total combined efficiency for the B\_CHARM.LOWPT and B\_CHARM triggers one also needs to take into account the effective prescales of the corresponding runs. The CDF Monte Carlo package does not perform prescale simulation for the triggers, so we obtain the effective prescales for the B\_CHARM.LOWPT and B\_CHARM triggers from the database for each run that made it into our good run list. The corresponding trigger efficiency is scaled by the effective prescale factor. Then the total efficiency is given by

$$\overline{\epsilon}_{tot} = \frac{\sum_i \mathcal{L}^i p_{\text{bcharm}}^i \epsilon_{\text{totbcharm}}^i}{\sum_i \mathcal{L}^i} + \frac{\sum_i \mathcal{L}^i g_{\text{lowpt}}^i \epsilon_{\text{totlowpt}}^i}{\sum_i \mathcal{L}^i} \quad (4.26)$$

where  $p_{\text{bcharm}}^i$  and  $g_{\text{lowpt}}^i$  are the effective per run prescales of the two datasets. The average prescale factor for the B\_CHARM dataset is about 1.1 which means that about 10% of the events in that dataset are being prescaled away. The average prescale factor for the B\_CHARM.LOWPT dataset is close to 3. The individual prescale factors for different runs take a variety of values with older runs with smaller instantaneous luminosities being close to 1, and for the newer runs, especially for the B\_CHARM.LOWPT data, being as much as 10. To demonstrate how the prescale procedure works we compare the run ranges used in prescaled Monte Carlo simulation and data. We do this for both  $B \rightarrow D\pi^+$  and  $B \rightarrow D\pi^+\pi^+\pi^-$  channels. Before the prescaling was implemented the shapes of the distributions we see in Monte Carlo and data were not the same. The results of the comparison is shown in Figures 4-34 and 4-35. We see the same ranges and shapes of distributions used in two Monte Carlo simulations and the Monte Carlo simulation shape represents that of data. The averaged prescaled efficiencies are listed in Table 4.4.

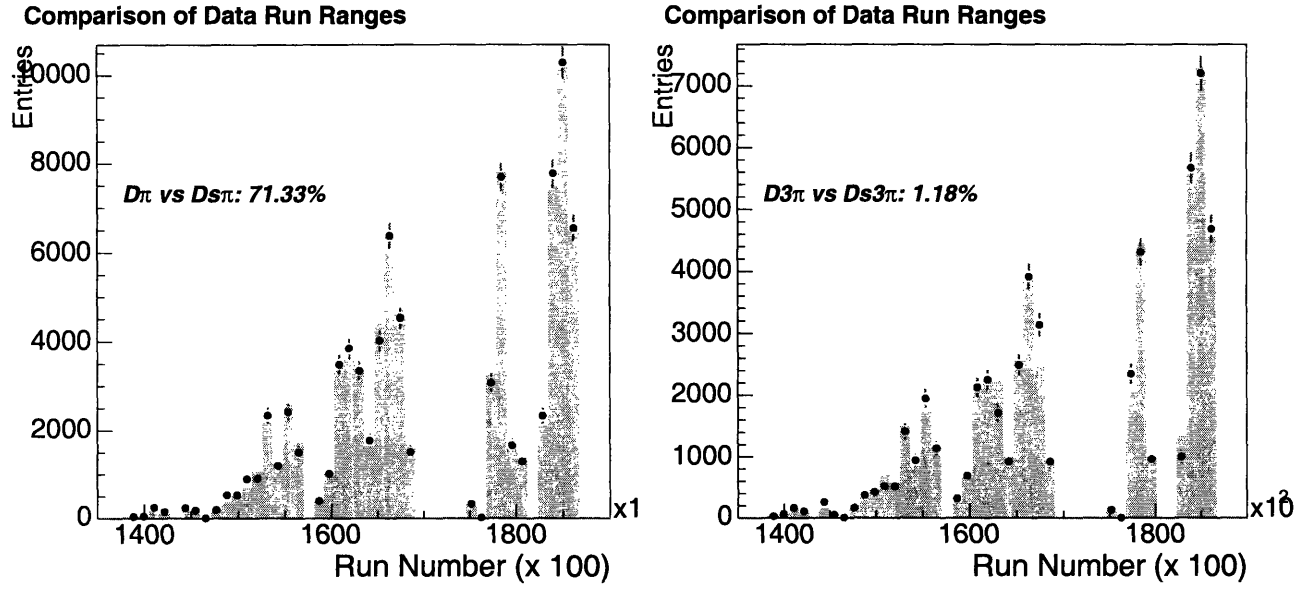


Figure 4-34: The comparison of run profile distributions in data for  $B^0 \rightarrow D^- \pi^+$  versus  $B_s^0 \rightarrow D_s^- \pi^+$  (left) and  $B^0 \rightarrow D^- \pi^+ \pi^+ \pi^-$  versus  $B_s^0 \rightarrow D_s^- \pi^+ \pi^+ \pi^-$  (right) decay.

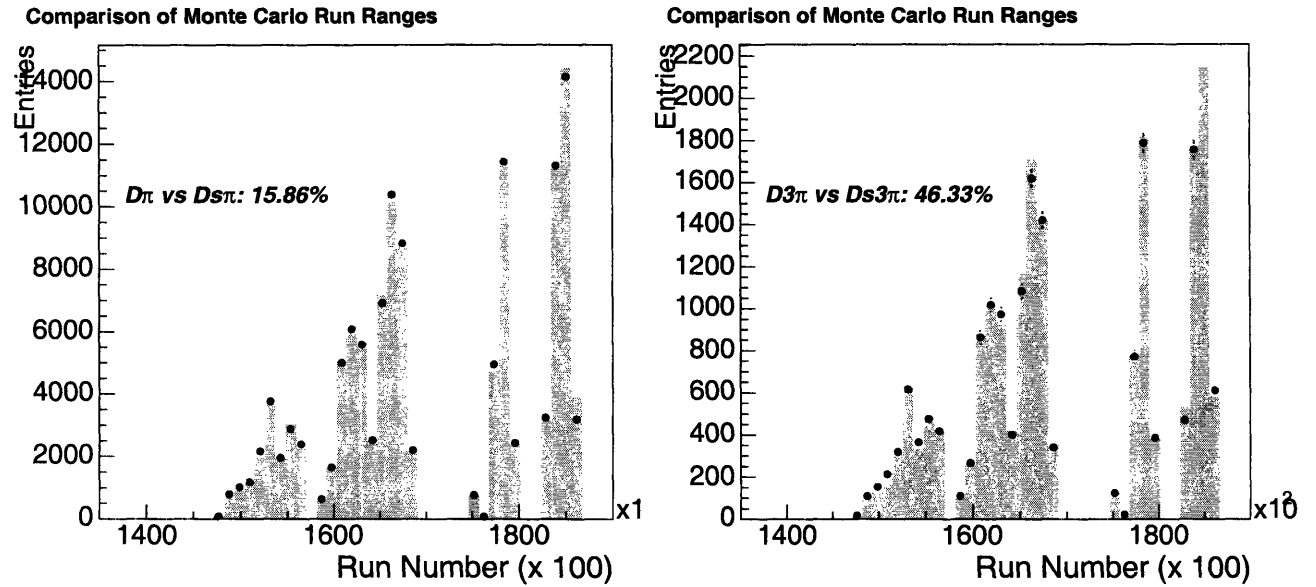


Figure 4-35: The comparison of run profile distribution in Monte Carlo for  $B^0 \rightarrow D^- \pi^+$  versus  $B_s^0 \rightarrow D_s^- \pi^+$  (left) and  $B^0 \rightarrow D^- \pi^+ \pi^+ \pi^-$  versus  $B_s^0 \rightarrow D_s^- \pi^+ \pi^+ \pi^-$  (right) decay.

Branching Ratio	Value
$D^- \rightarrow K^+ \pi^- \pi^-$	$[9.51 \pm 0.34] \cdot 10^{-2}$
$D_s^- \rightarrow \phi^0 (K^+ K^-) \pi^-$	$[2.16 \pm 0.28] \cdot 10^{-2}$
$f_s/f_d$	$0.259 \pm 0.038$

Table 4.5: External parameters used for calculations of the relative rates of  $B$  mesons [2].

## 4.7 Ratio of branching fractions

Having measured the rates of different  $B$ 's in the data, and having estimated the efficiencies of the trigger and analysis software, we can deduce the ratios of branching fractions in our dataset.

We apply the formulae:

$$\frac{f_s}{f_d} \cdot \frac{\mathcal{B}(B_s^0 \rightarrow D_s^- \pi^+)}{\mathcal{B}(B^0 \rightarrow D^- \pi^+)} = \frac{N(B_s^0)}{N(B^0)} \cdot \frac{\epsilon(B^0 \rightarrow D^- \pi^+)}{\epsilon(B_s^0 \rightarrow D_s^- \pi^+)} \cdot \frac{\mathcal{B}(D^- \rightarrow K^+ \pi^- \pi^-)}{\mathcal{B}(D_s^- \rightarrow \phi^0 \pi^-) \mathcal{B}(\phi^0 \rightarrow K^+ K^-)} \quad (4.27)$$

$$\frac{f_s}{f_d} \cdot \frac{\mathcal{B}(B_s^0 \rightarrow D_s^- \pi^+ \pi^+ \pi^-)}{\mathcal{B}(B^0 \rightarrow D^- \pi^+ \pi^+ \pi^-)} = \frac{N(B_s^0)}{N(B^0)} \cdot \frac{\epsilon(B^0 \rightarrow D^- \pi^+ \pi^+ \pi^-)}{\epsilon(B_s^0 \rightarrow D_s^- \pi^+ \pi^+ \pi^-)} \cdot \frac{\mathcal{B}(D^- \rightarrow K^+ \pi^- \pi^-)}{\mathcal{B}(D_s^- \rightarrow \phi^0 \pi^-) \mathcal{B}(\phi^0 \rightarrow K^+ K^-)} \quad (4.28)$$

Using values of efficiencies found in Table 4.4, rates of  $B$  mesons in Table 4.3, and using inputs in Table 4.5, we obtain:

$$\frac{f_s}{f_d} \cdot \frac{\mathcal{B}(B_s^0 \rightarrow D_s^- \pi^+)}{\mathcal{B}(B^0 \rightarrow D^- \pi^+)} = 0.292 \pm 0.020(\text{stat.}) \quad (4.29)$$

$$\frac{f_s}{f_d} \cdot \frac{\mathcal{B}(B_s^0 \rightarrow D_s^- \pi^+ \pi^+ \pi^-)}{\mathcal{B}(B^0 \rightarrow D^- \pi^+ \pi^+ \pi^-)} = 0.262 \pm 0.029(\text{stat.}) \quad (4.30)$$

The systematic uncertainties are discussed in the next chapter.

# Chapter 5

## Systematic Uncertainties

The previous sections dealt with the procedures of measuring the ratio of branching fractions. In this section, we estimate the systematic uncertainties of this measurement. Our eventual goal is to measure the ratios of branching fractions of two kinematically very similar decay channels of the  $B_s^0$  and the  $B^0$  mesons. We therefore expect that most of the systematic uncertainties for the individual channels cancel in the ratio, and expect a small systematic uncertainty on the measurement of the ratio. In order to determine the sources of systematic uncertainties, we have to consider the differences in reconstruction between the  $B_s^0$  and  $B^0$  decays.

### 5.1 Monte Carlo generation

There are several sources of systematic uncertainties in our analysis. The first category of systematic effects affects the ratio of efficiencies due to external inputs to the Monte Carlo simulation. These inputs are the  $B$  meson  $p_T$  spectrum, the lifetimes of  $B$  and  $D$  mesons, and the branching fractions of the resonant components of  $\pi^+\pi^+\pi^-$  system in  $B \rightarrow D\pi^+\pi^+\pi^-$  decay.

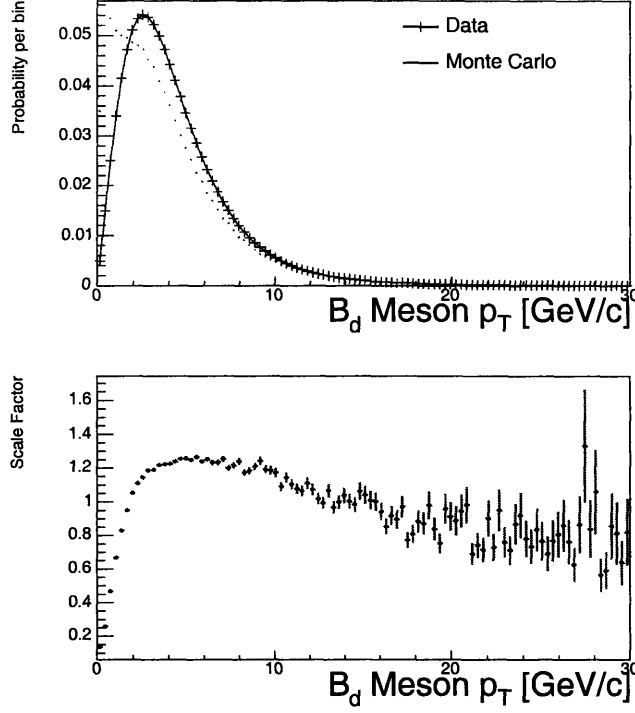


Figure 5-1: The  $p_T$  spectra of  $B^0$  mesons obtained from BGenerator Monte Carlo simulation with Peterson fragmentation compared to that measured in the  $J/\psi X$  analysis. The lower plot is the ratio of two spectra, which is used in the re-weighting procedure.

### 5.1.1 The $B$ $p_T$ spectrum

We noticed a discrepancy between the  $B$  meson  $p_T$  spectrum measured at CDF to that used by BGenerator Monte Carlo simulation, as shown in Figure 5-1. The CDF  $B$  hadron  $p_T$  spectrum is measured in the inclusive  $J/\psi$  channel with  $|\eta(J/\psi)| < 0.6$  [63] with acceptance corrections (corrected for trigger and detector effects). The Monte Carlo simulation spectrum is a raw  $B$  meson spectrum used by the BGenerator. It is obtained from the BGenerator output before the trigger requirements are applied. The discrepancy between data and Monte Carlo simulation is attributed to the fact that the Peterson fragmentation model [55] diverges at very low  $p_T$  of the  $b$  quark. To correct for the residual discrepancy, we introduce a re-weighting procedure for the  $B$  meson  $p_T$  spectrum. To obtain the systematic effect from imperfections in our  $p_T$  spectrum, we compare the ratios of the total efficiencies when the  $p_T$  spectra are



Meson	Lifetime
$B_s^0$	$1.461 \pm 0.057$ ps
$B^0$	$1.536 \pm 0.014$ ps
$D_s^-$	$490 \pm 9$ fs
$D^+$	$1040 \pm 7$ fs

Table 5.1:  $B$  and  $D$  meson lifetimes and uncertainties.

scaled to the case when they are not. From the difference in efficiencies, we assign a  $\pm 3.0\%$  systematic uncertainty on the ratio of efficiencies due to the  $B$  meson  $p_T$  modeling.

### 5.1.2 $B$ and $D$ lifetimes

Our knowledge of  $B$  and  $D$  lifetimes comes from the world average measurements. The values of the average lifetimes are used as input to the  $B$  meson decay simulation. Using an incorrect lifetime can result in calculating an incorrect trigger and reconstruction efficiency, as the analysis uses displacement as a selection criterion and the two-track trigger is based on track displacement, and therefore the efficiencies depend on the lifetimes and  $p_T$  spectra of the decaying particles. In order to estimate the size of this effect, we vary the  $B$  and  $D$  meson lifetimes by the uncertainties of their world averages as of January 2006 [2], as listed in Table 5.1. The variation is implemented by re-weighting the Monte Carlo events with a different lifetime, and recalculating the efficiencies. This method gives a very precise estimate of the effect of different lifetimes because we use the same events, and, therefore, the statistical uncertainty is minimized. We list the relative changes in efficiencies when rescaling the Monte Carlo simulation in Table 5.2. These are then propagated into our estimates of the total systematic uncertainties.

### 5.1.3 Resonance structure of the $\pi^+\pi^+\pi^-$ system

We know that our  $B^0 \rightarrow D^-\pi^+\pi^+\pi^-$  signal consists of three components:  $B^0 \rightarrow D^-a_1$ ,  $B^0 \rightarrow D^-\rho^0\pi^+$ , and non-resonant  $B^0 \rightarrow D^-\pi^+\pi^+\pi^-$ . The absolute branching

Effect	Syst. Uncertainty ( $\epsilon(B_s^0)/\epsilon(B^0)$ )[%]
$B_s^0$ lifetime	+1.9/ - 2.1
$D_s^+$ lifetime	+0.0/ - 0.0
$B^0$ lifetime	+0.4/ - 0.4
$D^+$ lifetime	+0.0/ - 0.0

Table 5.2: Systematic uncertainties on the ratio of efficiencies due to uncertainties on meson lifetimes.

Mode	$B^0 \rightarrow D^- a_1$	$B^0 \rightarrow D^- \rho \pi$	$B^0 \rightarrow D^- 3\pi$	Tot
Generated	59999335	19999345	19999345	59999335
Passed	16079	5370	5297	15862
$\epsilon^{tot}(\%)$	$0.0268 \pm 0.0002$	$0.0255 \pm 0.0002$	$0.0265 \pm 0.0002$	$0.0264 \pm 0.0002$

Table 5.3: Monte Carlo efficiencies for the components of the  $B^0 \rightarrow D^- \pi^+ \pi^+ \pi^-$  signal. The efficiencies are calculated for all triggers.

fractions for these components are not very well known, in fact the branching fractions of the corresponding  $B_s^0$  decays have never been measured. In the case of  $B_s^0$  decay, we assume that the fractions of the resonant components are identical to  $B^0$ . We test this hypothesis by comparing the  $\pi^+ \pi^+ \pi^-$  mass spectra in data for  $B^0 \rightarrow D^- \pi^+ \pi^+ \pi^-$  and  $B_s^0 \rightarrow D_s^- \pi^+ \pi^+ \pi^-$  decays. Figure 5-2 shows the result of such comparison. The distributions agree within the limited statistics of the  $B_s^0$  data sample.

The absolute Monte Carlo efficiencies for the components of the  $B^0 \rightarrow D^- \pi^+ \pi^+ \pi^-$  signal are not the same, so the total efficiency is a linear combination of the efficiencies of these various components and depends on their relative fractions. We generate a Monte Carlo sample for each of the three components of the signal. The resulting efficiencies are shown in Table 5.3.

The  $\pi^+ \pi^+ \pi^-$  mass spectra for various components were shown in Figure 4-23. The  $a_1$  component peaks in the low mass region, whereas  $\rho \pi^+$  and  $\pi^+ \pi^+ \pi^-$  non-resonant components produce smooth distributions. We also compare the sideband subtracted mass spectrum of the  $\pi^+ \pi^+ \pi^-$  system from  $B^0 \rightarrow D^- \pi^+ \pi^+ \pi^-$  and  $B_s^0 \rightarrow D_s^- \pi^+ \pi^+ \pi^-$  decay in data as shown in Figure 5-2. The peak in the low mass region indicates that the  $a_1$  component is dominant in data in both  $B^0 \rightarrow D^- \pi^+ \pi^+ \pi^-$  and  $B_s^0 \rightarrow D_s^- \pi^+ \pi^+ \pi^-$  decays.

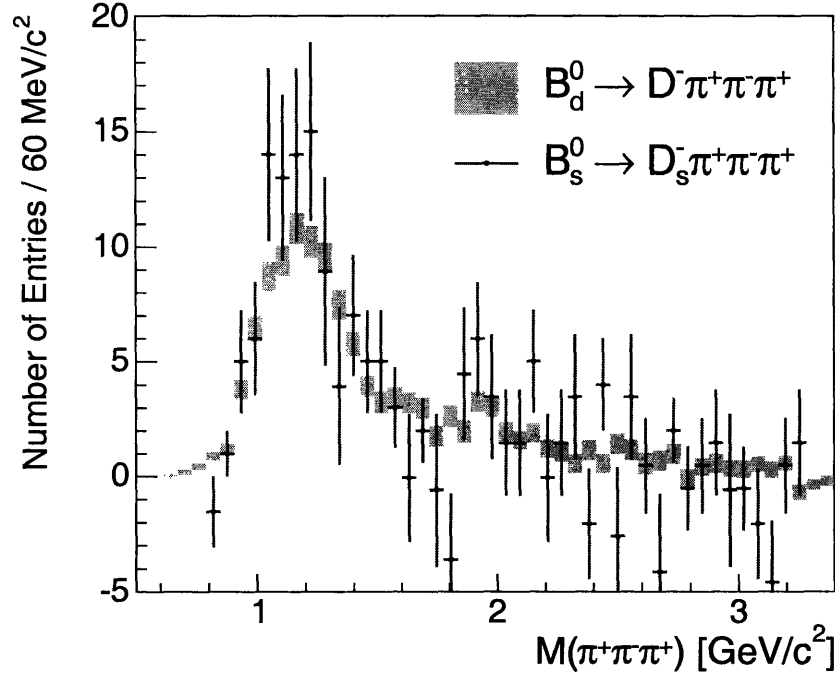


Figure 5-2: Comparison of the sideband subtracted mass spectrum of the  $\pi^+\pi^+\pi^-$  system from  $B^0$  and  $B_s^0$  decays. The  $B^0$  histogram is normalized to that of the  $B_s^0$ .

To calculate the relative systematic uncertainty on the efficiencies due to the uncertainty in these three components, we take the difference between the nominal efficiency with all three components present and the efficiency when the decay proceeds entirely via the  $a_1$ . The resulting systematic uncertainty on the efficiency is  $\pm 2.5\%$  of the nominal efficiency.

The comparison in Figure 5-2 serves another purpose as well. One could suggest, that if we try a larger variation for the  $a_1$  component in Monte Carlo simulation by setting  $a_1$  fraction to, say 50%, one could come up with a larger systematics for  $\pi^+\pi^+\pi^-$  resonant structure. This systematic, however, cancels in the ratio of efficiencies between  $B_s^0$  and  $B^0$  mesons thanks to the matching  $\pi^+\pi^+\pi^-$  spectra of  $B^0$  and  $B_s^0$ .

## 5.2 Detector description

Imperfections in the description of the CDF detector lead to the systematic uncertainty on the ratio of efficiencies of  $B_s^0$  to  $B^0$  mesons that we extract from the Monte Carlo simulation. There are two effects that we consider. The first one is related to the run range dependence of the Monte Carlo ratios of efficiencies. The second effect is due to different ionization patterns of pions and kaons in XFT. This effect is not reproduced by Monte Carlo simulation and is considered in Section 5.2.2.

### 5.2.1 Run range dependence systematic

To study the efficiency as a function of the running conditions signal Monte Carlo samples are divided into four run ranges with different running conditions:

1. Runs 138809-164304 corresponding to the old “4/5” configuration of SVT when hits in four out of five layers were required to fire the trigger.
2. Runs 164305-168889 — the next range up to the 2003 Tevatron shutdown.
3. Runs 168889-179056 — the runs up to the COT compromised period. (The COT started to experience aging problems in summer 2004, where COT occupancy fell below the level necessary to provide good tracking. COT problems have subsequently been solved by introducing some changes to the gas circulation system in the drift chamber.)
4. Runs 184208-186598 — post-COT recovery period and to the end of data set.

We obtain the Monte Carlo simulation efficiency for  $B^0 \rightarrow D^- \pi^+$  and  $B_s^0 \rightarrow D_s^- \pi^+$  for these four run ranges separately in B.CHARM and B.CHARM\_LOWPT triggers. We then plot the ratio ( $B_s^0$  to  $B^0$ ) of efficiencies as a function of the run range they represent. The resulting plots are shown in Figure 5-3. The behavior of the points is constant except for the point corresponding to the last run range, which is about 2 standard deviations lower than the average. There are two possible interpretations for this deviation.

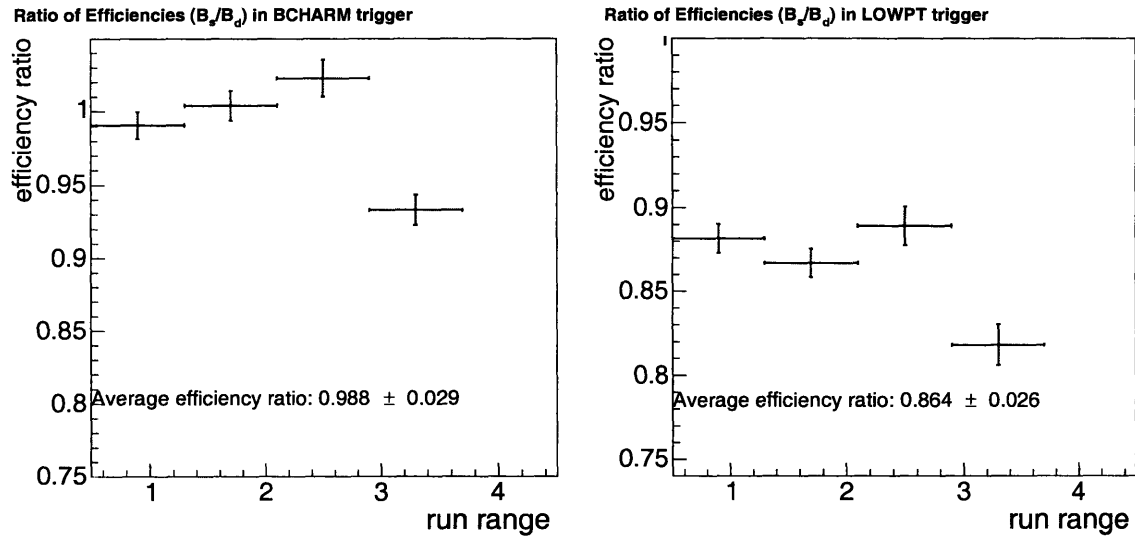


Figure 5-3: The ratio of efficiencies is plotted for four run ranges separately for B\_CHARM (left) and B\_CHARM\_LOWPT triggers (right). The last point deviates by 2 standard deviations from the average.

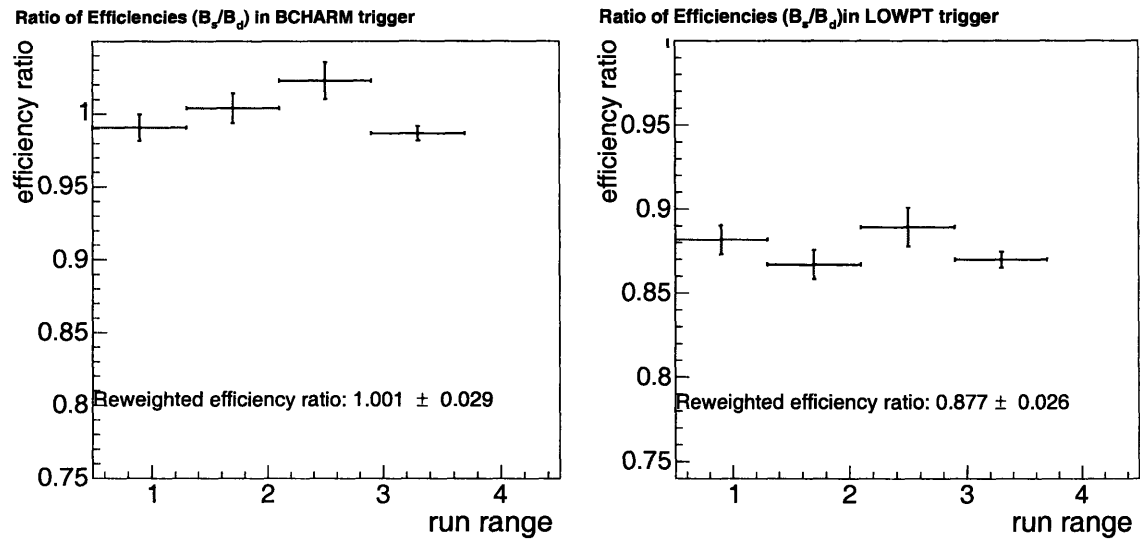


Figure 5-4: The ratio of efficiencies is plotted for four run ranges separately for B\_CHARM (left) and B\_CHARM\_LOWPT (right) triggers. The last point is reweighted to the average of the distribution.

Firstly, the changing trigger conditions in the last run period could affect reconstruction efficiency differently for the cases of  $B_s^0$  and  $B^0$  meson. Secondly, if the ratio of efficiencies is stable, the deviation could be due to imperfection in our simulation of the detector and trigger in the last run range. Conservatively, we assign a systematic uncertainty due to this deviation. The systematic is estimated in this case by reweighting the last point in Figure 5-3 to the average of all points and reestimating the total ratio of efficiencies as shown in Figure 5-4. We assign a systematic of  $\pm 1\%$  on the ratio of efficiencies due to this effect.

### 5.2.2 XFT efficiency for kaons relative to pions

It has been shown [64] that the XFT system has different efficiencies for tracks created by kaons and pions. For the study of direct CP asymmetry in  $D \rightarrow h^+ h^-$  decays, where  $h$  is a charged kaon or a pion, this difference is one of the dominant systematics. A detailed study of the XFT efficiency has been performed on a sample of  $D^- \rightarrow K^+ \pi^- \pi^-$  decays in data. For these decays one knows which track is the kaon and which is the pion. The kaon is the track that has the opposite charge from the other two tracks (pions). The study had the following conclusions:

- Pions and kaons have a different XFT efficiency due to different energy loss characteristics in the COT.
- This effect is not reproduced by the Monte Carlo simulation.
- The study in  $D^- \rightarrow K^+ \pi^- \pi^-$  sample shows a 6% inefficiency of kaons relative to pions in an XFT 1-miss configuration (XFT configurations are explained in Section 2.8.1).
- No relative inefficiency is found in a 2-miss configuration of XFT.

In order to evaluate the systematic uncertainty associated with this effect, we introduce it *a posteriori* into the Monte Carlo simulation as an extra 6% inefficiency for every kaon track to make a trigger track. We compare relative Monte Carlo efficiencies before and after the effect is introduced, as shown in Table 5.4. The

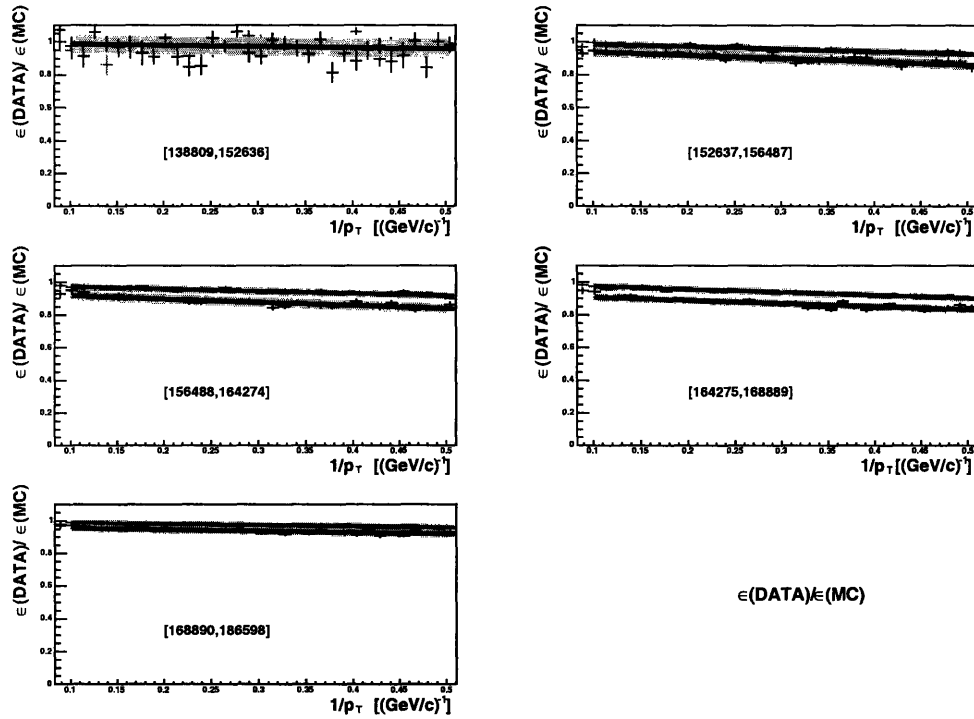


Figure 5-5: The ratio of XFT efficiencies in data and Monte Carlo simulation for kaons (in black) and pions (in red) as a function of the inverse  $p_T$ .

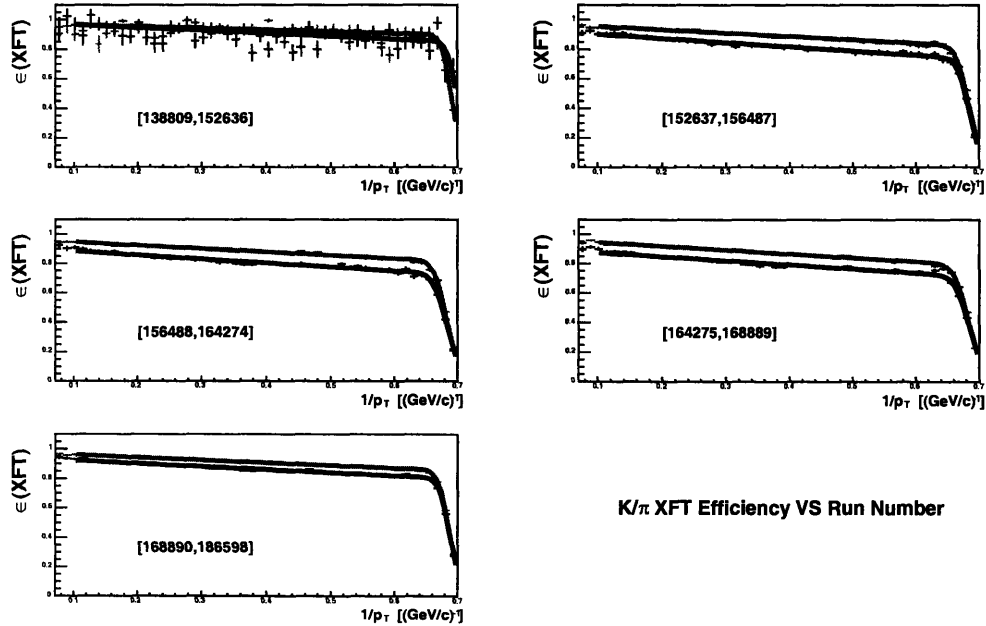


Figure 5-6: Kaon (in black) and pion (in red) XFT efficiencies in data as a function of the inverse  $p_T$ .

	$B^0 \rightarrow D^- \pi$	$B_s^0 \rightarrow D_s^- \pi$	$B^0 \rightarrow D^- 3\pi$	$B_s^0 \rightarrow D_s^- 3\pi$
Generated	59999335	59999335	59999335	59999335
Passed	110109	99453	15733	13330
$\epsilon^{tot}$ (%)	$0.1835 \pm 0.0006$	$0.1658 \pm 0.0005$	$0.0262 \pm 0.0002$	$0.0222 \pm 0.0002$
	old	new	old	new
Ratio( $B_s^0/B^0$ )	$0.8902 \pm 0.0040$	$0.9035 \pm 0.0040$	$0.8485 \pm 0.0010$	$0.8473 \pm 0.0010$

Table 5.4: The Luminosity averaged and prescaled efficiencies for the combined B.CHARM and B.CHARM\_LOWPT triggers. Efficiencies are obtained from Monte Carlo simulation that introduced the 6% inefficiency for a kaon to make a trigger track.

ratio of efficiencies ( $\epsilon(B_s^0)/\epsilon(B^0)$ ) changes by 1.5% for  $B_s^0 \rightarrow D_s^- \pi^+$ , and by 0.2% for  $B_s^0 \rightarrow D_s^- \pi^+ \pi^+ \pi^-$ .

In a more precise approach to the same study we use the  $p_T$  dependent XFT efficiency produced in Reference [64]. In this study the XFT efficiency is a function of the  $p_T$  of the track and the run range. The corresponding plots are shown in Figure 5-5. The change in the ratio of our B-signal efficiencies obtained by using these efficiency curves is 0.7% for  $B_s^0 \rightarrow D_s^- \pi^+$  and 0.1% for  $B_s^0 \rightarrow D_s^- \pi^+ \pi^+ \pi^-$ . We take the full value of the variation as an estimate of the systematic uncertainty due to XFT simulation:  $\pm 0.7\%$  and  $\pm 0.1\%$ , respectively.

## 5.3 Analysis

When we apply optimized selection requirements to the data we may introduce the systematic bias. To check that there is no bias we examine every quantity that is used for the selection. This is done in Sections 5.3.1 and 5.3.2. In Section 5.3.3 we study the properties of the  $B_s^0$  and  $B_s^0$  fits and how they affect the extracted yields.

### 5.3.1 Cut efficiencies

In Section 4.2 we explained a method for doing sideband subtraction to compare distributions in data to those from Monte Carlo simulation. One can apply a similar method to evaluate cut efficiencies. We expect the individual cut efficiencies of data and Monte Carlo simulation to match. If the relative cut efficiency for an individual



cut does not match, it is viewed as a result of poor simulation of this cut and is a source of systematic uncertainty.

We chose to compare  $(N-1)$ -type cut efficiencies, which means the efficiency of a single cut “ $i$ ” given that the other  $(N-1)$  cuts of the selection are applied. We define the number of events that pass the other  $(N-1)$  cuts for the signal region as  $N_s^i$  and for the sideband as  $N_b^i$ . The number of events that pass all  $N$  cuts is  $n_s^i$  for the signal region and  $n_b^i$  for the sideband region. We are interested in the ratio:

$$p_{cut-i}^{data} = \frac{n_s^i - n_b^i}{N_s^i - N_b^i} \quad (5.1)$$

which can be directly compared to the  $(N-1)$  cut efficiency that we determine for the same cut in Monte Carlo simulation. If we further define the probabilities for passing the  $N$ th cut given that the other  $(N-1)$  cuts are passed in the signal region as  $p_s = n_s/N_s$ , and for the background region  $p_b = n_b/N_b$ , then the statistical uncertainty on  $p_{cut}^{data}$  can be derived using the propagation of binomial uncertainties on  $n_s$  and  $n_b$ :

$$\sigma(p_{cut-i}^{data}) = \frac{\sqrt{N_s^i p_s^i (1 - p_s^i) + N_b^i p_b^i (1 - p_b^i)}}{N_s^i - N_b^i}. \quad (5.2)$$

To deduce the systematic uncertainty we need to compare ratios of cut efficiencies. So, in fact we compare the ratios  $p_{cut-i}^{data}(B_s^0)/p_{cut-i}^{data}(B^0)$  and  $p_{cut-i}^{MC}(B_s^0)/p_{cut-i}^{MC}(B^0)$ . This tells us how much the ratio of cut efficiencies for the different  $B$  mesons is different between data and Monte Carlo simulation, and therefore gives us an estimate of the potential systematic discrepancy due to incorrect modeling of distributions in the Monte Carlo simulation.

Then, the relevant quantity is  $R_i$ , the ratio of relative cut efficiencies in data and Monte Carlo simulation:

$$R_i = \frac{p_{cut-i}^{data}(B_s^0)/p_{cut-i}^{data}(B^0)}{p_{cut-i}^{MC}(B_s^0)/p_{cut-i}^{MC}(B^0)} \quad (5.3)$$

or actually, how much  $R_i$  differs from 1, which is to say  $R_i - 1$ . Tables 5.3.1 and 5.6 show a comparison of ratios of cut efficiencies in  $B_s^0$  and  $B^0$  decays between data and Monte Carlo simulation. In Tables 5.3.1 and 5.6 the statistical uncertainty is

Cut	$1 - R$	$\sigma(1 - R)$	Significance
$ d_0(B) $	0.003	0.007	0.43
$L_{xy}(B)/\sigma$	-0.015	0.011	-1.36
$\chi^2_{r-\phi}(B)$	-0.005	0.006	-0.83
$p_T(\pi_B)$	-0.019	0.096	-0.19
$L_{xy}(B \rightarrow D)$	0.003	0.005	0.60
$\chi^2_{r-\phi}(D)$	-0.0003	0.001	-0.30

Table 5.5: Comparison of the ratio ( $R$ ) of relative (N-1) type efficiencies of data to Monte Carlo simulation for different cut variables of  $B \rightarrow D\pi^+$  decays.

Cut	$1 - R$	$\sigma(1 - R)$	Significance
$L_{xy}(B)/\sigma$	0.011	0.024	0.46
$\chi^2_{r-\phi}(B)$	-0.109	0.160	-0.68
$ d_0(B) $	0.004	0.014	0.29
$p_T(B)$	-0.004	0.007	-0.57
$L_{xy}(D)/\sigma$	-0.070	0.093	-0.75
$L_{xy}(B \rightarrow D)$	0.016	0.055	0.29

Table 5.6: Comparison of the ratio ( $R$ ) of relative (N-1) type efficiencies of data to Monte Carlo simulation for different cut variables of  $B \rightarrow D\pi^+\pi^+\pi^-$  decays.

calculated using Equations 5.2 and 5.3.

We assign a systematic uncertainty due to a relative cut efficiency mis-measurement in case  $R - 1$  is at least  $2\sigma$  different from 0. This criteria is chosen to balance the competing interests of searching for systematic effects, yet not inflating the systematics on the account of statistical fluctuations. We find no such cuts that meet this criteria. No systematic uncertainty is assigned for this type of test.

### 5.3.2 The $\phi^0$ mass requirement

In reconstructing the  $B_s^0 \rightarrow D_s^- \pi^+$  and  $B_s^0 \rightarrow D_s^- \pi^+ \pi^+ \pi^-$  decays, where the  $D_s^-$  meson decays to  $\phi^0 \pi^-$  and the  $\phi^0$  meson to  $K^+ K^-$ , we require that the mass of the  $\phi^0$  in the  $\phi^0 \rightarrow K^+ K^-$  decay be between 1.010 and 1.029 GeV/ $c^2$ . If the mass spectrum of  $\phi^0 \rightarrow K^+ K^-$  decays in the Monte Carlo simulation does not agree with the distribution in data, the total efficiency is incorrect. This effect directly biases the  $B_s^0$  branching ratio measurement because no equivalent cut is applied to the  $B^0$  decay.

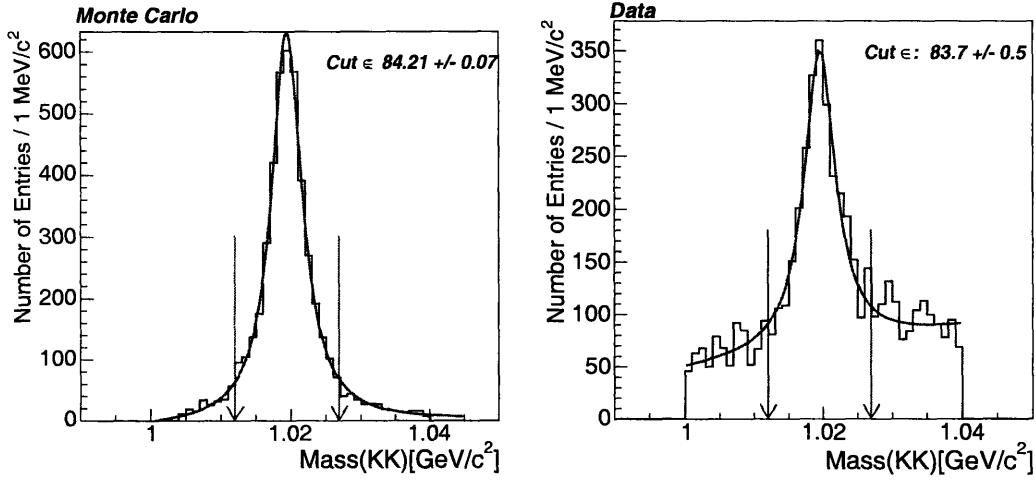


Figure 5-7: Comparison of  $\phi^0$  mass cut efficiency in Monte Carlo simulation and data. Both cut efficiencies are determined from the integral of the corresponding fits. Both the data and Monte Carlo simulation are fitted with a Breit Wigner convoluted with a Gaussian. The background is fitted with a linear function. On the left, the Monte Carlo simulation shows a slightly higher cut efficiency than what is depicted on the right, in  $B_s^0 \rightarrow D_s^- \pi^+ \pi^-$  in the data with no  $\phi^0$  mass cut applied. The difference is at the 0.5% level.

We have several cross-checks that we can use to determine if this is a significant effect in our analysis.

The  $\phi^0 \rightarrow K^+ K^-$  mass distribution is modeled with a Breit-Wigner function convoluted with a Gaussian representing the detector resolution. The world average value for the natural width of the  $\phi^0$  is  $4.26 \text{ MeV}/c^2$ . This is consistent with our fits of both Monte Carlo and data  $\phi^0$  mass distributions. Figure 5-7 shows fits of the Monte Carlo simulation and the data distributions. The background is modeled with a linear function. From the integral of the Breit-Wigner convolution in the signal region, we determine the absolute cut efficiency. In the Monte Carlo simulation, we find that this efficiency is  $84.21 \pm 0.17\%$ . As a crosscheck in data, we use the  $\phi^0$  mass distribution from  $B_s^0 \rightarrow D_s \pi^+ \pi^-$  decay with no  $\phi^0$  mass cut applied. We obtain the efficiency of the  $\phi^0$  mass cut of  $83.7 \pm 0.5\%$ .

$\phi^0 \rightarrow K^+ K^-$  decays have been studied independently using Time-Of-Flight particle identification [65]. These studies found that with low- $p_T$  kaons ( $p_T < 1.5 \text{ GeV}/c$ ), the Gaussian contribution to the  $\phi^0$  width is  $1.37 \pm 0.26 \text{ MeV}/c^2$ . This is again con-

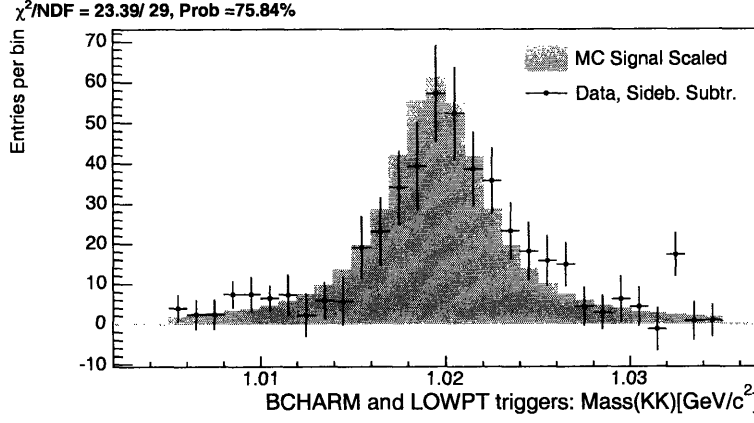


Figure 5-8: Comparison of Data and Monte Carlo distributions of the  $M(K^+K^-)$  for  $B_s^0 \rightarrow D_s^- \pi^+$  decays for combined B\_CHARM and B\_CHARM\_LOWPT triggers.

sistent with our findings in both data and Monte Carlo simulation.

Finally, we compare the mass distribution of the  $\phi^0$  resonance between Monte Carlo simulation and sideband subtracted data for  $B_s^0 \rightarrow D_s^- \pi^+$  decay. This is the most direct test of Monte Carlo performance although it suffers from low statistics in  $B_s^0 \rightarrow D_s^- \pi^+$  channel, where we reconstruct 494 signal candidates. The resulting distribution is shown in Figure 5-8. Within the uncertainties the distributions in data and Monte Carlo simulation agree, and we do not assign a systematic uncertainty for the  $\phi^0$  mass window cut.

### 5.3.3 Fitting systematics

Our fitting method uses templates to describe different background shapes. This means that certain parameters are fixed in the fit to the data. These values are extracted from Monte Carlo simulation and have an uncertainty associated with them. It is essential to clarify that there are two types of systematic uncertainties due to the fit models. The first type of uncertainty comes from the fact that the parameters of the fitting templates are known from Monte Carlo simulation with their corresponding statistical uncertainties. One can imagine generating a very big Monte Carlo simulation sample such that statistical uncertainty on the template parameters would vanish. The number of events after cuts in the Monte Carlo samples we use greatly

exceeds the number of events we observe in data. Therefore, we conclude that the systematic uncertainty due to the statistical uncertainty of the template parameters is negligible.

The second type of uncertainty comes from the fact that some properties possibly are simulated incorrectly in the Monte Carlo simulation in the first place. For instance, the branching fractions of most decays of  $B_s^0$  decays are not very well known and  $p_T$  spectrum of  $B$  mesons is not perfect, as is shown in Section 5.1.1.

In this section we describe the exercises we do to obtain an estimate of the systematic uncertainty due to the fit. We propagate the uncertainty due to every individual source in quadrature as shown in Tables 5.7 through 5.10.

We expand the range of the fit in the high mass region from 6.0 to 6.5 GeV/c<sup>2</sup>. In this case the normalization of the “ $B$ -continuum” background adjusts itself to the change in the values of the parameters of the combinatorial background. The fits for these tests are depicted in Figure 5-9. We see a very small increase in the number of  $B^0$  and  $B_s^0$  when this method is applied.

The fractions of the Cabibbo suppressed background under the  $B \rightarrow D\pi^+$  signal are estimated using the measured values of various branching fractions and Monte Carlo inputs. Since these backgrounds are the ones that affect the signal yield most we vary their normalizations by  $\pm 1\sigma$  to estimate the systematics associated with them. The branching fraction of Cabibbo suppressed decays has never been measured in  $B \rightarrow D\pi^+\pi^+\pi^-$  modes. However, the theoretical expectation would be that branching fraction of Cabibbo decays is order of  $\frac{|V_{us}|^2}{|V_{ud}|^2} \approx 0.05$  of the main signal. The measurements and our estimates of the branching fractions of different Cabibbo suppressed decays and their uncertainties are shown in Table 4.2. To estimate the systematics due to presence of the Cabibbo suppressed decay we fix the Cabibbo suppressed normalization fraction to zero. The plots in Figure 5.8 show the results of the fits. From the variation in the fitted yield we deduce the systematic uncertainty

Parameter	Variation	Syst. Uncertainty [%]
extending fit range	0.5 GeV/c <sup>2</sup>	$\pm 0.43$
fraction of Cabibbo	$\pm 1 \sigma$	$\pm 0.18$
fraction of $\Lambda_b$	$\pm 100\%$	$\pm 0.01$
fraction of $B_s^0$	$\pm 100\%$	$\pm 0.16$
Total	—	$\pm 0.49$

Table 5.7: Table of systematic uncertainties on the number of  $B^0 \rightarrow D^- \pi^+$  due to the fit model.

Parameter	Variation	Syst. Uncertainty [%]
extending fit range	0.5 GeV/c <sup>2</sup>	$\pm 0.42$
fraction of Cabibbo	$\pm 100\%$	$\pm 0.21$
fraction of $\Lambda_b$	$\pm 100\%$	$\pm 0.57$
Total	—	$\pm 0.74$

Table 5.8: Table of systematic uncertainties on the number of  $B^0 \rightarrow D^- \pi^+ \pi^+ \pi^-$  due to the fit model.

due to the limited knowledge of branching fractions of Cabibbo suppressed decays.

We also vary the normalizations of the  $\Lambda_b$  background and background coming from  $B_s^0$  to estimate the systematic uncertainty on the fit yield associated with them by again fixing the normalization of these backgrounds to zero. The results of the fits are shown in Figures 5-12 and 5-13.

It is a common problem that for the low statistics  $B_s^0 \rightarrow D_s^- \pi^+ \pi^+ \pi^-$  decay we would like to fix the signal width in data fit, because the uncertainty on the width is quite large due to the small sample size (see Table A.27 in Appendix A). The fitted width is correlated with the signal yield, and thereby translates into an appreciable uncertainty for our measurement.

It is observed that the widths of the signal Gaussians in Monte Carlo simulation are different from the ones measured in data. We remove this ambiguity by fixing the widths in data by the values obtained from Monte Carlo simulation by adding a

Parameter	Variation	Syst. Uncertainty [%]
extending fit range	0.5 GeV/c <sup>2</sup>	± 0.79
fraction of Cabibbo	± 1 $\sigma$	± 0.40
fraction of $\Lambda_b$	± 100%	± 0.20
shape of the continuum background	shape variations	± 1.20
Total	—	± 1.51

Table 5.9: Table of systematic uncertainties on the number of  $B_s^0 \rightarrow D_s^- \pi^+$  due to the fit model.

correction ( $2.0 \pm 0.5$  MeV/c<sup>2</sup>). The correction is obtained by comparing the width of the signal in data and the Monte Carlo signal template for the normalization mode  $B^0 \rightarrow D^- \pi^+ \pi^+ \pi^-$ . The uncertainty on the width correction is just the statistical uncertainty of the width of the  $B^0 \rightarrow D^- \pi^+ \pi^+ \pi^-$  fit in data. It is used to estimate the systematics due to the width of the signal template. The plots in Figure 5-14 show the variation in the number of  $B_s^0$  candidates.

Although the continuum physics background does not fall directly under the signal, the shape of this background distribution to the left of the signal indirectly affects the signal yields. The shape of the continuum background depends on the many branching fractions of various  $B$  decays that contribute to it. The corresponding branching fractions in the  $B^0$  case have been measured relatively well. Therefore, this systematics does not apply to  $B^0$  fit. The branching fractions for most of the  $B_s^0$  decays have not been measured yet. The current values used in the our decay simulation program come from  $SU(3)_f$  extrapolations from the analogous  $B^0$  branching fractions.

We divide the events which go into the semi-inclusive template into three categories:

- decays involving  $B_s^0$  decaying to  $D_s^-$  (the signal modes being subtracted)
- decays involving  $B_s^0$  decaying to  $D_s^{*-}$  (subtracting the main reflection modes and  $D_s^- D_s^{*-}$  mode to avoid double counting)

Parameter	Variation	Syst. Uncertainty [%]
extending fit range	0.5 GeV/c <sup>2</sup>	< 0.01
fraction of Cabibbo	±100%	< 0.01
fraction of $\Lambda_b$	±100%	< 0.01
signal Width	± 0.5 MeV/c <sup>2</sup>	± 0.64
shape of the continuum background	shape variations	± 3.85
Total	—	± 3.90

Table 5.10: Table of systematic uncertainties on the number of  $B_s^0 \rightarrow D_s^- \pi^+ \pi^+ \pi^-$  due to the fit model.

- other decays  $B_s^0$  not involving  $D_s^-$  and the “other” category which includes decays of  $B^0$  and  $B^+$ .

The resulting distributions are shown in Figure 5-18. All the events in the first category depend on the uncertainty of the measurement of the  $D_s^- \rightarrow \phi^0 \pi^-$  branching fraction, which gives the global scaling for this category. The  $D_s^- \rightarrow \phi^0 \pi^-$  branching fraction is only known to approximately 25% precision. The events in the second category depend on the branching fraction of  $D_s^{*-} \rightarrow D_s^- \gamma$  decay. So, a change in the value of the branching fraction of  $D_s^-$  decay in the corresponding category results in the change of the shape of the semi-inclusive template.

To estimate the systematics due to the shape of semi-inclusive background we do three templated fits with one of the three background component dropped. The parametrization we use to do the fits is the same as the one we use to fit the default semi-generic contribution. The resulting templated fits are shown in Figures 5-19 and 5-20. Using these templates we repeat the fits of data for the three cases. The fit results are shown in Figures 5-21 and 5-22. The numbers are shown in Tables 5.10 and 5.9. The variation of the yields goes into the estimate of the systematic uncertainty due to the shapes of semi-inclusive Monte Carlo simulation.



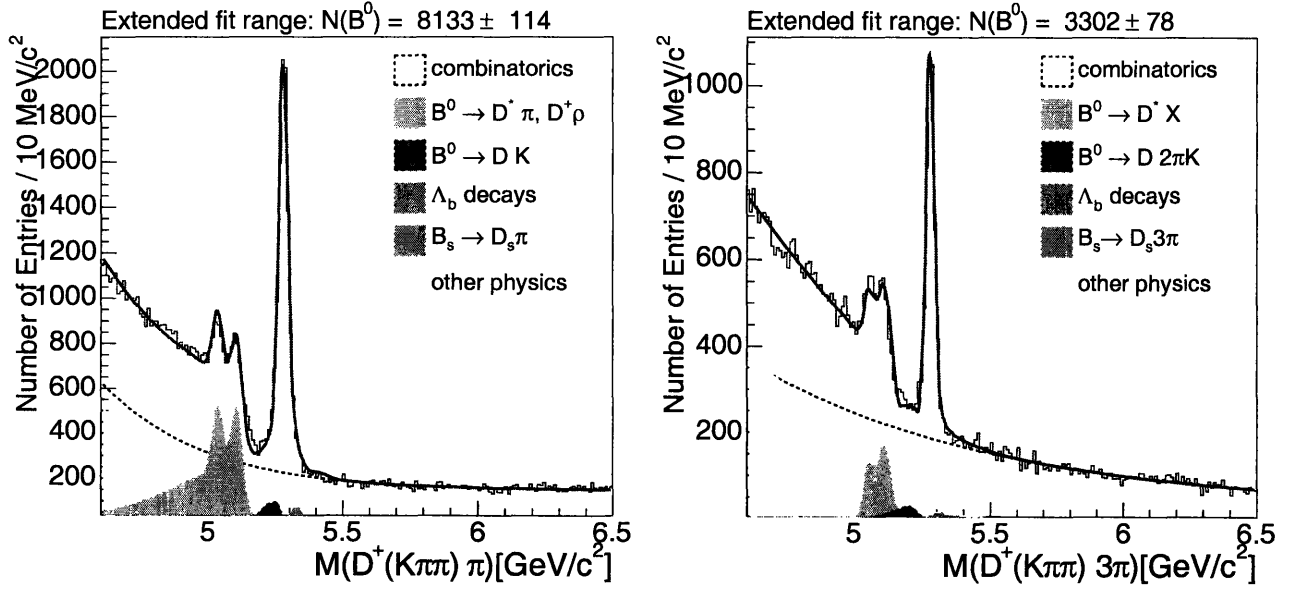


Figure 5-9: Fit results for extended fit range:  $B^0 \rightarrow D^- \pi^+$  (left) and  $B^0 \rightarrow D^- \pi^+ \pi^+ \pi^-$  (right). Fitted yields are used for estimating the systematic uncertainty due to limitations of the fitting model.

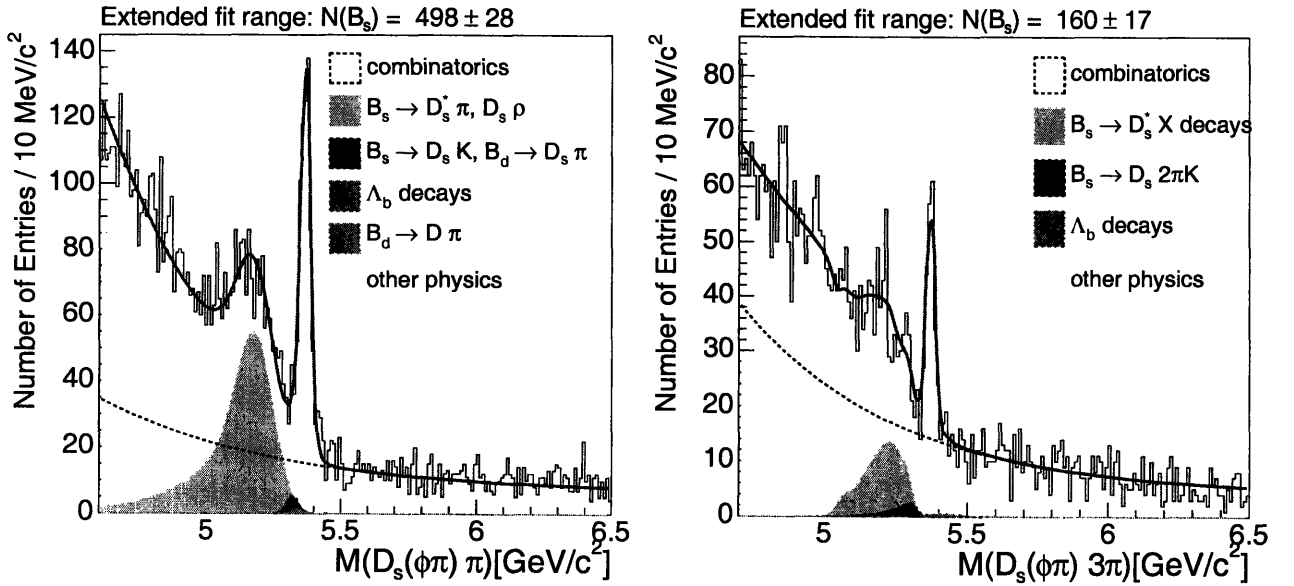


Figure 5-10: Fit results for extended fit range:  $B_s^0 \rightarrow D_s^- \pi^+$  (left) and  $B_s^0 \rightarrow D_s^- \pi^+ \pi^+ \pi^-$  (right). Fitted yields are used for estimating the systematic uncertainty due to limitations of the fitting model.

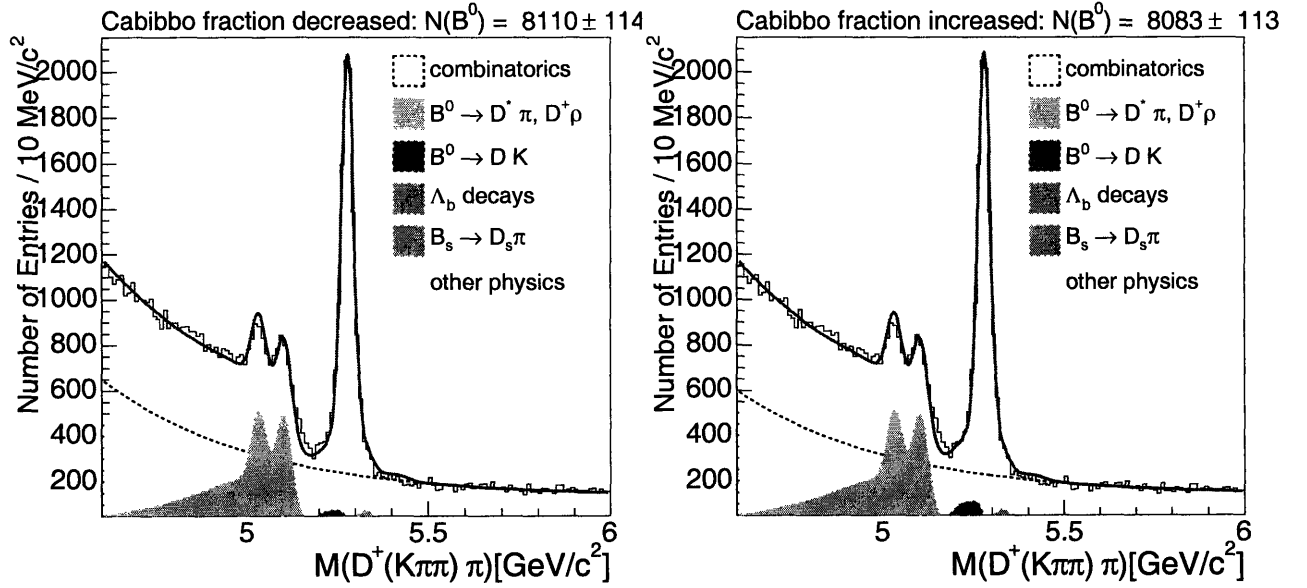


Figure 5-11: Fit results, for estimating the systematic uncertainty due to the fraction of Cabibbo suppressed modes in  $B^0 \rightarrow D^- \pi^+$  decays.

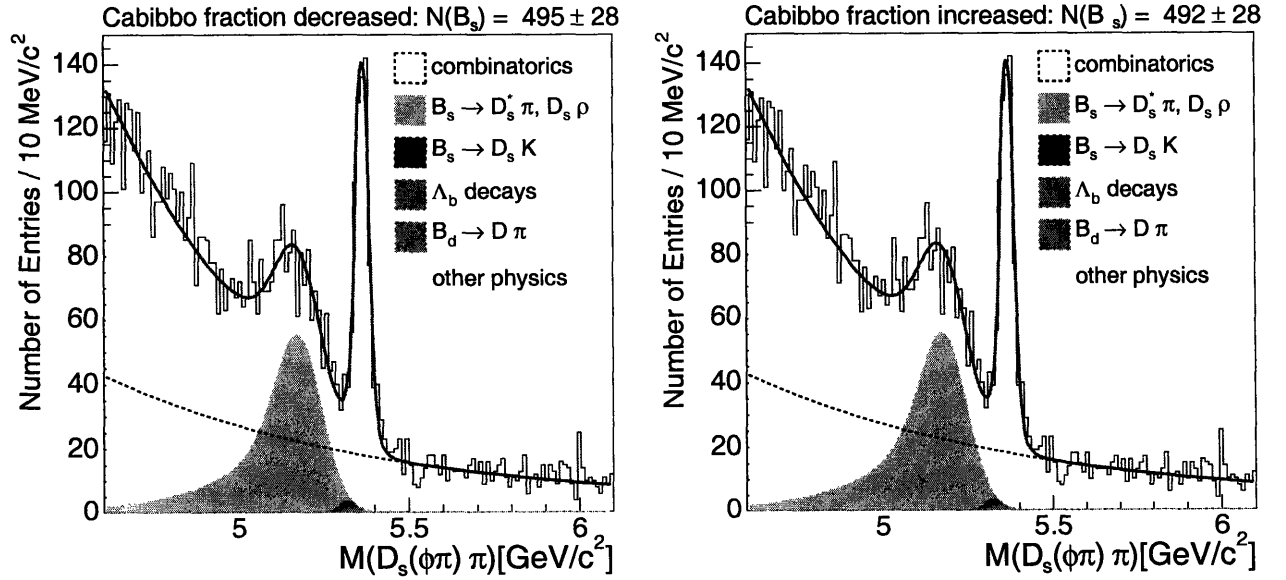


Figure 5-12: Fit results, for estimating the systematic uncertainty due to the fraction of Cabibbo suppressed modes in  $B_s^0 \rightarrow D_s^- \pi^+$  decays.

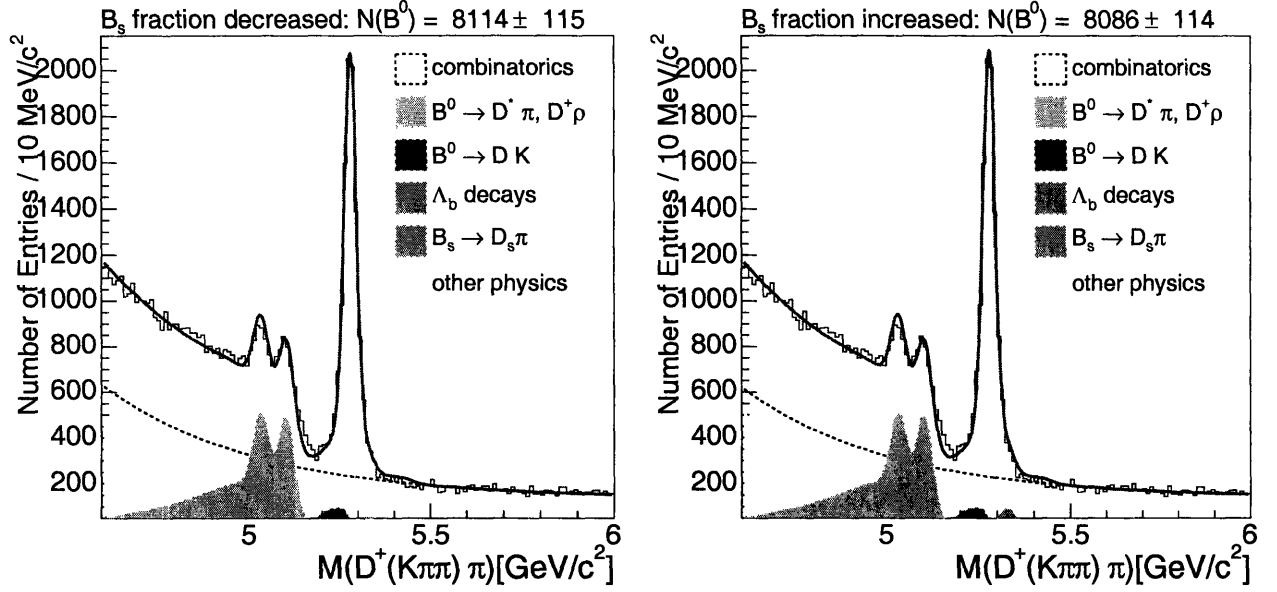


Figure 5-13: Fit results, for estimating the systematic uncertainty due to the fraction of  $B_s^0$  reflection under  $B^0 \rightarrow D^- \pi^+$  mass peak.

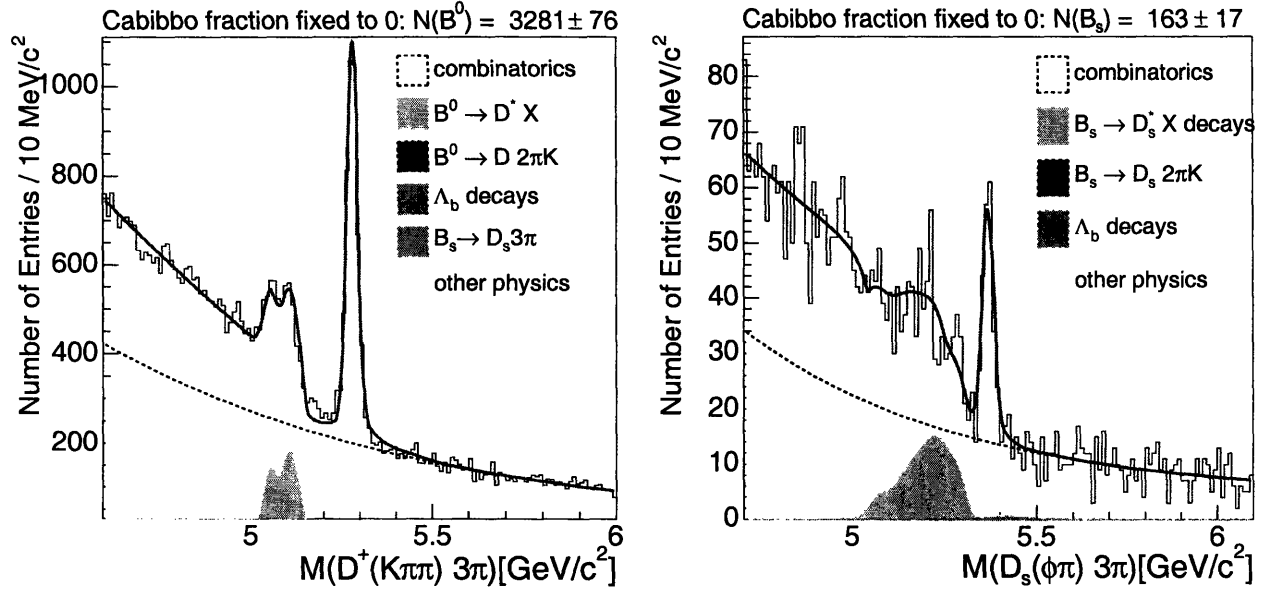


Figure 5-14: Fit results, for estimating the systematic uncertainty due to the fractions of Cabibbo suppressed background under  $B^0 \rightarrow D^- \pi^+ \pi^+ \pi^-$  (left) and  $B_s^0 \rightarrow D_s^- \pi^+ \pi^+ \pi^-$  (right) mass peak.

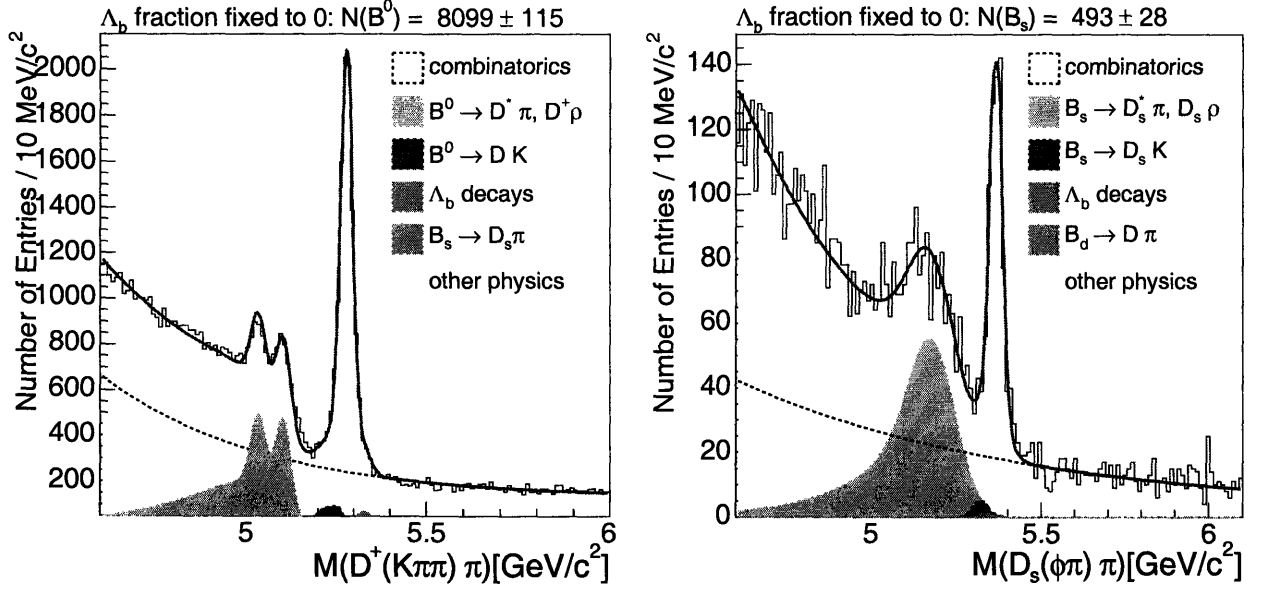


Figure 5-15: Fit results, for estimating the systematic uncertainty due to the fractions of  $\Lambda_b$  background under  $B^0 \rightarrow D^- \pi^+$  (left) and  $B_s^0 \rightarrow D_s^- \pi^+$  (right) mass peaks.

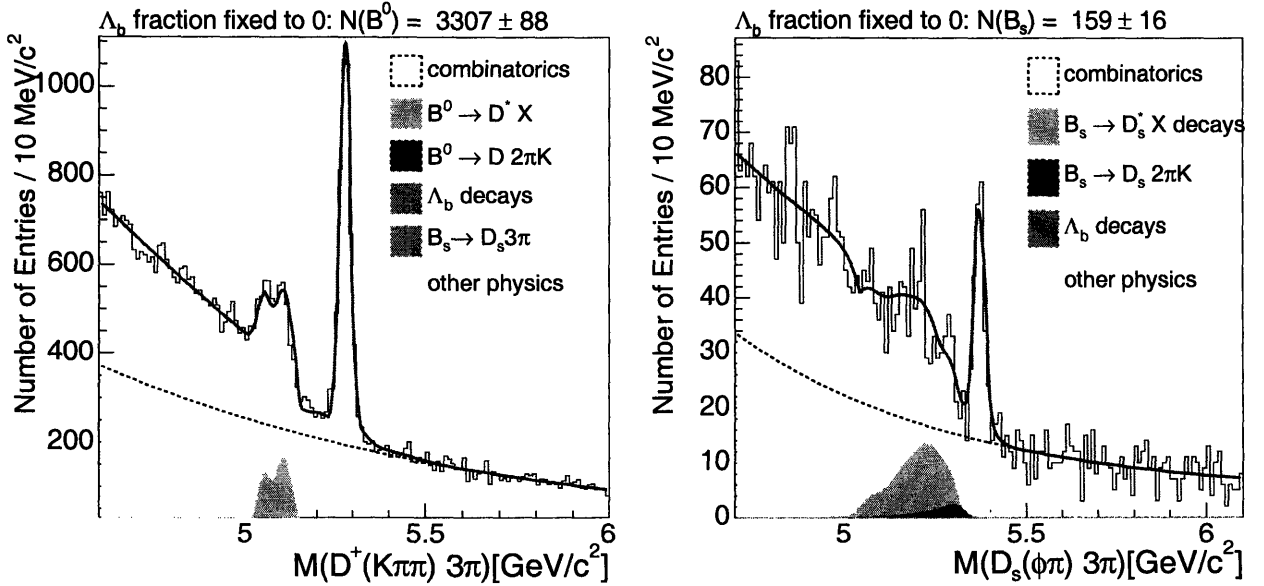


Figure 5-16: Fit results, for estimating the systematic uncertainty due to the fractions of  $\Lambda_b$  background under  $B^0 \rightarrow D^- \pi^+ \pi^+ \pi^-$  (left) and  $B_s^0 \rightarrow D_s^- \pi^+ \pi^+ \pi^-$  (right) mass peaks.

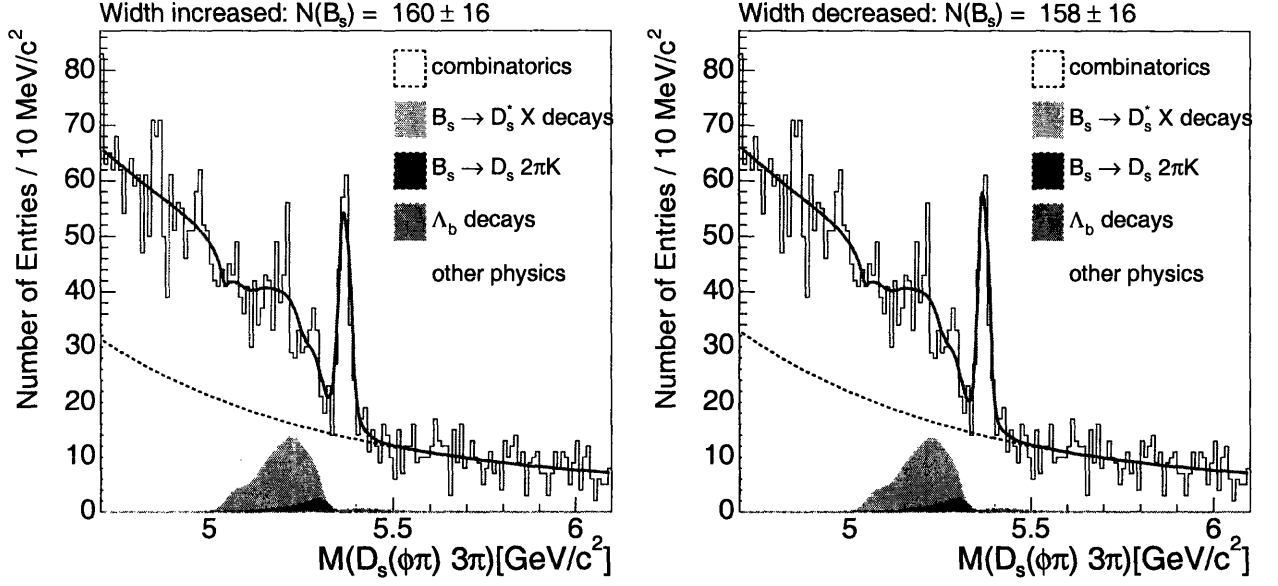


Figure 5-17: Fit results, for estimating the systematic uncertainty due to the signal width in  $B_s^0 \rightarrow D_s^- \pi^+ \pi^+ \pi^-$  decay.

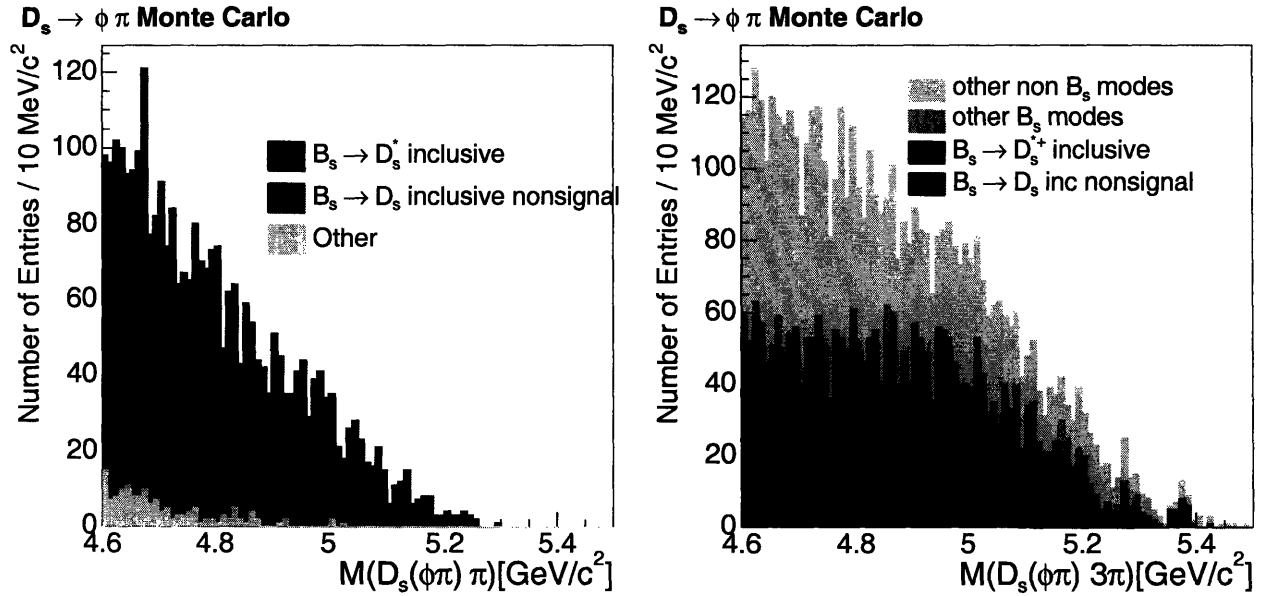


Figure 5-18: Decomposition of the continuum background for  $B_s^0 \rightarrow D_s^- \pi^+$  and  $B_s^0 \rightarrow D_s^- \pi^+ \pi^+ \pi^-$  decays used for evaluating the systematic uncertainty due to unknown branching fraction of  $B_s^0$  decays.

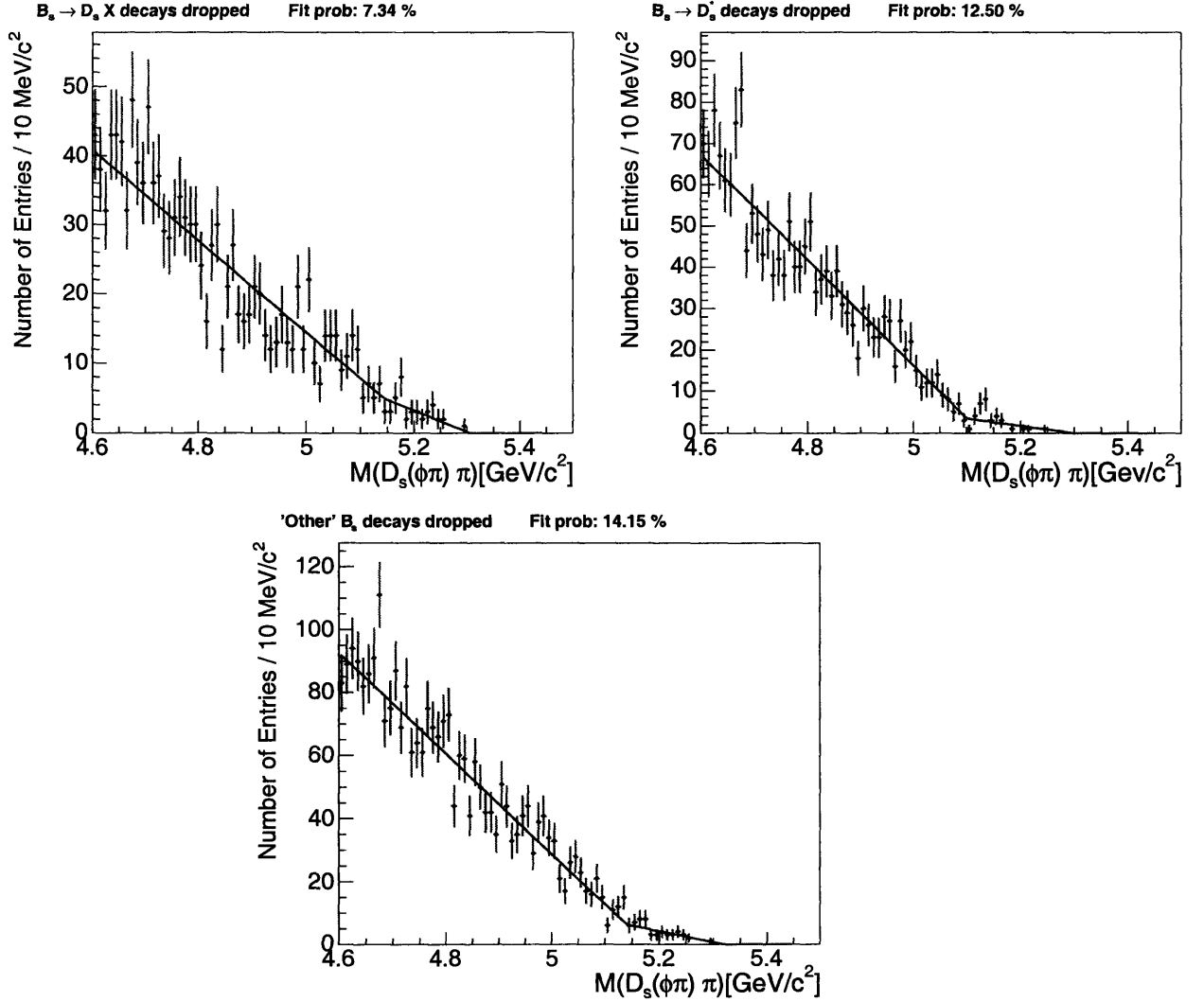


Figure 5-19: The  $B_s^0$  semi-generic templates used to estimate the systematics due to unknown  $B_s^0$  branching fractions. Top left plot corresponds to the background with  $D_s^- X$  contribution dropped, top right has the  $D_s^{*-} X$  contribution dropped, and the bottom has the “other” category dropped.

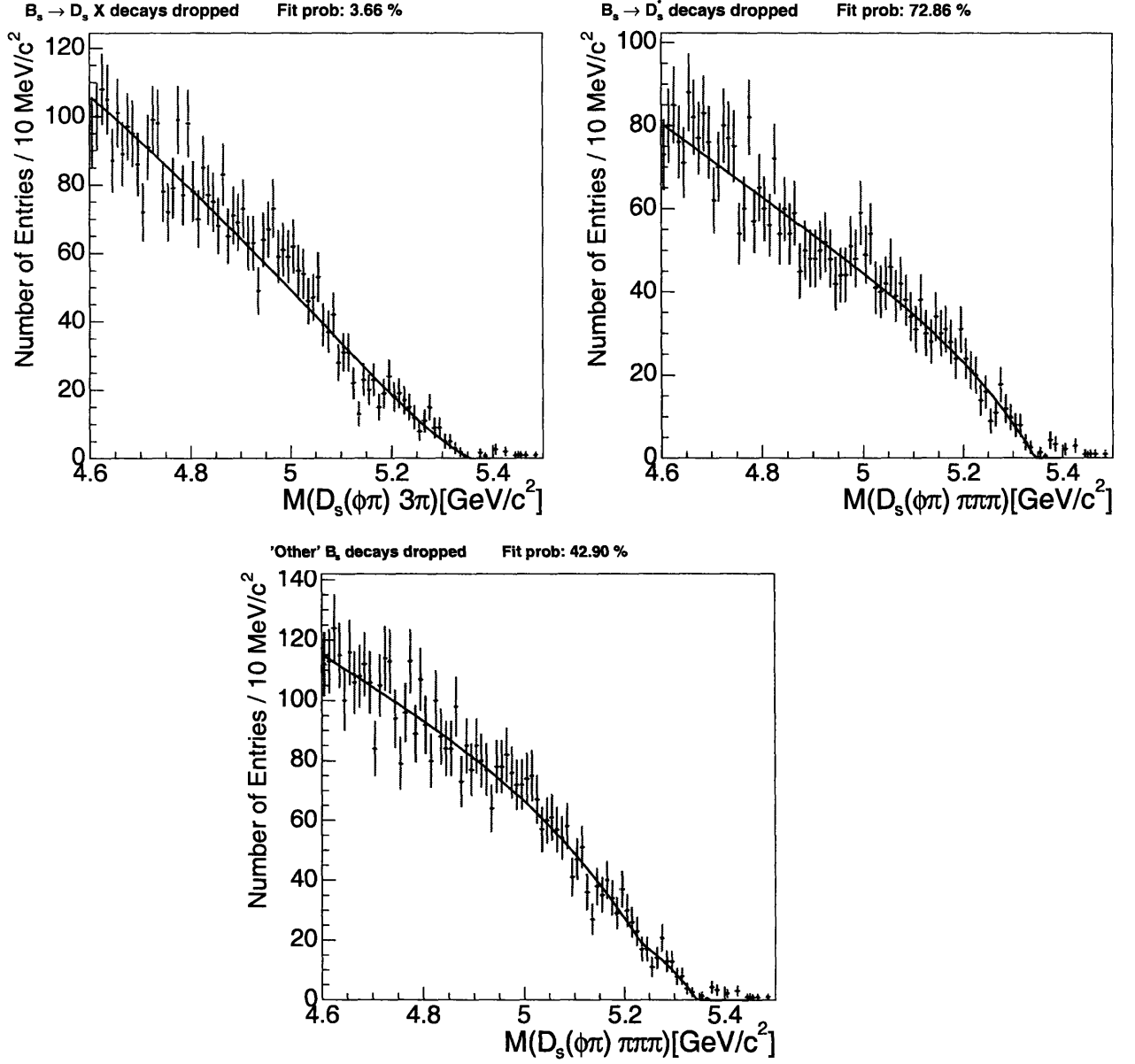


Figure 5-20: The top left corresponds to the background where  $D_s^- X$  contribution is dropped, top right has the  $D_s^{*-} X$  contribution dropped, and the bottom has the "other" category dropped.

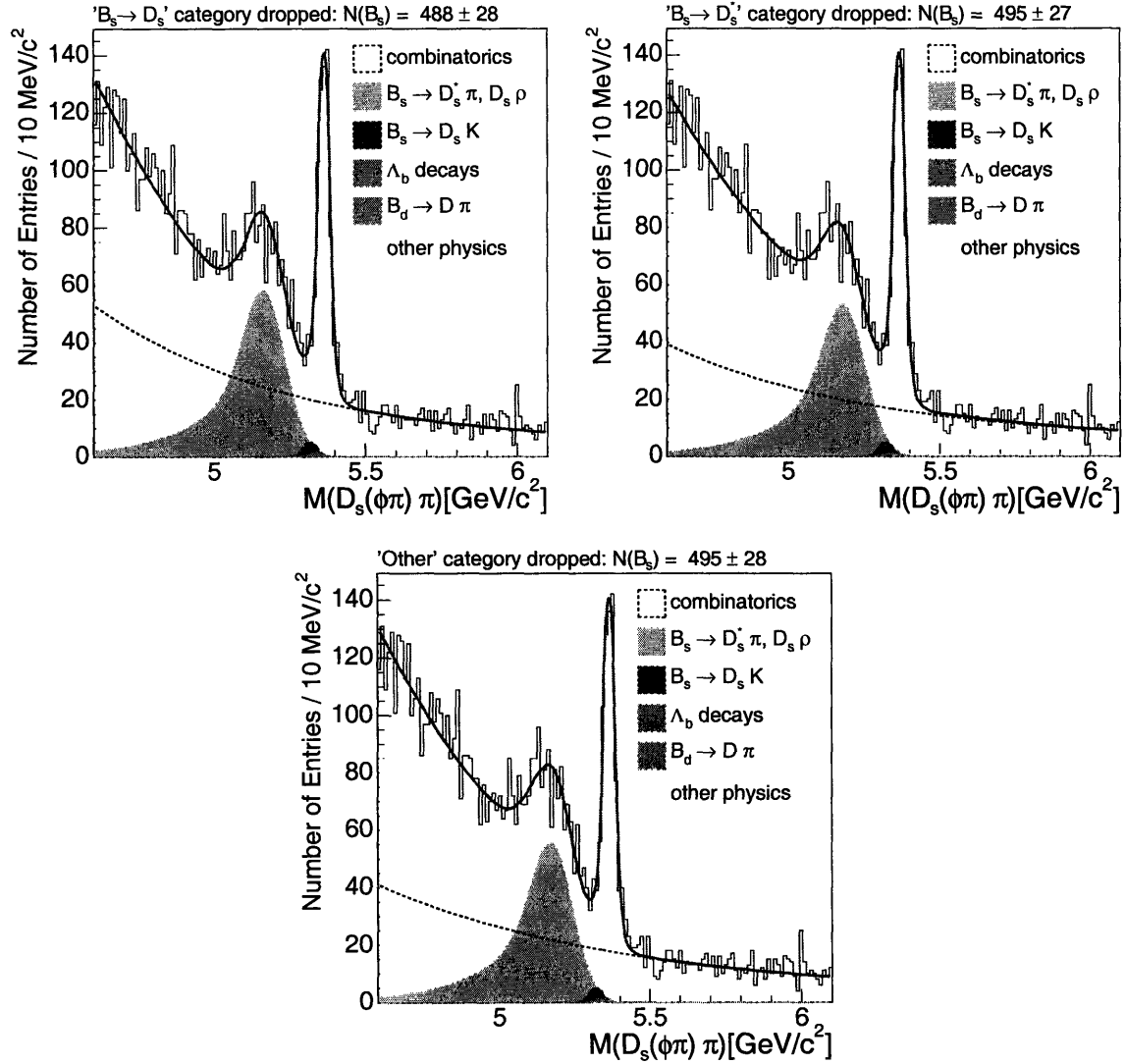


Figure 5-21: Fits of the  $B_s^0 \rightarrow D_s^- \pi^+$  data with three different semi-generic templates used to estimate the systematics due to unknown  $B_s^0$  branching fractions. The top left plot corresponds to the background where the  $D_s^- X$  contribution is dropped, top right has the  $D_s^{*-} X$  contribution dropped, and the bottom has the “other” category dropped.



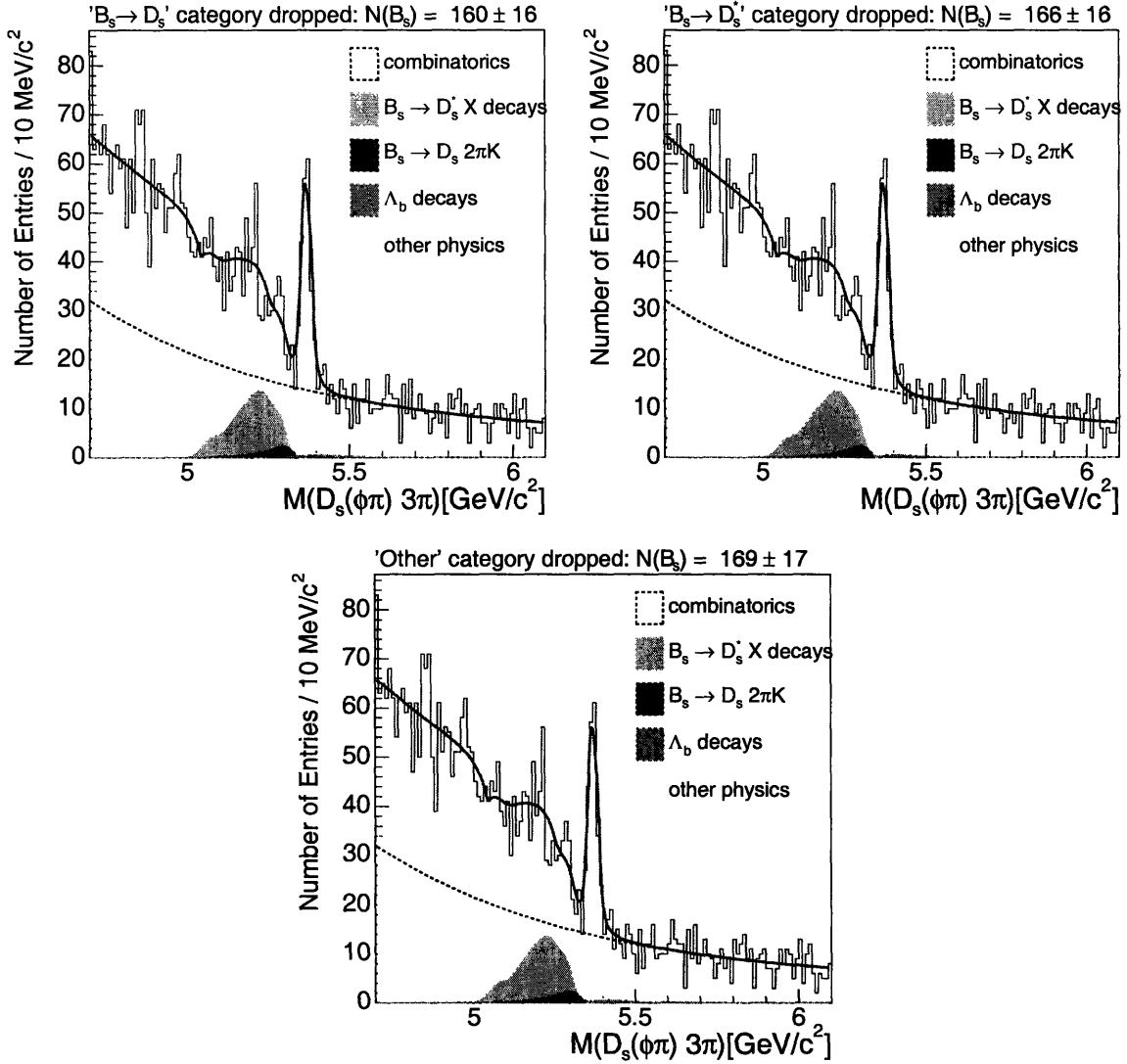


Figure 5-22: Fits of the  $B_s^0 \rightarrow D_s^- \pi^+ \pi^+ \pi^-$  data with three different semi-generic templates used to estimate the systematics due to unknown  $B_s^0$  branching fractions. The top left plot corresponds to the background where the  $D_s^- X$  contribution is dropped, top right has the  $D_s^- X$  contribution dropped, and the bottom has the “other” category dropped.

Branching Ratio	Value
$D^- \rightarrow K^+ \pi^- \pi^-$	$[9.51 \pm 0.34] \cdot 10^{-2}$
$D_s^- \rightarrow \phi^0 (K^+ K^-) \pi^-$	$[2.16 \pm 0.28] \cdot 10^{-2}$
$f_s/f_d$	$0.259 \pm 0.038$

Table 5.11: Summary of the external parameters used for calculations of the relative rates of  $B$  mesons [2].

## 5.4 External inputs

As was already explained in Section 4.7, we deduce the ratios of branching fractions in our dataset, applying the following formulae:

$$\frac{f_s}{f_d} \cdot \frac{\mathcal{B}(B_s^0 \rightarrow D_s^- \pi^+)}{\mathcal{B}(B^0 \rightarrow D^- \pi^+)} = \frac{N(B_s^0)}{N(B^0)} \cdot \frac{\epsilon(B^0 \rightarrow D^- \pi^+)}{\epsilon(B_s^0 \rightarrow D_s^- \pi^+)} \cdot \frac{\mathcal{B}(D^- \rightarrow K^+ \pi^- \pi^-)}{\mathcal{B}(D_s^- \rightarrow \phi^0 \pi^-, \phi^0 \rightarrow K^+ K^-)} \quad (5.4)$$

$$\frac{f_s}{f_d} \cdot \frac{\mathcal{B}(B_s^0 \rightarrow D_s^- \pi^+ \pi^+ \pi^-)}{\mathcal{B}(B^0 \rightarrow D^- \pi^+ \pi^+ \pi^-)} = \frac{N(B_s^0)}{N(B^0)} \cdot \frac{\epsilon(B^0 \rightarrow D^- \pi^+ \pi^+ \pi^-)}{\epsilon(B_s^0 \rightarrow D_s^- \pi^+ \pi^+ \pi^-)} \cdot \frac{\mathcal{B}(D^- \rightarrow K^+ \pi^- \pi^-)}{\mathcal{B}(D_s^- \rightarrow \phi^0 \pi^-, \phi^0 \rightarrow K^+ K^-)} \quad (5.5)$$

In these formulae,  $\mathcal{B}(D^- \rightarrow K^+ \pi^- \pi^-)$  and  $\mathcal{B}(D_s^- \rightarrow \phi^0 \pi^-, \phi^0 \rightarrow K^+ K^-)$  are the branching fractions of  $D$  mesons, and  $f_s/f_d$  is the ratio of the fragmentations fractions. These numbers are external input parameters for our analysis. We use the world averages as of January 2006 [2], which are listed in Table 5.11.

The uncertainties of the external parameters are propagated into the total systematic uncertainty in quadrature. Since the branching fractions of  $D$  mesons are not very precisely known, they are the dominant source of systematic uncertainty for our measurement. We choose to split the total systematics of our measurement into three categories: “the syst uncertainty” accounts for the effects described in the previous sections, “the BR uncertainty” refers to the uncertainty on the branching fractions of  $D$  mesons, and “the PR” uncertainty refers to the uncertainty on the world average measurement of the ratio of  $B_s^0$  to  $B^0$  production rates,  $f_s/f_d$ .

Effect	$(D_s^- \pi)[\%]$	$(D_s^- 3\pi)[\%]$
$B$ $p_T$ spectrum	$\pm 3.0$	$\pm 3.0$
trigger simulation	$\pm 1.2$	$\pm 1.1$
cut efficiencies	$< 0.1$	$< 0.1$
$B_s^0$ lifetime	$\pm 2.1$	$\pm 2.1$
$D_s^+$ lifetime	$\pm 0.0$	$\pm 0.0$
$B^0$ lifetime	$\pm 0.4$	$\pm 0.4$
$D^+$ lifetime	$< 0.1$	$< 0.1$
$B_s^0$ fitting	$\pm 1.5$	$\pm 3.9$
$B^0$ fitting	$\pm 0.5$	$\pm 0.7$
$3\pi$ resonance structure	n/a	$\pm 2.5$
Total	$\pm 4.2$	$\pm 6.1$
$D$ branching fractions	$\pm 13.3$	$\pm 13.3$
production fractions $f_s/f_d$	$\pm 15.0$	$\pm 15.0$

Table 5.12: Table of systematic uncertainties for the ratios of branching fractions measurements.

## 5.5 Summary of systematic effects

We add the above systematic uncertainties in quadrature and propagate them into the branching fractions to obtain the total systematic uncertainties for the relative branching fraction measurements, as listed in Table 5.12. Our systematic uncertainty is currently dominated by the uncertainties of the external parameters. The uncertainties on the external parameters will be reduced in the near future, when the new, more precise measurements of the branching fractions of  $D$  mesons and the ratio of  $B_s^0$  to  $B^0$  production rates are available.



# Chapter 6

## Conclusion

We analyzed the data set collected by the upgraded CDF detector corresponding to an integrated luminosity of  $355 \text{ pb}^{-1}$ . Using a novel trigger based on a pair of displaced tracks, we collected a sample rich in charm and bottom mesons. In this sample, we made a high statistics observation of the hadronic decay  $B_s^0 \rightarrow D_s^- \pi^+$  and the first observation of the decay  $B_s^0 \rightarrow D_s^- \pi^+ \pi^+ \pi^-$ .

Using optimized selection requirements, we reconstruct  $494 \pm 28 B_s^0 \rightarrow D_s^- \pi^+$ ,  $8098 \pm 114 B^0 \rightarrow D^- \pi^+$ ,  $159 \pm 17 B_s^0 \rightarrow D_s^- \pi^+ \pi^+ \pi^-$ , and  $3288 \pm 76 B^0 \rightarrow D^- \pi^+ \pi^+ \pi^-$  decays. After correcting for differences in trigger and reconstruction efficiencies, we find that the ratio of the production fractions multiplied by the ratio of branching fractions for these decays are:

$$\frac{f_s}{f_d} \cdot \frac{\mathcal{B}(B_s^0 \rightarrow D_s^- \pi^+)}{\mathcal{B}(B^0 \rightarrow D^- \pi^+)} = 0.292 \pm 0.020(\text{stat.}) \pm 0.012(\text{syst.}) \pm 0.039(\text{BR}) \quad (6.1)$$

$$\frac{f_s}{f_d} \cdot \frac{\mathcal{B}(B_s^0 \rightarrow D_s^- \pi^+ \pi^+ \pi^-)}{\mathcal{B}(B^0 \rightarrow D^- \pi^+ \pi^+ \pi^-)} = 0.262 \pm 0.029(\text{stat.}) \pm 0.016(\text{syst.}) \pm 0.035(\text{BR}), \quad (6.2)$$

where the first uncertainty is statistical, the second is due to systematic effects specific for this analysis, and the third is due to the current uncertainty on the world average  $D$  branching fractions.

Using the world average value of the ratio of  $B_s^0$  to  $B^0$  production rates  $f_s/f_d =$

$0.259 \pm 0.038$  [2], we infer that the ratios of branching fractions are:

$$\frac{\mathcal{B}(B_s^0 \rightarrow D_s^- \pi^+)}{\mathcal{B}(B^0 \rightarrow D^- \pi^+)} = 1.13 \pm 0.08(\text{stat.}) \pm 0.05(\text{syst.}) \pm 0.15(\text{BR}) \pm 0.17(\text{PR}) \quad (6.3)$$

$$\frac{\mathcal{B}(B_s^0 \rightarrow D_s^- \pi^+ \pi^+ \pi^-)}{\mathcal{B}(B^0 \rightarrow D^- \pi^+ \pi^+ \pi^-)} = 1.01 \pm 0.11(\text{stat.}) \pm 0.06(\text{syst.}) \pm 0.14(\text{BR}) \pm 0.15(\text{PR}), \quad (6.4)$$

where the last uncertainty is due to the uncertainty on the ratio of production rates,  $f_s/f_d$ .

At this point the precision of this analysis is limited by the systematic uncertainty on the external parameters. The systematic uncertainty will be reduced in the near future with improved measurements by CDF and other experiments.

It is interesting to compare the result of the measurement of  $\mathcal{B}(B_s^0 \rightarrow D_s^- \pi^+)/\mathcal{B}(B^0 \rightarrow D^- \pi^+)$  with the theoretical prediction we made in Chapter 1. As explained in Section 1.5, we have the following prediction for the branching fractions of  $B$  decays:

$$\frac{\mathcal{B}(B_s^0 \rightarrow D_s^- \pi^+)}{\mathcal{B}(B^0 \rightarrow D^- \pi^-)} = \frac{|T_{B_s^0}^{D\pi}|^2}{|T_{B^0}^{D\pi} + E_{B^0}^{D\pi}|^2} \frac{\Pi_{B_s^0} \tau_{B_s^0}}{\Pi_{B^0} \tau_{B^0}}, \quad (6.5)$$

where  $T_{B_s^0(B^0)}^{D\pi}$  and  $E_{B^0}^{D\pi}$  are the color-allowed tree and  $W$ -exchange contributions, respectively.  $\Pi_{B_s^0(B^0)}$  and  $\tau_{B_s^0(B^0)}$  denote the phase space factor and lifetime for the  $B_s^0$  ( $B^0$ ) meson.

If we assume factorization and neglect  $W$ -exchange contribution, then our measurement is a test of  $SU(3)_f$  symmetry in amplitude  $T$ . If  $SU(3)_f$  symmetry is good, we may compare the central value of our measurement with the  $SU(3)$  prediction  $\mathcal{B}(B_s^0 \rightarrow D_s^- \pi^+)/\mathcal{B}(B^0 \rightarrow D^- \pi^+) \approx 0.93$  (Equation 1.19) and find that they agree to better than one standard deviation. Of course, the precision of our measurements are limited, and a more critical test of  $SU(3)_f$  will be possible as both the external input and CDF measurements improve.

If we, on the other hand, assume  $SU(3)_f$  symmetry, then  $T_{B^0}^{D^- \pi} = T_{B_s^0}^{D_s^- \pi}$ . In addition, the  $SU(3)_f$  symmetry between  $B^0 \rightarrow D_s^- K^+$  and  $B_s^0 \rightarrow D_s^- \pi^+$  fixes the size of the exchange amplitude. If we then allow factorization to break down, we find the prediction  $\mathcal{B}(B_s^0 \rightarrow D_s^- \pi^+)/\mathcal{B}(B^0 \rightarrow D^- \pi^+) \approx 0.85$  (Equation 1.22), which is

further off from our measurement. This is an indication that  $SU(3)_f$  symmetry does not seem to be a better approximation than factorization for these decays.

In conclusion, we have presented the first observation of decay  $B_s^0 \rightarrow D_s^- \pi^+ \pi^+ \pi^-$  and have measured its branching fraction with respect to  $B^0 \rightarrow D^- \pi^+ \pi^+ \pi^-$ . We also have measured the ratio of branching fractions  $B_s^0 \rightarrow D_s^- \pi^+$  over  $B^0 \rightarrow D^- \pi^+$ , improving the statistical uncertainty over the previous measurement [66] by more than a factor of two.





# Appendix A

## Data fit parameters

Parameter	Meaning	Value	Error	Status
$N_C$	continuum overall norm	5.380	0.5	Float
$f_1$	continuum scale	39.10	0	Fix
$k$	continuum slope	0.001	0	Fix
$\mu$	continuum cutoff	5.140	0	Fix
$\tau$	continuum “lifetime”	0.261	0	Fix
$L_c$	continuum rad. tail scale	4.710	0	Fix
$k_c$	continuum rad. tail cutoff	5.300	0	Fix

Table A.1:  $B^0 \rightarrow D^- \pi^+$  fit continuum background parameters

Parameter	Meaning	Value	Error	Status
$N_R$	refl. overall norm	104.0	2.2	Float
$\lambda$	refl. "lifetime"	0.247	0	Fix
$f_G$	refl. base gaus fraction	0.195	0	Fix
$\mu - \nu$	refl. base gaus mean	5.020	0	Fix
$\sigma_R$	refl. base gaus width	0.052	0	Fix
$f_H$	refl. horn fraction	0.290	0	Fix
$\nu$	refl. horn offset	0.035	0	Fix
$\sigma_H$	refl. horn width	0.019	0	Fix
$\delta$	refl. horn separation	-0.046	0	Fix

Table A.2:  $B^0 \rightarrow D^- \pi^+$  fit reflection background parameters

Parameter	Meaning	Value	Error	Status
$N$	combin. background norm	230.0	12.2	Float
$\tau$	combin. background "lifetime"	2.360	0.129	Fix
$c$	combin. background constant	127.0	5.05	Fix

Table A.3:  $B^0 \rightarrow D^- \pi^+$  fit combinatorial background parameters

Parameter	Meaning	Value	Error	Status
$N_{Cab}$	Cabibbo background overall norm	50	0	Fix
$\mu$	Cabibbo background smeared mean	5.490	0	Fix
$\sigma$	Cabibbo background smeared width	0.295	0	Fix
$\tau$	Cabibbo background smeared "lifetime"	0.009	0	Fix
$f_1$	Cabibbo background plato fraction	0.844	0	Fix
$a$	Cabibbo background linear const	0.000	0	Fix
$b$	Cabibbo background slope	0.173	0	Fix
$\mu_1$	Cabibbo background plato mean 1	5.190	0	Fix
$\sigma_1$	Cabibbo background plato width 1	0.027	0	Fix
$\mu_2$	Cabibbo background plato mean 2	5.27	0	Fix
$\sigma_2$	Cabibbo background plato width 2	0.007	0	Fix

Table A.4:  $B^0 \rightarrow D^- \pi^+$  fit Cabibbo suppressed background parameters

Parameter	Meaning	Value	Error	Status
$N$	$\Lambda_b$ background overall norm	1.790	0	Fix
$\mu_1$	$\Lambda_b$ background mean 1	5.420	0	Fix
$\sigma_1$	$\Lambda_b$ background width 2	0.029	0	Fix
$f_1$	$\Lambda_b$ background gaus 2 fraction	0.248	0	Fix
$\mu_2$	$\Lambda_b$ background mean 2	5.280	0	Fix
$\sigma_2$	$\Lambda_b$ background width 2	0.094	0	Fix
$f_2$	$\Lambda_b$ background gaus 3 fraction	0.409	0	Fix
$\mu_3$	$\Lambda_b$ background mean 3	5.360	0	Fix
$\sigma_3$	$\Lambda_b$ background width 3	0.046	0	Fix

Table A.5:  $B^0 \rightarrow D^- \pi^+$  fit  $\Lambda_b$  background parameters

Parameter	Meaning	Value	Error	Status
$N_{ bs}$	$B_s^0$ background overall norm	1.220	0	Fix
$\mu_1$	$B_s^0$ background mean 1	5.330	0	Fix
$\sigma_1$	$B_s^0$ background width 1	0.018	0	Fix
$f_1$	$B_s^0$ background gaus 2 fraction	0.090	0	Fix
$\mu_2$	$B_s^0$ background mean 2	5.300	0	Fix
$\sigma_2$	$B_s^0$ background width 2	0.056	0	Fix
$f_2$	$B_s^0$ background gaus 3 fraction	0.482	0	Fix
$\mu_3$	$B_s^0$ background mean 3	5.320	0	Fix
$\sigma_3$	$B_s^0$ background width 3	0.027	0	Fix

Table A.6:  $B^0 \rightarrow D^- \pi^+$  fit  $B_s^0$  background parameters

Parameter	Meaning	Value	Error	Status
$N_S$	signal overall norm	84.40	1.190	Float
$f$	signal narrow gaus norm fraction	0.763	0	Fix
$\mu$	signal mean	5.280	0.0002	Float
$\sigma$	signal wide gaus width	0.031	0.0005	Float
$k$	signal narrow width fraction	0.533	0	Fix

Table A.7:  $B^0 \rightarrow D^- \pi^+$  fit signal parameters

Parameter	Meaning	Value	Error	Status
$N_C$	continuum overall norm	0.530	0.073	Float
$f_1$	continuum scale	59.60	0	Fix
$k$	continuum slope	0.979	0	Fix
$\mu$	continuum rad tail scale	20.90	0	Fix
$\tau$	continuum "lifetime"	0.129	0	Fix
$L_c$	continuum cutoff	5.180	0	Fix
$k_c$	continuum rad. tail cutoff	5.310	0	Fix

Table A.8:  $B_s^0 \rightarrow D_s^- \pi^+$  fit continuum background parameters

Parameter	Meaning	Value	Error	Status
$N_R$	refl. overall norm	11.60	0.671	Float
$f_r$	refl. gaus fraction	0.495	0	Fix
$\lambda$	refl. "lifetime"	0.187	0	Fix
$\mu_r$	refl. mean	5.190	0	Fix
$\sigma_r$	refl. width	0.066	0	Fix

Table A.9:  $B_s^0 \rightarrow D_s^- \pi^+$  fit reflection background parameters

Parameter	Meaning	Value	Error	Status
$N$	combin. background norm	12.00	3.33	Float
$\tau$	combin. background "lifetime"	1.330	0.822	Float
$c$	combin. background constant	3.250	0.319	Float

Table A.10:  $B_s^0 \rightarrow D_s^- \pi^+$  fit combinatorial background parameters

Parameter	Meaning	Value	Error	Status
$N$	Cabibbo background overall norm	0.333	0	Fix
$\mu$	Cabibbo background mean	5.320	0	Fix
$\sigma$	Cabibbo background width	0.022	0	Fix

Table A.11:  $B_s^0 \rightarrow D_s^- \pi^+$  fit Cabibbo suppressed background parameters

Parameter	Meaning	Value	Error	Status
$N_\Lambda$	$\Lambda_b$ background overall norm	0.030	0	Fix
$m_{0\lambda}$	$\Lambda_b$ background Breit Wigner mean	5.440	0	Fix
$\gamma_\lambda$	$\Lambda_b$ background Breit Wigner width	0.087	0	Fix

Table A.12:  $B_s^0 \rightarrow D_s^- \pi^+$  fit  $\Lambda_b$  background parameters

Parameter	Meaning	Value	Error	Status
$N$	$B^0$ background overall norm	0.073	0	Fix
$\mu$	$B^0$ background mean	5.340	0	Fix
$\sigma$	$B^0$ background width	0.020	0	Fix

Table A.13:  $B_s^0 \rightarrow D_s^- \pi^+$  fit  $B^0$  background parameters

Parameter	Meaning	Value	Error	Status
$N_S$	signal overall norm	5.180	0.292	Float
$f$	signal narrow gaus norm fraction	0.816	0	Fix
$\mu$	signal mean	5.370	0.001	Float
$\sigma$	signal wide gaus width	0.035	0.002	Float
$k$	signal narrow width fraction	0.502	0	Fix

Table A.14:  $B_s^0 \rightarrow D_s^- \pi^+$  fit signal background parameters

Parameter	Meaning	Value	Error	Status
$N_L$	continuum overall norm	4.980	0.474	Float
$s_1$	continuum rad. tail 1 scale	23.00	0	Fix
$k_1$	continuum rad. tail 1 slope	-0.004	0	Fix
$\tau_1$	continuum rad. tail 1 "lifetime"	8.370	0	Fix
$\mu_1$	continuum rad. tail 1 cutoff	5.240	0	Fix
$s_2$	continuum rad. tail 2 scale	35.40	0	Fix
$k_2$	continuum rad. tail 2 slope	3.540	0	Fix
$\tau_2$	continuum rad. tail 2 "lifetime"	99.00	0	Fix
$\mu_2$	continuum rad. tail 2 cutoff	5.150	0	Fix
$n_l$	continuum linear scale	9.320	0	Fix
$k$	continuum linear cutoff	5.540	0	Fix

Table A.15:  $B^0 \rightarrow D^- \pi^+ \pi^+ \pi^-$  fit continuum background parameters

Parameter	Meaning	Value	Error	Status
$N_R$	refl. overall norm	10.90	0.897	Float
$f_1$	refl. gaus 1 fraction	0.607	0	Fix
$f_2$	refl. gaus 2 fraction	0.317	0	Fix
$\mu$	refl. base gaus mean	4.980	0	Fix
$\delta_1$	refl. gaus 1 mean offset	-0.123	0	Fix
$\delta_2$	refl. gaus 2 mean offset	-0.068	0	Fix
$\sigma$	refl. base gaus width	0.199	0	Fix
$\sigma_1$	refl. gaus 1 width	0.022	0	Fix
$\sigma_2$	refl. gaus 2 width	0.016	0	Fix

Table A.16:  $B^0 \rightarrow D^- \pi^+ \pi^+ \pi^-$  fit reflection background parameters

Parameter	Meaning	Value	Error	Status
$N$	combin. background norm	221.0	62.40	Float
$\tau$	combin. background "lifetime"	0.636	0.325	Float
$c$	combin. background constant	54.90	70.30	Float

Table A.17:  $B^0 \rightarrow D^- \pi^+ \pi^+ \pi^-$  fit combinatorial background parameters

Parameter	Meaning	Value	Error	Status
$N_{Cab}$	Cabibbo background norm	3.150	0	Fix
$\mu$	Cabibbo background smeared mean	5.190	0	Fix
$\sigma$	Cabibbo background smeared width	0.194	0	Fix
$\tau$	Cabibbo background smeared "lifetime"	0.009	0	Fix
$1 - f_1$	Cabibbo background plateau norm	0.310	0	Fix
$a$	Cabibbo background linear const	3.570	0	Fix
$b$	Cabibbo background linear slope	8.312	0	Fix
$\mu_1$	Cabibbo background plateau mean 1	5.180	0	Fix
$\sigma_1$	Cabibbo background plateau width 1	0.097	0	Fix
$\mu_2$	Cabibbo background plateau mean 2	5.230	0	Fix
$\sigma_2$	Cabibbo background plateau width 2	0.027	0	Fix

Table A.18:  $B^0 \rightarrow D^- \pi^+ \pi^+ \pi^-$  fit Cabibbo background parameters

Parameter	Meaning	Value	Error	Status
$N$	$\Lambda_b$ background overall norm	5.661	0	Fix
$\mu_1$	$\Lambda_b$ background mean 1	5.371	0	Fix
$\sigma_1$	$\Lambda_b$ background width 1	0.045	0	Fix
$f_1$	$\Lambda_b$ background gaus 2 fraction	0.226	0	Fix
$\mu_2$	$\Lambda_b$ background mean 2	5.251	0	Fix
$\sigma_2$	$\Lambda_b$ background width 2	0.078	0	Fix
$f_2$	$\Lambda_b$ background gaus 3 fraction 3	0.359	0	Fix
$\mu_3$	$\Lambda_b$ background mean 3	5.191	0	Fix
$\sigma_3$	$\Lambda_b$ background width 3	0.261	0	Fix

Table A.19:  $B^0 \rightarrow D^- \pi^+ \pi^+ \pi^-$  fit  $\Lambda_b$  background parameters

Parameter	Meaning	Value	Error	Status
$N_{B_s^0}$	$B_s^0$ background overall norm	0.612	0	Fix
$\mu_1$	$B_s^0$ background mean 1	5.311	0	Fix
$\sigma_1$	$B_s^0$ background width 1	0.024	0	Fix
$f_1$	$B_s^0$ background gaus fraction 2	0.115	0	Fix
$\mu_2$	$B_s^0$ background mean 2	5.392	0	Fix
$\sigma_2$	$B_s^0$ background width 2	0.222	0	Fix
$f_2$	$B_s^0$ background gaus fraction3	0.209	0	Fix
$\mu_3$	$B_s^0$ background mean 3	5.251	0	Fix
$\sigma_3$	$B_s^0$ background width 3	0.054	0	Fix

Table A.20:  $B^0 \rightarrow D^- \pi^+ \pi^+ \pi^-$  fit  $B_s^0$  background parameters

Parameter	Meaning	Value	Error	Status
$N_S$	signal overall norm	25.612	0.678	Float
$f$	signal narrow gaus norm fraction	0.905	0	Fix
$\mu$	signal mean	5.279	0.0004	Float
$\sigma$	signal wide gaus width	0.036	0.001	Float
$k$	signal narrow width fraction	0.404	0	Fix

Table A.21:  $B^0 \rightarrow D^- \pi^+ \pi^+ \pi^-$  fit signal parameters

Parameter	Meaning	Value	Error	Status
$N_C$	continuum overall norm	0.265	0.042	Float
$s_1$	continuum rad. tail 1 scale	24.00	0	Fix
$k_1$	continuum rad. tail 1 slope	0.005	0	Fix
$\tau_1$	continuum rad. tail 1 "lifetime"	43.41	0	Fix
$\mu_1$	continuum rad. tail 1 cutoff	5.041	0	Fix
$s_2$	continuum rad. tail 2 scale	62.90	0	Fix
$k_2$	continuum rad. tail 2 slope	0.000	0	Fix
$\tau_2$	continuum rad. tail 2 "lifetime"	8.411	0	Fix
$\mu_2$	continuum rad. tail 2 cutoff	5.263	0	Fix
$n_l$	continuum linear scale	33.71	0	Fix
$k$	continuum linear cutoff	5.461	0	Fix

Table A.22:  $B_s^0 \rightarrow D_s^- \pi^+ \pi^+ \pi^-$  fit continuum background parameters

Parameter	Meaning	Value	Error	Status
$N_R$	refl. overall norm	1.511	0.241	Fix
$f_1$	refl. gaus 1 fraction	0.344	0	Fix
$\mu_1$	refl. gaus 1 mean	5.161	0	Fix
$\sigma_1$	refl. gaus 1 width	0.044	0	Fix
$f_2$	refl. gaus 2 norm frac	0.075	0	Fix
$\mu_2$	refl. gaus 2 mean	5.071	0	Fix
$\sigma_2$	refl. gaus 2 width	0.025	0	Fix
$f_3$	refl. gaus 3 frac	0.341	0	Fix
$\mu_3$	refl. gaus 3 mean	5.231	0	Fix
$\sigma_3$	refl. gaus 3 width	0.036	0	Fix
$\mu_r$	refl. smeared mean	5.312	0	Fix
$\sigma_r$	refl. smeared width	0.014	0	Fix
$\lambda_r$	refl. smeared "lifetime"	0.060	0	Fix

Table A.23:  $B_s^0 \rightarrow D_s^- \pi^+ \pi^+ \pi^-$  fit reflection background parameters

Parameter	Meaning	Value	Error	Status
$N$	combin. background norm	17.61	3.022	Float
$\tau$	combin. background "lifetime"	1.651	0.241	Float
$c$	combin. background constant	4.092	0.023	Float

Table A.24:  $B_s^0 \rightarrow D_s^- \pi^+ \pi^+ \pi^-$  fit combinatorial background parameters



Parameter	Meaning	Value	Error	Status
$N_{Cab}$	Cabibbo background norm	25.22	0	Fix
$\mu$	Cabibbo background smeared mean	6.351	0	Fix
$\sigma$	Cabibbo background smeared width	0.328	0	Fix
$\tau$	Cabibbo background smeared “lifetime”	1.291	0	Fix
$1 - f_1$	Cabibbo background plateau norm	0.607	0	Fix
$a$	Cabibbo background linear const	-41.1	0	Fix
$b$	Cabibbo background linear slope	9.482	0	Fix
$\mu_1$	Cabibbo background plateau mean 1	4.751	0	Fix
$\sigma_1$	Cabibbo background plateau width 1	0.011	0	Fix
$\mu_2$	Cabibbo background plateau mean 2	5.322	0	Fix
$\sigma_2$	Cabibbo background plateau width 2	0.023	0	Fix

Table A.25:  $B_s^0 \rightarrow D_s^- \pi^+ \pi^+ \pi^-$  fit Cabibbo background parameters

Parameter	Meaning	Value	Error	Status
$N_\Lambda$	$\Lambda_b$ background overall norm	0.001	0	Fix
$m_{0\lambda}$	$\Lambda_b$ background Breit Wigner mean	5.422	0	Fix
$\gamma_\lambda$	$\Lambda_b$ background Breit Wigner width	0.144	0	Fix

Table A.26:  $B_s^0 \rightarrow D_s^- \pi^+ \pi^+ \pi^-$  fit  $\Lambda_b$  background parameters

Parameter	Meaning	Value	Error	Status
$N_S$	signal overall norm	1.671	0.174	Float
$f$	signal narrow gaus norm fraction	0.852	0	Fix
$\mu$	signal mean	5.369	0.001	Float
$\sigma$	signal wide gaus width	0.030	0	Fix
$k$	signal narrow width fraction	0.479	0	Fix

Table A.27:  $B_s^0 \rightarrow D_s^- \pi^+ \pi^+ \pi^-$  fit signal parameters



## Acknowledgments

I would like to thank my family first and foremost. Thank you for being supportive and always being so excited at each milestone that I have reached along the way. Without your unconditional support I would have never been able to make it this far.

I want to thank my adviser Christoph Paus for his guidance, teaching, and support during completion of this analysis, demanding that things always “make sense” and that I understood them. I thank my first adviser Frank Wuerthwein for giving me the opportunity to join the CDF group.

I would like to thank MIT group for sharing graduate life experience with me. In particular, I would like to thank Ivan Furic, on whose footsteps I followed and who made vital contributions to this analysis. I thank senior MIT students Konstantin Anikeev, Alexander Rakitin, Mike Mulhearn, Andreas Korn for their friendship and helping me with software and in life. I thank younger MIT students Jeff Miles, Alberto Belloni, Khaldoun Makhoul, Georgios Choudalakis for taking over the hardware responsibility and letting me concentrate on my physics project. It has been an honor to work on Level 3 with Jeff Tseng and share office with him. Ilya Kravchenko has always been a great help and ready to answer any question I might have. I thank Steve Tether for his Java wisdom lessons. I admire Gerry Bauer for his broad scientific knowledge. Discussions with Conor Henderson were always fascinating. I am indebted to Bruce Knuteson for being the nicest person at MIT.

I have profited in this analysis enormously from the help of many experts and grateful to them for the support and constructive criticism. In particular, I would like to thank Rolf Oldeman, Alex Cerri, Tommaso Dorigo, Rob Harr, Matt Herndon, Stefano Giagu, Rick Tesarek for answering many questions that came up in the process. I thank my “God Parents” Jim Russ, Marco Rescigno and William Wester for improving the paper draft and helping me go public with this analysis.

Gratitude beyond words is reserved for Katya Korobkova for her love, for giving me strength and being ears to my endless stream of conscience.



# Bibliography

- [1] S. W. Herb *et al.*, Phys. Rev. Lett. **39**, 252 (1977).
- [2] Particle Data Group, W. M. Yao *et al.*, J. Phys.**G** **33**, 1 (2006).
- [3] A. Abulencia *et al.* [CDF Collaboration], Phys. Rev. Lett. **97**, 062003 (2006).
- [4] A. Abulencia *et al.* [CDF Collaboration], Submitted to Phys. Rev. Lett., hep-ex/0609040.
- [5] P. Colangelo and R. Ferrandes, Phys. Lett. **B 627**, 77 (2005).
- [6] C. S. Kim, S. Oh, and C. Yu, Phys. Lett. **B 621**, 259 (2005), hep-ph/0412418.
- [7] Z. Z. Xing, Nucl. Phys. **26**, 100 (2002).
- [8] S. Glashow, Nucl. Phys. **19**, 579 (1961).
- [9] S. Weinberg, Phys. Rev. Lett **19**, 1264 (1967).
- [10] *Elementary Particle Theory*, edited by N. Svartholm (Almquist and Wiksells, Stockholm, 1969).
- [11] See for example J. Schwinger, *Quantum Mechanics*, Dover Publications Inc., New York (1958).
- [12] G. Arniston *et al.* [UA1 Collaboration], Phys. Lett. **B 122**, 103 (1983).
- [13] P. Bagnaia *et al.* [UA2 Collaboration], Phys. Lett. **B 122**, 476 (1983).
- [14] G. Arniston *et al.* [UA1 Collaboration], Phys. Lett. **B 126**, 398 (1983).

- [15] P. Bagnaia *et al.* [UA2 Collaboration], Phys. Lett. **B 129**, 130 (1983).
- [16] R. K. Ellis, W. J. Stirling, *QCD and Collider Physics*, Cambridge University Press, Cambridge, UK (1996).
- [17] E. Eichten and B. Hill, Phys. Lett. **B 234**, 511 (1990).
- [18] M. Bauer, B. Stech, and M. Wirbel, Z.Phys. **C 29**, 637 (1985).
- [19] M. Bauer, B. Stech, and M. Wirbel, Z.Phys. **C 34**, 103 (1987).
- [20] K. Anikeev *et al.*, *B physics at the Tevatron: Run II and beyond*, hep-ph/0201071.
- [21] See for example F. Halzen and A. Martin, *Quarks and Leptons: An Introductory Course in Modern Particle Physics*, John Wiley and Sons, New York (1984).
- [22] M. Imbeault, A. Datta and D. London, hep-ph/0603214.
- [23] C. S. Kim, T. Morozumi, S. Oh and C. Yu, work in preparation.
- [24] C. W. Schmidt, *The Fermilab 400-MeV Linac upgrade* FERMILAB-CONF-93-111 (1993).
- [25] J. Marriner, *Stochastic Cooling Overview*, FERMILAB-CONF-03-158 (2003).
- [26] R. Blair *et al.*, *The CDF-II detector: Technical design report*, FERMILAB-PUB-96/390-E (1996).
- [27] T. K. Nelson *et al.*, FERMILAB-CONF-01/357-E.
- [28] A. Sill *et al.*, Nucl. Instrum. Meth., **A 447**, 1 (2000).
- [29] T. Affolder *et al.*, Nucl. Instrum. Meth., **A 485**, 6 (2002).
- [30] R. Blair *et al.*, *The CDF-II detector: Technical design report*, FERMILAB-PUB-96/390-E (1996).
- [31] K. T. Pitts *et al.*, FERMILAB-CONF-96-443-E.

- [32] D. Acosta *et al.*, Nucl. Instrum. Methods, **A 518**, 605 (2004).
- [33] M. Mulhearn, PhD thesis, MIT (2004).
- [34] S. Hahn, <http://www-cdfonline.fnal.gov/ops/ace2help/aceacronyms.html>.
- [35] L. Balka, *et al.*, Nucl. Instrum. Methods, **A 267**, 272 (1988).
- [36] S. Bertolucci, *et al.*, Nucl. Instrum. Methods, **A 267**, 301 (1988).
- [37] T. Moulik, *Offline Central PreRadiator Reconstruction*, CDF note 6192.
- [38] G. Apollinary *et al.*, Nucl. Instrum. Meth. **A 412** 515-526, (1998).
- [39] P. Schlabach, *CDF Central Muon Detector*,  
<http://www-cdf.fnal.gov/internal/upgrades/muon/cmu.html>.
- [40] P. Schlabach, *CDF Muon Upgrade Detector*,  
<http://www-cdf.fnal.gov/internal/upgrades/muon/cmp.html>.
- [41] P. Schlabach, *CDF Central Muon Extension Detector*,  
<http://www-cdf.fnal.gov/internal/upgrades/muon/cmx.html>.
- [42] E. J. Thomson *et al.*, IEEE Trans. Nucl. Sci **49**, 1063 (2002).
- [43] W. Ashmanskas *et al.*, Nucl. Instrum Methods Phys Res. **A 447**, 218 (2000);  
W. Ashmanskas *et al.*, FERMILAB-CONF-02/035-E;  
A. Bardi *et al.*, Nucl. Instrum Methods Phys Res. **A 485**, 6 (2002).
- [44] I. Yu and J. Lewis, *Study of  $B \rightarrow \pi^+ \pi^-$  trigger rate for Run II*, CDF Note 4095.
- [45] A. Belloni, I.K. Furic, Ch. Paus, *Multibody Trigger Paths in the Two Track Trigger Data*, CDF Note 6526.
- [46] W. Badgett, *The CDF Run II Run Database and Online Java API*, CDF Note 5672.
- [47] Ch. Paus *et. al.*, see CdfCode browser:  
<http://cdfkits.fnal.gov/CdfCode/source/BottomMods/> .

- [48] P. Murat *et al.*, see CdfCode browser:  
<http://cdfkits.fnal.gov/CdfCode/source/Stntuple/> .
- [49] M. Campanelli, *Calibration of the momentum scale for Kalman Fitter using  $J/\psi$  events*, CDF Note 6905.
- [50] M. Feindt, S. Menzemer, K. Rinnert, P. Schemitz, and A. Skiba, *KalKalmanFitter - A Fast and Versatile Kalman Track-Fitter for CDF II*, CDF Note 5388.
- [51] B. Ashmanskas and A. Cerri, see CdfCode browser:  
<http://cdfcodebrowser.fnal.gov/CdfCode/source/svtsim/> .
- [52] J. Marriner, *Secondary Vertex Fit with Mass and Pointing Constraints (CT-VMFT)*, CDF Note 1996.
- [53] K. Anikeev, P. Murat, and Ch. Paus, *Description of Bgenerator II*, CDF Note 5092.
- [54] P. Nason, S. Dawson and R.K. Ellis, Nucl. Phys. **B 303**, 607 (1988); Nucl. Phys. **B 327**, 49 (1989).
- [55] C. Peterson *et al.*, Phys. Rev. **D 27** 105 (1983).
- [56] M. Cacciari *et al.*, *QCD Analysis of First B Cross-Section Data at 1.96 TeV*, hep-ph/0312132.
- [57] W. Bell, J.P. Fernandez, L. Flores, F. Wuerthwein, R.J. Tesarek, *User Guide For EvtGen CDF*, CDF Note 5618.
- [58] E. H. Thorndike *et al.* [CLEO Collaboration], AIP Conf. Proc. **68**, 705 (1980).
- [59] D. Boutigny *et al.*, *BaBar technical design report*, SLAC-R-0457 (1995).
- [60] R. Brun, K. Hakelberg, M. Hansroul, and J.C. Lasalle, CERN-DD-78-2-REV; CERN-DD-78-2.



- [61] D. Boutigny et al., SLAC-R-0457.
- [62] A. Abulencia *et al.* [CDF Collaboration], Submitted to Phys. Rev. Lett., hep-ex/0601003.
- [63] D. Acosta *et al.* [CDF Collaboration], Phys. Rev. **D 71**, 032001 (2005).
- [64] S. Giagu *et al.*, *BR ratios and Direct CP violation in Cabibbo suppressed decay of  $D^0$* , CDF Note 6391.
- [65] M. Jones, *Initial Performance Studies of the CDF-II Time-of-Flight Detector*, CDF Note 5930.
- [66] A. Abulencia *et al.* [CDF Collaboration], Phys. Rev. Lett. **96**, 191801 (2006).